

Aptamer functionalized nanostructured biosensing platforms for enteric pathogenic bacteria

Harmanjit Kaur

*A thesis submitted for the partial fulfillment of
the degree of Doctor of Philosophy*



Institute of Nano Science and Technology

Knowledge city, Sector 81, SAS Nagar, Mohali, Punjab 140306, India

Indian Institute of Science Education and Research Mohali

Knowledge city, Sector 81, SAS Nagar, Mohali, Punjab 140306, India

February 2021

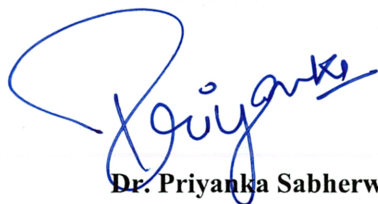
Declaration

The work presented in this thesis has been carried out by me under the guidance of Dr. Priyanka Sabherwal and Dr. Sharmistha Sinha at Institute of Nano Science & Technology, Mohali. This work has not been submitted in part or in full for a degree, a diploma, or a fellowship to any other university or institute. Whenever contributions of others are involved, every effort is made to indicate this clearly, with due acknowledgment of collaborative research and discussions. This thesis is a bonafide record of original work done by me, and all sources listed within have been detailed in the bibliography.



Ms. Harmanjit Kaur

In my capacity as the supervisor of the candidate's thesis work, I certify that the above statements by the candidate are true to the best of my knowledge.



Dr. Priyanka Sabherwal



Dr. Sharmistha Sinha

Acknowledgement

An intellectual quest it has been, since I began my doctorate in the Institute of Nano Science & Technology (INST) and IISER-Mohali. Though my words below do not do much justice to the cumulative efforts of all those who have contributed to the work presented in this thesis, I am honestly appreciative of their presence and support in all forms.

I am immensely grateful to Dr. Priyanka Sabherwal, whose expertise, understanding, and guidance made it possible for me to carry out my thesis work. It was a pleasure working with her, and words would fall short of describing her importance in shaping this doctoral work. I am thankful to her for believing in my research capabilities and giving me a delightful break to follow research in the field of applied nano-sciences and setting an example of how to work & present yourself in the versatile area of biosensors. She gave me various opportunities and platforms to prove my scientific research and effectively troubleshoot when there were difficulties. Along this road, I learned a lot from her experiences and suggestions, which had always helped me in carrying forth the experiments even when I had given up. I take this opportunity to thank her for being a mentor all along and giving her valuable scientific inputs & time for evaluating this doctoral thesis.

I would like to express my gratitude to Dr. Sharmistha Sinha for being generous to provide me with her support, knowledge and the facilities of her lab. I am deeply indebted to her, for her extensive cooperation & encouragement in this rollercoaster tenure. I express deep gratitude to her for going out of her way at multiple occasions to support me in my scientific endeavors and making this thesis compilation a reality.

I am equally thankful to Prof. Amitava Patra (Director) & Prof. Hirendra Nath Ghosh (ex-Off. Director) for allowing me to carry on my thesis work in this esteemed institution. My sincere and heartfelt thanks to Prof. Ashok Kumar Ganguli (founder Director) for his constant support and leadership. His unmarked spirit has always inspired me to work hard and conscientiously.

I also thank my doctoral committee members, Dr. Sangita Roy and Dr. Surajit Karmakar, for giving me valuable suggestions to improve my research work and supporting me throughout my doctoral studies. My particular words of thanks to Prof. C.R. Suri and his lab members, who has been a cheerful motivator and mentor and helpful in my scientific works. I'd also take this opportunity to thank all the scientists, notably Dr. Kiran Hazra, Dr. Vivek Bagchi, Dr. Menaka Jha, Dr. Neha Sardana, Dr. Deepa Ghosh, Dr. Abir De Sarkar & Dr. Kaushik Ghosh, for their kind and generous words which have uplifted my spirits to move forward. A special thanks to Prof. Navakanta Bhat for allowing our lab members to utilize the state-of-the art nanofabrication facility at CeNSE, IISc. I thank all the non-teaching staff viz., Late Mr. P.K. Dutta, Mr. U.C. Prasad, Mr. J.N. Ahuja, Mr. Surinder, Mr. Mukesh, Ms. Vibha, Ms. Gurveen, Ms. Suman, Mr. Dhanjit, Mr. Rajeev and Ms. Shewta, for sharing their experiences and helping me in various ways throughout my doctoral study time in INST.

During my doctoral studies, I have had a great association with fellow lab-mates for whom I have high regard; Dr. Vinod Kumar, who motivated and supported me from the very beginning of this journey; Dr. Kulvinder Singh & Dr. Vijay K. Tomer, who helped enhance my exposure to the scientific community; Munish Shorie, who made my stay in INST a memorable and exciting time. I would like to express thanks for your affection, constant help, assistance, explanation of basic facts, key details, and practical aspects of the lab.

I am deeply thankful to my dear friends- Pulkit, Pushpendra, Harsimran, Ruchi, Neha, Renu, Ashmeet and Sandeep whose companionship allowed me to work in my best capacity in lab. My dear fellow mates- Atul, Anirban, Rajendra, Swati, Naimat, Ritu & Rashmi, Ankush, Silky, Pooja, Krishna, Sushil, Mahima, Komal, Himadari, Avinash, Bandana, Harpreet, Deepika, Krishna and Sunaina, who supported me during my time at the institute. Special thanks to Dr. Gagandeep for her constant support in dry lab studies. This acknowledgment would be empty without thanking my friends and classmates with whom I started this ride of biotechnology; Maleeka, Harpreet, Manvi, Reena, Gursimran, Simranbir, Manisha, Parminder, Prashant, Sourabh, Monika, Neetu & Jashan.

Finally, I owe my loving thanks to my family, who stood by me through thick & thin. To my elder brother, Pavitra, who has been my emergency back support and especially my mother Arminderjit, a constant inspiration for hard work and selflessness, who put her faith in me and urged me to do better at every step no matter what the circumstances were. My humble salutation with a bowed head to the God almighty who made everything; known, unknown, and all that's beyond the grasp of science, observation & measurement. My father late Surinder Paul, who taught me to observe, question when in doubt, and for instilling a scientific temperament in our house. I will always be your student, Papa. My late aunt Sarabjit Vohra, a mother figure who gave a lot more than just love. My dearest late grandmother Harbans Kaur, who instilled iron-strength will and never-give-up aptitude and all those godly figures who made it possible for me to pursue my higher education and thus, making this thesis possible.

Many I haven't mentioned but certainly not forgotten; your constant support, guidance & cooperation has made me an improved person, and this thesis a reality.

Thank you!

Harmanjit Kaur

Table of contents

Table of contents	i-ii
Abbreviations	iii-iv
Nomenclature	v
Abstract	vii-ix
<hr/>	
1 Introduction	1-40
<hr/>	
1.1 Preface	1
1.2 Enteric pathogenic bacteria	2
1.3 Conventional microbial detection methods	9
1.4 The need for improved diagnostic platforms	14
1.5 Sensors	15
1.6 Biosensor	16
1.7 Nanostructured sensing platforms	24
1.8 Our bio-sensing approach	31
Bibliography	34
<hr/>	
2 Nanostructured aptasensor for enterotoxigenic <i>E. coli</i>	41-66
<hr/>	
2.1 Introduction	41
2.2 Experimental procedure	44
2.3 Results & discussion	52
2.4 Conclusion	65
Bibliography	65
<hr/>	
3 Nanostructured aptasensor for enterohemorrhagic <i>E. coli</i>	67-102
<hr/>	
3.1 Introduction	67
3.2 Experimental procedure	70
3.3 Results & discussion	75
3.4 Microfluidics- An introduction	88
3.5 Conclusion	99
Bibliography	99
<hr/>	
4 Aptasensing optical assay for <i>E. coli</i> surface antigens	103-128
<hr/>	
4.1 Introduction	103
4.2 Experimental procedure	107
4.3 Results & discussion	112
4.4 Conclusion	125
Bibliography	126
<hr/>	
5 Nanostructured aptasensor for <i>E. coli</i> Stx subtypes	129-154
<hr/>	
5.1 Introduction	129
5.2 Experimental Procedure	132
5.3 Results & Discussion	137
5.4 Conclusion	152
Bibliography	152
<hr/>	
6 Conclusion	155-162
<hr/>	

6.1	Summary of the thesis	155
6.2	Concluding remarks & future perspectives	161
	Bibliography	162

	Publications	163
	Vita	165

Abbreviations

Apt	Aptamer
AR2G	Amine Reactive 2 nd Generation
ATCC	American Type Culture Collection
BC-Ni	Boron Carbon nanorods decorated with Nickle Nanoparticles
BET	Brunauer-Emmett-Teller
BLI	Biolayer Interferometry
BRG	Bridged Rebar Graphene
C _{dl}	Double Layer Capacitance
C-dots	Carbon Dots
CE	Counter Electrode
cfu	Colony-Forming Units
Chito	Chitosan
CNT	Carbon Nanotubes
CV	Cyclic Voltammetry
DLS	Dynamic Light Scattering
DNA	Deoxyribonucleic Acid
<i>E. coli</i>	<i>Escherichia coli</i>
EDX	Energy Dispersive X-Ray Spectroscopy
EHEC	Enterohemorrhagic <i>E. coli</i>
EIS	Electrochemical Impedance Spectroscopy
ETEC	Enterotoxigenic <i>E. coli</i>
FDA	Food and Drug Administration (US National Body)
FPLC	Fast Protein Liquid Chromatography
FTIR	Fourier Transform Infrared
GI	Gastrointestinal
GO	Graphene Oxide
G-quad	Guanine Quadruplex
H	Flagellar Antigen
K _d	Dissociation Constant
LOD	Limit of Detection
LB	Luria-Bertani
LPS	Lipopolysaccharides
MTCC	Microbial Type Culture Collection
MWCNT	Multi-Walled Carbon Nanotubes

nt	Nucleotide
NP	Nanoparticles
O	Somatic Antigen
OD	Optical Density
PB	Phosphate Buffer
PBS	Phosphate Buffer Saline
PCR	Polymerase Chain Reaction
PLL	Poly-L-Lysine
PoC	Point of Care
QD	Quantum Dots
QGRS	Quadruplex Forming G-Rich Sequences
R_{ct}	Charge Transfer Resistance
RCF	Relative Centrifugal Force
rGO	Reduced Graphene Oxide
RFU	Relative Fluorescence Units
RPM	Rotations Per Min
SAM	Self-Assembled Monolayer
SELEX	Systemic Evolution of Ligands by Exponential Enrichment
SEM	Scanning Electron Microscope
SMAC	Sorbitol MacConkey
SPE	Screen-Printed Electrode
ss	Single-Stranded
SSA	Super-Streptavidin
STEC	Shiga-Toxin Producing <i>E. coli</i>
Stx	<i>E. coli</i> Shiga Like Toxin
SWV	Square Wave Voltammetry
TEM	Transmission Electron Microscope
T_m	Melting Temperature
TSB	Tryptone Soya Broth
UV-Vis	Ultraviolet-Visible
WE	Working Electrode
WHO	World Health Organization
WSe ₂	Tungsten Diselenide
XRD	X-Ray Diffraction
Z	Impedance

Nomenclature

x^{-1}	Per (where x defines a variable)
\pm	Standard Error
$\times g$	Times Gravity
μ	Micro (10^{-6})
μg	Microgram
μM	Micromolar
∞	Infinity
$^{\circ}C$	Degree Celsius
\AA	Angstrom (10^{-10})
cc	Cubic Centimeter
cm	Centimeter (10^{-2} m)
g	Gram
H	Enthalpy
h	Hour
k	Kilo
K	Kelvin
kV	Kilo volt
L	Liter
m	Milli (10^{-3})
min	Minute
n	Nano (10^{-9})
ng	Nanogram
nM	Nanomolar
p	Pico (10^{-12})
pM	Picomolar
s	Second
S	Entropy
Δ	Change
ζ	Zeta Potential
θ	Theta Angle
λ	Wavelength
Ω	Ohms

Abstract

Out of the vast myriad of bacterial species that colonize the gastrointestinal tract, *Escherichia coli* has been a persistent member of the mammalian gut microflora where a majority of its strains maintain a commensal or mutualistic relationship with the human host¹. However, its disease-causing variants (pathogens) genetically encoded with specific virulence factors also exist^{2,3}. Pathogenic *E. coli* has been reported as a significant etiological agent of bacterial gastroenteritis with an infectious dose as low as ~100 cells^{4,5}. These are responsible for chronic or persistent diarrhea, with certain pathotypes producing enterotoxins responsible for the hemolytic uremic syndrome as sequela⁶⁻⁸. Conventional 'gold standard' microbiological tools require 2-3 days for identification, while the current diagnostic approaches majorly reliant on antibody-based assays or mass spectrometry, utilize costly reagents and require specific instrumentations for estimation^{9,10,11}. Thus, the challenge lies in developing sensitive, rapid, non-culture dependent, and cost-effective methodologies for the sensing of enteric pathogenic bacteria, which are required for timely monitoring in food, clinical, and municipal sectors.

Integrated biosensing platforms with specific bio-receptor (nucleic acid aptamers) and sensitive transducer (nanostructured materials), providing near real-time information on the presence of enteric targets, are proposed in this doctoral thesis. Nanostructures of various dimensions based on carbon, metal-carbon nanohybrids, and more recently, its 2D analogs transition metal chalcogenides, harboring fascinating electronic, optoelectronic, and physical qualities such as abundant surface charges, high surface-to-volume ratio, and easy functionalization abilities were synthesized indigenously via various top-down and bottom-up approaches and utilized as transducers in the biosensing platforms. Simultaneously, for the bio-receptor component, deoxynucleic acid (DNA) aptamers (single-stranded oligomers with high binding affinity with the specific target) were chosen, providing low cross-reactivity than conventionally available counterparts^{12,13}. The studies reported in this thesis majorly gravitate around biosensing pathogenic *E. coli* (serotypes O78:H11 and O157:H7) with aptamer-based nanostructured sensing technology as the critical line of detection approach.

We devised a three-way approach for aptamer generation stemming from alternative enhanced binding affinities for the target in various environments, which was based on the hypothesis that the presence of both whole-cell or its components is possible for monitoring the bacterial targets. Therefore, multiple respective aptamers were screened against the avirulent strains of whole-cell *E. coli* (enterotoxigenic serotype O78:H11 and enterohemorrhagic serotype O157:H7), surface antigens (endotoxin, flagellar protein) for serotype O157:H7, and Shiga-like toxins (Stx1 and Stx2) utilized as bio-recognition moieties, which are comprehensively explored one-by-one during the doctoral studies. The objective was also to explore methodologies for aptamer generation and the simultaneous synthesis of nanostructures relevant for aptasensing via

spectroscopic and electrochemical tools. Thus, in line with our aim, various fully characterized DNA aptamers with an excellent affinity (nanomolar K_d) to the selected bacterial targets were successfully screened from a naïve oligomer library of 81 nucleotides with 45 nucleotide random region, implementing indigenous in-vitro selection SELEX (systematic evolution of ligands by exponential enrichment) methodologies of oligomer panning for the selected targets:

- (i) **Microtiter cell-SELEX** using phenylboronic acid as a capturing agent for *E. coli* bacteria accompanied by counter screening to mitigate aptamer cross-talk with other closely related bacterial species (K_d of 14 nM for O78:H11 and 69 nM for O157:H7 serotype, respectively) was developed.
- (ii) **Competitive microtiter-SELEX** employing rival ligands for raising stringency for purified *E. coli* O157:H7 endotoxin and flagellar proteins (K_d of 5.3 and 4.6 nM, respectively) was developed.
- (iii) **Biolayer interferometry (BLI)-SELEX** using Octet Red96 system, a one-step technique for rapidly generating aptamers against *E. coli* Shiga toxin subtypes viz., Stx1 & Stx2 via specific epitopic peptides (K_d of 47 pM & 29 pM, respectively) in a dip microtiter plate format, obliterating the need for multiple oligomer enrichment cycles was designed and demonstrated.

Parallely, novel nanomaterials of various nano-dimensions (0D, 1D, 2D, 3D) exhibiting excellent transducer properties were synthesized and characterized using microscopic (scanning electron microscopy, transmission electron microscopy), spectroscopic (ultraviolet-visible and fluorescence spectroscopy, confocal Raman spectroscopy, Fourier transform Infra-red spectroscopy, X-ray diffraction and, energy-dispersive X-ray elemental mapping), electrochemical (cyclic voltammetry, impedance spectroscopy, square wave voltammetry) and other analytical techniques (dynamic light scattering, zeta potential and Brunauer–Emmett–Teller (BET) surface area analysis) techniques.

The specific aptamers conjugated with enhanced nanostructures conferred both selectivity and sensitivity in spiked water samples and complex matrices like juices and sera, with minor pre-processing steps mentioned in respective chapters. The following biosensing platforms were demonstrated for the selected targets:

- (i) Label-free impedimetric sensing of *E. coli* O78:H11 was successfully demonstrated using novel selected **aptamer functionalized bridged rebar graphene** (synthesized by un-scrolling of multiwall carbon nanotubes and bridged using terephthalaldehyde forming 3D nano-construct) onto disposable screen-printed electrodes demonstrating a limit of detection ~ 10 cells and a dynamic response range from 10^1 to 10^6 cells.
- (ii) Label-free impedimetric sensing of *E. coli* O157:H7 was showed using specific **aptamer functionalized boron-carbon nanorods decorated by nickel nanoparticles** with a similar limit of detection and a dynamic detection range of 10^0 to 10^5 cells in water and juice samples.
- (iii) Fluorescence ‘turn on’ bioassay based on fluorescence quenching of **aptamer functionalized carbon-dots by silver nanoparticles**, which in the presence of the *E. coli* O157:H7

purified O-antigen and H-antigen was recovered, showing a limit of 0.12 pg mL⁻¹, a wide dynamic range of detection (1 pg mL⁻¹ – 10 ng mL⁻¹) and the stable response recorded even in pure water.

(iv) A voltammetric diagnostic assay via aptamer functionalized onto **chitosan exfoliated 2D tungsten diselenide (WSe₂) nanosheet** platform showing a dynamic response range from 50 pg mL⁻¹ – 100 ng mL⁻¹, and detection limit of 44.5 pg mL⁻¹ & 41.3 pg mL⁻¹ for Stx1 and Stx2, respectively, which showed minimal cross-reactivity in spiked sera samples.

These nanostructured aptasensors showed quick results, negating the enrichment of bacterial load in test samples as required in conventional systems. The aptamers also showed admirable application as capture & detection for bacterial populations onto soft-lithographed polydimethylsiloxane based microfluidic biosensing platforms.

In toto, this thesis addresses the issues of conventional detection of enteric pathogenic *E. coli* species and, the unique detection methodologies presented in the studies can be further extended to other clinically or environmentally relevant bacterial species, antigens or biomolecules, including viral diseases like COVID-19, hepatitis, and influenza. The scientific works included herein are advantageous for the development of analytical platforms using cost & reagent-effective protocols for pathogen or bio-analyte determination and thus, holds promising future perspectives in the field of in-vitro clinical diagnostics.

Bibliography

- (1) Biomechanics of the Digestive System. In *Integrated Nano-Biomechanics*; Elsevier, 2018; pp 71–99. <https://doi.org/10.1016/b978-0-323-38944-0.00003-6>.
- (2) Kaper, J. B.; Nataro, J. P.; Mobley, H. L. T. Pathogenic Escherichia Coli. *Nat. Rev. Microbiol.* **2004**, *2* (2), 123–140. <https://doi.org/10.1038/nrmicro818>.
- (3) Leimbach, A.; Hacker, J.; Dobrindt, U. E. Coli as an All-Rounder: The Thin Line between Commensalism and Pathogenicity. *Curr. Top. Microbiol. Immunol.* **2013**, *358*, 3–32. https://doi.org/10.1007/82_2012_303.
- (4) Pennington, H. Escherichia Coli O157. *Lancet* **2010**, *376* (9750), 1428–1435. [https://doi.org/10.1016/S0140-6736\(10\)60963-4](https://doi.org/10.1016/S0140-6736(10)60963-4).
- (5) Nataro, J. P.; Kaper, J. B. Diarrheagenic Escherichia Coli. *Clinical Microbiology Reviews*. January 1998, pp 142–201. <https://doi.org/10.1128/cmr.11.1.142>.
- (6) Saxena, T.; Kaushik, P.; Krishna Mohan, M. Prevalence of E. Coli O157: H7 in Water Sources: An Overview on Associated Diseases, Outbreaks and Detection Methods. *Diagn. Microbiol. Infect. Dis.* **2015**, *82* (3), 249–264. <https://doi.org/10.1016/j.diagmicrobio.2015.03.015>.
- (7) Yang, S. C.; Lin, C. H.; Aljuffali, I. A.; Fang, J. Y. Current Pathogenic Escherichia Coli Foodborne Outbreak Cases and Therapy Development. *Arch. Microbiol.* **2017**, *199* (6), 811–825. <https://doi.org/10.1007/s00203-017-1393-y>.
- (8) Croxen, M. A.; Law, R. J.; Scholz, R.; Keeney, K. M.; Wlodarska, M.; Finlay, B. B. Recent Advances in Understanding Enteric Pathogenic Escherichia Coli. *Clin. Microbiol. Rev.* **2013**, *26* (4), 822–880. <https://doi.org/10.1128/CMR.00022-13>.
- (9) Lazcka, O.; Campo, F. J. Del; Muñoz, F. X. Pathogen Detection: A Perspective of Traditional Methods and Biosensors. *Biosens. Bioelectron.* **2007**, *22* (7), 1205–1217. <https://doi.org/10.1016/j.bios.2006.06.036>.
- (10) Humphries, R. M.; Linscott, A. J. Laboratory Diagnosis of Bacterial Gastroenteritis. *Clin. Microbiol. Rev.* **2015**, *28* (1), 3–31. <https://doi.org/10.1128/CMR.00073-14>.
- (11) BAM Chapter 4A: Diarrheagenic Escherichia coli | FDA <https://www.fda.gov/food/laboratory-methods-food/bam-chapter-4a-diarrheagenic-escherichia-coli> (accessed Aug 22, 2020).
- (12) Wu, Y. X.; Kwon, Y. J. Aptamers: The “Evolution” of SELEX. *Methods* **2016**, *106*, 21–28. <https://doi.org/10.1016/j.ymeth.2016.04.020>.
- (13) Ali, M. H.; Elsherbiny, M. E. Updates on Aptamer Research. **2019**, 1–23.



Chapter 1

Introduction



Chapter 1

Introduction

This chapter provides an overview of conventional & currently used sensing techniques for enteric pathogenic bacteria, primarily focusing on the generation of aptamer as bio-recognition moiety and synthesis of nanostructures integrated as aptamer functionalized nano-sensing platforms.

1.1 Preface

Microorganisms are found ubiquitously in nature, widely distributed from water & food sources to both on the surface and inside the body of animals. Though disease inflicting organisms (pathogens) account for less than 1% of the identified microbes, they have been documented for significant epidemic episodes throughout the human history¹. The most common food & waterborne diseases like diarrhea, typhoid, cholera, have causative organisms abundantly present in the fecal matter of the infected animal. These diseases are infectious and contagious, quickly spread unless monitored regularly, and curtailed at the root. The food and waterborne pathogens affect ~600 million people globally due to easier penetration via oral route². Diarrheal illnesses are responsible for ~1.5 million deaths annually³.

Out of the vast myriad of bacterial species that colonize the gastrointestinal tract, *Escherichia coli* (abbreviated as *E. coli*) has been a versatile member of the mammalian gut microflora⁴. Even though its commensal strains rarely cause disease except in immunocompromised hosts or where the natural gastrointestinal barriers are breached, its pathogenic variants are genetically encoded with specific virulence factors that lead to disease manifestation^{5,6}. Pathogenic *E. coli* has been reported as a significant etiological agent responsible for bacterial gastroenteritis via infectious dose as low as ~100 cells and with a substantial burden of disease in children under the age of five, pervasive in both developing and developed countries with a large number of its outbreaks attributed to consumption of contaminated water and raw or undercooked food^{7,8}. Pathogenic *E. coli* strains show high fecundity even in water and are, therefore, responsible for deplorable morbidity with chronic or persistent diarrhea and certain strains producing enterotoxins inducing systemic meningitis or nephron damage as sequela⁹⁻¹¹. Thus, timely monitoring and detection have become essential in food, clinical, and municipal sectors required to abate outbreaks. Conventional microbiological tools like culturing, staining, and microscopic evaluation require 2-3 days for identification and are mostly qualitative in nature^{12,13}. The current diagnostic approaches are majorly reliant on antibody-based assays or mass spectrometry, which utilize costly reagents and require specific instrumentations for estimation¹⁴. Hence, the development of sensors for a myriad of clinically or environmentally significant molecules is a hot research area. Especially for pathogens, the sensing of each microbial species demands different sample processing and detection

methodology, requiring multi-step and laborious techniques for diagnosis. Thus, the challenge was to develop sensitive, rapid, non-culture dependent, and cost-effective methodologies for the detection of enteric pathogenic bacteria.

The prime focus of this thesis work is the research & development of specific and sensitive aptasensors with the help of nanosensing techniques for enteric bacterial pathogens. The studies in the impending chapters of the thesis majorly gravitate around sensing pathogenic *E. coli* (serotypes O78:H11 and O157:H7) and associated biomolecules with aptamer-based nanostructured sensing technology. Aptamer-based receptors have gained recognition as next-generation antibody mimics due to their comparable binding affinities & target specificities to antibodies. Through the rapid progress in molecular biology and material science, the amalgamation of specific bio-receptors and sensitive nanomaterials has paved the way for noteworthy biosensors. These functionalized nanostructures have revolutionized, expanded, and encouraged transdisciplinary nano-biosciences, which is crucial for developing efficient platforms for both clinical diagnostics & environmental monitoring.

1.2 Enteric pathogenic bacteria

Enteric bacteria are predominantly Gram-negative bacilli with facultative metabolism that colonize and flourish in the gastrointestinal (GI) tract of various groups of the Animalia kingdom¹⁵. The species of the Enterobacteriaceae family form a significant portion of the known enteric bacteria¹⁶. These are usually present in the normal microflora of the animals as commensals but may harbor virulent factors leading to disease manifestation. These disease-causing subspecies are referred to as enteric pathogenic bacteria and are responsible for a significant number of gastrointestinal and diarrheal illnesses. Based on serological Kauffman classification, bacterial strains may be denoted based on the presence of O (somatic antigen) and H (flagellar antigen), and this nomenclature is widely used for the denotation of pathogenic *E. coli* species.

1.2.1 Bacterial gastroenteritis

The word gastroenteritis (origin: *Greek*) denotes *gastron*: stomach and *enteron*:intestine, meaning flu of the stomach & intestine, and thus, defined as inflammation of the GI tract. Physiologically it is defined as an increase in stool frequency i.e., three or more loose stools in 24 hours (h) accompanied with or without vomiting, fever, and abdominal pain. These are further described as acute (<14 days), persistent (>14-30 days), chronic (>30 days), or recurrent (relapse in 7 days)¹⁷. The causative organisms may range from viruses to bacteria, and thus, when bacteria are the cause of enteric infection, it is called bacterial gastroenteritis.

Various pathogenic bacterial species, mostly belonging to the Enterobacteriaceae family, are responsible for gastroenteritis viz., *Escherichia*, *Campylobacter*, *Clostridium*, *Salmonella*, *Shigella*, *Yersinia*, and even *Staphylococcus*. The pathological route of disease manifestation primarily includes:

- (i) Excessive secretion of fluids in the proximal small intestine induced by the action of toxins of enteropathogens.
- (ii) Cytotoxic damage of the ileal or colonic mucosa leading to a hematoma.
- (iii) Penetration of the bacterium through the mucosa to the reticuloendothelial system, inducing systemic shock and fever¹⁸.

Many bacterial gastroenteritis cases are caused by enteric bacteria and are not treated effectively with antibiotic-based treatments. This is majorly attributed to the fact that microorganisms have developed a mechanism to evade antibiotics-induced damage, and gradually, the percentage of multi-antibiotic resistant strains is rapidly increasing. Unrestrained use of antibiotics, in fact, inimically affects the normal microbiota of the gut leading to dysbiosis¹⁸. Additionally, antibiotics-based therapies in toxin-producing bacteria may lead to further complications due to antibiotic-induced toxin release in the patient, which causes septic shock¹⁹. Thus, methodologies for specific detection of the bacteria pathotype are essential to aid in correct and quick clinical diagnosis, especially in communicable diseases.

1.2.2 Pathogenic *E. coli*

In 1885, the German pediatrician Theodor Escherich discovered *Bacterium coli commune* (now called as *Escherichia coli* in his honor) in the feces of a child suffering diarrheal illness^{20,21}. Later in 1893, a Danish veterinarian suggested certain strains of *E. coli* are pathogenic in nature²². Although *E. coli* is part of the healthy flora of the intestinal tract, certain pathogenic strains harbor virulence factors²³. Pathogenic *E. coli* predominately manifests diarrheal illness, urinary tract infections (UTI), and meningitis. These six significant *E. coli* pathotypes viz., enteropathogenic *E. coli* (EPEC), enterohemorrhagic *E. coli* (EHEC), enteroinvasive *E. coli* (EIEC), enterotoxigenic *E. coli* (ETEC), diffusely adherent *E. coli* (DAEC), and enteroaggregative *E. coli* (EAEC) have been widely reported so far^{8,24}.

The evolution of pathogenic *E. coli* strains has risen with the transfer of this genetic information from other pathogens, and numerous lineages have been described, which are still evolving. It is reportedly anticipated that pathogenic strains like O157:H7 diverged from a common ancestor of *E. coli* K-12 about 4.5 million years ago and that the natural selection has and is still favoring the development of virulence^{25,26}. Another study comparing 186 *E. coli* genomes found approximately only 1,700 homologous gene clusters shared amongst each other in about 16,400 gene clusters²⁷. Figure 1.1 shows the evolutionary distance between various pathotypes of *E. coli* in a study using multi-locus enzyme electrophoresis at ten enzyme loci and verified with the help of sequencing of *mdh* housekeeping gene encoding for Malate dehydrogenase²⁸. Thus, the evolution

of virulence determinants encoded on genes directly affects the immense mutational plasticity and transferrable nature of the microbial genome.

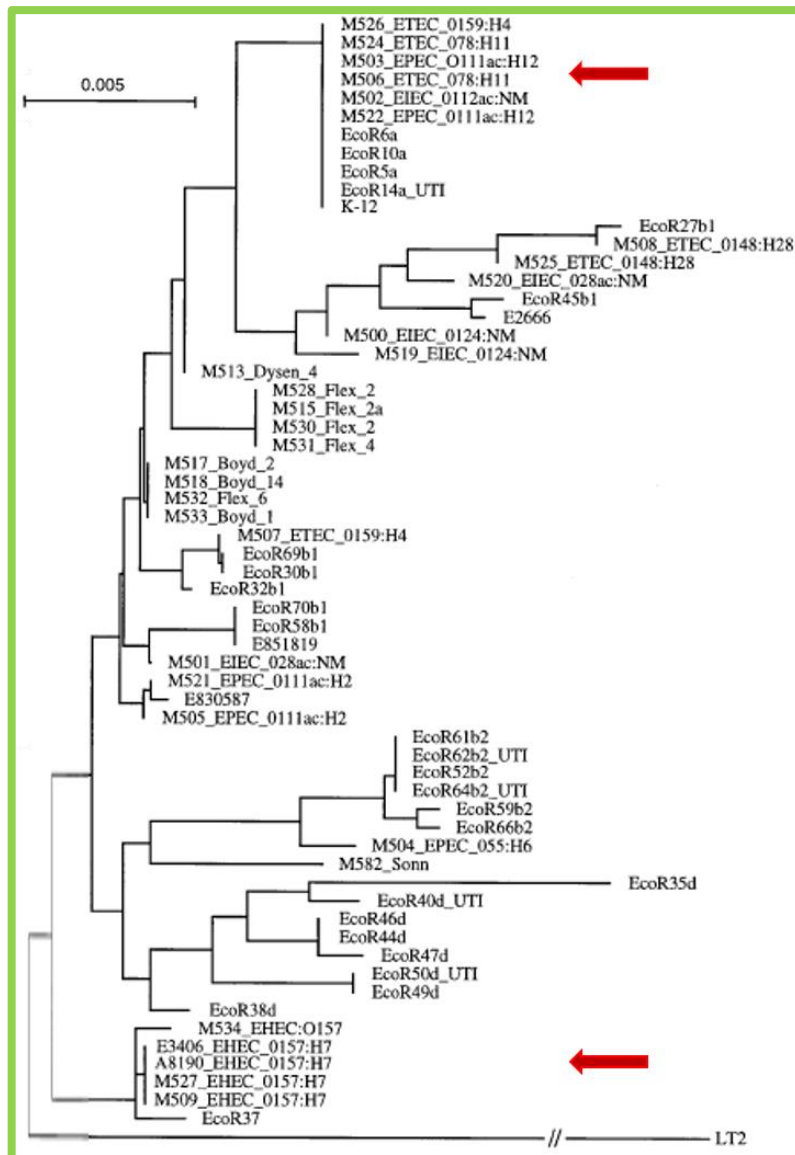


Figure 1.1: Relationship amongst different *E. coli* strains: Genetic map (*mdh* housekeeping gene sequencing data) denoting that pathogenic *E. coli* of various pathotypes arose during multiple evolutionary events²⁸. Red arrow indicates the two serotypes chosen for detection in this thesis.

In the case of pathogenic *E. coli* species, this genetic information may include virulent genes (encoding adhesins), virulent plasmids (encoding pathogenicity islands like loci of enterocyte effacement and hemolysin), and viral DNA (encoding Shiga-like toxins)²⁹. The two significant pathotypes ETEC (example of representative serotypes include- O6:H16, O8:H9, O11:H27, O78:H11, O128:H7, O148:H28, O172:NM) and EHEC (example of representative serotypes include- O26:H11, O55:H7, O111:H8, O117:H14, O157:H7) are responsible for chronic enteritis in addition to diarrhea and also affect organs other than GI tract with the secretion of enterotoxins³⁰. The avirulent strains of these two serotypes were chosen for further study in the incoming chapters of this thesis.

1.2.2.1 Pathogenesis

The pathogenic bacteria enter the human body via an oral or fecal route, evading the primary host defense mechanisms. These pathogenic strains then enter the GI tract, attaching to the enterocytes via specific surface factors, and upon localization, these may manifest themselves by effacing the villi present on the surface of GI cells and disrupting Cl^-/K^+ ion channels leading to loss of nutrient uptake and result in persistent diarrhea (Figure 1.2). In the case of ETEC that produce heat-stable and heat-labile enterotoxins, the net increased Cl^- secretion from secretory crypt cells is brought into effect by the permanent activation of adenylate cyclase in the host gut cells leading to increased levels of intracellular cyclic adenosine monophosphate, activating its dependent kinases, and the eventual activation of the main chloride channel of epithelial cells: the cystic fibrosis transmembrane conductance regulator.

In enterohemorrhagic species like *E. coli* O157:H11 upon cellular lysis, hemolytic Shiga-like toxins (Stx) are released, which may enter the blood circulation and result in Hemolytic Uremic Syndrome (HUS). Shiga toxin-producing *E. coli* (STEC) is a significant source of food poisoning & gastroenteritis, with a very low infectious dose of 100 cells enough for disease manifestation. Thus, it is associated with high morbidity worldwide, with more than 2.5 million cases annually^{2,31}.

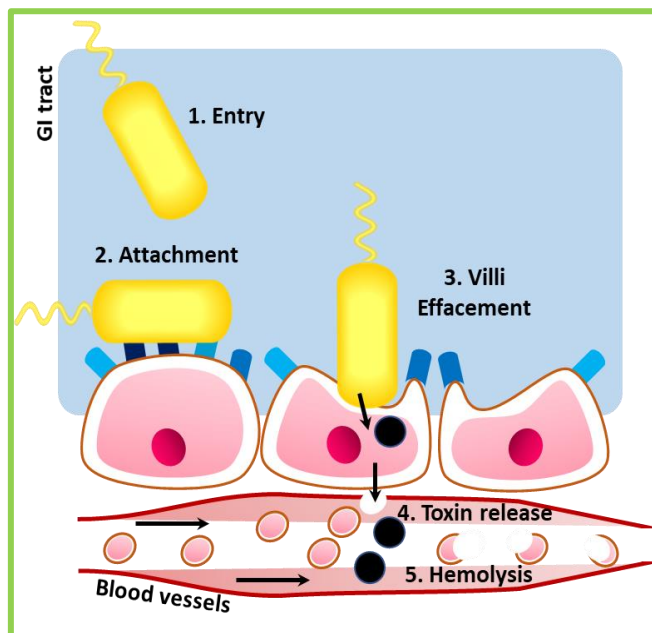


Figure 1.2: Pathogenesis: A pictorial view of the various steps of pathogenic *E. coli* localization and infection inside the GI tract.

The most severe STEC complication is typically manifested 5-13 days after the onset of preliminary symptoms. HUS entails hemolytic anemia, thrombocytopenia, nephron damage and persists in 5-15% cases, with children and elders as significant target groups. This damage is due to the rRNA-glycosidase activity of either Shiga toxin subtypes viz., Stx1, or Stx2. These AB₅ ribosomal-inactivating globular proteins bind via B₅ subunit to glycolipids (Gb3/Gb4) abundantly present on microvascular glomeruli and proximal tubule cells of the nephron and microvascular endothelial

cells. Though similar in action, these subtypes are antigenically distinct, sharing only ~56% sequence identity amongst themselves.

Moreover, with a lethal dose (LD₅₀) of 50 ng kg⁻¹ for Stx2 in mice, the apparent lethality of Stx2 has been reported to be 100-fold compared to Stx1³². Currently, no vaccines or therapies are present for this syndrome. The application of antibiotic treatment in STEC infection instead aggravates the condition leading to the systemic release of toxin affecting other organs also. Thus, specific and systematic identification of toxins in food and infected patients is necessary to contain any outbreak. Table 1.1 summarizes the various virulence factors that have been discovered to play prominent roles in ETEC and EHEC²⁴.

Factor	Pathotype	Activity
Intimin	EHEC	Adhesion
CFA	ETEC	Adhesion
OmpA	EHEC	Adhesion
Curli	EHEC	Adhesion
Flagellin	All	Motility
LPS	All	Induce cytokine expression
LT/ST	ETEC	Ion secretion
Ehx	EHEC	Erythrocyte cell lysis
Stx	EHEC	Inhibit protein synthesis and induce apoptosis
CDT	Various	Dnase1 activity
Urease	EHEC	Degrades urea to ammonia and carbon dioxide
EspP	EHEC	Serine protease inducing ion secretion

Table 1.1: Virulence factors: A few essential determinants of virulence in *E. coli* pathotypes. (CFA: Colonization Factor Antigen, Omp: Outer membrane protein, LPS: Lipopolysaccharide, LT: heat-Labile toxin, ST: heat-stable toxin, Stx: Shiga-toxin, Ehx: enterohemolysin, CdT: Cytolethal distending toxin, Esp: Extracellular serine protease)²⁴

1.2.2.2 Prevalence

According to the World Health Organization (WHO), diarrheal diseases are listed in the top ten causes of death (Figure 1.3). A higher mortality rate in the Southeast Asian region is observed, which may be attributed to lower sanitation standards and ineffective patient treatment. However,

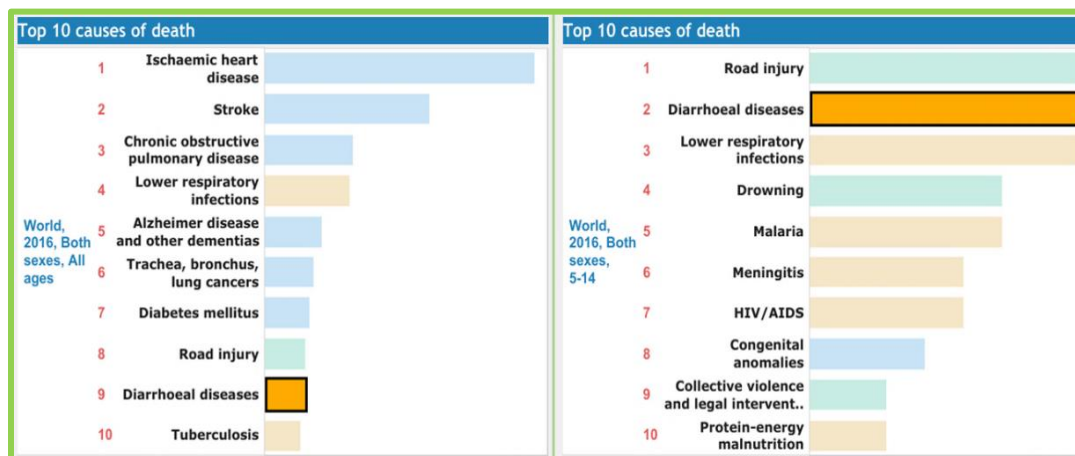


Figure 1.3: WHO report: The top causes of death in the World. Source: WHO, https://www.who.int/gho/mortality_burden_disease/causes_death/top_10/en/

these are the most common cause of mortality after accidental deaths (due to road mishaps or drowning) in children aged 5-14 years, showing the vulnerability of youngsters to gastroenteritis, which undoubtedly, reflects on the weak physical and mental growth of the coming generation³³.

Higher mortality is seen mainly in high-risk groups, i.e., under 5 year-old, elderly, and immunocompromised individuals who are susceptible to infections owing to weaker immune response (Figure 1.4). India, Bangladesh, and African countries seem like possible hotspots for diarrheal diseases, with a significant traveler advisory issued for people traveling to these regions for infections due to enterotoxigenic *E. coli* responsible for travelers' diarrhea colloquially known as 'Montezuma's revenge' or 'Delhi belly'³⁴⁻³⁶. A correlation can be drawn from the fact that the Asian subcontinent is mostly an agrarian society dependent on cattle, which serve as the primary carrier and asymptomatic reservoir of pathogenic *E. coli*. Thus, bacterial transmission from animals to humans via direct or indirect exposure through the environment or food products and later community transfer is a high possibility scenario³⁷. Food and water monitoring are essential at multiple checkpoints from production, preparation to consumption, lack of which renders the consumers increased morbidity or may lead to outbreaks.

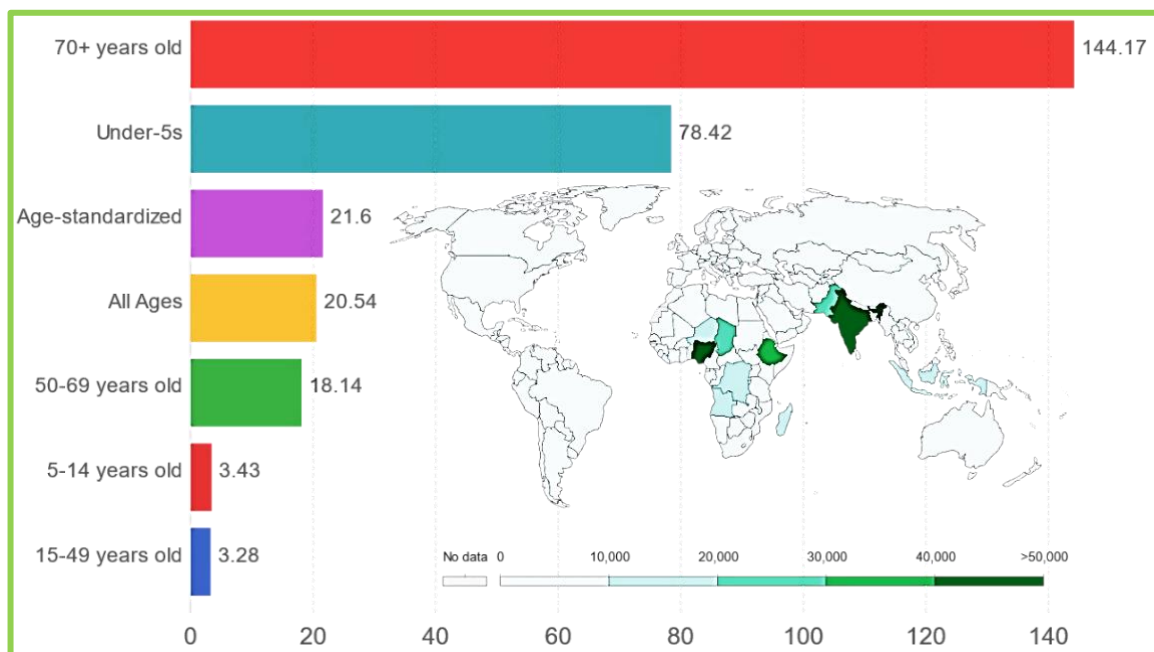


Figure 1.4: Diarrheal disease mortality by age: Death rates measured per 100,000 individuals across age categories and (inset) country-wise mortality in the under-5s age group. Source: IHME, Global burden of disease (GBD), <https://ourworldindata.org/>

1.2.3 Microbiological standards & regulations

The local municipalities and food industries must regularly detect and maintain zero bacterial content in drinking water and food items³⁸. *E. coli* detection is necessary by many nations, especially for food product manufacturing companies. Nestle Ltd. affirms that *E. coli* is regarded as a hygiene indicator, and its presence should be low on raw produce but not present on processed or Ready-to-Eat foods³⁹.

1.2.2.3 Indian standards

(A) Microbiological standards for drinking water

The Indian standard drinking water specification issued by ‘Bureau of Indian Standards’ in Section 4.1.1 states, ‘Ideally, all samples taken from the distribution system including consumers’ premises, should be free from coliform organisms...’⁴⁰. Additionally, it has been tabulated that *E. coli* shall not be detectable in any 100 mL sample in:

- (i) All water intended for drinking
- (ii) Treated water entering the distribution system
- (iii) Treated water in the distribution system

(B) Microbiological standards for food products

The Food Safety and Standards (Food Products Standards and Food Additives) Regulations, 2011 of the Government of India, states that *E. coli* should be absent in 0.1 g of milk food, 25 g of meat products, and other food products. The tests of microbiological analysis are listed as per IS14397^{41,42}.

1.2.2.4 Other international standards

The three major standardizing and regulating international authorities are the European Union, the US Environmental Protection Agency, and the WHO. Both the WHO and IS 10500:2012 drinking water standards adopted by governments worldwide stress that the consumption is safe only if it contains no detectable *E. coli* per 100 mL water sample³.

(A) Europe

(i) Microbiological standards for drinking water

The European Union Water Quality Directive (98/83/EC) and The Water Framework Directive (2006/60/EC) instructs no microorganisms in 1 mL for safe drinking water. The constituent member states follow similar directives with minor variations regionally.

(ii) Microbiological standards for food products

The European Union’s Commission regulation on microorganisms in foodstuff also lists *E. coli* as an indicator for fecal contamination and follows ISO16649-1/2 standards for *E. coli* presence in meat, fish, and Ready-to-Eat products with the minimum acceptable load as 500 colony forming units (cfu) per gram (g), 1 cfu per g and 100 cfu per g. Infant foods must maintain absence in 10 g, as per food safety regulations^{43,44}.

(B) United States of America

(i) Microbiological standards for drinking water

In the USA, water quality is monitored using ‘National Primary Drinking Water Regulations’ established in 2001 with the major microbial indicators’ total coliform, fecal coliform, and *E. coli*

are augmented by *Cryptosporidium*, *Giardia*, *Legionella*, and enteric virus, which are not common in other national standard listed. The presence of pathogenic *E. coli* should be zero in drinking water samples.

(ii) Microbiological standards for food products

The Food and Agriculture Organisation (FAO) and The International Commission on Microbiological Specifications for Foods (ICMSF) has a standard manual for food quality control which lists the presence of pathogenic *E. coli* with special reference to *E. coli* O157 as absent in food products^{45,46}.

(C) Australia & New Zealand

(i) Microbiological Standards for drinking water

In Australia, the drinking water standard maintains the none detectable per 100 mL standard, with the state regulations, require routine microbial tests per week^{47,48}.

(ii) Microbiological Standards for food products

Australia and New Zealand Standard 1.6.1 regulates the microorganism presence and analysis in food samples which lists no pathogenic *E. coli* should be detectable in food samples. Additionally, the rule stresses upon the detection of *Listeria monocytogenes*, which is also a food pathogen^{49,50}.

1.3 Conventional microbial detection methods

Conventionally, bacterial diagnosis is carried out mainly via culture-based or biochemical assays. Although they are slow and do not offer sufficient information to make timely decisions for treatment. These methods described below collectively may be considered ‘gold standards’ but are laborious, time taking and with significant overlapping qualitative parameters used for detection. The diagnostic tests currently available are based commonly on nucleic acid-based molecular techniques viz., specific PCR, DNA microarrays, 16S rRNA sequencing, and antibody-based assays or platforms. These are more specific compared to culture-based methods, but these require extensive sample preparation, expensive resources, and skilled personal trained on this sophisticated yet bulky instruments¹³. The major conventional methods utilized for detection of microbes are discussed in this section.

1.3.1 Culture-based methods

For the estimation of bacteria, the samples are enriched and grown on selective nutrient-rich mediums for 24 – 48 h before sensing their presence. Then a set of microscopic and biochemical assays is carried out to figure if the sample contains the target pathogen. Differential staining is a process that uses more than one chemical stain to differentiate between different microorganisms or their structures/cellular components. The most commonly recognizable differential staining is the Gram staining, which stains violet for Gram positive bacterial cells and pink (as in the case of all *E. coli* species) for Gram negative bacterial cells.

This easy to use methodology has several limitations: (i) smear might be too thick and hold dye, creating a false positive, (ii) old cultures and too strong decolorization can create a false negative. Besides, the preparation of gram stains using fecal samples is very tedious.

Alongside this, enriched bacterial samples are identified by streaking on selective media plates, and estimation of bacterial species is done by observation of growth and the morphological characteristics of the bacterial colonies. Selective media commonly used for fecal cultures include salmonella-shigella (SS), sorbitol-MacConkey (SMAC) agar, brilliant green (BG), or CHROMagar (a chromogenic medium designed for the recovery and detection of specific enteropathogens)¹⁴. Figure 1.5 (A-C) shows the streaked cultures showing colony characteristics in nutrient agar medium and (D-G) for selective SMAC media after 24 h growth at 35°C. A typical culture takes 12-24 h on solidified agar media to show growth, which can be easily misjudged for other bacteria unless a trained microbiologist observes it. Typical *E. coli* strains can ferment sorbitol within 24 h and produce the enzyme β -glucuronidase, whereas the O157 serotype does not produce the enzyme. However, this differential mechanism is not universal, and certain O157 strains have been reported to be sorbitol positive^{51,52}.

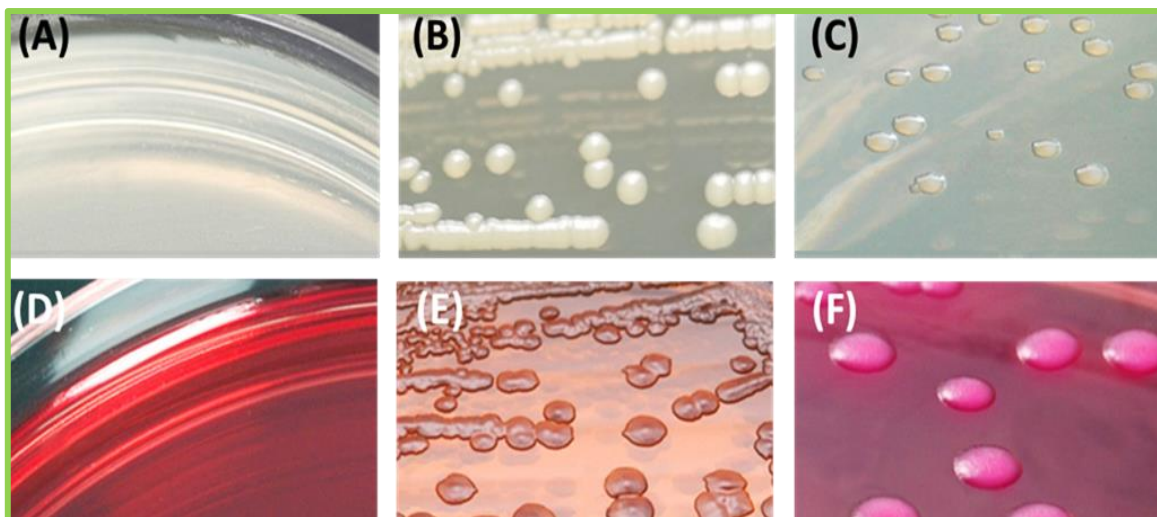


Figure 1.5: Microbiological culture plates: Showing nutrient agar plate with (A) Uninoculated plate, (B) Colonies of *E. coli* (ATCC® 25922) growing on Nutrient agar plates, (C) *Staphylococcus epidermidis* (ATCC® 12228). Showing SMAC plate with (D) Uninoculated plate (E) *E. coli* O157:H7 (ATCC® 35150) showing translucent colonies (no sorbitol fermentation) and (F) *E. coli* (ATCC® 25922) showing pink colonies (sorbitol fermentation) Source: Hardy Diagnostics Catalog.

Consequently, detection based solely on differential microbiological media or biochemical screening is not fool proof. Nonetheless, these media are relatively costly than conventional media and are not usually employed for in-vitro diagnostics. Cefixime and potassium tellurite may be added to the SMAC (CT-SMAC) to increase selectivity in heavily contaminated samples. This is the media of choice in the ISO standard protocol (ISO 16654) for *E. coli* O157, together with a second appropriate selective agar⁵³. Table 1.2 gives a list of selective microbiological media used for pathogenic *E. coli* detection.

Selective Microbiological Media	Serotype
SMAC	O157
SMAC+ Potassium Tellurite + Cefixime (CT-SMAC)	O157
5-bromo-4-chloro-3-indolyl-B-D-glucoronide (BCIG) Agar	O157
SMAC-BCIG	O157
4-methylumbelliferyl-B-D-glucoronide (MUG)	O157
Enterohemolysin Agar	STEC
Enterohemolysin Agar with Vancomycin + Cefixime + Cefsulodin	STEC
Phenol Red Sorbitol Agar +MUG	O157
Fluorocult <i>E. coli</i> O157 Agar	O157
CHROMagar O157	O157
Chromocult	O157, O111, O26, O103
Rainbow Agar O157	O157, O26, O111, O48
Rhamnose MacConkey Agar	O26, O157

Table 1.2: Microbiological media: Selective Agar types used for various pathogenic *E. coli* serotypes⁵³.

1.3.2 PCR based method

Nucleic acid-specific screening using specific primers for LEE virulence genes viz., *eae* (intimin), *bfp* (bundle forming pilli), *ehx4* (hemolysin), *stx1* (Shiga like-toxin subtype1), *stx2* (Shiga-like toxin subtype 2) are used for amplification and sensing²³. It is accurate but requires extensive sample enrichment and purification before detection & analysis. In principle, polymerase chain reaction (PCR) allows focusing on a particular signature region in DNA and amplifies it exponentially for detection (Figure 1.6). Commercial platforms like RIDA[®]GENE real-time PCR for *E. coli* diagnostics, Qiagen[®] mericon *E. coli* O157 Screen Plus Kit, BIOFIRE[®] FILMARRAY[®] system, Hygiena BAX[®] System are also available which claim results in 60-90 minutes (min) with

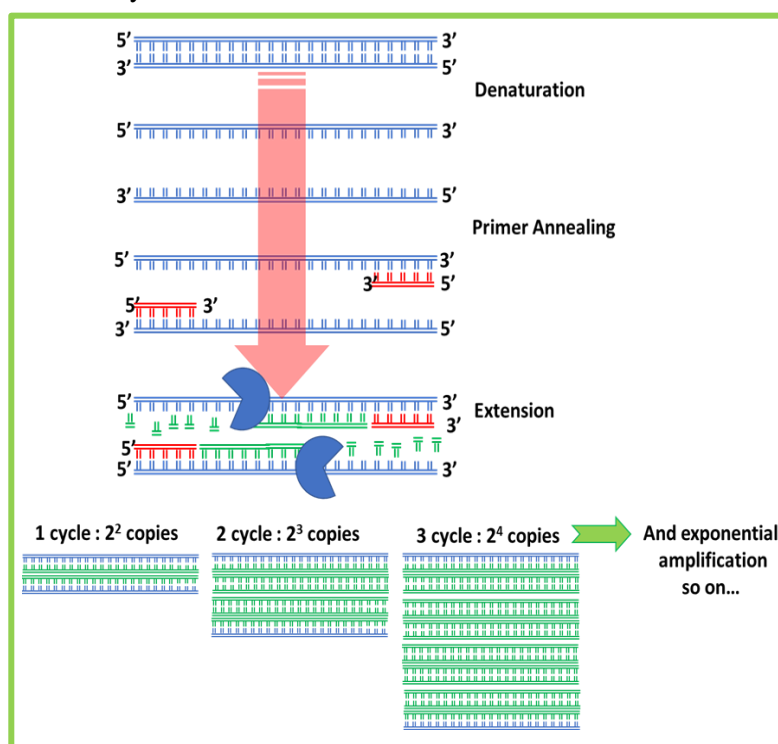


Figure 1.6: PCR-based sensing: Steps of PCR amplification and detection using specific biomarker gene primers.

bacterial samples⁵⁴⁻⁵⁷. Although PCR as a detection strategy is extensively employed for pathogenic *E. coli* sensing, it has several limitations, namely; **(i)** high probability of contamination in non-purified samples, **(ii)** essential prior knowledge of the genome for identification (the presence or absence) of a specific DNA or RNA stretch and, **(iii)** process parameters optimization (sample volume, concentration, primer concentration, melting temperature, annealing temperature, number of cycles) is necessary without which non-specific sensing (false-positives or false-negatives) of unrelated targets may occur.^{58,59}

1.3.3 Pulsed-field gel electrophoresis

Pulsed-field gel electrophoresis (PFGE) is currently considered as the ‘gold standard’ method for typing of *E. coli* O157. Herein, with specific restriction enzymes, the bacterial genome is cleaved to generate smaller fragments, and restriction profiles are generated for each different isolate, which is characteristic for a particular strain type. These cleaved products are separated in the alternated

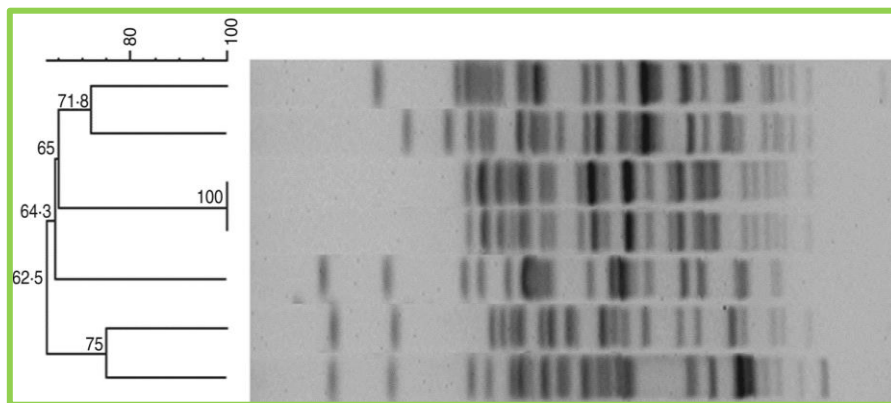


Figure 1.7: Pulsed-field gel electrophoresis: Dendrogram showing the cluster analysis on the basis of *XbaI* pulsed-field gel electrophoresis of the seven sorbitol non-fermenting *E. coli* isolates.

current field; hence electrophoresis is carried out. The PFGE technique has been vastly exploited in laboratory settings and has excellent value in epidemiological analysis, differentiation of pathogenic strains, and the monitoring of their spread among communities (Figure 1.7). This molecular fingerprinting technique is reliable and reproducible, but requires vastly technically expert workers for carrying the wet-lab work and statistical analysis^{53,60,61}.

1.3.4 Bacterial phylogenetic analysis

The 16S rRNA gene is ideal for mapping genetic variations due to its conservation in similar species and dis-similarity in unrelated species. Thus, variability in the gene sequence allows making phylogenetic comparisons. Post PCR amplification, the gene is sequenced, and comparisons with other members are made. Also, whole-genome sequencing has become a standard tool for deducing phylogenetic relationships amongst microbes^{62,63}. Its limitations as a viable sensing tool are; **(i)** DNA extraction & isolation of every strain is a very time-consuming process, and **(ii)** the reagents and sequencing labor costs are high for routine sample analysis.

1.3.5 Mass spectroscopy-based detection

In matrix-assisted laser desorption ionization (MALDI)-mass spectroscopy (MS), the bacterial sample is mixed and crystalized with a matrix bombarded with a laser. The molecules are ionized and accelerated through a flight tube, where they are separated according to their time-of-flight creating an m/z spectrum⁶⁴. The sample analysis can be carried out as a whole bacterium or its purified proteins to generate a proteomic profile⁶⁵⁻⁶⁷. The resultant spectrum is referenced with signature microbial spectra for identification. VITEK[®]MS is an automated commercial mass spectrometry microbial identification system famous for detection⁶⁸. Though specific at the genus level, it has been reported that this technique shows overlapping results for *Escherichia* and *Shigella* species. However, the instrumentation and reagents are costly and require skilled individuals for processing and analyzing samples.

1.3.6 DNA microarray-based assays

A microarray is a 2D array on a glass slide or silicon cell that assays genetic material employing a high-throughput methodology. The array is miniaturized, multiplexed, and can carry out parallel processing and is used to measure the expression levels of large numbers of genes simultaneously. Each DNA spot contains a specific DNA sequence, known as probes (or reporters or oligos that are used to hybridize a complementary RNA or DNA extracted from the target. Probe-target hybridization is usually detected and quantified by detecting the fluorophore or chemiluminescence-labeled targets to determine the relative abundance of nucleic acid sequences in the target⁶⁹⁻⁷¹. Out of the many studies for pathogenic bacteria detection, a DNA microarray for detecting and typing of ETEC using various genes encoding the enterotoxins LT and ST, and the serogroup-specific genes *wzx* and *wzy* were used for the typing of the 19 most common ETEC O serotypes showed significant results (Figure 1.8)⁷². Limitations of DNA microarray technology are

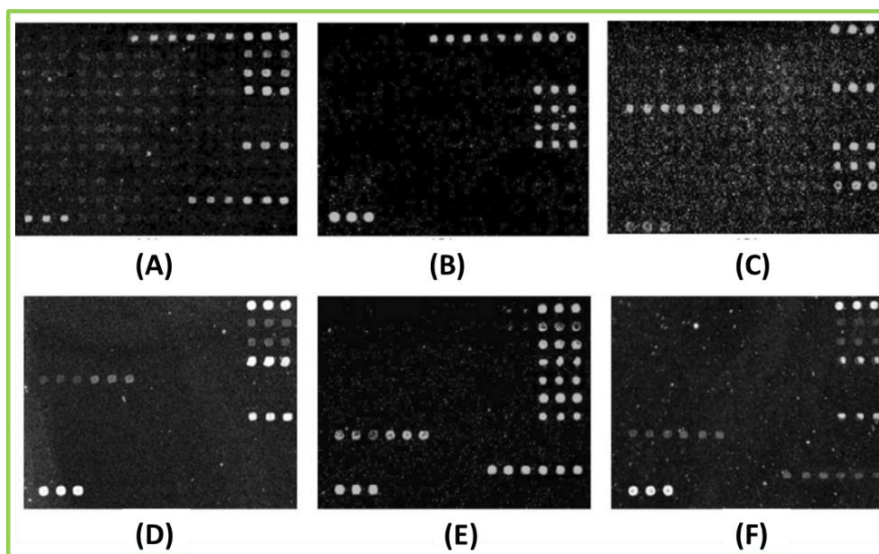


Figure 1.8: Microarray: Microarray differentiation of some clinical isolates of *E. coli*. (A) *E. coli* O8, (B) *E. coli* O8, (C) *E. coli* O114, (D) *E. coli* O114, (E) *E. coli* O149, (F) *E. coli* O149⁷².

its high cost of gene-specific primers labeled with fluorophores for spotting and fluorescence signal response interpretation, especially in genetic cross-talk yielding false positives.

1.3.7 Immunoassays

An immunoassay is a biochemical test that measures the presence or concentration in a solution using a specific antibody raised against the target. Berson and Yalow described the first immunoassay in 1959, and their work won the Nobel Prize in Medicine in 1977. Enzyme immunoassay and enzyme-linked immunosorbent assay (ELISA) are widely used as diagnostic tools⁷³. ELISA-based sensing formats are limited in accuracy since the enzyme-mediated color change reacts indefinitely, and over an extended period, the color strength inaccurately reflects the amount of primary antibody present, leading to false positives. Correspondingly, polyclonal antibodies show high cross-reactivity amongst closely related species, while specific monoclonal antibodies are expensive to raise (Figure 1.9). Another major disadvantage of traditional immunoassays is that they comprise a number of multiple sensitive steps viz., coating, blocking, washing, incubation of primary and secondary antibodies, and substrate development, which requires a lot of time and costly and temperature-sensitive reagents.

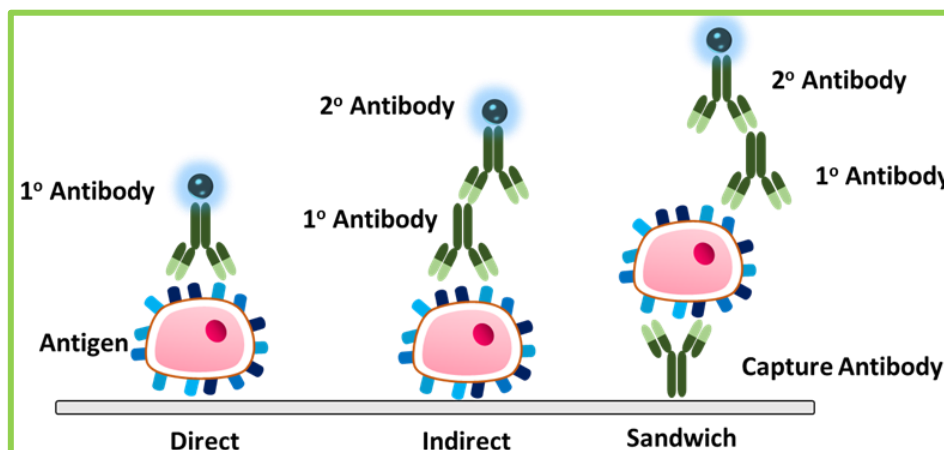


Figure 1.9: Immunoassay types: Various formats of antibody-based sensing assays. ELISA based tests require expensive, labeled specific antibodies for sensing.

1.4 The need for improved diagnostic platforms

The conventional methods for bacterial diagnosis and their various limitations as rapid and sensitive platforms, the development of improved diagnostic platforms that provide minimal cross-reactivity amongst species, low detection limit, and wide range of detection in both water samples and food samples is critical. Furthermore, the clinical manifestation of gastrointestinal diseases usually shows overlapping symptoms of loose motions, vomiting, nausea, and which may or may not include fever or bloody stool. Gastroenteritis is thus challenging to diagnose symptomatically, and its clinical diagnosis is an essential step and an integral part of correct therapy⁷⁴. However, a majority of clinicians owing to time-taking lab processes, bypass the ideal protocol to administer

broad range antibiotics even when they are not recommended for treatment of STEC. Antimicrobial agents though essential but their unwarranted abuse, has led pathogens to develop multidrug resistance leading to the emergence of superbugs⁷⁵. In 2010, an epidemiology study in Lancet reported carbapenem resistance gene bla_{NDM-1} in *Enterobacteriaceae* isolates of *E. coli* and *Klebsiella pneumoniae*, which were highly resistant to all antibiotics except to tigecycline and colistin from patients with travel history to India and Pakistan^{76,77}. Keeping in view the current state of globalization, international outbreaks associated with infectious diseases are a natural threat. Thus, timely, specific, and sensitive detection of bacterial pathogens, its associated antigen markers, and toxins is the need of the hour. Our ultimate focus is on the development of robust point-of-care (PoC) sensors for the detection of pathogenic *E. coli* species with application in both clinical diagnostics and as well as in food & environmental monitoring (Figure 1.10).

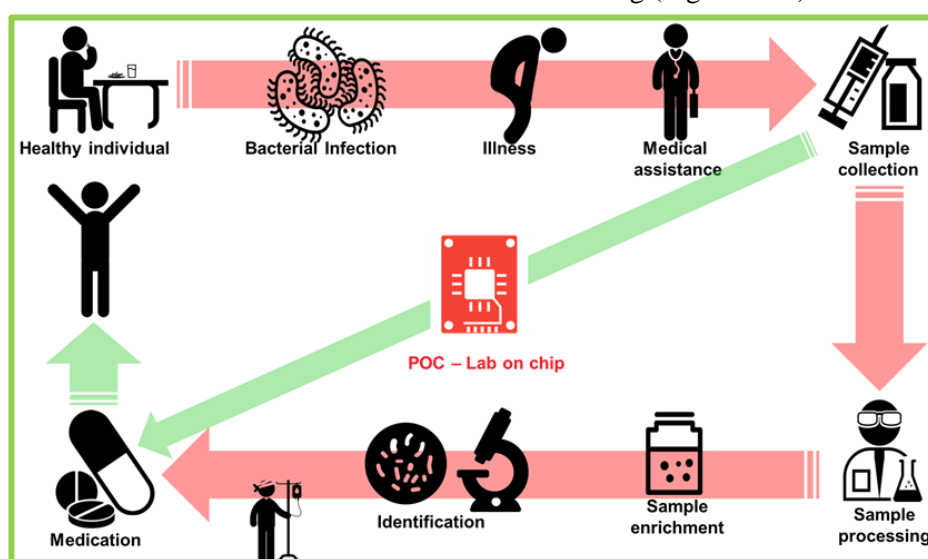


Figure 1.10: Importance of improved diagnostics: Diagnostics play a significant role in clinical treatments and timely bacterial disease mitigation.

1.5 Sensors

A sensor is a compound system with the capability to respond to a target qualitatively or quantitatively. The target can be anything from a physical parameter, small inorganic molecules, gases, or biomolecules like proteins, DNA, or even whole cells.

1.5.1 Classification of sensors

Sensors measuring physical parameters like temperature, pressure, potential, mass, light intensity are simpler and operate by measuring the changes in the physical properties of a standard substance. In contrast, the sensors quantifying analytes require more sophisticated components to pertain to the sensor with the highest fidelity levels. The increased fidelity is provided by using a biological receptor moiety. Additionally, sensors may be classified as labeled and label-free sensors:

- (i) A labeled sensor uses a label that is an extrinsic entity (usually optically active dye) and may be conjugated with the receptor moiety aiding in signal transduction or amplification.
- (ii) Label-free sensors can measure direct ligand-receptor interaction.

While label-free sensing technology (electrochemical, electrical, piezo sensors) holds a lucrative position in sensors, nanomaterials derived fluorescent labels with a high quantum yield at par of organic dyes, long shelf-life, stability, and tunable properties has also garnered much attention.

1.6 Biosensor

The first milestone in the history of sensors dates back to the beginning of the 20th century with the fabrication of a pH sensor by Søren Sørensen. However, the era of biosensors took off in 1962 by L.C. Clark with the development of glucose oxidase based amperometric oxygen electrode for sensing of glucose in blood samples. According to the 1992 IUPAC definition, a device that uses specific biochemical reactions mediated by isolated enzymes, immunosystems, tissues, organelles, or whole cells to detect chemical compounds usually by electrical, thermal, or optical signals is called a ‘biosensor’. However, since then, it has been a vast multitude of other receptors viz., organic molecules, aptamers, antimicrobial peptides, lectins, phages also. A biosensor consists of:

- (i) **Bio-receptor:** The recognition moiety responsible for interacting with the target analyte.
- (ii) **Transducer:** A material that converts the bio-interaction signal from the receptor-analyte interaction to a readable optical or electrical or electrochemical or mechanical signal.
- (iii) **Readout unit:** Displays the signal generated via the transducer into a readable format.

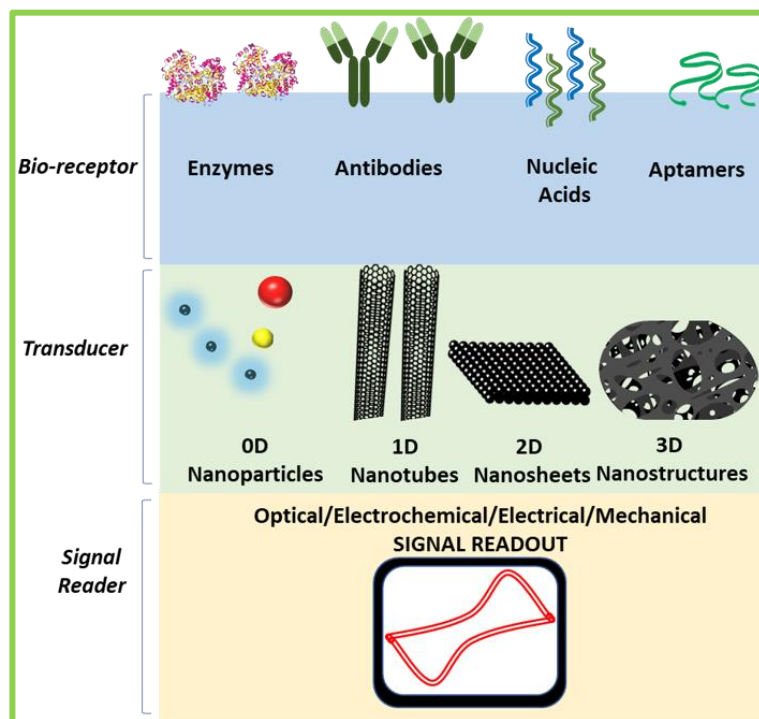


Figure 1.11: Biosensor: Three significant elements of biosensor viz., bio-receptor, transducer & signal reader.

Thus, in a more elaborate sense, a biosensor comprises a biological element that interacts with the ligand resulting in a physical/chemical change that is amplified into a readable electrical or optical signal with the help of a transducer element (Figure 1.11). The molecular recognition via these bio-receptors takes place at epitope regions, which comprises of amino-acid rich binding pockets in antibodies & enzymes. Simultaneously, 3D folded nucleic acid structures that non-covalently interact specifically with the target molecules in aptamers. Bio-receptors that specifically interact with antigenic sites (epitopes) present on the target instead of other non-targets, provide enhanced selectivity for sensing a narrow range of species. The response sensitivity of the bio-interaction is further determined by the transducer material owing to their unique physio-chemical properties as well as the methodological approaches used to observe the bio-interaction. Thus, the significant parameters that govern biosensor performance are selectivity, sensitivity, and detection range.

1.6.1 Aptamers as bio-receptors

In August 1990, two significant publications appeared back-to-back in Science and, Nature journals discussing a similar concept of screening out RNA based receptors from a milieu of random RNA sequences. Tuerk & Gold reported high-affinity RNA based nucleic acid ligands for T4 DNA polymerase by alternate cycles of ligand selection from a calculated pool of 65,536 variant sequences and amplification of bound species, which were exponentially enriched for the highest affinity species that can be clonally isolated and characterized⁷⁸. The discoverers named this new technology as ‘systematic evolution of ligands by exponential enrichment’, an in-vitro combinatorial chemistry method in which the compound library were single-stranded nucleic acids. They proposed that such bewildering structural diversity single-stranded nucleic acids could lead to ‘nucleic acid antibodies’ of equivalent richness to real antibodies. Ellington & Szostak appointed the term **SELEX** (**S**ystemic **E**volution of **L**igands by **EX**ponential enrichment) and discovered subpopulations of RNA molecules that bind specifically to a variety of organic dyes viz., Cibacron Blue 3GA, Reactive Red 120, Reactive Yellow, Reactive Brown 10, Reactive Green 19 and Reactive Blue 4 attached to crosslinked beaded agarose had been isolated from a population of 10^{10} random sequence RNA molecules out of which a few folds in such a way as to create a specific binding site for small ligands⁷⁹. They chose these molecules because they have many possible hydrogen-bond donor and acceptor groups and planar surfaces for stacking interactions. These receptors, called aptamers (word chimera composed of Latin *aptus*: fit and Greek suffix *-meros*: part), have shown unique selectivity for diverse target analytes in their native states.

Over 30 years, numerous publications on aptamers for their both synthesis and application have been reported. It has emerged as a reliable alternative to antibody/enzyme receptor-based diagnostic assays, especially after the approval of Macugen[®], an aptamer-based anti-angiogenic medicine for age-related macular degeneration by FDA in 2004^{80,81}. Aptamer screening

methodologies have been modified by various research groups based on the feasibility of interaction with the target and rapid screening time, and avidity and affinity of the aptameric molecules. Various aptasensors have been developed using both RNA, DNA, and modified residues, which show remarkable flexibility, stability, and binding with the target of interest⁸²⁻⁸⁴. Besides, aptamer & ligand interaction studies highlight the conformation of the molecules, chemical bonding, or binding properties, a strong emphasis has been placed on the bioconjugation of these aptamers with functional groups, fluorophores, nanoparticles. A crucial step in the fabrication of aptasensors is the immobilization of the aptamer onto the sensor surface, which may be facilitated with the addition of polymers or site-directional functional groups helping in the formation of sensing layers and thus controlling the sensitivity of the platform. Our lab has explored this approach in the research article, Kumar *et al.* 2016⁸⁵.

Since the discovery of these aptamers, numerous studies have been conducted on the structural and interaction dynamics of these molecules for the generation of specific ligands for various targets ranging from small heavy metal ions to larger biomolecules and even whole cells⁸⁶. In a diseased human being (non-infectious diseases like cancer & diabetes), multiple biomarkers are released at different stages of the disease, significantly different from the animal models currently used for antibody generation. Likewise, in the case of infectious diseases due to bacterial, fungal, or viral pathogens, multiple surface antigens adorn the outer membrane of these whole microbial cells which contain certain hidden trans-membrane regions and conformations in the diseased state which are not found in purified counterparts used to elicit response during generation & maturation of antibodies. In contrast, aptamers are generated against targets in their naturally occurring states due to their in-vitro generation route^{81,87}. Though conventional labs and diagnostic platforms still gravitate on the superiority of antibodies and antibody fragments over aptamers in terms of specificity, it has been well reported over the past decade that high affinity ($K_d \sim$ nanomolar to picomolar) aptamers are the most explored alternative for diagnostic & theranostic approach.

1.6.2 Systemic evolution of ligands by exponential enrichment

SELEX is an iterative method, which relies on the exposure of milieu of naïve oligomer molecules to target populations followed by the screening of binding oligomers, their amplification, and re-exposure of these screened oligomers repetitively till the enrichment of high-affinity ligands to the exposed target analyte. These higher affinity oligomers with strong recognition & interaction capabilities are then aptly labeled ‘aptamer’ for that particular target. The selection cycle is repeated, leading to increased stringency of binding conditions to screen aptamers with affinities comparable to that of antibodies. Once the sequence of the aptamer has been identified, it can be re-synthesized with high purity for further applications. In early studies, RNA libraries were preferred over DNA due to better-folded structures and additional -OH group providing stronger molecular interactions with the target. However, RNA aptamers are generally reported to be

superior counterparts of DNA aptamers in terms of specificity but are highly susceptible to nuclease degradation. For application as a bioreceptor in in-vitro formats, nuclease resistance is not necessary, but an associated need during sampling of body fluids or in-vivo applications. Several studies revolving around aptamer selection, modification, and use in diagnosis and therapeutics have been reported^{88,89}. The conventional process is affected by various environmental parameters, target features, and partitioning methods.

Recent developments have yielded several SELEX variants devised by researchers tailored according to the target or its application. To mention a few, AEGIS-SELEX (artificially expanded genetic information systems SELEX)⁹⁰, CE-SELEX (capillary electrophoresis SELEX)⁹¹, ECEEM (equilibrium capillary electrophoresis of equilibrium mixtures)⁹², EMSA-SELEX (electrophoretic mobility shift assay SELEX)⁹³, FACS-SELEX (fluorescence-activated cell sorting SELEX)⁹⁴, GO-SELEX (graphene oxide SELEX)⁹⁵, LIGS (ligand-guided selection)⁹⁶, MAI-SELEX (multivalent aptamer isolation)⁹⁷, MARAS (magnetic-assisted rapid aptamer selection)⁹⁸, MSD-SELEX (monoclonal surface display SELEX)⁹⁹, NECEEM (non-equilibrium capillary electrophoresis of equilibrium mixture)¹⁰⁰ have been reported in the literature. Several of these modified SELEX processes have been employed by other researchers for obtaining high affinity aptamers against multitude of target. Figure 1.12 shows a schematic representation depicting the necessary cell-SELEX process. This combinatorial methodology is initiated by chemical synthesis of a single-stranded nucleic acid library composed of a random region flanked with priming binding sites at 5' and 3' ends. It is believed that each individual ssDNA has a different random region sequence, and the diversity of the naïve library depends on the length of the random region. The initial naïve library pool comprises of various different sequences that are allowed to interact with the target.

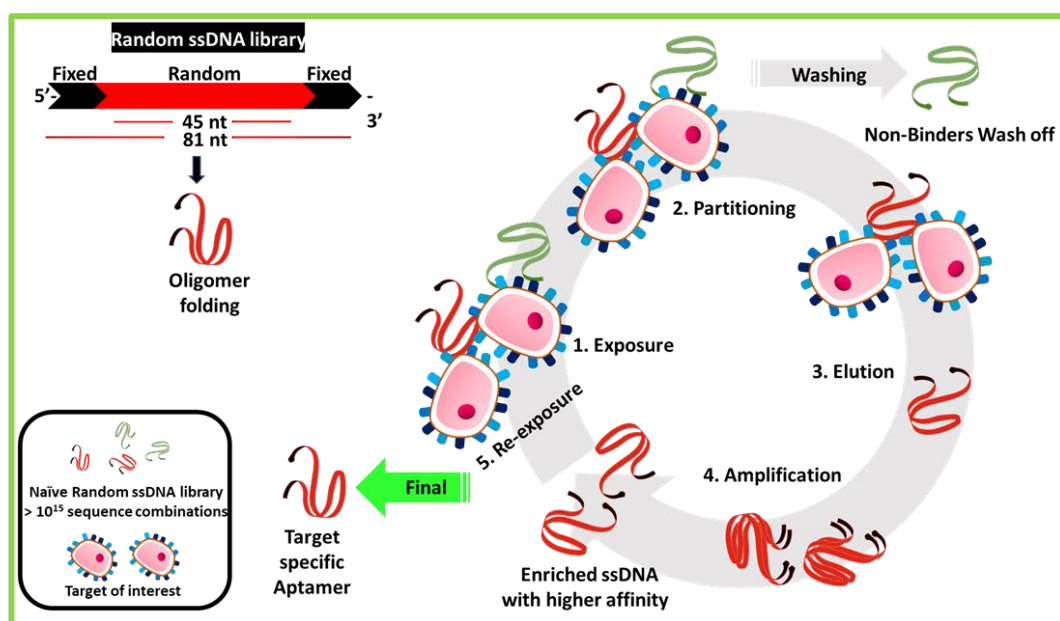


Figure 1.12: Conventional cell-SELEX: Various steps of a conventional cell-SELEX procedure. Single-stranded DNA 81-nt naïve library used in our studies for aptamer selection against whole cells, toxins, and surface antigens was adapted from established protocol¹⁶⁷.

1.6.2.1 Conventional SELEX protocol

All the variants involve the necessary steps of a conventional **SELEX protocol**, which are as follows:

- (i) **Binding:** The random naïve library is exposed to the target molecules either free in the system or adhered to the substrate and allowed to interact.
- (ii) **Selection:** The binders are retained, and non-binders are washed off. This is the most crucial step for the isolation of high-affinity oligomers. The oligomers that bind to the target are eluted out via heating, ionic/pH variation, denaturant addition, or competitive binder.
- (iii) **Amplification:** The selected ss pool is amplified using PCR or related techniques. Too many PCR cycles lead to non-specific amplification and multiple sized amplicons. Thus, 10-15 cycles are usually sufficient or mostly optimized per every SELEX.
- (iv) **Partitioning:** After PCR, the oligomer exists as ds PCR amplicon which is partitioned to single strand again either through denaturation and filtration or biotin-streptavidin probe, wherein the biotin-labeled reverse primer is used for amplification which is incorporated in the double-stranded PCR amplicon, and this biotin-labeled ds DNA is then stripped off to ssDNA using streptavidin-coated nanoparticles or beads (Figure 1.13).

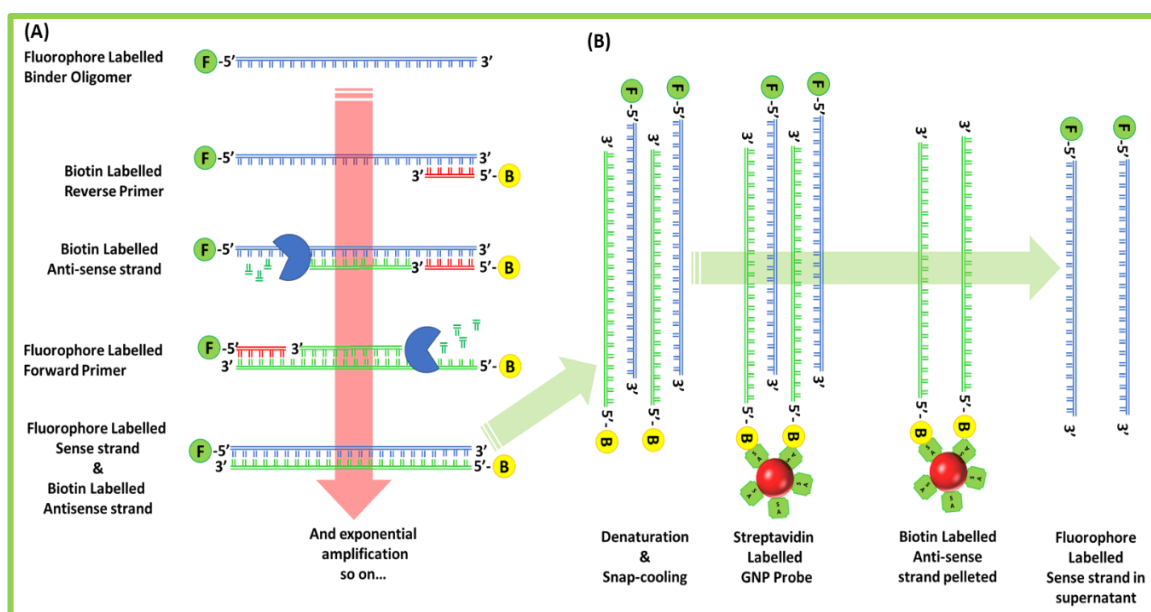


Figure 1.13: Amplification & partitioning steps of SELEX: Various stages of (A) PCR amplification of binder sequences using biotinylated antisense primer and (B) partitioning using streptavidin-coated gold nanoparticle probe. The single sense strand is used as a refined aptamer library for the next iterative rounds. Using fluorophore labeling is optional and best suited as per application.

The separated sense strand is further exposed to target with increased stringency as in Step 1. With further iterations, the diversity in the pool is decreased, and the enrichment of higher affinity oligomers takes place, thus dominating the pool in each successive cycle. This process can be

monitored at each SELEX cycle, increasing nucleic acid concentration at λ_{280} nm. The process is repeated until a high-affinity aptamer pool with proper molecular recognition for the target is selected. In addition to these SELEX steps against the target molecule or cell, a counter-selection or counter selection is carried out to eliminate the non-specific oligomers binding to other related molecules or the substrate absence of target. Herein, the cross-related species are incubated with oligomers instead of the target, and those binding to these are washed off. The non-binder population partitioned off for the next positive selection round. This addition of a counter-selective step gives an edge over other receptor generation technologies and aids in the generation of highly specific aptamers. The final pool containing the aptamer for the target is selected and amplified using unmodified primers and cloned for sequencing.

The sequence of the aptamer helps in the prediction of the secondary structure, the binding pocket, and possible interaction sites with the target. Online available tools like ‘m-fold’ and ‘RNA composer’ are widely used to predict the secondary structure and thermodynamic properties and tertiary structure, respectively^{101,102}. For a randomly generated sequence of length n , there are 4^n possible sequences. Thus, a 45-nucleotide (nt) random region library theoretically contains $4^{45} = 1,23,79,40,03,92,85,38,02,74,89,91,24,224$ different sequences. Unfortunately, this vast theoretical diversity of 10^{27} distinct sequences are not realized in real applications, and nanomoles of the initial naïve library containing around 10^{14-15} different sequences are used, which is assumed to generate different molecular interactions or structural recognition pockets for the target.

1.6.2.2 Aptamer recognition motifs

The molecular recognition of aptamer is due to a mix of many non-covalent intermolecular interactions viz., stacking of nitrogenous bases, electrostatic interactions, van der Waals interactions, hydrogen bonding. These interactions in supplementation to the induced-fit mechanism, which focuses the limelight on the unique 3D folded structures adopted by the aptamers to fit their cognate target¹⁰³. Aptamer secondary structures typically consist of motifs of high complexity like k-turns, stem-loops, pseudoknots, or G-quadruplexes (G-quad) (Figure 1.14). The incomparable capacity of aptamers to bind to various targets is due to these folded secondary structures that oligomers can adopt other than Watson-Crick hydrogen bonding or mere base to base hybridization. The k-turn is a type of bulge of three nucleotides flanked by paired bases leading to the formation of a kink in the aptamer. Stem-loops are the most-common motifs stabilized by mismatched base pairing with long stretches of bases complementary to one another and form Watson-Crick base pairs¹⁰⁴. Pseudoknots consist of two stem-loops wherein half of the stem intercalates between two halves of the other stem. Guanine-rich segments tend to form Hoogsteen-paired tetrad, which stacks upon another guanine tetrad¹⁰⁵. This G-quad is usually stabilized with the presence of mono or divalent cation, which provides spatial stability¹⁰⁶. The molecular target

recognition is an interplay of all these various non-covalent molecular interactions. Expectedly, G-quads have been mentioned as an integral motif in many published aptamers^{107–109}.

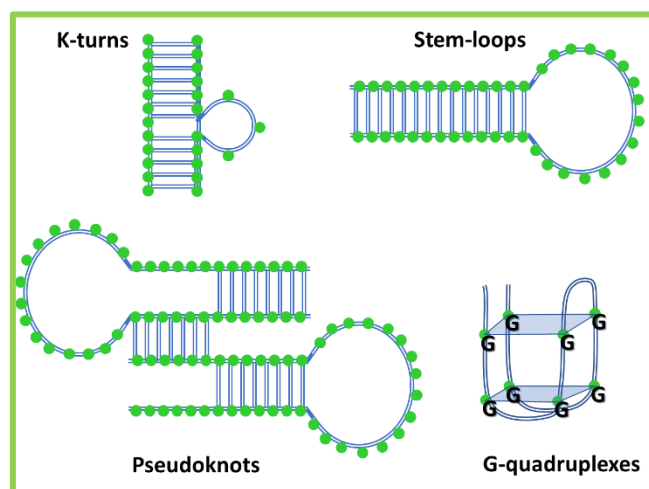
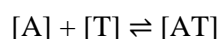


Figure 1.14: Aptamer structural motifs: Commonly reported complex tertiary structures attributed to the specific binding of ss-nucleic acid sequences.

1.6.2.3 Characteristic parameters of a bioreceptor

1.6.2.3.1 Affinity

Affinity refers to the binding interaction existing between the aptamer and its target. It is evaluated by measuring at equilibrium the association constant (K_a) for the forward reaction or the dissociation constant (K_d) for the reverse reaction, which is inversely proportional to the K_a . Oligomers that have slow-off rates exhibit strong interactions with their target and are often known by dissociation constants for affinity denoted as K_d , which is the ratio of k_{off}/k_{on} equilibrium constants for reverse and forward reactions for:



where A is an aptamer, and T is Target.

1.6.2.3.2 Specificity & cross-reactivity

Specificity is a measure of the degree to which the receptors differentiate between different antigens. Alongside, cross-reactivity is a measure of the extent to which different antigens appear similar to the receptor. Thus, a functional receptor shows high specificity and low cross-reactivity during bio-recognition. These high-affinity aptamers, therefore, consequently can bind even a few molecules of target present in samples. This sensitivity is advantageous in the detection of biomarkers that are present in a shallow concentration in the pathological state, especially during the onset of a disease.

1.6.3 Aptamers vs. antibodies

Since their discovery, aptamers have been purported as antibody mimetics due to similar application in diagnostics, but are instead very different in both structure and methodology of interaction with

the target analyte. Out of the various advantages of aptamers in comparison to antibodies, some are listed below as:

- (i) **Ease of synthesis:** Nucleic acid-based aptamers can be easily screened on a bench and amplified using PCR, unlike other receptors.
- (ii) **Ease of scaling:** Aptamers are produced chemically in a readily scalable process can be generated & is not prone to viral or bacterial contamination, and these show no batch-batch variation, and purified aptamers are way cheaper.
- (iii) **Safer:** No animals are harmed during the synthesis & selection of aptamers and have an added advantage in case of generation of receptors against toxic compounds or those that show structural similarity to molecules present in the model physiological environment.
- (iv) **Faster production:** Custom aptamers can be synthesized in under a week, which is significantly quicker than what antibody generation requires.
- (v) **Non-immunogenic:** There are no reported cases of immunogenicity when aptamers are used as in-vivo probes.
- (vi) **Counter-selection:** Able to select for and against specific targets and to select against cell-surface targets.
- (vii) **Thermostability:** Retain functional ability even after denaturation and phosphodiester bond is exceptionally chemically stable, and this excellent flexibility helps confer thermostability.
- (viii) **Ease of modification:** Conjugation with fluorescent dyes or functional groups can be readily introduced during synthesis and also, they can be immobilized on different surfaces and substrates, retaining their specificity.
- (ix) **Excellent bio-receptor element:** High affinity, specificity, small size, high stability confers the ability to act as a functional receptor element in a biosensing platform.
- (x) **Conformational flexibility:** Single strands of nucleic acid can restructure themselves during target binding, while antibodies are rigid and bulky.

1.6.4 Biosensors: Market & industry

Biosensors have been able to find applications in multiple sectors, majorly and not limited to pharma, food, and environmental monitoring. The global biosensor market was valued at almost 20 billion US\$ in 2019 and is expected to have an annual growth rate of 7.9%. In recent times, the particular demand for biosensors is increasing due to various applications of biosensors in the medical field, rising diabetic population, high demand for miniature diagnostic devices, and rapid technological advancements. In 2020, with Covid-19 infections rising globally, there is a crucial need for development and manufacturing of a wide range of diagnostic test-kits (disposable, cost-efficient, and user-friendly with fast response time) for early and precise disease diagnosis¹¹⁰. Various antibody-based platforms for bacterial detection based on various techniques have been

reported viz., amperometric, electrochemical impedance, quartz crystalline microbalance (QCM), surface plasmon resonance (SPR), and field-effect transistors (FET)^{111,112}.

In the contest of these immune-platforms, aptasensors offer high stability, selectivity & sensitivity¹². Since the discovery of SELEX, numerous labs worldwide have adopted the methodology and its variants to develop aptamer functionalized sensors, which can be observed by increasing the number of publications in this interdisciplinary field (Figure 1.15). However, still, aptasensing technologies have taken the research arena by storm, their market acceptance has been slower than anticipated, mainly due to well established standard procedures validated by governmental laws for antibody-based systems¹¹³. These lacunae can be overcome by only keeping in view the numerous pros of aptamers and cons of antibodies¹¹⁴.

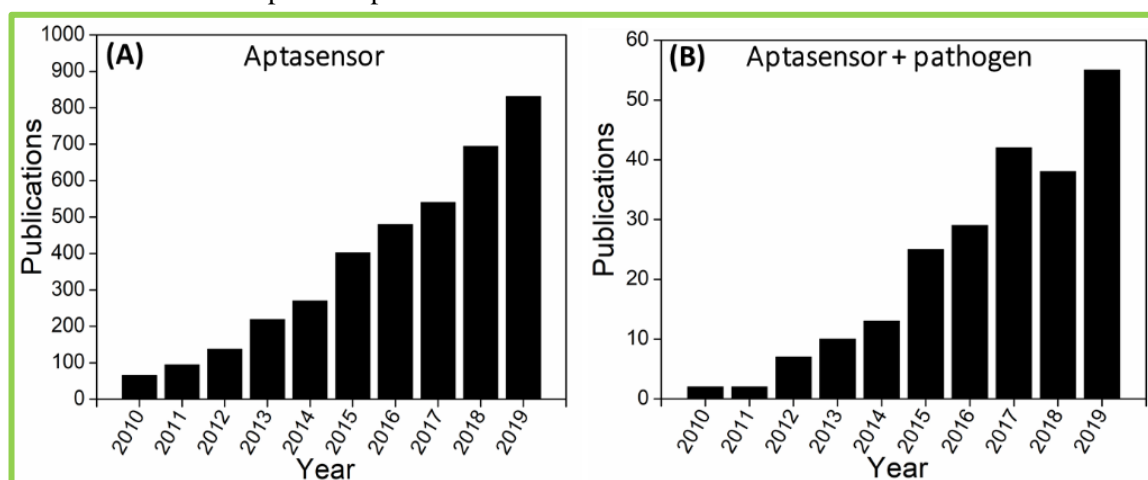


Figure 1.15: Aptasensor publication record: (A) A year-wise publication record with the term 'Aptasensor' and (B) with the term 'Aptasensor and Pathogen'. Source: Web of Science

1.7 Nanostructured sensing platforms

In Richard Feynman's famous 1959 speech *There is plenty of room at the bottom*, he emphasized on the miniaturization of the techniques for manipulation of matter at molecular or atomic subscale¹¹⁵. This vision was further expanded and explored in the subsequent years by material scientists worldwide. Nanoscience studies particles at a tiny scale in the range of 1-100 nanometers (10^{-9} m). It is an interdisciplinary domain, and the material properties are significantly different from bulk material due to quantum confinement, high surface area, and energy properties. These nanomaterials can be suitably modified by introducing functional groups or functionalized with chemo or bio-molecules that enhance their interaction and, subsequently, their sensing capability. Nanomaterials have recently been widely used for the fabrication of various biosensors for both clinical & environmental sensing¹¹⁶. These, along with aptamers (next-generation nucleic acid-based antibody mimics), have improved the selectivity & sensitivity of the functionalized biosensors for a multitude of ligands, including whole cells present in water as well as complex matrices present in food samples.

1.7.1 Nanostructured materials

The properties are drastically changed when a material enters nano-regime as rules of quantum science show more effect than classical Newtonian science. The following properties are conferred to nano-sized materials:

- (i) Wave-particle duality
- (ii) Particle penetration into forbidden energy barriers via quantum tunneling
- (iii) Size-tunable plasmonic properties due to quantum confinement
- (iv) Increased surface-to-volume ratio enhancing the physical and surface properties¹¹⁷.

In nano-regime for a material, not only the elemental composition but also the structural and surface properties immensely alter their properties, not just from bulk to nanostructures, but also between different dimensions of the same nanomaterial. These alterations may lead to enhancement of specific features, like conductivity, reactivity, catalytic activity, plasmonic, which are then exploited for transducers in sensing platforms. The nanostructures can be synthesized in various dimensions and defined as follows:

- (i) **Zero-Dimensional:** Structures having all dimensional aspects (x,y,z) lesser than 100 nanometer (nm), e.g., metal nanoparticles and those with dimensions lower than 5 nm, e.g., quantum dots (QDs) possess supreme electronic and optical properties.
- (ii) **One-Dimensional:** Structures having spatial dimensions of one of the two-axis in nano range (x,y), e.g., nanorods, nanotubes.
- (iii) **Two-Dimensional:** Structures having spatial dimensions of one of the three-axis in nano range (x,y,z), e.g., nanosheets like graphene and transition metal dichalcogenides (TMD).
- (iv) **Three-Dimensional:** Structures made out of nanostructures but themselves having all three axes (x,y,z) above the nano-regime. These exploit the features of the smaller units, e.g., 3D graphene.

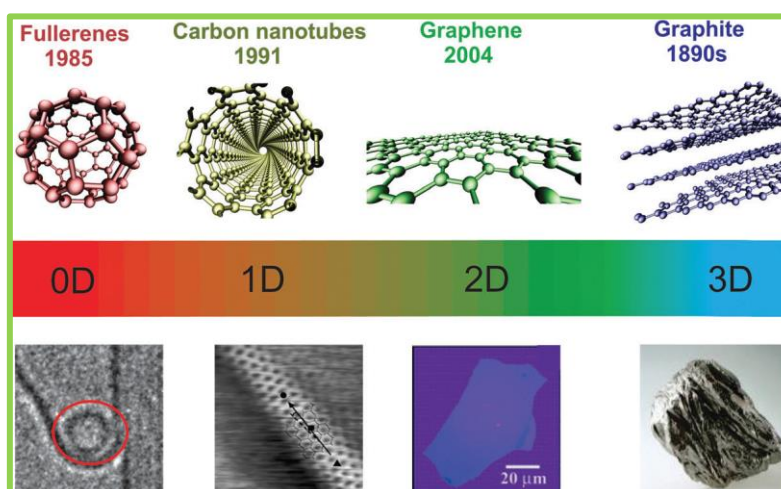


Figure 1.16: Nanostructure dimensions: Carbon-based nanostructures with different form nanostructures ranging from 0D to 3D. The top panel shows the cartoon figures for carbon analogs and their date of discovery, and the bottom panel shows the electron micrographs of the respective structures¹¹⁸.

Figure 1.16 shows the various allotropic forms of carbon constituting the different dimensions. Carbon-based nanostructures dominate the current nanomaterial area. The first carbon nanotubes were synthesized by Iijima using arc discharge in 1991, the first prominent carbon-based nanostructure development after fullerenes^{119–121}. In 2010, Andre Geim and Kostya Novoselov were awarded the Nobel Prize in Physics for groundbreaking experiments regarding the two-dimensional material graphene’ just six years after their seminal work article boosted graphene and nanotechnology research and development worldwide^{122,123}. Graphene consists of a single layer of a honeycomb lattice of covalently bonded sp^2 carbon atoms with fully conjugated π -electrons¹¹⁸. For transducer properties, the reduced form of free graphene easily oxidized to form graphene oxide (GO) is generated by chemical reduction using agents like hydrazine hydrate and/or sodium borohydride. Additionally, GO can be generated from graphite by a chemical method called Hummer’s method, whose several modifications have been carried out to optimize the reaction conditions¹²⁴.

Since the discovery of graphene, many 2D nanomaterials have emerged which have been explored on basis of their band gap for various applications ranging from metals to insulators^{125–128}. There has been a particular emphasis on transition metal dichalcogenides, which are semiconductors of the type MX_2 , where M is a transition metal (Mo, W,) and X is a chalcogen (such as S, Se or Te), which are also layered materials analogous to graphite. The fast-paced ongoing research, e.g., MoS_2 , WS_2 , $MoSe_2$, and WSe_2 , point it as the hot-area of research to find better alternatives than graphene^{128,129}. The stacked layers are relatively weakly bonded with each other by non-covalent interactions like van der Waals forces (Figure 1.17). This allows the material to be

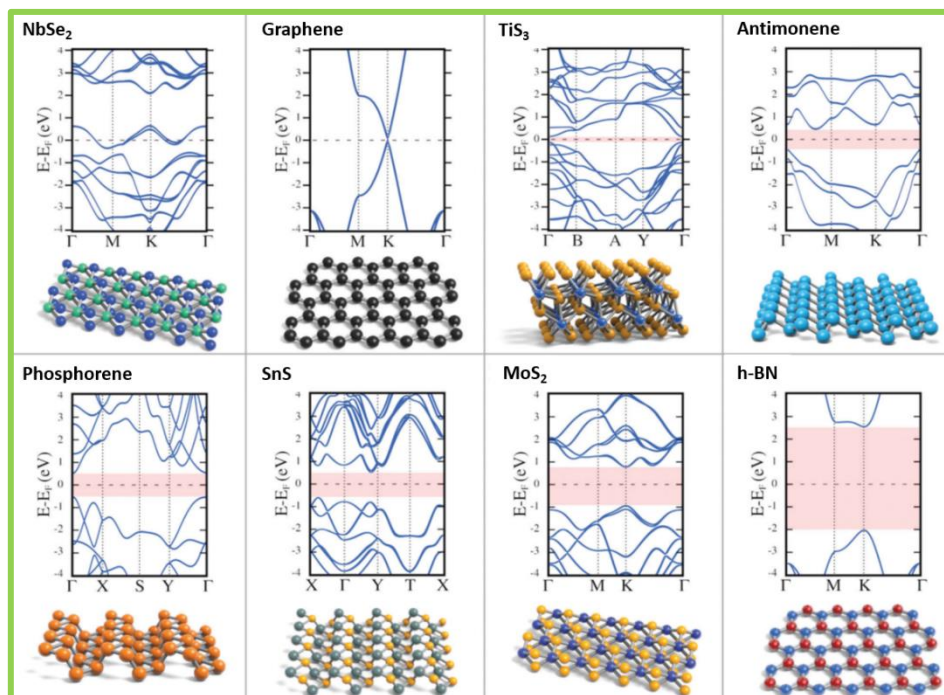


Figure 1.17: Crystal lattice & band structures: Various layered materials explored in order of increasing band gap (red shadowed area)¹⁶⁸.

peeled out into individual layers with several routes of synthesis. These nanostructures are explored for biosensing approaches since they confer excellent electrical and/or optical properties, high surface area, abundant functional groups on the surface, which help in easy functionalization and develop high sensitivity biosensing platforms.

1.7.2 Nanostructure fabrication

For the synthesis of nanostructures, many techniques like ‘top-bottom’ nanofabrication methodologies, for example, ball milling, grinding, liquid exfoliation, laser/electron lithography, scotch-tape method, and ‘bottom-up’ approach like chemical vapor-phase deposition, electrodeposition, sol-gel assembly, hydrothermal synthesis has been extensively explored over due course of last two decades^{130,131}. Table 1.3 tabulates the various methodologies conventionally approached for nanostructure synthesis supplemented with their merits and demerits¹³². The choice of fabrication technique depends on; **(i)** need of resolution, **(ii)** required optical/electrical/thermal/piezoelectric properties, **(iii)** surface groups for functionalization, and **(iv)** availability and cost-effectiveness.

Top-down	Merits	Demerits
<i>Optical lithography</i>	Long-standing, sufficient level of resolution at high throughputs	Depends on resist process sensitivity and resolution, requiring expensive cleanroom
<i>E-beam lithography</i>	An extremely accurate method for < 20 nm nanostructure fabrication	Expensive, low throughput and a slow process
<i>Soft & nanoimprint lithography</i>	Pattern transfer based simple, useful nanofabrication tool for fabricating < 10 nm features	Difficult for large-scale production of densely packed nanostructures
<i>Block copolymer lithography</i>	High-throughput, low-cost method, suitable for diverse shapes of nanostructures	Challenging to make self-assembled nanopatterns with variable periodicity
Bottom-up	Merits	Demerits
<i>Atomic layer deposition</i>	Allows the atomic level precision, and adhesion due to the formation of chemical bonds at the first atomic layer	Slow and expensive method for large scale synthesis of complex nanostructures
<i>Sol-gel</i>	Chemical synthesis method	Difficult to control synthesis and the subsequent drying steps
<i>Molecular self-assembly</i>	Allows self-assembly of deep molecular nanopatterns < 20 nm	Challenging to design and fabricate
<i>Chemical vapor-phase deposition</i>	Versatile, scalable, and controlled method deposition of materials	Requires dedicated furnaces with a supply of toxic and corrosive gases

Table 1.3: Nanofabrication methods: List of primary commonly employed nanostructure fabrication methods along with their merits and demerits¹³².

1.7.3 Transducer signaling methods

The choice of nanomaterial employed for the sensor is dictated by the signal transduction method used, and hence, these are like opposite sides of the same coin. The nanosensors are mainly classified into optical & electrochemical nanosensors, mainly based on how the output of bio-

interaction between the target and analyte is measured. Nanoparticles-based platforms usually dominate visual signal transduction, while semiconducting 1D, 2D, and 3D nanomaterials dominate the electrochemical and electrical signal transduction methods.

1.7.3.1 Optical transduction

In 1996, Davis *et al.* published the first work using aptamers as bio-receptors for sensing¹³³. The modulation of various radiations (absorption, reflectance, resonance) in the electromagnetic spectrum is used to indicate the presence/absence of target bacteria or biomolecules. Thus, optically active nanostructures like metal nanoparticles, harvest size-dependent property, and interact with light appearing colored. Colloidal gold nanoparticles (<20 nm) switch from red color ($\lambda_{\max}=520$ nm) to purple to blue coloration as aggregation increases the particle size. This phenomenon can be visually observed or with the help of a spectrophotometer for quantification. Nanoparticles of various structures like rods, shells, and cages show different optical phenomena and colorations, as

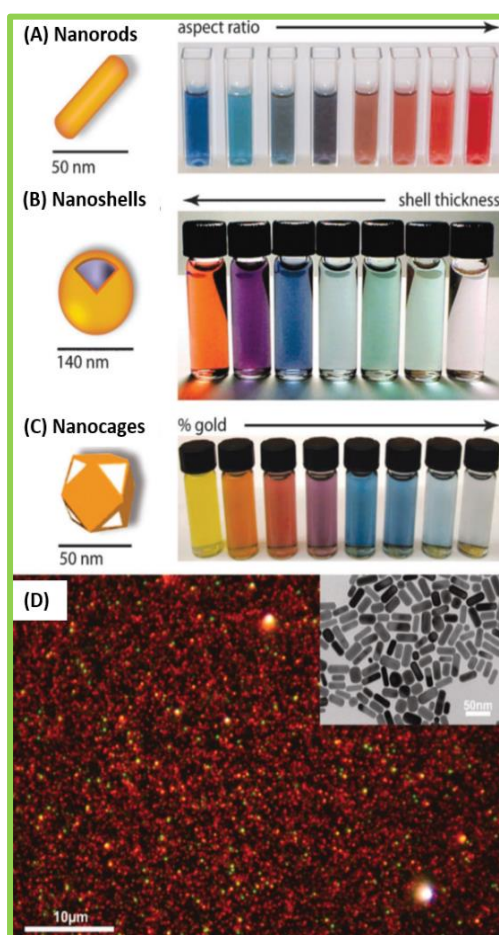


Figure 1.18: Gold nanostructures: (A) Nanorods, (B) nanoshells and (C) nanocages showing color variation with change in size and geometry. (D) Optical dark-field scattering of gold nanorods (electron micrograph in the inset) showing resonant scattering from their transverse plasmon mode (green) and their lower energy, longitudinal plasmon mode (red)¹³⁶.

visible in Figure 1.18¹³⁴. Noble metal (e.g., gold, silver, copper) nanoparticles are widely used as optical probes due to the existence of stable localized surface plasmon resonances (LSPR), which is the collective oscillation of conductive band electrons present on the surface of nanoparticle in response to electromagnetic radiation exposure. This LSPR of metal nanoparticles is sensitive to surface variations and inter-particle distance, and thus mostly positive recognition results in redshift, which is exploited for sensing. Regrettably, aggregation-based strategies prove non-beneficial in complex matrices or samples with a milieu of other competing molecules. Likewise, surface-enhanced Raman spectroscopy is a highly exploited optical phenomenon for sensing biomolecules^{135,136}.

Quantum dots with excellent photoluminescent properties are used as fluorescent sensors, which in conjugation with other enhancing or quencher molecules, are heavily employed in nanosensing optical assays. QDs fluorescence emission is tunable according to the nanoparticle's size, i.e., larger QDs fluoresce at the longest wavelengths. In contrast, the smallest QDs fluoresces at shorter wavelengths,

which visibly means large QDs emit red fluorescence and small QDs emit blue fluorescence, and medium-sized QDs producing green fluorescence, which emerges as the result of the quantum confinement effect. Their generation methods (microwave, hydrothermal, pyrolysis) for green synthesis as fluorescent tags with a wide range of excitation and emission bands is a hotspot of research. QDs based on noble metals and especially carbon dots (c-dots), have gained fame as nanoparticles that confer high quantum yield and show stability far beyond commonly used organic fluorophores¹³⁷.

1.7.3.2 Electrochemical transduction

Electrochemical sensing is a rapid signal transduction methodology where bio-interactions are observed by changes in the electrochemical reduction-oxidation (redox) signals¹³⁸. The sensing is dependent on the changes in the current/potential from faradaic processes at the electrode surface between a receptor on the surface and analyte, which is read by an oscilloscope or potentiometer. The most common techniques are voltammetric, which scan variable potentials and measure the current changes resulting in the electrode interface and impedance, which relies on the alterations in the charge-transfer or resistance of the system. Impedance observation known as electrochemical impedance spectroscopy (EIS) is a label-free technique, where the analyte itself facilitates conductance or residence on the electrode surface^{138,139}. In this thesis, both these techniques are exploited for characterization of the nanostructures as well as for apta-assays using screen-printed electrodes (SPE) with working electrode (WE), the counter electrode (CE), and reference all on a small chip through the help of a sophisticated electrochemical workstation. SPE sensors were chosen as they are cost-effective, need low sample volume, and are easy to use, which is desirable in biosensing measurements for point-of-care diagnosis¹⁴⁰. When designing an electrochemical biosensor, quite a few vital aspects must be considered: **(i)** the choice of bio-receptor concerning its size and electronic behavior, **(ii)** immobilization of the bio-receptor; **(iii)** functionalization ability of the transducer material and its **(iv)** sensitivity. The bio-interaction should occur close to the electrode interface to detect the redox reaction, thus requiring bio-receptors with a smaller size (aptamers overpower antibodies) and deployment of small-functional groups on the surface (long functionalization molecules dampen response) of the electrode. Thus, specific aptamers in the conjugation of functional conductive nanomaterials for modification of the working electrode, usually made of metals or carbon, are of immense interest. So, in a typical electrochemical apta-nanosensor, the surface of the working electrode is modified with nanomaterial with enhanced conductive properties functionalized with aptamer and where the electrochemical circuit is mediated by the movement of electrons from the electrolyte (usually supplemented with a redox probe, e.g., $[\text{Fe}(\text{CN})_6]^{3-/4-}$) to the surface of the electrode. The techniques mostly utilized in this thesis for sensing purposes are discussed briefly in this section (Figure 1.19).

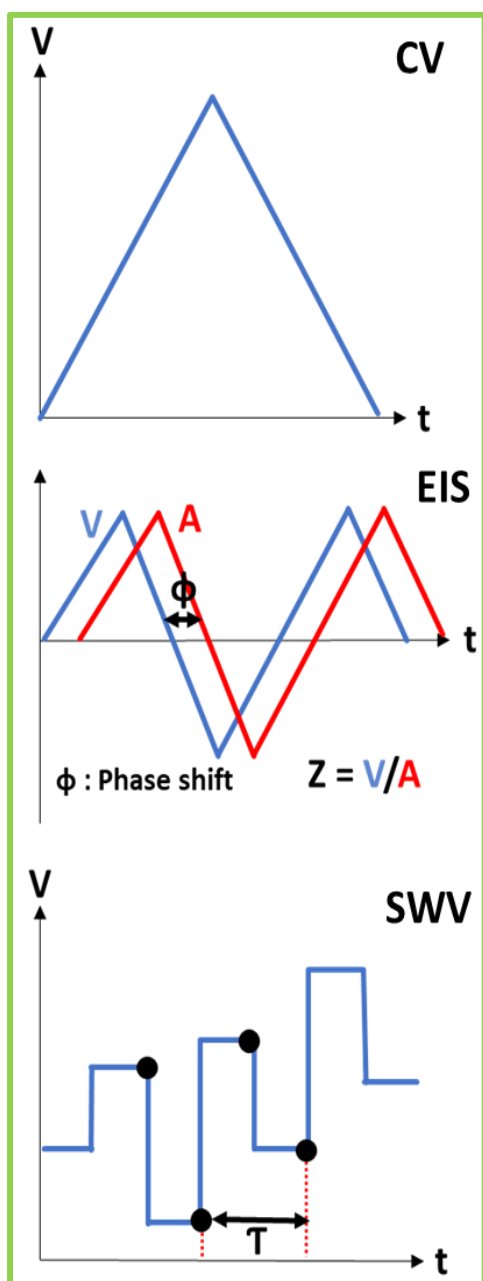


Figure 1.19: Electrochemical techniques: Waveforms for electrochemical techniques mostly used for sensing; CV, EIS and SWV.

Cyclic voltammetry (CV) is a well-known and prevalent electrochemical technique commonly used for monitoring the redox processes of molecular species present in the solution or WE surface. This is usually used to characterize the electrode surface, where the corresponding current for the potential sweep is recorded cyclically.

Alternatively, a more sensitive pulsed electrochemical technique called square wave voltammetry (SWV) is used for analytical sensing, a form of potential sweep voltammetry that combines square wave and staircase potential applied to an electrode. Here, the current response is recorded twice—firstly at the end of the forward potential pulse and again at the end of the reverse potential pulse, which reduces the current response from non-faradaic processes. Thus, increasing the ratio of faradaic response to non-faradaic response, allowing for higher sensitivity.

EIS measures alternating current impedance and are mostly utilized for recognition of biomolecules or cells, which are resistive and hinder the flow of electrons to the sensor surface. By varying the intensity of the excitation potential through a frequency range, an impedance spectrum of the electrochemical system is acquired and analyzed. As in electrical analysis, the real component of impedance (Z') corresponds to a resistance in-phase with the applied voltage. The imaginary part (Z'') corresponds to a reactance 90° out-of-phase with the applied voltage, which provides information about the kinetic, capacitive, and mass transport properties of the electrochemical system. The total complex impedance of the cell is divided into real, Z'' , and an imaginary, Z' component. The Nyquist plot consisting of $-Z''$ vs. Z' is plotted to generate a semi-circle curve. When a reaction occurs on the electrode surface at the electrode-electrolyte interface, a change either the charge transfer resistance (R_{ct}) or the double-layer capacitance (C_{dl}), the Warburg impedance (Z_w), which represents the diffusion of ions in the media are affected. This spectrum is fitted using the Randles-Sevcik circuit, which is the modified equivalent circuit model for, the SPE based electrochemical aptasensor as displayed in Figure 1.20.

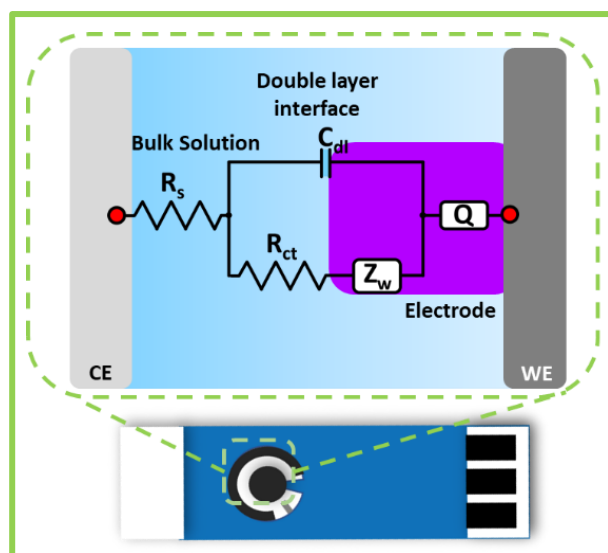


Figure 1.20: Randles-Sevcik circuit fitting for aptasensor: SPE was modified with aptamer functionalized nanostructures for bio-sensing.

1.8 Recent biosensing platforms

Several advances in biosensing platforms based on variety of bio-receptors mentioned in section 1.6 and transducer methodologies in section 1.7 have been reported in recent years. Majorly antibody, aptamer and antibody-aptamer hybrid platforms have come up as an area of extensive study^{141–143}. These platforms have been widely studied for the detection of clinically and environmentally significant molecules viz., disease biomarkers, drugs and antibiotics, pathogens (including bacteria and virus), toxins (mycotoxins, phytotoxins), heavy metal contaminants, pesticides and herbicides, etc., in food and water sources^{144–152}. Nanotechnology based biosensors have been technologically advanced for monitoring of organic compounds like aldehydes, 2,4,6-trinitrotoluene, 2,4-dichlorophenoxyacetic acid, acetamiprid, chlorpyrifos, malathion, arsenic, mercury, radioactive waste, to name a few which have severe effects on the environment and dependent living organisms^{153–160}. Biological contaminants in food products and water sources have been extensively studied for monitoring and optimal detection up to single cell level by super sophisticated technologies¹⁶¹. *Salmonella* sp., *Listeria* sp., *Campylobacter* sp., *Staphylococcus* sp., *Pseudomonas* sp., etc., have been detected in clinical blood and sera samples and advancements for non-invasive techniques are being rapidly developed by researchers worldwide^{162–165}. Still, there lies a substantial challenge ahead for the implementation of sensors based on novel nanostructures and bio-receptors that retain high sensitivity, stability and reusability independent of costly reagents and instrumentations¹⁶⁶.

1.9 Our biosensing approach

To battle out the current problem of infectious diseases at hand, as discussed in this chapter, we took an aptamer functionalized nanomaterial-based sensing technology as the first line of approach. The generation of aptamer-based bio-receptor against a pathogen gives an added advantage to

synthetically produced aptamers versus antibodies raised in animal models both physiologically and ethically. Additionally, our three-way approach for bio-receptor generation stems from alternative enhanced binding affinities for target in various environments (Figure 1.21). In our opinion, the presence of both whole-cell or its components is possible for monitoring targets. Therefore, multiple aptamers were screened against the whole-cell and its components and utilized for bio-sensing.

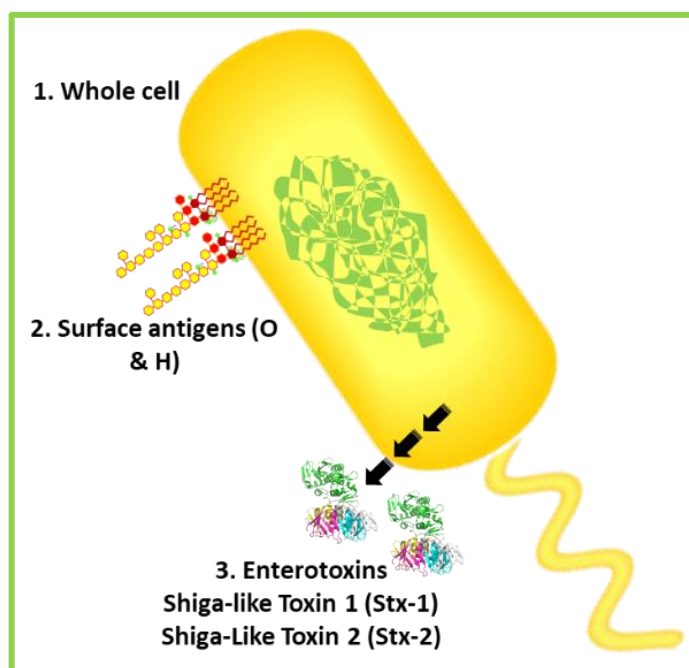


Figure 1.21: Three-way approach for bioreceptor generation: Multiple strategies for producing high-affinity aptamers for specific estimation of bacterial cells have been undertaken for aptamer screening using 1) whole-cell bacteria, 2) surface antigens (O & H antigens), and 3) enterotoxins (Stx subtypes).

In summary, the overall aim of this thesis is the development of aptasensing platforms for bacterial detection of pathogenic *E. coli* and its surface antigen and toxins. The objective is to explore novel methods for aptamer generation and the simultaneous application of these aptamers as bio-recognition moieties onto nanostructured platforms. The thesis also aims at the synthesis of nanostructures relevant for aptasensing optically and electrochemically.

1.9.1 Objectives

The primary goals furnished to meet the requirements of our studies are:

- (i) Identification of potentially pathogenic enteric bacteria, surface markers, and toxins.
- (ii) Generation & characterization of specific bio-receptors against the selected targets and modeling studies to evaluate the best bio-receptor against the antigenic markers.
- (iii) Synthesis & characterization of novel nanostructures for transducer application.
- (iv) Bio-conjugation of generated bio-receptors with various modified nanostructures for assay development.
- (v) Design & fabrication of nanostructured sensing platform.
- (vi) Testing & validation of real food & environmental samples.

1.9.2 Outline of the thesis

In this last section of the chapter, an outline of the thesis is presented.

1.9.2.1 Chapter 1 overview

It is the introductory chapter which details on five main topics viz., enteric pathogenic bacteria with a prime focus on pathogenic *E. coli*, conventional microbial detection methods and their limitations, our biosensor components – aptamers; their generation and characteristics and nanostructures; their features and prominently explored sensing techniques.

1.9.2.2 Chapter 2 overview

The chapter discusses the apta-sensing of *E. coli* O78:H11, an enterotoxigenic *E. coli* strain, which is a leading cause of diarrhea, especially in African & south-east Asian countries. For this, we generated a specific anti-*E. coli* O78:H11 aptamer via a novel in-situ developed SELEX method using phenylboronic acid as capture moiety on a microtiter plate. Simultaneously, we synthesized a 3D-hierarchical bridged rebar graphene nano-construct via un-scrolling of multiwall carbon nanotubes and subsequent bridging with terephthalaldehyde, which exhibited enhanced electrical properties. The specific aptamer was used to functionalize the BRG modified electrode for label-free impedimetric sensing of *E. coli* O78:H11 in spiked water and juices samples.

1.9.2.3 Chapter 3 overview

The chapter accounts in detail the apta-sensing of enterohemorrhagic *E. coli* serotype O157:H7. This serotype is well documented as the leading cause of bacterial gastroenteritis and its associated hemolytic-uremic syndrome worldwide. Herein, we generated a specific anti-*E. coli* O157:H7 aptamer via microtiter SELEX methodology. Subsequently, we fabricated nickel nanoparticle decorated boron infused carbon nanorods nanostructured platform, which was functionalized with a specific aptamer to develop a label-free impedimetric aptasensor for rapid & sensitive detection of *E. coli* O157:H7 in spiked water and juice samples. The thesis is supplemented with allied proof-of-concept work in the development of microfluidic bacterial monitoring platform.

1.9.2.4 Chapter 4 overview

The chapter brings forth the studies related to optical apta-sensing of major bacterial surface antigens, O-antigen and H-antigen of *E. coli* O157:H7. These surface markers are potent superantigens in themselves, causing sepsis. This chapter details the selection of aptamers against these markers, and the synthesis of novel carbon dots for a sensitive nano-bioassay is based on the quenching of c-dots fluorescence by silver nanoparticles via fluorescence resonance energy transfer. In the presence of the target, the quenched fluorescence was significantly recovered.

1.9.2.5 Chapter 5 overview

The chapter accounts for developing bilayer interferometry based in-vitro SELEX technique for fishing out specific aptamers against *E. coli* Shiga toxin subtypes viz., Stx1 & Stx2 via specific epitopically relevant peptides and its voltammetric detection using liquid-exfoliated chitosan WSe₂ nanosheets modified electrochemical sensor.

1.9.2.6 Chapter 6 overview

The chapter recapitulates the proposed platforms and experimental studies of the thesis and projects the future perspectives of the work.

Bibliography

- (1) Microbiology by Numbers. *Nature Reviews Microbiology*. Nature Publishing Group September 12, 2011, p 628. <https://doi.org/10.1038/nrmicro2644>.
- (2) WHO. Estimates of the Global Burden of Foodborne Diseases 2007-2015. **2015**, 09–265.
- (3) WHO. *WHO | Diseases and Risks*; World Health Organization, 2019.
- (4) Biomechanics of the Digestive System. In *Integrated Nano-Biomechanics*; Elsevier, 2018; pp 71–99. <https://doi.org/10.1016/b978-0-323-38944-0.00003-6>.
- (5) Kaper, J. B.; Nataro, J. P.; Mobley, H. L. T. Pathogenic Escherichia Coli. *Nat. Rev. Microbiol.* **2004**, 2 (2), 123–140. <https://doi.org/10.1038/nrmicro818>.
- (6) Leimbach, A.; Hacker, J.; Dobrindt, U. E. Coli as an All-Rounder: The Thin Line between Commensalism and Pathogenicity. *Curr. Top. Microbiol. Immunol.* **2013**, 358, 3–32. https://doi.org/10.1007/82_2012_303.
- (7) Pennington, H. Escherichia Coli O157. *Lancet* **2010**, 376 (9750), 1428–1435. [https://doi.org/10.1016/S0140-6736\(10\)60963-4](https://doi.org/10.1016/S0140-6736(10)60963-4).
- (8) Nataro, J. P.; Kaper, J. B. Diarrheagenic Escherichia Coli. *Clinical Microbiology Reviews*. January 1998, pp 142–201. <https://doi.org/10.1128/cmr.11.1.142>.
- (9) Saxena, T.; Kaushik, P.; Krishna Mohan, M. Prevalence of E. Coli O157: H7 in Water Sources: An Overview on Associated Diseases, Outbreaks and Detection Methods. *Diagn. Microbiol. Infect. Dis.* **2015**, 82 (3), 249–264. <https://doi.org/10.1016/j.diagmicrobio.2015.03.015>.
- (10) Yang, S. C.; Lin, C. H.; Aljuffali, I. A.; Fang, J. Y. Current Pathogenic Escherichia Coli Foodborne Outbreak Cases and Therapy Development. *Arch. Microbiol.* **2017**, 199 (6), 811–825. <https://doi.org/10.1007/s00203-017-1393-y>.
- (11) Croxen, M. A.; Law, R. J.; Scholz, R.; Keeney, K. M.; Wlodarska, M.; Finlay, B. B. Recent Advances in Understanding Enteric Pathogenic Escherichia Coli. *Clin. Microbiol. Rev.* **2013**, 26 (4), 822–880. <https://doi.org/10.1128/CMR.00022-13>.
- (12) Lazcka, O.; Campo, F. J. Del; Muñoz, F. X. Pathogen Detection: A Perspective of Traditional Methods and Biosensors. *Biosens. Bioelectron.* **2007**, 22 (7), 1205–1217. <https://doi.org/10.1016/j.bios.2006.06.036>.
- (13) Humphries, R. M.; Linscott, A. J. Laboratory Diagnosis of Bacterial Gastroenteritis. *Clin. Microbiol. Rev.* **2015**, 28 (1), 3–31. <https://doi.org/10.1128/CMR.00073-14>.
- (14) BAM Chapter 4A: Diarrheagenic Escherichia coli | FDA <https://www.fda.gov/food/laboratory-methods-food/bam-chapter-4a-diarrheagenic-escherichia-coli> (accessed Aug 22, 2020).
- (15) Batt, R. M.; Rutgers, H. C.; Sancak, A. A. Enteric Bacteria: Friend or Foe? *J. Small Anim. Pract.* **1996**, 37 (6), 261–267. <https://doi.org/10.1111/j.1748-5827.1996.tb02376.x>.
- (16) Bacterial Pathogens of Humans http://textbookofbacteriology.net/medical_3.html (accessed Sep 29, 2020).
- (17) Sattar, S. B. A.; Singh, S. *Gastroenteritis, Bacterial*; 2018.
- (18) Schlenker, C.; Surawicz, C. M. Emerging Infections of the Gastrointestinal Tract. *Best Pract. Res. Clin. Gastroenterol.* **2009**, 23 (1), 89–99. <https://doi.org/10.1016/j.bpg.2008.11.014>.
- (19) Kaushik, M.; Khare, N.; Kumar, S.; Gulati, P. High Prevalence of Antibiotic Resistance and Integrons in *Escherichia Coli* Isolated from Urban River Water, India. *Microb. Drug Resist.* **2019**, 25 (3), 359–370. <https://doi.org/10.1089/mdr.2018.0194>.
- (20) Hacker, J.; Microbiology, G. B.-O.-N. R.; 2007, undefined. In Appreciation of Theodor Escherich. *nature.com*.
- (21) Escherich, T. Die Darmbakterien Des Neugeborenen Und Säuglings. *Fortschr. Med.* **1885**, 3 (47–54), 515–522.
- (22) Law, D. The History and Evolution of Escherichia Coli O157 and Other Shiga Toxin-Producing E. Coli. *World J. Microbiol. Biotechnol.* **2000**, 16 (8–9), 701–709. <https://doi.org/10.1023/A:1008927820535>.
- (23) Mainil, J. Escherichia Coli Virulence Factors. *Vet. Immunol. Immunopathol.* **2013**, 152 (1–2), 2–12. <https://doi.org/10.1016/j.vetimm.2012.09.032>.
- (24) Kaper, J. B.; Nataro, J. P.; Mobley, H. L. T. Pathogenic Escherichia Coli. *Nature Reviews Microbiology*. February 2004, pp 123–140. <https://doi.org/10.1038/nrmicro818>.
- (25) Kaper, J. B.; Karmali, M. A. *The Continuing Evolution of a Bacterial Pathogen*; 2008.
- (26) Mcdaniel, T. K.; Jarvis, K. G.; Donnenberg, M. S.; Kaper, J. B. A Genetic Locus of Enterocyte Effacement

- Conserved among Diverse Enterobacterial Pathogens. *Proc. Natl. Acad. Sci. U. S. A.* **1995**, 92 (5), 1664–1668. <https://doi.org/10.1073/pnas.92.5.1664>.
- (27) Blount, Z. D. The Unexhausted Potential of E. Coli. *eLife*. March 25, 2015. <https://doi.org/10.7554/eLife.05826>.
- (28) Pupo, G. M.; Lan, R.; Reeves, P. R. Multiple Independent Origins of Shigella Clones of Escherichia Coli and Convergent Evolution of Many of Their Characteristics. *Proc. Natl. Acad. Sci. U. S. A.* **2000**, 97 (19), 10567–10572. <https://doi.org/10.1073/pnas.180094797>.
- (29) Reid, S. D.; Herbelin, C. J.; Bumbaugh, A. C.; Selander, R. K.; Whittam, T. S. Parallel Evolution of Virulence in Pathogenic Escherichia Coli. *Nature* **2000**, 406 (6791), 64–67. <https://doi.org/10.1038/35017546>.
- (30) DuPont, H. L. Bacterial Diarrhea. *N. Engl. J. Med.* **2009**, 361 (16), 1560–1569. <https://doi.org/10.1056/NEJMcp0904162>.
- (31) Kirk, M. D.; Pires, S. M.; Black, R. E.; Caipo, M.; Crump, J. A.; Devleeschauwer, B.; Döpfer, D.; Fazil, A.; Fischer-Walker, C. L.; Hald, T.; Hall, A. J.; Keddy, K. H.; Lake, R. J.; Lanata, C. F.; Torgerson, P. R.; Havelaar, A. H.; Angulo, F. J. World Health Organization Estimates of the Global and Regional Disease Burden of 22 Foodborne Bacterial, Protozoal, and Viral Diseases, 2010: A Data Synthesis. *PLOS Med.* **2015**, 12 (12), e1001921. <https://doi.org/10.1371/journal.pmed.1001921>.
- (32) Rahman, M.; Nabi, A.; Asadulghani, M.; Faruque, S. M.; Islam, M. A. Toxigenic Properties and Stx Phage Characterization of Escherichia Coli O157 Isolated from Animal Sources in a Developing Country Setting. *BMC Microbiol.* **2018**, 18 (1), 98. <https://doi.org/10.1186/s12866-018-1235-3>.
- (33) World Health Organisation (WHO). *Ten Threats to Global Health in 2019*; 2019.
- (34) Travelers' Diarrhea - Chapter 2 - 2020 Yellow Book | Travelers' Health | CDC <https://wwwnc.cdc.gov/travel/yellowbook/2020/preparing-international-travelers/travelers-diarrhea> (accessed Jul 14, 2020).
- (35) Anderson, J. D.; Bagamian, K. H.; Muhib, F.; Amaya, M. P.; Laytner, L. A.; Wierzbica, T.; Rheingans, R. Burden of Enterotoxigenic Escherichia Coli and Shigella Non-Fatal Diarrhoeal Infections in 79 Low-Income and Lower Middle-Income Countries: A Modelling Analysis. *Lancet Glob. Heal.* **2019**, 7 (3), e321–e330. [https://doi.org/10.1016/S2214-109X\(18\)30483-2](https://doi.org/10.1016/S2214-109X(18)30483-2).
- (36) Qadri, F.; Svennerholm, A. M.; Faruque, A. S. G.; Sack, R. B. Enterotoxigenic Escherichia Coli in Developing Countries: Epidemiology, Microbiology, Clinical Features, Treatment, and Prevention. *Clinical Microbiology Reviews*. American Society for Microbiology (ASM) July 2005, pp 465–483. <https://doi.org/10.1128/CMR.18.3.465-483.2005>.
- (37) Terajima, J.; Izumiya, H.; Hara-Kudo, Y.; Ohnishi, M. Shiga Toxin (Verotoxin)-Producing *Escherichia Coli* and Foodborne Disease: A Review. *Food Saf.* **2017**, 5 (2), 35–53. <https://doi.org/10.14252/foodsafetyfscj.2016029>.
- (38) Kumar, M.; Puri, A. A Review of Permissible Limits of Drinking Water. *Indian Journal of Occupational and Environmental Medicine*. January 2012, pp 40–44. <https://doi.org/10.4103/0019-5278.99696>.
- (39) NESTLE. Microbiological Specifications. *Nestec Ltd., Vevey (Switzerland)* **2014**.
- (40) BIS. Indian Standards Drinking Water Specifications IS 10500:2012. *Bur. Indian Stand. Indian Stand. Drink. Water Specif.* **2012**, 2 (May), 11.
- (41) Ministry of Health and Family Welfare India. Manual of Methods of Analysis of Foods Food Safety and Standards Authority. **2015**.
- (42) Food Safety and Standards Authority of India. Food Safety and Standards (Food Products Standards and Food Additives) Regulations, 2011. **2011**, 1–776.
- (43) European Commission. Commission Regulation (EU) No 365/2010 of 28 April 2010 Amending Regulation (EC) No 2073/2005 on Microbiological Criteria for Foodstuffs as Regards Enterobacteriaceae in Pasteurised Milk and Other Pasteurised Liquid Dairy Products and Listeria Monocytogae. *Oj L* **2010**, 107 (365), 9.
- (44) Commission Regulation (EC) No 2073/2005 on Microbiological Criteria for Foodstuffs. *Off. J. Eur. Union* **2005**.
- (45) *Microorganisms in Foods 7: Microbiological Testing in Food Safety Management, Second Edition*; Springer International Publishing, 2018. <https://doi.org/10.1007/978-3-319-68460-4>.
- (46) *MICROBIOLOGICAL RISK ASSESSMENT SERIES 32 Attributing Illness Caused by Shiga Toxin-Producing Escherichia Coli (STEC) to Specific Foods REPORT*.
- (47) Wen, X.; Chen, F.; Lin, Y.; Zhu, H.; Yuan, F.; Kuang, D.; Jia, Z.; Yuan, Z. Microbial Indicators and Their Use for Monitoring Drinking Water Quality — A Review. 1–14.
- (48) Fewtrell, L.; Bartram, J.; Ashbolt, N. J.; Grabow, W. O. K.; Snozzi, M. *Indicators of Microbial Water Quality*; 2001.
- (49) Australia New Zealand Food Standards Code – Standard 1.6.1 – Microbiological limits in food <https://www.legislation.gov.au/Details/F2018C00939> (accessed Oct 6, 2020).
- (50) Food Standards Australia New Zealand. *Compendium of Microbiological Criteria for Food*; 2016. <https://doi.org/978-0-642-34594-3>.
- (51) Fratamico, P. M.; DebRoy, C.; Liu, Y.; Needleman, D. S.; Baranzoni, G. M.; Feng, P. Advances in Molecular Serotyping and Subtyping of Escherichia Coli†. *Front. Microbiol.* **2016**, 7 (MAY), 644. <https://doi.org/10.3389/fmicb.2016.00644>.
- (52) Robins-Browne, R. M.; Holt, K. E.; Ingle, D. J.; Hocking, D. M.; Yang, J.; Tauschek, M. Are Escherichia Coli Pathotypes Still Relevant in the Era of Whole-Genome Sequencing? *Front. Cell. Infect. Microbiol.* **2016**, 6 (NOV), 1–9. <https://doi.org/10.3389/fcimb.2016.00141>.
- (53) O'sullivan, J.; Bolton, D. J.; Duffy, G.; Baylis, C.; Tozzoli, R.; Wasteson, Y.; Lofdahl, S. *Methods for Detection and Molecular Characterisation of Pathogenic Escherichia Coli CO-ORDINATION ACTION FOOD-CT-2006-036256 Pathogenic Escherichia Coli Network*.
- (54) *Pathogenic E. Coli Diagnostics Rapid and Reliable Detection by Real-Time PCR • RIDA®GENE EHEC/EPEC*

- RIDA®GENE EAEC • RIDA®GENE ETEC/EIEC • RIDA®GENE STEC • RIDA®GENE E. Coli Stool Panel I.
- (55) mericon E. coli O157 Detection Kits - QIAGEN Online Shop <https://www.qiagen.com/be/products/discovery-and-translational-research/pcr-qpcr-dpcr/qpcr-assays-and-instruments/food-safety-testing/mericon-e-coli-o157-detection-kits/#orderinginformation> (accessed Sep 29, 2020).
 - (56) FilmArray Gastrointestinal Panel | bioMérieux Clinical Diagnostics <https://www.biomerieux-diagnostics.com/filmarray-gi-panel> (accessed Sep 29, 2020).
 - (57) STEC Testing - Real-Time BAX® System detection | Assay Specs | BAX Assays | Diagnostics | Hygiene - Rapid Solutions for Hygiene Monitoring <https://www.hygiene.com/bax-ecoli-stec-rt.html> (accessed Sep 29, 2020).
 - (58) Singh, P.; Liu, Y.; Bosilevac, J. M.; Mustapha, A. Detection of Shiga Toxin-Producing Escherichia Coli, Stx1, Stx2 and Salmonella by Two High Resolution Melt Curve Multiplex Real-Time PCR. *Food Control* **2019**, *96*, 251–259. <https://doi.org/10.1016/j.foodcont.2018.09.024>.
 - (59) Bai, J.; Paddock, Z. D.; Shi, X.; Li, S.; An, B.; Nagaraja, T. G. Applicability of a Multiplex PCR to Detect the Seven Major Shiga Toxin-Producing Escherichia Coli Based on Genes That Code for Serogroup-Specific O-Antigens and Major Virulence Factors in Cattle Feces. *Foodborne Pathog. Dis.* **2012**, *9* (6), 541–548. <https://doi.org/10.1089/fpd.2011.1082>.
 - (60) Hahm, B. K.; Maldonado, Y.; Schreiber, E.; Bhunia, A. K.; Nakatsu, C. H. Subtyping of Foodborne and Environmental Isolates of Escherichia Coli by Multiplex-PCR, Rep-PCR, PFGE, Ribotyping and AFLP. *J. Microbiol. Methods* **2003**, *53* (3), 387–399. [https://doi.org/10.1016/S0167-7012\(02\)00259-2](https://doi.org/10.1016/S0167-7012(02)00259-2).
 - (61) Shima, K.; Yoshii, N.; Akiba, M.; Nishimura, K.; Nakazawa, M.; Yamasaki, S. Comparison of PCR-RFLP and PFGE for Determining the Clonality of Enterohemorrhagic Escherichia Coli Strains. *FEMS Microbiol. Lett.* **2006**, *257* (1), 124–131. <https://doi.org/10.1111/j.1574-6968.2006.00174.x>.
 - (62) Rumore, J.; Tschetter, L.; Kearney, A.; Kandar, R.; McCormick, R.; Walker, M.; Peterson, C. L.; Reimer, A.; Nadon, C. Evaluation of Whole-Genome Sequencing for Outbreak Detection of Verotoxigenic Escherichia Coli O157:H7 from the Canadian Perspective. *BMC Genomics* **2018**, *19* (1), 1–13. <https://doi.org/10.1186/s12864-018-5243-3>.
 - (63) Joensen, K. G.; Scheutz, F.; Lund, O.; Hasman, H.; Kaas, R. S.; Nielsen, E. M.; Aarestrup, F. M. Real-Time Whole-Genome Sequencing for Routine Typing, Surveillance, and Outbreak Detection of Verotoxigenic Escherichia Coli. *J. Clin. Microbiol.* **2014**, *52* (5), 1501–1510. <https://doi.org/10.1128/JCM.03617-13>.
 - (64) Vila, J.; Gómez, M. D.; Salavert, M.; Bosch, J. Methods of Rapid Diagnosis in Clinical Microbiology: Clinical Needs. *Enfermedades Infecc. y Microbiol. Clin. (English ed.)* **2017**, *35* (1), 41–46. <https://doi.org/10.1016/j.eimce.2017.01.014>.
 - (65) Ho, Y. P.; Muralidhar Reddy, P. Identification of Pathogens by Mass Spectrometry. *Clinical Chemistry*. Oxford University Press April 1, 2010, pp 525–536. <https://doi.org/10.1373/clinchem.2009.138867>.
 - (66) Weiss, A.; Heinold, S.; Brunisholz, R.; Schmidt, H.; Drissner, D. Application of MALDI-TOF Mass Spectrometry and Specific PCR for Tracking of E. Coli O157:H – Strain 431/97 in Batavia Lettuce. *Chem. Biol. Technol. Agric.* **2019**, *6* (1), 1–9. <https://doi.org/10.1186/s40538-018-0141-0>.
 - (67) Chui, H.; Chan, M.; Hernandez, D.; Chong, P.; McCorrister, S.; Robinson, A.; Walker, M.; Peterson, L. A. M.; Ratnam, S.; Haldane, D. J. M.; Bekal, S.; Wylie, J.; Chui, L.; Westmacott, G.; Xu, B.; Drobot, M.; Nadon, C.; Knox, J. D.; Wang, G.; Chenga, K. Rapid, Sensitive, and Specific Escherichia Coli H Antigen Typing by Matrix-Assisted Laser Desorption Ionization-Time of Flight-Based Peptide Mass Fingerprinting. *J. Clin. Microbiol.* **2015**, *53* (8), 2480–2485. <https://doi.org/10.1128/JCM.00593-15>.
 - (68) VITEK MS | bioMérieux Clinical Diagnostics <https://www.biomerieux-diagnostics.com/vitek-rs-ms-0> (accessed Sep 29, 2020).
 - (69) Morris, G. E.; Rockberg, J.; Editors, J. N. Epitope Mapping Protocols (Third Edition). *Methods Mol. Biol.* **2018**, *1785*, 231–238. <https://doi.org/10.1007/978-1-4939-7841-0>.
 - (70) Jin, H. Y.; Tao, K. H.; Li, Y. X.; Li, F. Q.; Li, S. Q. Microarray Analysis of Escherichia Coli O157:H7. *World J. Gastroenterol.* **2005**, *11* (37), 5811–5815. <https://doi.org/10.3748/wjg.v11.i37.5811>.
 - (71) Garaizar, J.; Rementeria, A.; Porwollik, S. DNA Microarray Technology: A New Tool for the Epidemiological Typing of Bacterial Pathogens? *FEMS Immunol. Med. Microbiol.* **2006**, *47* (2), 178–189. <https://doi.org/10.1111/j.1574-695X.2006.00081.x>.
 - (72) Wang, Q.; Wang, S.; Beutin, L.; Cao, B.; Feng, L.; Wang, L. Development of a DNA Microarray for Detection and Serotyping of Enterotoxigenic Escherichia Coli. *J. Clin. Microbiol.* **2010**, *48* (6), 2066–2074. <https://doi.org/10.1128/JCM.02014-09>.
 - (73) Wu, A. H. B. A Selected History and Future of Immunoassay Development and Applications in Clinical Chemistry. *Clinica Chimica Acta. Clin Chim Acta* July 31, 2006, pp 119–124. <https://doi.org/10.1016/j.cca.2006.02.045>.
 - (74) Croxen, M. A.; Law, R. J.; Scholz, R.; Keeney, K. M.; Wlodarska, M.; Finlay, B. B. Recent Advances in Understanding Enteric Pathogenic Escherichia Coli. *Clinical Microbiology Reviews*. October 2013, pp 822–880. <https://doi.org/10.1128/CMR.00022-13>.
 - (75) Sharma, B.; Parul; Verma, A. K.; Jain, U.; Yadav, J. K.; Singh, R.; Mishra, R. Occurrence of Multidrug Resistant Escherichia Coli in Groundwater of Brij Region (Uttar Pradesh) and Its Public Health Implications. *Vet. World* **2017**, *10* (3), 293–301. <https://doi.org/10.14202/vetworld.2017.293-301>.
 - (76) Kumarasamy, K. K.; Toleman, M. A.; Walsh, T. R.; Bagaria, J.; Butt, F.; Balakrishnan, R.; Chaudhary, U.; Doumith, M.; Giske, C. G.; Irfan, S.; Krishnan, P.; Kumar, A. V.; Maharjan, S.; Mushtaq, S.; Noorie, T.; Paterson, D. L.; Pearson, A.; Perry, C.; Pike, R.; Rao, B.; Ray, U.; Sarma, J. B.; Sharma, M.; Sheridan, E.; Thirunaryan, M. A.; Turton, J.; Upadhyay, S.; Warner, M.; Welfare, W.; Livermore, D. M.; Woodford, N.

- Emergence of a New Antibiotic Resistance Mechanism in India, Pakistan, and the UK: A Molecular, Biological, and Epidemiological Study. *Lancet Infect. Dis.* **2010**, *10* (9), 597–602. [https://doi.org/10.1016/S1473-3099\(10\)70143-2](https://doi.org/10.1016/S1473-3099(10)70143-2).
- (77) Walsh, T. R.; Weeks, J.; Livermore, D. M.; Toleman, M. A. Dissemination of NDM-1 Positive Bacteria in the New Delhi Environment and Its Implications for Human Health: An Environmental Point Prevalence Study. *Lancet Infect. Dis.* **2011**, *11* (5), 355–362. [https://doi.org/10.1016/S1473-3099\(11\)70059-7](https://doi.org/10.1016/S1473-3099(11)70059-7).
- (78) Tuerk, C.; Gold, L. Systematic Evolution of Ligands by Exponential Enrichment: RNA Ligands to Bacteriophage T4 DNA Polymerase. *Science* (80-.). **1990**, *249* (4968), 505–510. <https://doi.org/10.1126/science.2200121>.
- (79) Ellington, A. D.; Szostak, J. W. In Vitro Selection of RNA Molecules That Bind Specific Ligands. *Nature* **1990**, *346* (6287), 818–822. <https://doi.org/10.1038/346818a0>.
- (80) MACUGEN - (pegaptanib sodium injection) <https://www.bauschretinarx.com/macugen/ecp/about/> (accessed May 18, 2020).
- (81) Dunn, M. R.; Jimenez, R. M.; Chaput, J. C. Analysis of Aptamer Discovery and Technology. *Nat. Rev. Chem.* **2017**, *1* (10), 0076. <https://doi.org/10.1038/s41570-017-0076>.
- (82) Kuwahara, M.; Obika, S. In Vitro Selection of BNA (LNA) Aptamers. *Artif. DNA PNA XNA* **2013**, *4* (2), 39–48. <https://doi.org/10.4161/adna.25786>.
- (83) Wang, T.; Chen, C.; Larcher, L. M.; Barrero, R. A.; Veedu, R. N. Three Decades of Nucleic Acid Aptamer Technologies: Lessons Learned, Progress and Opportunities on Aptamer Development. *Biotechnol. Adv.* **2019**, *37* (1), 28–50. <https://doi.org/10.1016/j.biotechadv.2018.11.001>.
- (84) Jijakli, K.; Khraiweh, B.; Fu, W.; Luo, L.; Alzahmi, A.; Koussa, J.; Chaiboonchoe, A.; Kirmizialtin, S.; Yen, L.; Salehi-Ashtiani, K. The in Vitro Selection World. *Methods* **2016**, *106*, 3–13. <https://doi.org/10.1016/j.ymeth.2016.06.003>.
- (85) Kumar, V.; Brent, J. R.; Shorie, M.; Kaur, H.; Chadha, G.; Thomas, A. G.; Lewis, E. A.; Rooney, A. P.; Nguyen, L.; Zhong, X. L.; Burke, M. G.; Haigh, S. J.; Walton, A.; McNaughton, P. D.; Tedstone, A. A.; Savjani, N.; Muryn, C. A.; O'Brien, P.; Ganguli, A. K.; Lewis, D. J.; Sabherwal, P. Nanostructured Aptamer-Functionalized Black Phosphorus Sensing Platform for Label-Free Detection of Myoglobin, a Cardiovascular Disease Biomarker. *ACS Appl. Mater. Interfaces* **2016**, *8* (35), 22860–22868. <https://doi.org/10.1021/acsami.6b06488>.
- (86) Ali, M. H.; Elsherbiny, M. E. Updates on Aptamer Research. **2019**, 1–23.
- (87) Lakhin, A. V.; Tarantul, V. Z.; Gening, L. V. Aptamers: Problems, Solutions and Prospects. *Acta Naturae* **2013**, *5* (4), 34–43.
- (88) Stoltenburg, R.; Reinemann, C.; Strehlitz, B. SELEX-A (r)Evolutionary Method to Generate High-Affinity Nucleic Acid Ligands. *Biomol. Eng.* **2007**, *24* (4), 381–403. <https://doi.org/10.1016/j.bioeng.2007.06.001>.
- (89) Challa, S.; Tzipori, S.; Sheoran, A. Selective Evolution of Ligands by Exponential Enrichment to Identify RNA Aptamers against Shiga Toxins. **2014**. <https://doi.org/10.1155/2014/214929>.
- (90) Sefah, K.; Yang, Z.; Bradley, K. M.; Hoshika, S.; Jiménez, E.; Zhang, L.; Zhu, G.; Shanker, S.; Yu, F.; Turek, D.; Tan, W.; Benner, S. A. In Vitro Selection with Artificial Expanded Genetic Information Systems. *Proc. Natl. Acad. Sci. U. S. A.* **2014**, *111* (4), 1449–1454. <https://doi.org/10.1073/pnas.1311778111>.
- (91) Mendonsa, S. D.; Bowser, M. T. In Vitro Evolution of Functional DNA Using Capillary Electrophoresis. *J. Am. Chem. Soc.* **2004**, *126* (1), 20–21. <https://doi.org/10.1021/ja037832s>.
- (92) Drabovich, A.; Berezovski, M.; Krylov, S. N. Selection of Smart Aptamers by Equilibrium Capillary Electrophoresis of Equilibrium Mixtures (ECEEM). *J. Am. Chem. Soc.* **2005**, *127* (32), 11224–11225. <https://doi.org/10.1021/ja0530016>.
- (93) Gu, G.; Wang, T.; Yang, Y.; Xu, X.; Wang, J. An Improved SELEX-Seq Strategy for Characterizing DNA-Binding Specificity of Transcription Factor: NF-KB as an Example. *PLoS One* **2013**, *8* (10), e76109. <https://doi.org/10.1371/journal.pone.0076109>.
- (94) Mayer, G.; Ahmed, M. S. L.; Dolf, A.; Endl, E.; Knolle, P. A.; Famulok, M. Fluorescence-Activated Cell Sorting for Aptamer SELEX with Cell Mixtures. *Nat. Protoc.* **2010**, *5* (12), 1993–2004. <https://doi.org/10.1038/nprot.2010.163>.
- (95) Nguyen, V. T.; Kwon, Y. S.; Kim, J. H.; Gu, M. B. Multiple GO-SELEX for Efficient Screening of Flexible Aptamers. *Chem. Commun.* **2014**, *50* (72), 10513–10516. <https://doi.org/10.1039/c4cc03953j>.
- (96) Zumrut, H. E.; Ara, M. N.; Fraile, M.; Maio, G.; Mallikaratchy, P. Ligand-Guided Selection of Target-Specific Aptamers: A Screening Technology for Identifying Specific Aptamers against Cell-Surface Proteins. *Nucleic Acid Ther.* **2016**, *26* (3), 190–198. <https://doi.org/10.1089/nat.2016.0611>.
- (97) Gong, Q.; Wang, J.; Ahmad, K. M.; Csordas, A. T.; Zhou, J.; Nie, J.; Stewart, R.; Thomson, J. A.; Rossi, J. J.; Soh, H. T. Selection Strategy to Generate Aptamer Pairs That Bind to Distinct Sites on Protein Targets. *Anal. Chem.* **2012**, *84* (12), 5365–5371. <https://doi.org/10.1021/ac300873p>.
- (98) Lai, J. C.; Hong, C. Y. Magnetic-Assisted Rapid Aptamer Selection (MARAS) for Generating High-Affinity DNA Aptamer Using Rotating Magnetic Fields. *ACS Comb. Sci.* **2014**, *16* (7), 321–327. <https://doi.org/10.1021/co5000272>.
- (99) Zhu, Z.; Song, Y.; Li, C.; Zou, Y.; Zhu, L.; An, Y.; Yang, C. J. Monoclonal Surface Display SELEX for Simple, Rapid, Efficient, and Cost-Effective Aptamer Enrichment and Identification. *Anal. Chem.* **2014**, *86* (12), 5881–5888. <https://doi.org/10.1021/ac501423g>.
- (100) Berezovski, M. V.; Musheev, M. U.; Drabovich, A. P.; Jitkova, J. V.; Krylov, S. N. Non-SELEX: Selection of Aptamers without Intermediate Amplification of Candidate Oligonucleotides. *Nat. Protoc.* **2006**, *1* (3), 1359–1369. <https://doi.org/10.1038/nprot.2006.200>.
- (101) Zuker, M. Mfold Web Server for Nucleic Acid Folding and Hybridization Prediction. *Nucleic Acids Res.* **2003**,

- 31 (13), 3406–3415. <https://doi.org/10.1093/nar/gkg595>.
- (102) Antczak, M.; Popena, M.; Zok, T.; Sarzynska, J.; Ratajczak, T.; Tomczyk, K.; Adamiak, R. W.; Szachniuk, M. New Functionality of RNAComposer: An Application to Shape the Axis of MiR160 Precursor Structure. *Acta Biochim. Pol.* **2016**, *63* (4), 737–744. https://doi.org/10.18388/abp.2016_1329.
- (103) Gu, M. B.; Kim, H. S. Biosensors Based on Aptamers and Enzymes. *Adv. Biochem. Eng. Biotechnol.* **2014**, *140*. <https://doi.org/10.1007/978-3-642-54143-8>.
- (104) Blouin, S.; Lafontaine, D. A. A Loop-Loop Interaction and a K-Turn Motif Located in the Lysine Aptamer Domain Are Important for the Riboswitch Gene Regulation Control. *RNA* **2007**, *13* (8), 1256–1267. <https://doi.org/10.1261/rna.560307>.
- (105) Cerofolini, L.; Amato, J.; Giachetti, A.; Limongelli, V.; Novellino, E.; Parrinello, M.; Fragai, M.; Randazzo, A.; Luchinat, C. G-Triplex Structure and Formation Propensity. *Nucleic Acids Res.* **2014**, *42* (21), 13393–13404. <https://doi.org/10.1093/nar/gku1084>.
- (106) Kwok, C. K.; Merrick, C. J. G-Quadruplexes: Prediction, Characterization, and Biological Application. *Trends Biotechnol.* **2017**, *35* (10), 997–1013. <https://doi.org/10.1016/j.tibtech.2017.06.012>.
- (107) Pagano, B.; Martino, L.; Randazzo, A.; Giancola, C. Stability and Binding Properties of a Modified Thrombin Binding Aptamer. *Biophys. J.* **2008**, *94* (2), 562–569. <https://doi.org/10.1529/biophysj.107.117382>.
- (108) Chen, H. L.; Hsiao, W. H.; Lee, H. C.; Wu, S. C.; Cheng, J. W. Selection and Characterization of DNA Aptamers Targeting All Four Serotypes of Dengue Viruses. *PLoS One* **2015**, *10* (6), 1–13. <https://doi.org/10.1371/journal.pone.0131240>.
- (109) Chen, S.; Li, Y.; Fu, Z.; Zeng, Y.; He, L.; Zhou, K.; Ao, X.; Liu, S.; Zou, L. Label-Free and Enzyme-Free Sensitive Fluorescent Method for Detection of Viable Escherichia Coli O157:H7. *Anal. Biochem.* **2018**, *556* (May), 145–151. <https://doi.org/10.1016/j.ab.2018.07.003>.
- (110) Biosensors Market Size & Share, Global Industry Report, 2027 <https://www.grandviewresearch.com/industry-analysis/biosensors-market> (accessed Sep 10, 2020).
- (111) Zare, H. R.; Shekari, Z. *Types of Monitoring Biosensor Signals*; Elsevier Inc., 2019. <https://doi.org/10.1016/B978-0-12-816491-4.00006-1>.
- (112) Kaur, H.; Shorie, M. Nanomaterial Based Aptasensors for Clinical and Environmental Diagnostic Applications. *Nanoscale Adv.* **2019**. <https://doi.org/10.1039/C9NA00153K>.
- (113) Zhou, W.; Jimmy Huang, P. J.; Ding, J.; Liu, J. Aptamer-Based Biosensors for Biomedical Diagnostics. *Analyst*. The Royal Society of Chemistry May 6, 2014, pp 2627–2640. <https://doi.org/10.1039/c4an00132j>.
- (114) Schoukroun-Barnes, L. R.; Macazo, F. C.; Gutierrez, B.; Lottermoser, J.; Liu, J.; White, R. J. Reagentless, Structure-Switching, Electrochemical Aptamer-Based Sensors. *Annu. Rev. Anal. Chem.* **2016**, *9* (1), 163–181. <https://doi.org/10.1146/annurev-anchem-071015-041446>.
- (115) Feynman, R. P. *Plenty of Room at the Bottom*.
- (116) Negahdary, M. Aptamers in Nanostructure-Based Electrochemical Biosensors for Cardiac Biomarkers and Cancer Biomarkers: A Review. *Biosensors and Bioelectronics*. Elsevier Ltd March 15, 2020, p 112018. <https://doi.org/10.1016/j.bios.2020.112018>.
- (117) Büyüktiryakli, S.; Keçili, R.; Hussain, C. M. Modern Age of Analytical Chemistry: Nanomaterials. *Handb. Nanomater. Anal. Chem. Mod. Trends Anal.* **2019**, 29–40. <https://doi.org/10.1016/B978-0-12-816699-4.00002-5>.
- (118) Shehzad, K.; Xu, Y.; Gao, C.; Duan, X. Three-Dimensional Macro-Structures of Two-Dimensional Nanomaterials. *Chem. Soc. Rev.* **2016**, *45* (20), 5541–5588. <https://doi.org/10.1039/c6cs00218h>.
- (119) Iijima, S. Helical Microtubules of Graphitic Carbon. *Nature* **1991**, *354* (6348), 56–58. <https://doi.org/10.1038/354056a0>.
- (120) Iijima, S.; Ichihashi, T. Single-Shell Carbon Nanotubes of 1-Nm Diameter. *Nature* **1993**, *363* (6430), 603–605. <https://doi.org/10.1038/363603a0>.
- (121) Kroto, H. W.; Heath, J. R.; O'Brien, S. C.; Curl, R. F.; Smalley, R. E. C60: Buckminsterfullerene. *Nature* **1985**, *318* (6042), 162–163. <https://doi.org/10.1038/318162a0>.
- (122) Geim, A. K.; Novoselov, K. S. The Rise of Graphene. *Nat. Mater.* **2007**, *6* (3), 183–191. <https://doi.org/10.1038/nmat1849>.
- (123) Novoselov, K. S.; Geim, A. K.; Morozov, S. V.; Jiang, D.; Zhang, Y.; Dubonos, S. V.; Grigorieva, I. V.; Firsov, A. A. Electric Field in Atomically Thin Carbon Films. *Science* (80-.). **2004**, *306* (5696), 666–669. <https://doi.org/10.1126/science.1102896>.
- (124) Hummers, W. S.; Offeman, R. E. Preparation of Graphitic Oxide. *J. Am. Chem. Soc.* **1958**, *80* (6), 1339. <https://doi.org/10.1021/ja01539a017>.
- (125) Roldán, R.; Chirrolli, L.; Prada, E.; Silva-Guillén, J. A.; San-Jose, P.; Guinea, F. Theory of 2D Crystals: Graphene and Beyond. *Chem. Soc. Rev.* **2017**, *46* (15), 4387–4399. <https://doi.org/10.1039/c7cs00210f>.
- (126) Rohaizad, N.; Mayorga-Martinez, C. C.; Sofer, Z.; Pumera, M. 1T-Phase Transition Metal Dichalcogenides (MoS₂, MoSe₂, WS₂, and WSe₂) with Fast Heterogeneous Electron Transfer: Application on Second-Generation Enzyme-Based Biosensor. *ACS Appl. Mater. Interfaces* **2017**, *9* (46), 40697–40706. <https://doi.org/10.1021/acsami.7b13090>.
- (127) Zhang, H. Ultrathin Two-Dimensional Nanomaterials. *ACS Nano* **2015**, *9* (10), 9451–9469. <https://doi.org/10.1021/acsnano.5b05040>.
- (128) Manzeli, S.; Ovchinnikov, D.; Pasquier, D.; Yazyev, O. V.; Kis, A. 2D Transition Metal Dichalcogenides. *Nature Reviews Materials*. Nature Publishing Group June 13, 2017, pp 1–15. <https://doi.org/10.1038/natrevmats.2017.33>.
- (129) Choi, W.; Choudhary, N.; Han, G. H.; Park, J.; Akinwande, D.; Lee, Y. H. Recent Development of Two-

- Dimensional Transition Metal Dichalcogenides and Their Applications. *Materials Today*. Elsevier B.V. April 1, 2017, pp 116–130. <https://doi.org/10.1016/j.mattod.2016.10.002>.
- (130) Chen, Y.; Fan, Z.; Zhang, Z.; Niu, W.; Li, C.; Yang, N.; Chen, B.; Zhang, H. Two-Dimensional Metal Nanomaterials: Synthesis, Properties, and Applications. *Chem. Rev.* **2018**, *118* (13), 6409–6455. <https://doi.org/10.1021/acs.chemrev.7b00727>.
- (131) Han, J. H.; Kwak, M.; Kim, Y.; Cheon, J. Recent Advances in the Solution-Based Preparation of Two-Dimensional Layered Transition Metal Chalcogenide Nanostructures. *Chem. Rev.* **2018**, *118* (13), 6151–6188. <https://doi.org/10.1021/acs.chemrev.8b00264>.
- (132) Biswas, A.; Bayer, I. S.; Biris, A. S.; Wang, T.; Dervishi, E.; Faupel, F. Advances in Top-down and Bottom-up Surface Nanofabrication: Techniques, Applications & Future Prospects. *Advances in Colloid and Interface Science*. Elsevier January 15, 2012, pp 2–27. <https://doi.org/10.1016/j.cis.2011.11.001>.
- (133) Davis, K. A.; Abrams, B.; Lin, Y.; Jayasena, S. D. *Use of a High Affinity DNA Ligand in Flow Cytometry*; 1996; Vol. 24.
- (134) Dreaden, E. C.; Alkilany, A. M.; Huang, X.; Murphy, C. J.; El-Sayed, M. A. The Golden Age: Gold Nanoparticles for Biomedicine. *Chem. Soc. Rev.* **2012**, *41* (7), 2740–2779. <https://doi.org/10.1039/c1cs15237h>.
- (135) Su, S.; Sun, Q.; Gu, X.; Xu, Y.; Shen, J.; Zhu, D.; Chao, J.; Fan, C.; Wang, L. Two-Dimensional Nanomaterials for Biosensing Applications. *TrAC - Trends in Analytical Chemistry*. Elsevier B.V. October 1, 2019, p 115610. <https://doi.org/10.1016/j.trac.2019.07.021>.
- (136) Corro, E.; Terrones, H.; Elias, A.; Fantini, C.; Feng, S.; Nguyen, M. A.; Mallouk, T. E.; Terrones, M.; Pimenta, M. A.; Fisica, D. De; Federal, U.; Gerais, D. M.; Carlos, A. A.; Postal, C.; Horizonte, B.; Corro, D. E. L.; Al, E. T. And Bulk WSe₂ Observed by Resonant Raman Spectroscopy. *ACS Nano* **2014**, *8* (9), 9629–9635.
- (137) Online, V. A.; Li, L.; Peng, J.; Zhao, J.; Zhu, J. Focusing on Luminescent Graphene Quantum Dots: Current Status and Future Perspectives. **2013**, 4015–4039. <https://doi.org/10.1039/c3nr33849e>.
- (138) Rezaei, B.; Irannejad, N. *Electrochemical Detection Techniques in Biosensor Applications*; Elsevier Inc., 2019. <https://doi.org/10.1016/B978-0-12-816491-4.00002-4>.
- (139) Ensafi, A. A. *An Introduction to Sensors and Biosensors*; Elsevier Inc., 2019. <https://doi.org/10.1016/B978-0-12-816491-4.00001-2>.
- (140) Aller Pellitero, M.; Kitsara, M.; Eibensteiner, F.; Del Campo, F. J. Rapid Prototyping of Electrochemical Lateral Flow Devices: Stencilled Electrodes. *Analyst* **2016**, *141* (8), 2515–2522. <https://doi.org/10.1039/c5an02424b>.
- (141) Jarczewska, M.; Malinowska, E. The Application of Antibody-Aptamer Hybrid Biosensors in Clinical Diagnostics and Environmental Analysis. *Analytical Methods*. Royal Society of Chemistry July 7, 2020, pp 3183–3199. <https://doi.org/10.1039/d0ay00678e>.
- (142) Hanif, A.; Farooq, R.; Rehman, M. U.; Khan, R.; Majid, S.; Ganaie, M. A. Aptamer Based Nanobiosensors: Promising Healthcare Devices. *Saudi Pharmaceutical Journal*. Elsevier B.V. March 1, 2019, pp 312–319. <https://doi.org/10.1016/j.jsps.2018.11.013>.
- (143) Singh, S.; Kumar, V.; Dhanjal, D. S.; Datta, S.; Prasad, R.; Singh, J. Biological Biosensors for Monitoring and Diagnosis; Springer, Singapore, 2020; pp 317–335. https://doi.org/10.1007/978-981-15-2817-0_14.
- (144) Kumar, V.; Shorie, M.; Ganguli, A. K.; Sabherwal, P. Graphene-CNT Nanohybrid Aptasensor for Label Free Detection of Cardiac Biomarker Myoglobin. *Biosens. Bioelectron.* **2015**, *72*, 56–60. <https://doi.org/10.1016/J.BIOS.2015.04.089>.
- (145) Sharma, R.; Raghav, R.; Priyanka, K.; Rishi, P.; Sharma, S.; Srivastava, S.; Verma, I. Exploiting Chitosan and Gold Nanoparticles for Antimycobacterial Activity of in Silico Identified Antimicrobial Motif of Human Neutrophil Peptide-1. *Sci. Rep.* **2019**, *9* (1), 1–14. <https://doi.org/10.1038/s41598-019-44256-6>.
- (146) Li, F.; Yu, Z.; Han, X.; Lai, R. Y. Electrochemical Aptamer-Based Sensors for Food and Water Analysis: A Review. *Analytica Chimica Acta*. Elsevier B.V. March 21, 2019, pp 1–23. <https://doi.org/10.1016/j.aca.2018.10.058>.
- (147) Phaneuf, C. R.; Mangadu, B.; Piccini, M. E.; Singh, A. K.; Koh, C. Y. Rapid, Portable, Multiplexed Detection of Bacterial Pathogens Directly from Clinical Sample Matrices. *Biosensors* **2016**, *6* (4), 1–10. <https://doi.org/10.3390/bios6040049>.
- (148) Narayan, C.; Kwon, J.; Kim, C.; Kim, S. J.; Jang, S. K. Virus-Based SELEX (Viro-SELEX) Allows Development of Aptamers Targeting Knotty Proteins. *Analyst* **2020**, *145* (4), 1473–1482. <https://doi.org/10.1039/c9an01943j>.
- (149) Li, F.; Yu, Z.; Han, X.; Lai, R. Y. Electrochemical Aptamer-Based Sensors for Food and Water Analysis: A Review. *Anal. Chim. Acta* **2019**, *1051*, 1–23. <https://doi.org/10.1016/j.aca.2018.10.058>.
- (150) Shorie, M.; Kaur, H.; Chadha, G.; Singh, K.; Sabherwal, P. Graphitic Carbon Nitride QDs Impregnated Biocompatible Agarose Cartridge for Removal of Heavy Metals from Contaminated Water Samples. *J. Hazard. Mater.* **2019**, *367* (September 2018), 629–638. <https://doi.org/10.1016/j.jhazmat.2018.12.115>.
- (151) Bala, R.; Sharma, R. K.; Wangoo, N. Highly Sensitive Colorimetric Detection of Ethyl Parathion Using Gold Nanoprobes. *Sensors Actuators, B Chem.* **2015**, *210*, 425–430. <https://doi.org/10.1016/j.snb.2014.12.123>.
- (152) Weng, X.; Neethirajan, S. Ensuring Food Safety: Quality Monitoring Using Microfluidics. *Trends Food Sci. Technol.* **2017**, *65* (May), 10–22. <https://doi.org/10.1016/j.tifs.2017.04.015>.
- (153) Kaur, K.; Kaur, M.; Kaur, A.; Singh, J.; Singh, N.; Mittal, S. K.; Kaur, N. Polymer-Based Biocompatible Fluorescent Sensor for Nano-Molar Detection of Zn²⁺ in Aqueous Medium and Biological Samples. *Inorg. Chem. Front.* **2014**, *1* (1), 99–108. <https://doi.org/10.1039/c3qi00031a>.
- (154) Chaudhary, S.; Sonkusre, P.; Chopra, A.; Bhasin, K. K.; Suri, C. R. UV-FIA: UV-Induced Fluoro-Immunochemical Assay for Ultra-Trace Detection of PETN, RDX, and TNT. *Anal. Chim. Acta* **2019**, *1077*, 266–272. <https://doi.org/10.1016/j.aca.2019.05.048>.

- (155) Gupta, S.; Saxena, M.; Saini, N.; Mahmooduzzafar; Kumar, R.; Kumar, A. An Effective Strategy for a Whole-Cell Biosensor Based on Putative Effector Interaction Site of the Regulatory DmpR Protein. *PLoS One* **2012**, *7* (8), e43527. <https://doi.org/10.1371/journal.pone.0043527>.
- (156) Jiao, Z.; Zhang, H.; Jiao, S.; Guo, Z.; Zhu, D.; Zhao, X. A Turn-on Biosensor-Based Aptamer-Mediated Carbon Quantum Dots Nanoaggregate for Acetamiprid Detection in Complex Samples. *Food Anal. Methods* **2019**, *12* (3), 668–676. <https://doi.org/10.1007/s12161-018-1393-9>.
- (157) Bala, R.; Mittal, S.; Sharma, R. K.; Wangoo, N. A Supersensitive Silver Nanoprobe Based Aptasensor for Low Cost Detection of Malathion Residues in Water and Food Samples. *Spectrochim. Acta - Part A Mol. Biomol. Spectrosc.* **2018**, *196*, 268–273. <https://doi.org/10.1016/j.saa.2018.02.007>.
- (158) Vaseashta, A.; Vaclavikova, M.; Vaseashta, S.; Gallios, G.; Roy, P.; Pummakarnchana, O. Nanostructures in Environmental Pollution Detection, Monitoring, and Remediation. *Sci. Technol. Adv. Mater.* **2007**, *8* (1–2), 47–59. <https://doi.org/10.1016/j.stam.2006.11.003>.
- (159) Kaur, N.; Singh, J.; Raj, P.; Singh, N.; Singh, H.; Sharma, S. K.; Kim, D. Y.; Kaur, N. ZnO Decorated with Organic Nanoparticles Based Sensor for the Ratiometric Selective Determination of Mercury Ions. *New J. Chem.* **2016**, *40* (2), 1529–1534. <https://doi.org/10.1039/c5nj03099d>.
- (160) Tripathi, A.; Melo, J. S. Synthesis of a Low-Density Biopolymeric Chitosan- Agarose Cryomatrix and Its Surface Functionalization with Bio-Transformed Melanin for the Enhanced Recovery of Uranium(VI) from Aqueous Subsurfaces. *RSC Adv.* **2016**, *6* (43), 37067–37078. <https://doi.org/10.1039/c6ra04686j>.
- (161) Huang, N. T.; Zhang, H. L.; Chung, M. T.; Seo, J. H.; Kurabayashi, K. Recent Advancements in Optofluidics-Based Single-Cell Analysis: Optical on-Chip Cellular Manipulation, Treatment, and Property Detection. *Lab Chip* **2014**, *14* (7), 1230–1245. <https://doi.org/10.1039/c3lc51211h>.
- (162) Labib, M.; Zamay, A. S.; Kolovskaya, O. S.; Reshetneva, I. T.; Zamay, G. S.; Kibbee, R. J.; Sattar, S. A.; Zamay, T. N.; Berezovski, M. V.; Zheleznyaka str, P. Aptamer-Based Viability Impedimetric Sensor for Bacteria. *Anal. Chem.* **2012**, *84*, 16. <https://doi.org/10.1021/ac302902s>.
- (163) Kim, S.; Park, M.; Kim, J.; Chuong, P. D.; Lee, Y.; Yoon, B.; Hwang, K.; Lim, Y.-K. Development of a Sandwich ELISA for the Detection of *Listeria Spp.* Using Specific Flagella Antibodies. **2005**, *6*, 41–46.
- (164) Litvinov, J.; Moen, S. T.; Koh, C. Y.; Singh, A. K. Centrifugal Sedimentation Immunoassays for Multiplexed Detection of Enteric Bacteria in Ground Water. *Biomicrofluidics* **2016**, *10* (1). <https://doi.org/10.1063/1.4939099>.
- (165) Kumar, V.; Nath, G.; Kotnala, R. K.; Saxena, P. S.; Srivastava, A. Biofunctional Magnetic Nanotube Probe for Recognition and Separation of Specific Bacteria from a Mixed Culture. *RSC Adv.* **2013**, *3* (34), 14634–14641. <https://doi.org/10.1039/c3ra42307g>.
- (166) Soleymani, L.; Li, F. Mechanistic Challenges and Advantages of Biosensor Miniaturization into the Nanoscale. *ACS Sensors* **2017**, *2* (4), 458–467. <https://doi.org/10.1021/acssensors.7b00069>.
- (167) Sefah, K.; Shangguan, D.; Xiong, X.; O'Donoghue, M. B.; Tan, W. Development of DNA Aptamers Using Cell-SELEX. *Nat. Protoc.* **2010**, *5* (6), 1169–1185. <https://doi.org/10.1038/nprot.2010.66>.
- (168) Roldán, R.; Chirolli, L.; Prada, E.; Silva-Guillén, J. A.; San-Jose, P.; Guinea, F. Theory of 2D Crystals: Graphene and Beyond. *Chemical Society Reviews*. Royal Society of Chemistry August 7, 2017, pp 4387–4399. <https://doi.org/10.1039/c7cs00210f>.



Chapter 2

*Nanostructured
aptasensor for
enterotoxigenic
E. coli*



Chapter 2

Nanostructured aptasensor for enterotoxigenic

E. coli

*The contents of this chapter are adapted from: **Kaur, H.**; Shorie, M.; Sharma, M.; Ganguli, A. K.; Sabherwal, P. Bridged rebar graphene functionalized aptasensor for pathogenic *E. coli* O78:H11 detection. Biosens. Bioelectron. 2017, 98 (June), 486–493.*

2.1 Introduction

Food and waterborne diseases caused due to pathogenic *E. coli* are a major cause of morbidity in developing nations. Enterotoxigenic *E. coli* (ETEC) is the eighth leading cause of diarrhea mortality among all age groups, accounting for the highest morbidity and mortality, significantly in Congo, Nigeria, India, and Pakistan^{1–3}. These enteric bacteria initiate infections by crossing the stomach acid- barrier and further adhering to the villi of the intestinal epithelium causing gastroenteritis⁴. Although discovered 65 years ago, new ETEC virulence factors continue to emerge with still no vaccine developed against it.

2.1.1 Target bacteria *E. coli* O78:H11 - A background

E. coli O78:H11 is classified in phylogroup A as an enterotoxigenic strain isolated from Bangladesh and reported in 1973 as responsible for adult diarrhea with cholera-like symptoms and was found repeatedly from different geographical locations^{5–7}. Further epidemiological and genetic analysis presented that the strain was probably a commensal that acquired plasmid encoding virulence genes⁸. The serotype O78:H11 expresses several colonization factors for adherence to the microvilli present on the enterocytes and enterotoxins, which induce water and electrolyte loss from the intestinal lumen^{9,10}. These pose a serious environmental threat, thereby placing enteric diseases as a major albeit a substantially neglected public health problem¹¹.

2.1.2 The need of improved sensing platform

Most of the diagnostic assays designed for its detection are based on multiplexed PCR, which require purified samples and the presence of non-target microorganisms hinders the sensitivity of the assay by a great magnitude^{12,13}. A variety of antibody-based sensing platforms for *E. coli* detection have been studied viz., amperometric, electrochemical impedance, quartz crystalline microbalance, surface plasmon resonance and field-effect transistors^{14–18}. However, the temperature instability, cost and associated ethical concerns of antibodies limit the market of these biosensors¹⁹. Regrettably, despite many conventionally availed techniques and molecular methods, no cost-effective diagnostic is viable for local clinical labs, where routine microbiological testing is done.

The major bottlenecks in development of biosensors for pathogens is the complex yet overlapping nature of close species, temperature or pH instability of bio-receptor which is of grave importance in clinical or environmental samples and, signal saturation of the sensor due to bulky whole-cells. Keeping these issues in mind, an electrochemical platform using a specific low-cost bio-recognition element- ‘aptamer’ and graphene derived nanomaterial for enhanced platform sensitivity was devised.

2.1.3 Objectives

- (i) **Bio-receptor generation:** Development of specific aptamer-based receptors against selected *E. coli* O78:H11 using whole-cell target approach.
- (ii) **Transducer development:** Synthesis of carbon-based nanostructured material for modification of electrochemical electrode surface.
- (iii) **Aptasensor fabrication:** Functionalization of generated high affinity aptamers onto electrically active nanostructures for apta-assay.
- (iv) **Platform validation:** Testing & validation of aptasensor in spiked food & water samples.

2.1.4 Proposed biosensing platform for *E. coli* O78:H11

2.1.4.1 Preface

Biomolecular assays using specific aptamers offer a preferential alternate approach for bacteria detection in virtue of their high selectivity, sensitivity and rapidity. Nucleic-acid based aptamers have been utilized as antibody alternatives in a variety of diagnostic formats showing versatile applications²⁰. Moreover, advances in nano-layered structures have facilitated the development of highly sensitive biosensing platforms. The development of 3D-hierarchical carbon-based nanostructures from interconnected nanoscale building blocks is intriguing because of their unique physical, chemical, and electrical properties²¹. However, covalent linkages between individual nano-blocks, without losing their distinctive properties still remains a challenge²². Recently, partially unzipped CNTs acting as a reinforcing bar (rebar) to form a seamless 2D conjoined hybrid through both π - π stacking domains and covalent bonding has been reported^{23,24}. The excellent electronic and spin transport properties of this graphene make it an attractive material in wide range of biosensing applications²⁵.

2.1.4.2 Our aptasensing approach: Whole-cell bacteria

As illustrated in Figure 2.1, an aptamer functionalized electrochemical nanosensing platform was developed wherein a synergistic approach with advancements in both nucleic acid-based aptamer & bridged rebar graphene modified electrochemical transducer were used. The present work demonstrates the unscrolling of multiwalled carbon nanotubes (MWCNT) in transverse and

longitudinal directions and the subsequent bridging with terephthalaldehyde (TPA) to form 3D bridged rebar graphene (BRG), which showed enhanced electrical properties and facile chemical functionality for the development of compatible bio-interface on sensing platform. In this chapter, we report novel fabrication method of functionalized BRG for our nanostructured aptasensor for pathogenic *E. coli* detection. Specific DNA aptamers were screened effectively on microtiter plate

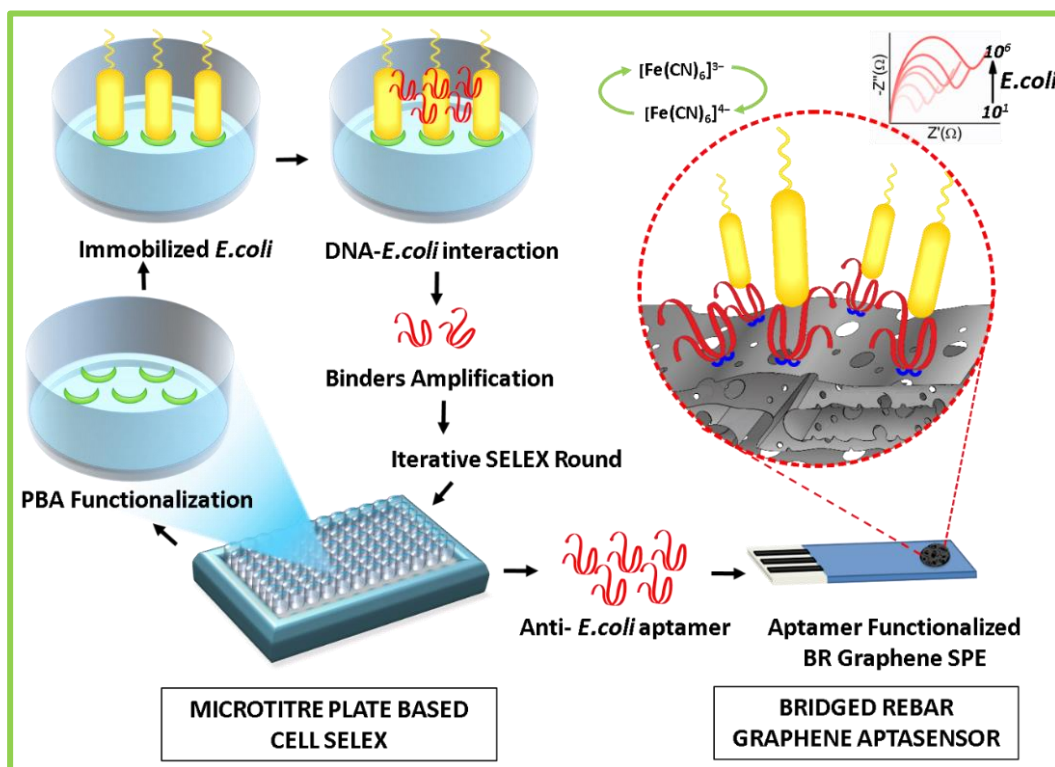


Figure 2.1: Schematic Illustration: Showing the novel in-situ developed microtiter plate-based cell-SELEX methodology using phenylboronic acid as capturing agent for bacteria immobilization and naïve DNA aptamer library containing a random pool of oligomers which is exposed to bacteria immobilized bacteria. The selected anti-*E. coli* aptamer was used as a bio-receptor on BRG nanostructured screen-printed electrode using electrochemical impedance spectroscopy.

by in-situ developed phenylboronic acid (PBA) mediated SELEX method showing high affinity $K_d \sim 14$ nM towards the selected strain. The newly developed aptasensing platform demonstrated a low limit of detection (LOD) of $\sim 10^1$ cells towards *E. coli* O78: H11 with a dynamic response range from 10^1 to 10^6 cells in spiked water, milk and juice samples.

2.1.4.3 Novelty of experimental work

- (i) **Bio-receptor:** Aptamer selection using modified cell-SELEX for a whole bacterial cell using a phenylboronic acid-coated microtiter plater for immobilization and selection.
- (ii) **Nanostructures:** Bridged rebar graphene synthesized via un-scrolling of MWCNT in transverse and longitudinal directions and the subsequent bridging with TPA to form a 3D structure which showed enhanced electrical properties and a compatible bio-interface for bacterial sensing.

2.2 Experimental procedure

The detailed procedures for the selection of nucleic-acid based aptamer for bacteria and its characterization, synthesis of BRG nanostructure and its characterization, nanostructure functionalization and assay development are described in the following respective sub-sections.

2.2.1 Aptamer technology: Cell-SELEX

2.2.1.1 Materials

(A) Chemicals & reagents

Phenylboronic acid 95% (PBA), 3-Aminophenylboronic acid monohydrate 98% (APBA), 4',6-diamidino-2-phenylindole (DAPI), 4-Morpholineethanesulfonic acid (MES) buffer, PCR mastermix (2x), PCR grade Dimethyl sulfoxide (DMSO), Streptavidin-Gold from *Streptomyces avidinii* and Poly-L-lysine solution 0.1% w/v in water (PLL) were procured from Sigma-Aldrich (India). *N*-Ethyl-*N'*-(3-dimethylaminopropyl) carbodiimide hydrochloride (EDC), *N*-Hydroxy succinimide (NHS) were purchased from Merck (India). Glycine, Magnesium chloride, Tris base, Tris-HCl, Tryptone soya broth (TSB) and Luria Bertani agar (LB) were purchased from Himedia (India). Nunc Maxisorp F96 microtitre plates and InsTAclone PCR cloning kit from Thermo Fisher Scientific (India) and QIAprep spin miniprep kit from Qiagen (USA) were used.

(B) Aptamer library

HPLC purified DNA library consisting of a central random region of 45 nt flanked by two 18 nt primer binding sequences at 5' and 3' ends (5'-ATCCAGAGTGACGCAGCA-(N45)-TGGACACGGTGGCTTAGT-3') and amplified with Fluorescein isothiocyanate (FITC) labeled forward primer (5'-FITC-ATCCAGAGTGACGCAGCA-3'), biotin-labeled reverse primer (5'-biotin-ACTAAGCCACCGTGTCCA-3') were procured from Sigma-Aldrich (India)²⁶.

(C) Bacterial culture

The lyophilized bacterial strain of *E. coli* O78:K80:H11 (MTCC 726) was procured from MTCC, Chandigarh, India.

(D) Optimized recipes

(i) Microbiological media

Prepared for 1 L as per manufacturers weight by volume ratio, autoclave at 121.5°C, 15 psi for 15 min and cool to 37°C before bacterial inoculation.

(ii) Carbonate buffer

Added 5.7 mM NaHCO₃, 4.3 mM Na₂HCO₃ and made up to 500 mL volume with sterile water after adjusting to pH 9.8.

(iii) Tris-HCl binding buffer

Added 10 mM Tris-HCl, 150 mM NaCl, 5 mM MgCl₂ and made up to 500 mL volume sterile nuclease free water after adjusting to pH 7.6.

(iv) Glycine-HCl elution buffer

Added 10 mM glycine, 2 mM HCl and made up to 100 mL volume with sterile nuclease free water after adjusting to pH 3.0.

(v) Tris neutralisation solution

Prepared 100 mM Tris base in sterile nuclease free water and adjusted to pH 11.

(vi) Phenylboronic acid coating solution

Prepared a 1 mg mL⁻¹ solution of PBA in Carbonate buffer (pH 9.5).

(vii) Phosphate buffered saline (PBS)

Mixed 109.9 mg Na₂HPO₄, 27.1 mg NaH₂PO₄, 900 mg NaCl and made up the volume to 100 mL with sterile water after adjusting to pH 7.4.

2.2.1.2 Growth & optimization of *E. coli* O78:H11 culture

Lyophilized *E. coli* O78:K80:H11 was grown on Luria-Bertani (LB) agar medium for culture revival 37°C for 24 h. A single colony was isolated and sub-cultured onto fresh Sorbitol MacConkey (SMAC) plates to ensure purity using identical growth conditions. The axenic culture was maintained on LB agar plates as well as SMAC agar plates with transfers every four weeks to fresh medium and stored at 4°C. To further optimize the bacterial growth conditions, the target bacterial strain *E. coli* O78:H11 was grown in 10 mL Tryptone Soya Broth (TSB) in 50 mL Erlenmeyer flask overnight. From the seed culture, 1 mL was used as an inoculum and was sub-cultured into 100 mL fresh medium incubated (37°C at 2500×g) in shaker incubator. The OD₆₀₀ was measured after every 30 min and the growth curve was generated. The cultured cells were harvested down at 2500×g for 10 min, followed by washing with PBS (10 mM, pH 7.4) to remove residual media components.

2.2.1.3 Aptamer generation for *E. coli* O78:H11

Like a conventional SELEX, the microtiter plate-based cell-SELEX involves iterative rounds of binding, elution, amplification & ss-DNA partitioning. These steps were carried out on a PBA functionalized microtiter plate to capture bacteria for the generation of specific aptamers. It was used as a capture agent as it is well established that boronic acid derivatives show selective & stable interactions with *cis-diols*, which are abundantly present in glycans, present on the bacterial surface.

2.2.1.3.1 Bacterial cell & boronic acid interaction

To experimentally ascertain its binding with the bacteria, we set up a Biolayer interferometry (BLI) based binding assay, wherein we used amine-functionalized PBA (APBA) and attached it to carbodiimide modified amine-reactive sensor (AR2G biosensor, FortéBio) and allowed it to interact with the bacterial cells suspended in binding buffer (10 mM Tris-HCl (pH 7.5), 5 mM MgCl₂, 100 mM NaCl) in a microtiter plate well for bio-interaction. Before this, for the activation of the AR2G sensor, it was exposed to an equimolar mixture of 400 mM EDC and 100 mM NHS in MES buffer

(50 mM) at pH 5.5, optimized as per BLI technical note²⁷. The activated surface was then allowed to load with amino-phenylboronic acid till saturated, and then the activated sensor surface was exposed to 50 mM ethanolamine solution at pH 8.5 to quench any residual activated sites on the biosensor surface. The bio-interaction was carried out using this APBA modified AR2G biosensor, which showed functional association/dissociation kinetics between *E. coli* and PBA.

2.2.1.3.2 Microtiter plate-based cell-SELEX

(A) Naïve library preparation

For the first SELEX selection round, ssDNA naive library (2 μ L of 100 μ M) was mixed with 198 μ L of binding buffer, followed by heating at 95°C for 10 min to denature DNA strands and then snap-cooled at 4°C to prevent inter-strand hybridization. The optimal volume for chosen to include at least 10^{15} molecules for library panning. This mixture was held at 4°C for 30 min and at 25°C for 60 min to allow the DNA oligomers to fold into their respective 3D conformations.

(B) Initial SELEX

A sterile microtiter plate was coated with 100 μ L of PBA prepared in carbonate buffer (pH 9.2) and incubated overnight at 4°C. This basic pH was preferred as it aids in higher hydrophobic interactions with the polystyrene microtiter plate. Subsequently, the plate was washed thrice with sterile water and 10^3 cells of *E. coli* O78:H11 was dispensed per well and incubated for one hour at 25°C. The cell number was optimized, keeping in view the surface area of the well and of the cell (assumed to be a cylinder) for maximum coverage of the well, provided no crowding takes place. These bacteria immobilized wells were then exposed to 100 μ L of folded ssDNA naive aptamer library for 1 h at 25°C, followed by washing with the wash buffer (10 mM Phosphate buffer) to

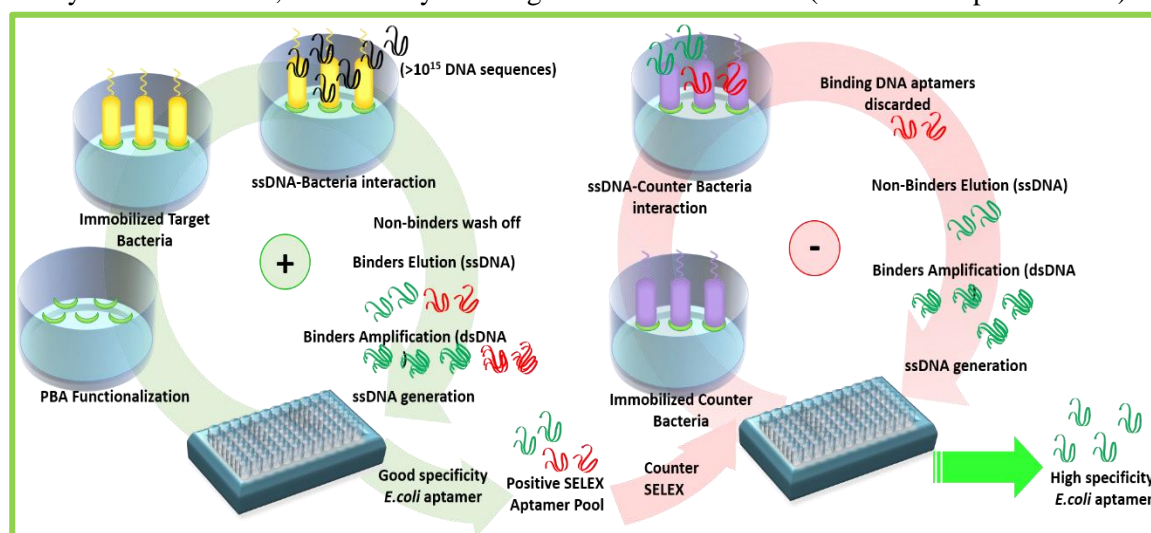


Figure 2.2: Cell-SELEX: Microtiter plate-based cell-SELEX methodology employing phenylboronic acid (PBA) for immobilization of bacteria, naïve library exposure, elution and amplification of binder oligonucleotides, conversion to ssDNA using Strep-Gold probe and further iterations of this positive cycle are done to obtain aptamer populations with excellent specificity towards target bacteria. Furthermore, the introduction of counter-SELEX rounds with cross-reactive strains helps in the removal of aptamers that bind to other bacteria, thus aiding in obtaining an excellent binder fraction specific to the target, which is aptly called an ‘aptamer’.

remove any unbound oligomer. The binders on the microtiter plate were eluted using elution buffer (0.1 M Glycine-HCl buffer, pH 3.4) and the elute was pH neutralized to stop any acidic degradation of the DNA using neutralization buffer (1 M Tris, pH 12.0). The eluted samples were stored at -20°C for amplification & partitioning steps. Herein, we performed 12 iterations, involving 1-5 cycles of positive selection against target bacteria and 6-11 cycles of counter-selection against other enteric bacteria viz., *Enterobacter aerogenes*, *Citrobacter braakii*, *E. coli* DH5 α , *Proteus vulgaris*, *Listeria monocytogenes*, and *Bacillus subtilis*. Further, to increase the selectivity of the aptamers, a final positive 12th selection cycle was performed to regenerate the depleted DNA binder pool concentration (Figure 2.2). The binders eluted were PCR amplified using optimized conditions, as mentioned in Figure 2.3. The FITC-labeled sense strand was separated from the anti-sense biotinylated strand by using a streptavidin coated gold nano-probe, as described in Chapter 1, Section 1.2.6.1. The PCR amplicon was heat-denatured by incubating at 95°C for 15 min, snap-cooled on ice, the streptavidin-gold nano-bio probe was added to the PCR product in 1:10 ratio and incubated on ice for 30 min to have efficient binding. In final step, the concoction was centrifuged at 15,000 \times g for 30 min to pellet down the anti-sense strand bound with a strep-gold probe, and the FITC labeled ssDNA was eluted as the supernatant. This amplified binder fraction obtained from the nth round was further exposed to the (n+1)th round immobilized *E. coli* O78:H11 wells. With each passing round, an increment in the number of the exposed wells was done.

(A)	PCR Components	Volume (μ L)	(B)	PCR Step	Temp ($^{\circ}$ C)	Time (s)
	Template	5.0		Hot Start	95	150
	FITC- and Biotin-primer mix	2.5 (10 μ M)		Denaturation	95	30
	PCR Master Mix (2x)	25.0		Annealing	56	30
	DMSO	2.5		Extension	72	180
	Nuclease-free water	15.0		Hold	4	∞

Figure 2.3: Optimized PCR reaction conditions: (A) PCR reaction mixture components used in a typical SELEX amplification reaction and (B) the PCR steps used during the amplification protocol.

2.2.1.3.3 Aptamer characterization

(A) Spectrophotometric measurement

During the SELEX process, the quantity and purity of the elutes was assessed after each SELEX round using nanodrop spectrophotometer, where the absorbance values at 260 nm, 260/280 and 260/230 ratio were observed, which are a measure for amount of DNA present in the fraction, protein contamination and carbohydrates or phenol or contaminants that absorb at 230 nm.

(B) Biolayer Interferometry (BLI) studies

BLI bio-interaction studies were performed to confirm binding between the bacteria and the screened aptamer using the Octet Red96 system (FortéBio, USA). For this biotin-labeled reverse primer (100 μ M), having complementarity with 3' end of aptamer was loaded onto Super

Streptavidin biosensor (SSA) after 600 s incubation for maximal binding. The modified sensor was dipped into stock aptamer solution till an association plateau was achieved, followed by washing with the binding buffer to remove unbound sequences. Subsequently, the aptamer loaded biosensor was allowed to interact with three-fold dilutions of bacterial cells (1×10^7 , 3×10^6 , 1×10^5), and the association/dissociation kinetics was carried out to determine the bio-interaction. These bacterial BLI studies were carried out with the help of Pall Lifesciences application scientists, Tao Chen & Sushil Vaidya.

(C) Fluorescence binding assay

Later on, since deduction of the dissociation coefficient (K_d) value for a cell (an entity which cannot be quantified in molarity) was not possible from the BLI binding studies, a fluorescence saturation plate binding assay was employed. To assess the binding and affinity of the aptamer to *E. coli* O78:H11, a binding assay was performed using PBA functionalized microtiter plate wherein; 10^3 cells (similar conditions used in SELEX process) were incubated with an increasing amount of FITC-labelled ssDNA (0.05 - 5000 nM) in 100 μ L of binding buffer for an hour at 25°C. The wells were washed twice with washing buffer, and the fluorescence signal intensity of FITC in each well was measured using a multimode microtiter plate reader (BioTek Synergy HI, USA) at $\lambda_{excitation}$ and $\lambda_{emission}$ wavelengths of 485 and 525 nm, respectively²⁸. The K_d of the aptamer to its target bacterium was estimated by plotting the fluorescence signal intensity vs. the DNA concentration via a non-linear fit model of specific binding, using the GraphPad Prism 7.01 software. A saturation curve was obtained, and the K_d was calculated using the equation $Y = B_{max}X/(K_d + X)$, where B_{max} is the maximal fluorescent intensity measured, X is the concentration of the aptamer added, and Y represents the mean fluorescent intensity²⁹.

(D) Confocal microscopy study

For a visual understanding of the interaction of the whole with the aptamer, confocal microscopy studies were also carried out. In brief, the log-phase bacterial cells were washed three times solution and resuspended in PBS (10 mM, pH 7.4). Subsequently, equal volume of FITC labeled DNA is added to the cells and incubated at room temperature for two hours in the dark, followed by washings to remove unbound aptamer. The cells were then incubated with equal volume of DAPI dye (50 ng mL⁻¹) in the dark for 30 min and washed. Finally, the labeled cells were drop cast onto a clean glass slide, gently heat-fixed, and mounted with 10% glycerol prepared in PBS. The slides were then observed under the laser scan confocal microscope (Zeiss LSM 800 Airyscan, Germany), and digital images were captured at 630 \times magnification using iPlan-Apochromat 63 \times objective with two channels of laser 488 nm and 405 nm. The confocal microscopy images were visualized with help of Sujoy Dey, Carl Zeiss (India).

(E) Aptamer sequencing

The selected aptamer pool was PCR amplified with an elongated extension of 20 min using unmodified primers. DNA was amplified using unlabelled forward and reverse primers with an

elongated extension step to increase adenylation at 3' ends for efficient ligation in the cloning vector having T-overhangs. The oligomer fractions selected of the final SELEX round were purified using miniprep kit (QIAprep spin miniprep kit, Qiagen, USA) and were successfully inserted into pTZ57R/T vector and transformed into competent *E. coli* DH5 α cells using InsTAclone PCR cloning kit (Thermo Scientific, USA) and screened using XGal/IPTG for positive white colonies, which were further outsourced for sequencing using Sanger method³⁰⁻³². The deduced sequences were later evaluated using bioinformatic tools for putative structure formation.

(F) Putative aptamer structure modelling

The putative secondary structures of the obtained sequences along with their thermodynamic properties were predicted their using mfold web server (<http://unafold.rna.albany.edu/?q=mfold/DNA-Folding-Form>). The structures are calculated for linear DNA at 37°C with ionic conditions: [Na⁺] = 0.15 M, [Mg⁺⁺] = 0.005 M with standard errors of $\pm 5\%$, $\pm 10\%$, $\pm 11\%$ and 2-4°C for free energy, enthalpy, entropy and T_m, respectively. Using the Vienna output format from the mfold result, the 3D structure was evaluated using available online RNA Composer, which operates on the RNA FRABASE database acting as the dictionary relating RNA secondary structure and tertiary structure elements (<http://rnacomposer.cs.put.poznan.pl/>). In the RNA structure, uracil to thymine residues mutated to DNA form and structure minimized using PyMOL³³⁻³⁵. G-quad prediction was carried using the Quadruplex forming G-rich Sequences (QGRS) analyzer (<http://bioinformatics.ramapo.edu/QGRS/analyze.php>).

2.2.2 Nanostructured biosensing platform

2.2.2.1 Materials

Carboxyl-functionalized MWCNT and Graphene were procured from AD-Nano Technologies Pvt. Ltd. (India). Potassium permanganate (KMnO₄), Hydrazine monohydrate 65% (N₂H₄), Terephthalaldehyde 99% (TPA), Potassium ferrocyanide (K₄[Fe(CN)₆]·3H₂O), Potassium ferricyanide (K₃[Fe(CN)₆]) and were procured from Sigma-Aldrich (India). Sulphuric Acid 98% (H₂SO₄), Hydrogen Peroxide 30% (H₂O₂), N, N-Dimethylformamide (DMF), and Ortho-Phosphoric Acid 85% (H₃PO₄) were procured from Merck (India). TE 100 screen-printed carbon electrodes (SPE) were products of CH Instruments (USA).

2.2.2.2 Nanostructure synthesis: Bridged rebar graphene

Coming to the other major element of our biosensing platform, a novel graphene-based nanostructured transducing platform capable of showing high sensitivity was fabricated. For this, BRG was synthesized from multiwalled carbon nanotubes (MWCNT) using a modified chemical facilitated un-scrolling method followed by intra-sheet bridging with terephthalaldehyde (TPA) to form a 3D hierarchical nanostructure as illustrated in Figure 2.4. TPA is used as a cross-linker molecule as it has two reactive hydroxyl groups which helps in bridging molecules, but never

employed before for graphene derivatization³⁶. Also, TPA has inherent conductive properties, which would help further, when used for synthesis of nanomaterial for electrode modification. For its synthesis, MWCNT were vigorously stirred in H₂SO₄/H₃PO₄ (9:1) and KMnO₄ for two hours at room temperature²¹. The solution vial was transferred to an ice bath, and H₂O₂ (30%) was added to the mixture. The resulting unzipped MWCNT solution was washed and centrifuged with HCl and water consecutively until the pH was neutralized. The synthesized rebar graphene oxide (Rebar

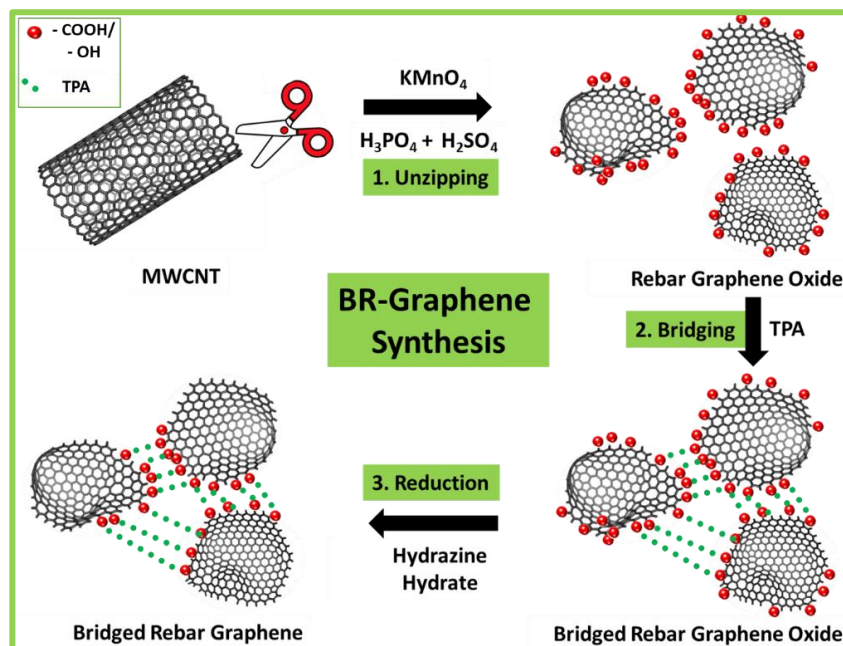


Figure 2.4: BRG Synthesis: The step-by-step synthesis process illustrated.

GO) was filtered and dried. For bridging, Rebar GO and TPA ratio was optimized and sonicated to obtain bridged rebar graphene oxide (BRGO), which was followed by lyophilization. Further, the reduction of lyophilized BRGO was carried out overnight with hydrazine hydrate (N₂H₄), which provided a reducing environment for conversion of BRGO to BRG (Figure 2.4).

2.2.2.3 Nanostructure & sensor characterization

The synthesized BRG was characterized microscopically by SEM, spectrophotometrically by UV-Vis, Raman, DLS techniques and, electrochemically by CV and EIS techniques.

(A) Scanning electron microscopy

For SEM sample preparation, silicon wafers were used as the substrate, and four samples were prepared by drop-casting BRG dispersion onto substrates followed by baking at 60°C. Onto this, PLL (0.001% w v⁻¹) was drop casted on 2nd, 3rd, and 4th modified substrate, and subsequently, amplified screened aptamer was then used to functionalize 3rd and 4th substrate. The volumes were optimized to obtain images with clarity and in accordance with the working electrode preparation. Ethanol dehydrated *E. coli* were exposed to 4th substrate and kept for incubation at room temperature for an hour. The samples were gold spray-coated and visualized under JSM IT300

(JEOL) with an acceleration voltage of 20 kV for clear morphological study of the nanostructures and bacteria without charging or charring of the sample.

(B) UV-Vis spectroscopy

The UV-Vis spectroscopic measurements of BRG, BRG coated with PLL, and; PLL coated BRG conjugate functionalized with aptamer was carried out using UV-2600 spectrophotometer (Shimadzu) to confirm the binding of DNA onto PLL functionalized BR-Graphene surface. For this 10-fold dilutions of the samples prepared for SEM were used to get proper absorbance signals.

(C) Raman spectroscopy

Raman spectroscopic analysis was carried out with a WiTech Raman spectrophotometer ($\alpha 300R$) at integration time of 1s (to obtain good peak resolution) using 532 nm Nd:YAG laser source to characterize the MWCNTs, synthesized Rebar GO, BRGO, and BRG. Samples were prepared similar to those mentioned in sub-section A.

(D) Zeta potential

To understand the binding of PLL and subsequently the aptamer on to the BRG surface, zeta potential (ζ) measurements were further carried out using Zetasizer Nano ZSP (Malvern, UK). The sample solutions were prepared in binding buffer to minimize the effect of pH on the readings and to mimic the real experimental conditions of nanostructure, linker molecule and aptamer functionalization.

(E) Cyclic voltammetry

BRG was used to modify the working electrode of SPE. Cyclic voltammetry (CV) studies were carried out using the CHI660E electrochemical workstation (CH Instruments) as shown in Figure 2.5. For bio-interface development, working electrode were modified with PLL ($0.001\% \text{ w v}^{-1}$) to

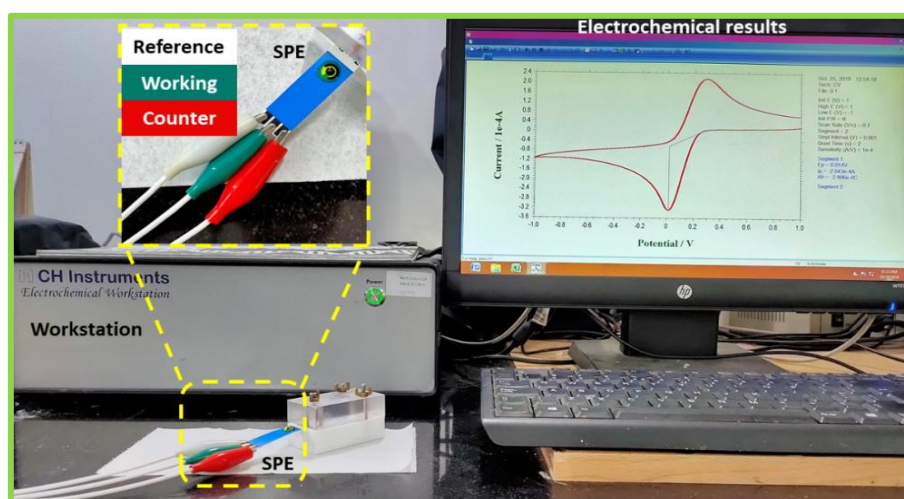


Figure 2.5: Electrochemical workstation setup: Screen-printed electrode (SPE) were used in the study as sensors.

immobilize DNA wherein, aptamer was drop cast and incubated overnight at 4°C . Higher concentrations are PLL significantly dampened the current response and were thus avoided to minimize sensor saturation. CV experiments were conducted using a scan rate of 100 mV s^{-1} and sweeping potential ranging from -1 to +1 V using $1.5 \text{ mM K}_3[\text{Fe}(\text{CN})_6]/\text{K}_4[\text{Fe}(\text{CN})_6]$ (100 mM

PBS). The potential change was chosen considering the redox peak current maxima of the redox probe and as well as the electrode material³⁷. The amount of BRG deposited was optimized by CV measurements. The electrochemical performance of conventional graphene, unbridged rebar graphene, and BRG was also studied using similar optimal parameters.

(F) Electrochemical impedance spectroscopy

Electrochemical impedance spectroscopy (EIS) studies were recorded for the bare electrode surface and then with the modified electrode with increasing *E. coli* O78:H11 colony forming units (cfu) from 10^1 to 10^6 over the optimal wide frequency range (100 kHz to 0.1 Hz) using an alternative voltage of 0.25 V amplitude as per previous studies for bacterial electrochemical detection³⁷. The different concentrations of *E. coli* O78:H11 (10^1 to 10^6 cfu) in water were incubated at room temperature for an hour, and then EIS measurements was performed at each concentration, sequentially. A modified Randles-Sevcik circuit was used to fit the electrical double layer (C_{dl}) between the electrode surface and the electrolyte using solution resistance (R_{sol}), charge transfer resistance (R_{ct}), Warburg impedance (W) and constant phase element (Q) as parameters. The real and imaginary part of the EIS spectra is represented by Nyquist plots (Z' vs $-Z''$) for the modified nanostructured SPE.

The cross-reactivity and interference studies of the fabricated aptasensor for *E. coli* O78:H11 was also carried out using EIS with the closely related bacterial species viz., *E. coli* DH5 α , *P. vulgaris*, *L. monocytogenes*, *S. boydii*, *S. flexneri*, *E. aerogenes*, *C. braakii* and *B. subtilis* by spiking 1×10^1 , 1×10^3 , 1×10^6 cells of these bacteria individually in water and further exposed to the aptamer functionalized BRG nanostructured electrodes.

2.2.2.4 Food sample pre-processing

Furthermore, the efficacy of the aptasensor was evaluated in real samples by spiking *E. coli* O78:H11 at different concentrations (1×10^1 , 1×10^3 , 1×10^6 cells) in various fruit juices and milk samples. Prior to analysis, these juice and milk samples were pre-processed by centrifugation at $2500 \times g$ for 10 min to remove the pulp/solids, and the pH of the resultant supernatant was adjusted to 7.2 using 1 M Tris base (pH 12.0), as required for optimal bacteria-aptamer interaction.

2.3 Results & discussion

2.3.1 Optimization of *E. coli* O78:H11 culture

The pure culture of *E. coli* O78:H11 was revived on LB agar medium and sub-cultured onto selective SMAC medium to ensure purity. Further, the bacterial growth conditions for harvesting the target bacterial strain were optimized in TSB and its OD₆₀₀ was measured after every 30 min and the growth curve was generated and cells in early log phase after 90 min (encircled) were harvested and used for further experiments (Figure 2.6). The cell-surface differs in its composition

at varying growth stages, thus all the experiments were conducted using cells harvested at exponential phase only, to maintain continuity amongst experiments.

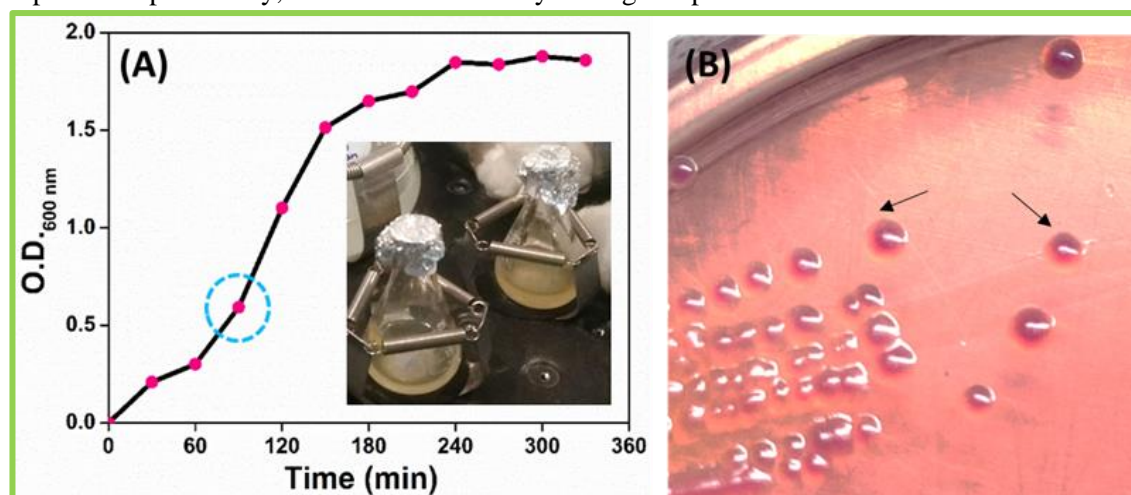


Figure 2.6: Bacterial growth curve: (A) Growth curve of *E. coli* O78:H11 in TSB media shown (inset). The bacterial cells in early log phase (encircled) were harvested & used in the study. (B) Culture plate showing pink colonies of pure culture maintained on SMAC media.

2.3.2 Aptamer technology: Cell-SELEX

2.3.2.1 BLI studies for bacteria-boronic acid interaction

To experimentally ascertain its binding with the bacteria, we set up a BLI based binding assay, wherein we used amine modified PBA and attached it to carbodiimide modified AR2G sensor (FortéBio) and allowed it to interact with the bacterial cells suspended in binding buffer in a

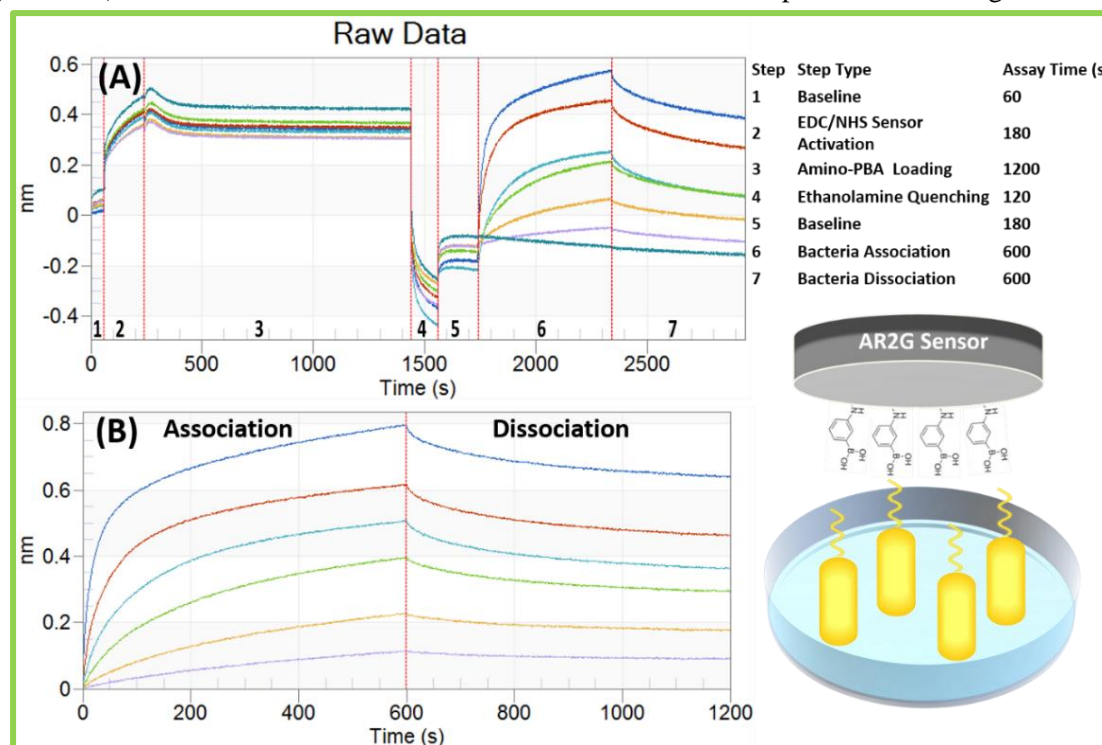


Figure 2.7: BLI Sensogram showing bacteria-PBA interaction: (A) Raw data showing step-by-step real-time analysis of the entire method; the table in the right panel shows the processing parameters and time of each step. (B) Processed sensogram is showing association-dissociation kinetics with exposure to increasing bacterial concentrations.

microtiter plate well for prolonged 600 s for bio-interaction, which showed functional association/dissociation kinetics between *E. coli* cells and PBA (Figure 2.7).

2.3.2.2 Anti-*E. coli* O78:H11 aptamer characterization

The quantity and purity of the eluted oligomer fractions after each SELEX round was quantified via nanodrop readings and the absorbance values at 260 nm, 260/280 and 260/230 ratio were measured (Figure 2.8).

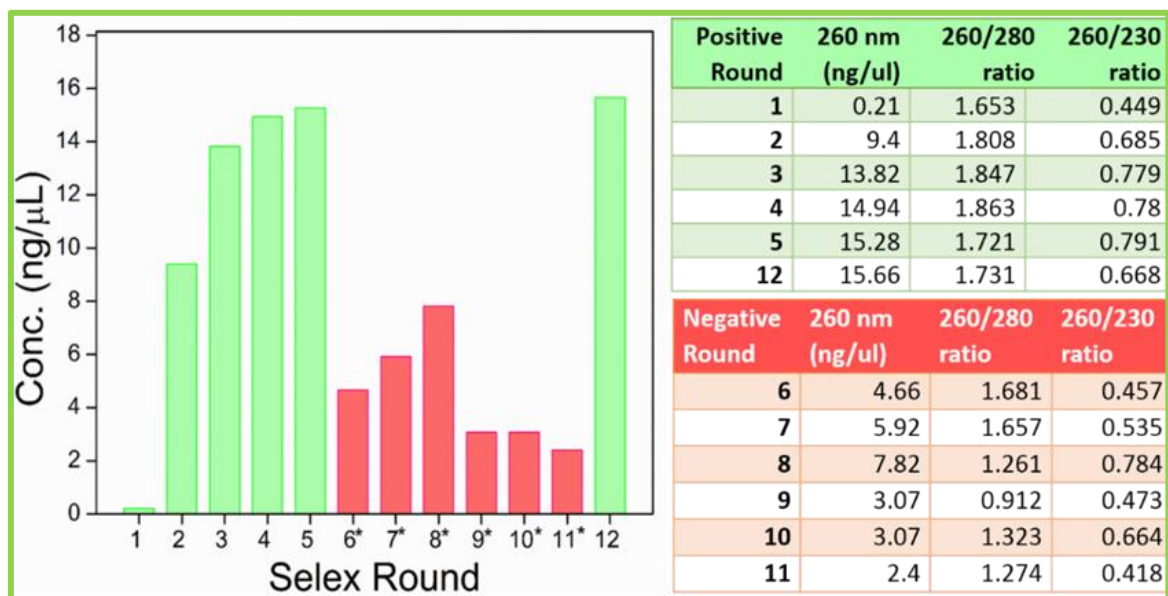


Figure 2.8: Cell-SELEX progression: Positive selection rounds (denoted in green) 1-5 and 12th are against *E. coli* O78:H11 and 6th-11th counter SELEX rounds (denoted in red) against different bacteria viz., *P. vulgaris*, *L. monocytogenes*, *E. coli* DH5 α , *E. aerogenes*, *C. braakii* and *B. subtilis*, respectively. Also showing the DNA quality assessment and quantity of the elutes at each round.

It was observed that the concentration of DNA increased gradually with the progression of SELEX rounds (1st - 5th), where the random pool oligomers were being exposed to target cells, amplified, partitioned to ssDNA and re-exposed to the target cells. However, during counter selection, binding was also observed and for this, the fraction of bound DNA was discarded, and the unbound enriched DNA pool was amplified, partitioned and used for further studies. The gradual increase in positive rounds is indicative of binding of DNA oligomers to a single target of interest, whereas each negative round includes the binding of screened and enriched DNA oligomers to respective different counter bacterial strains mentioned in Section 2.2.1.3.2. showing distinctive variation in binding. These screened sequences thus, bound specifically to the target only and not the cross-reactive bacterial cells. Furthermore, a final positive round was carried out to enrich sequences binding to the target and confirm their interaction with our target bacteria. The sequences were purified, inserted into pTZ57R/T vector and transformed into competent *E. coli* DH5 α cells and

were further outsourced for sequencing as mentioned earlier³⁸. The deduced sequences were later evaluated using bioinformatic tools for putative structure formation.

2.3.2.3 Aptamer bio-interaction studies

2.3.2.3.1 BLI studies

BLI bio-interaction studies were performed to confirm binding between the bacteria and the screened aptamer using the Octet Red96 system as per our designed protocol. The aptamer functionalized BLI streptavidin sensor was allowed to interact with three-fold dilutions of bacteria

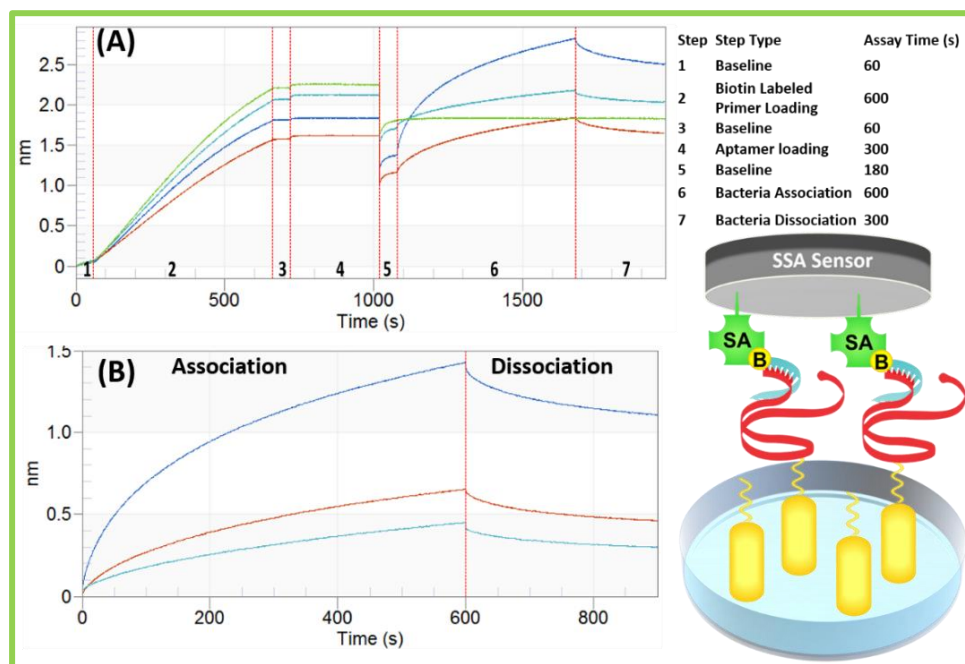


Figure 2.9: Aptamer-bacteria interaction: BLI Sensograms (A) Raw data presenting a step-by-step real-time analysis of aptamer-bacteria association-dissociation kinetics; the table in the right panel shows individual step parameters and assay time. (B) An overlay of sensograms for three-fold dilutions of bacteria (1×10^7 , 3×10^6 , 1×10^5) depicting the characteristic association-dissociation curve.

(1×10^7 , 3×10^6 , 1×10^5), and the association/dissociation kinetics was carried out to determine the bio-interaction (illustrated in Figure 2.9). The significant association and dissociation kinetics indicate active binding, as evident from the sensograms (Figure 2.9). Based on the literature survey, it was deduced that the bacterial cell envelope has a variety of surface antigens viz., flagellar proteins, glycoproteins, polysaccharides, and lipopolysaccharides which can act as targets for bio-recognition. This bio-interaction between the surface molecules and the aptamer bio-receptor moieties takes place via an interplay of a multitude of intermolecular interactions viz., van der Waals forces, electrostatic interactions, three-dimensional shape, stacking and hydrogen bonds, which are thus supposedly responsible for the strong binding of the aptamer to its target analyte³⁹.

2.3.2.3.2 Fluorescence binding assay

The K_d of the aptamer to its target bacterium was estimated by plotting the fluorescence signal intensity vs. the DNA concentration via a non-linear fit model of specific binding, using the

GraphPad Prism 7.01 software (Figure 2.10). This well-characterized aptamer with a K_d value of 14 nM was used for further experiments in detecting the target *E. coli* O78:H11.

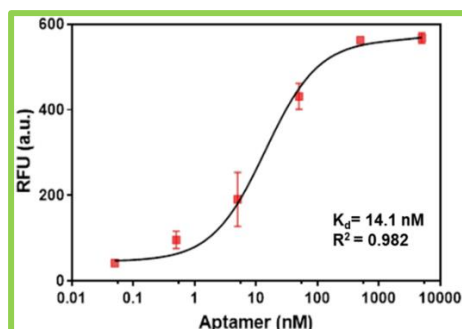


Figure 2.10: Aptamer-bacteria interaction: Fluorescence binding assay using increasing concentrations of FITC labeled aptamer and *E. coli* cells. The fitting and K_d value estimation have been carried out using GraphPad Prism software.

2.3.2.3.3 Confocal microscopy studies

Confocal microscopy supported the specific DNA-bacteria interactions, thereby confirming the precise bio-molecular interactions of FITC labeled aptamer with DAPI stained bacteria cells. The slides were then observed under the laser scan confocal microscope and digital images were

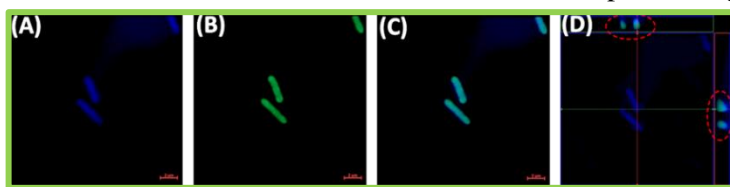


Figure 2.11: Aptamer-bacteria interaction: Aptamer labelled bacteria at 630 \times using the filter for (A) DAPI (B) FITC (C) merge (D) orthographic view of z-stack images to confirm aptamer binding to cell surface; showing 3D view at the point of cross-section.

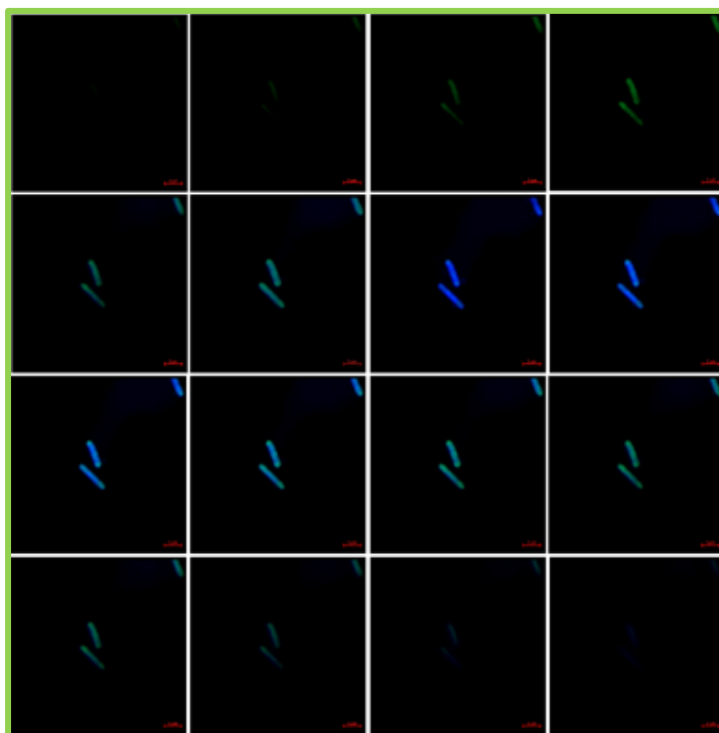


Figure 2.12: Z-stack imaging: Sixteen Z-stack slicing images of the bacteria (blue) and DNA (green) interaction.

captured at 630× magnification using iPlan-Apochromat 63× objective with two channels of laser 488 nm and 405 nm (Figure 2.11). Z-stack imaging having 16 slices was also carried out and used to generate the orthographic view of the bacteria-aptamer interaction (Figure 2.12).

2.3.2.3.4 Putative aptamer structure

The putative secondary structures of the obtained sequences along with their thermodynamic properties were predicted their using ‘mfold’ web server. The sequence with the lowest ΔG was chosen, owing to its higher thermal stability (Figure 2.13). As mentioned in Section 1.6.2.2 guanine tetrads provide spatial stability and the propensity of the selected sequence to contain the G-quad region was mapped using QGRS mapper online tool, which confirmed a G-quad at N-54 of 22 nt region, with a G-score of 13. The G-score is evaluated on its likelihood to form a stable G-quad, where the scoring method used by the QGRS mapper is principled over: (i) shorter loops are more common, (ii) equality in size and (iii) number of tetrads.

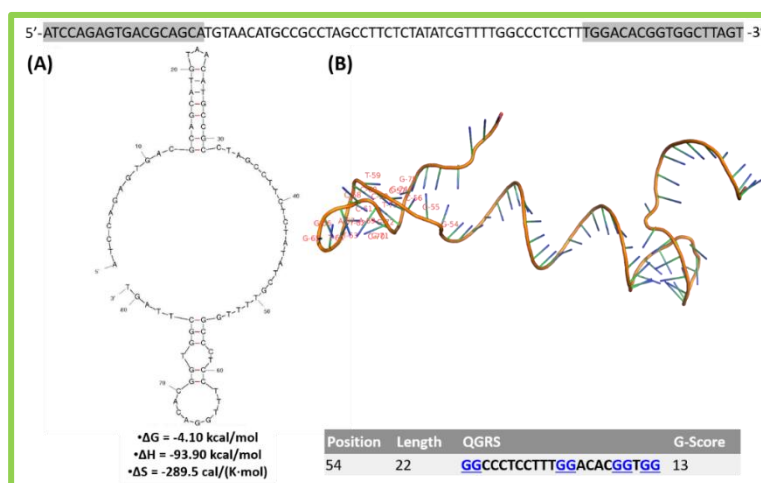


Figure 2.13: Putative aptamer structure: (Top) Sequence of selected aptamer and (A) mfold prediction of the structure. (B) 3D structure elucidated from the RNA composer modeling server and visualized using PyMOL. (Bottom) G-quadruplex prediction carried using the QGRS analyzer showed an excellent probability of G-quad formation between a 22-base stretch of nt (N-54 to N-76), which have been denoted in red.

2.3.3 Bridged rebar graphene: Synthesis & characterization

2.3.3.1 Synthesis of bridged rebar graphene

The BRG was synthesized from chemically un-scrolling MWCNT, followed by bridging the rebar GO with TPA to form a 3D bridged rebar GO nanostructure, which was lyophilized and reduced to form BRG in presence of hydrazine. To alleviate the issues of other conventional crosslinkers such as glutaraldehyde, in our study, we have used TPA as it carries an aromatic π -conjugated ring which

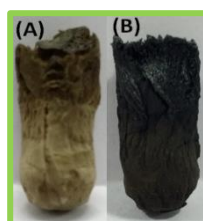


Figure 2.14: Bridged rebar graphene. (A) BRGO after lyophilization and (B) BRG after reduction.

is actively involved in the electron transfer process³⁶. This fast electron kinetics was desirable on the fabricated aptasensor imparting rapidity and high sensitivity. During the synthesis of BRG, the chemical reduction of lyophilized BRGO showed a color change from brown to black attributed to the removal of intrinsic hydroxyl groups, as seen in Figure 2.14.

2.3.3.2 Scanning electron microscopy

The SEM micrographs depicted the unzipping of MWCNT and subsequent 3D cross-linkage of synthesized BRG. As visualized in Figure 2.15, the SEM micrographs clearly showed the unzipping of MWCNT and subsequent 3D cross-linkage of synthesized BRG. The functionalization of PLL and DNA aptamer over BRG did not alter the morphology of our synthesized nanomaterial.

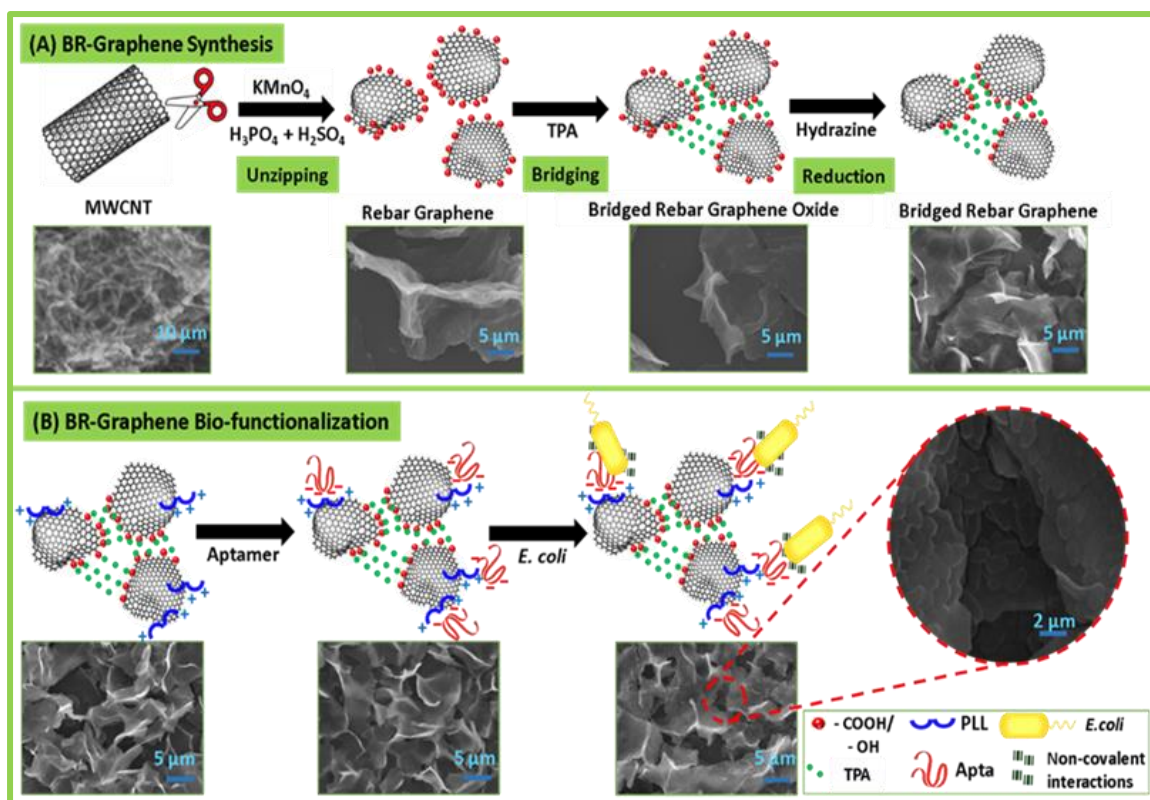


Figure 2.15: SEM microscopy: SEM micrographs of the nanomaterial at various steps of (A) synthesis, (B) functionalization, and sensing. The magnified view (10,000x) of the SEM micrograph shows cells immobilized on the BRG/PLL/Apta surface.

2.3.3.3 Spectroscopic analysis

(A) UV-Vis spectroscopy

The UV-Vis spectroscopic characterization of the synthesized material demonstrated an increase in absorption by π - π^* electron transition at 210 nm and 225 nm, respectively, due to the presence of abundant sp^2 -carbon atoms present in Rebar GO and BRG (Figure 2.16). After PLL functionalization, the formed BRG/PLL nanohybrid showed an absorption peak at 232 nm with a significant redshift, indicating the interaction of PLL side chains and carbonyl groups with n - π^*

and π - π^* electron transitions. Upon conjugation with DNA, an additional peak at 260 nm was observed, clearly indicating the presence of immobilized DNA over BRG/PLL nanohybrid.

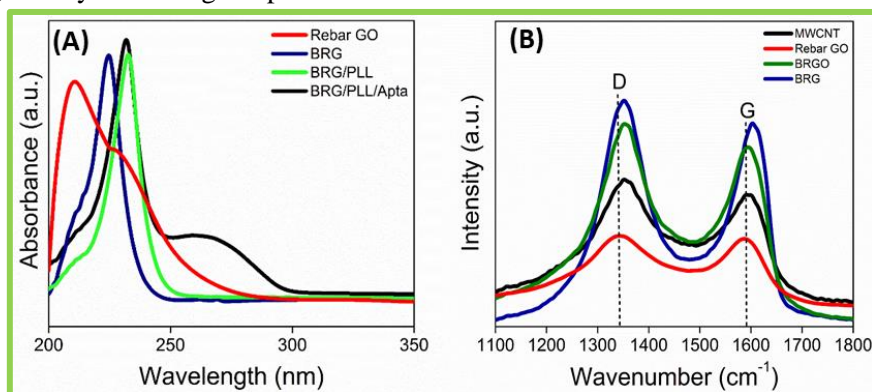


Figure 2.16: Spectroscopic characterization of BRG: (A) UV-Vis absorption and (B) Raman spectra.

(B) Raman spectroscopy

Raman spectroscopic analysis was carried out with a WiTech Raman spectrophotometer using a 532 nm laser source to characterize the MWCNTs, synthesized Rebar GO, BRGO, and BRG (Figure 2.16). Raman spectroscopic studies further indicate the formation of BRG by showing characteristic D and G bands, at $\sim 1350\text{ cm}^{-1}$ and $\sim 1600\text{ cm}^{-1}$ corresponding to A_{1g} and E_{2g} mode of Graphene⁴⁰. The Raman spectra suggested a remarkable shift in G band from 1596 cm^{-1} (MWCNT), 1588 cm^{-1} (Rebar GO), 1592 cm^{-1} (BRGO) to 1600 cm^{-1} (BRG). The ratio of the integrated intensities of the D and G bands (I_D/I_G) ratio for Rebar GO, BRGO, and BRG were observed to be 1.022, 1.005, 1.031, 1.066 respectively, indicating a high degree of order due to restoration of sp^2 network during the chemical reduction process.

(C) Zeta potential studies

To understand the binding of PLL and subsequently the aptamer on to the BRG surface, zeta potential (ζ) measurements were further carried out. The measurements suggested that BRG was negatively charged with a ζ value of -25.7 mV and increased to $+8.4\text{ mV}$ upon PLL functionalization. After aptamer immobilization, ζ changed to -6.39 mV for BRG/PLL/Apta (Figure 2.17). The positive ζ value of BRG/PLL is conferred by the presence of positively charged $-NH_3^+$ groups of PLL, which further helped in the binding of the negatively charged DNA aptamer to form BRG/PLL/Apta. This characterized anionic aptamer was conjugated to the cationic BRG/PLL by

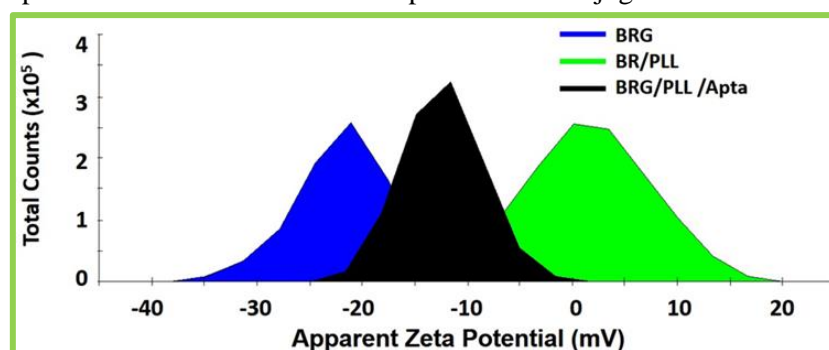


Figure 2.17: Zeta Potential measurements: Surface zeta potential measurements of BRG, BRG/PLL, and BRG/PLL/Apta.

coulombic interactions, thus creating a stable bio-interface of BRG/PLL/Apta. The target analyte *E. coli* interacts with anti-*E. coli* aptamer of BRG/PLL/Apta complex via non-covalent interactions viz., electrostatic interactions, van der Waals forces, and hydrogen bonding.

2.3.4 Nanostructured biosensing platform

2.3.4.1 Aptasensor fabrication & characterization

Electrochemical performance of rebar graphene bridged with different % of TPA was analyzed electrochemically to optimize the best ratio showing good electrochemical performance using 1.5 mM $K_3[Fe(CN)_6]/K_4[Fe(CN)_6]$ (100 mM PBS) at a sweeping potential ranging from -1 to +1 V with a scan rate of 100 mV s^{-1} (Figure 2.18 A). It was observed that 0.5% TPA with rebar graphene showed highest increase in redox peak current, as opposed to higher concentrations. This concentration was chosen and optimized for synthesis of BRG for subsequent studies. Additionally, conventional graphene, unbridged rebar graphene, and BRG was studied to observe the enhancement of signal response with BRG (Figure 2.18 B). These were drop cast onto the SPE, and it was observed that the nanostructured electrode modified with conventional graphene showed a 7.5-fold increase, unbridged rebar graphene showed 10-fold increase.

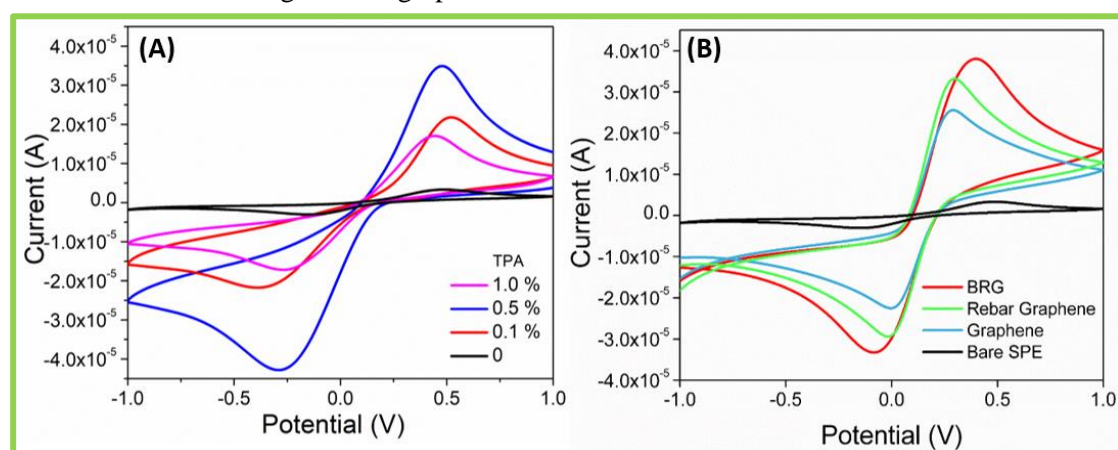


Figure 2.18: Optimization & comparative of nanomaterial performance: (A) CV response of rebar graphene bridged with different ratios of crosslinker TPA. (B) CV response curve of bare and modified SPE with 0.25 μg Graphene, Rebar Graphene and BRG.

The electrochemical characterization of aptamer functionalized BRG (BRG/PLL/Apta) showed good current response along with the specificity towards target bacteria. The amount of BRG deposited onto working electrode of SPE was optimized by CV measurements and the maximum current response was observed for 0.250 μg BRG, and this optimized concentration was used for further experiments. This surface modification is of grave importance that it will allow the change in current response to be monitored with high sensitivity.

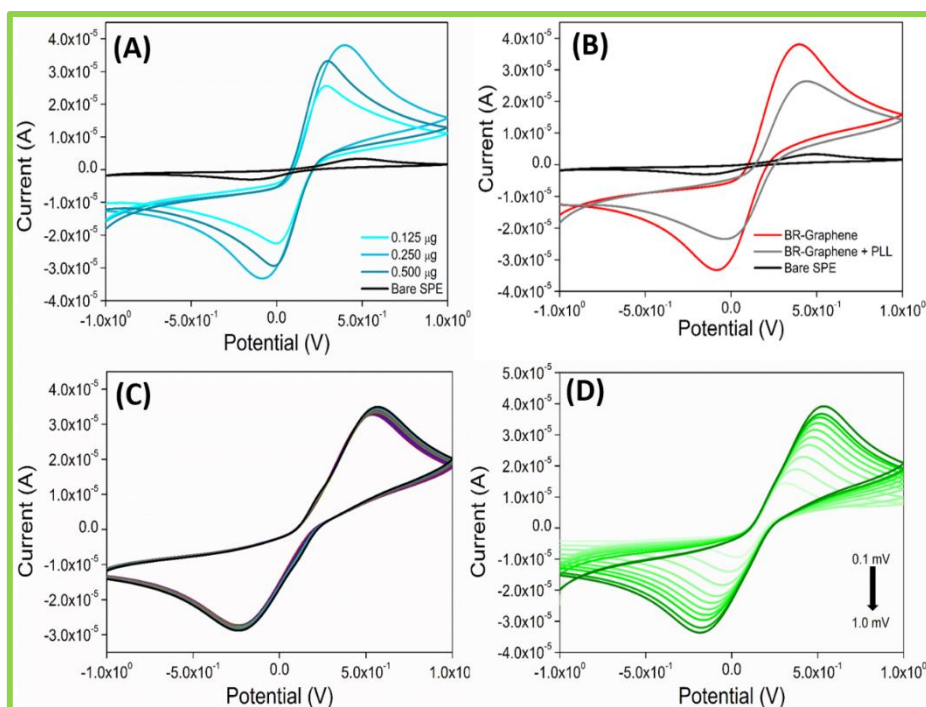


Figure 2.19: Sensing platform performance: CV response curves of (A) bare and modified SPE with increasing concentrations of drop cast BRG. (B) BRG and BRG/PLL modified electrodes using 1.5 mM $K_3[Fe(CN)_6]/K_4[Fe(CN)_6]$ (100 mM PBS) at a sweeping potential ranging from -1 to +1 V with a scan rate of 100 $mV s^{-1}$. (C) Twenty-five cycles scan of the BRG electrode showing the stability of the drop cast electrode. (D) Scans recorded at different scan rates.

In contrast, our selected nanomaterial showed eleven-fold increase in the current as compared to the bare electrode. Upon addition of PLL, there was a slight decrease in mobility of the redox-species due to the insulating effect imposed by the presence of organic moiety. The electrochemical stability of modified SPE was tested by repeated cycling (25 cycles), which showed insignificant change in the peak current. The nanostructured SPE showed a linear increase in the cathodic peak intensity with an increasing scan rate (0.1 $V s^{-1}$ to 1.0 $V s^{-1}$), indicating that the process is under diffusion control (Figure 2.19). The modification of bare SPE with BRG resulted in an enhanced electrochemical current response as indicated by a lower charge transfer resistance (R_{ct}) value (Figure 2.20). The anti-*E. coli* aptamer was immobilized on PLL modified BRG nanostructured SPE electrodes. The modified electrode was functionalized with PLL linker molecules to enhance the binding of our aptamer onto the electrode surface for bacterial binding

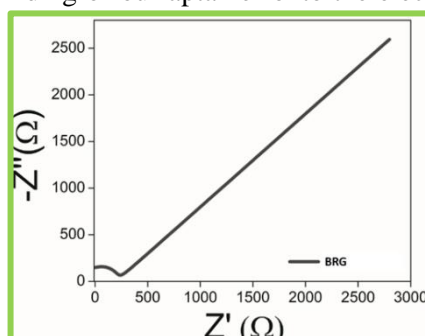


Figure 2.20: BRG EIS plot: The modification of bare SPE with BRG resulted in a steep increase in the electro-conductivity as indicated by a lower charge transfer resistance (R_{ct}) value of 212.8 Ω .

and hence carry out the aptamer mediated sensing assay. However, the functionalization with PLL and the immobilization of anti-*E. coli* aptamer on the sensor surface showed an increase in R_{ct} value due to the formation of an insulating biolayer.

2.3.4.2 *E. coli* O78:H11 aptasensing assay

The modified electrode was functionalized with PLL linker molecules to enhance the binding of our aptamer onto the electrode surface for bacterial binding and hence carry out the aptamer mediated sensing assay (Figure 2.21).

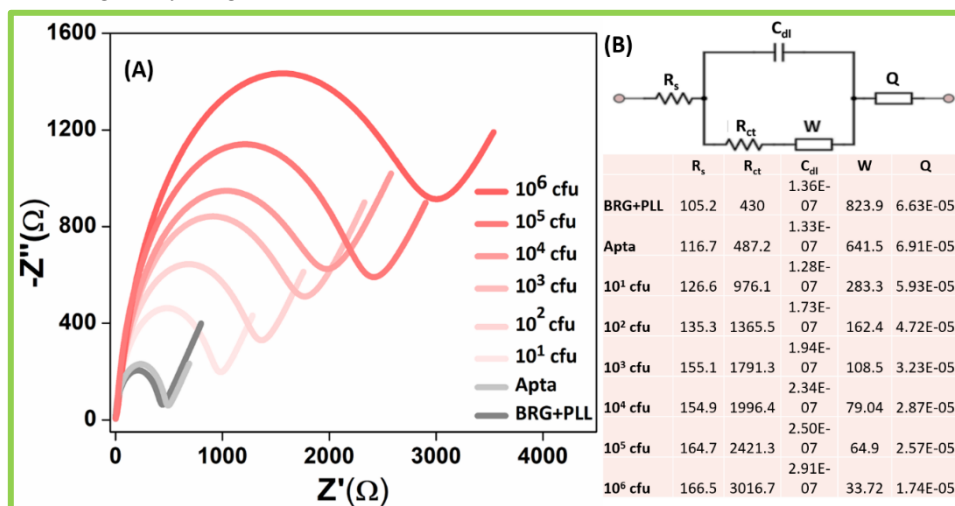


Figure 2.21: Nyquist plot for *E. coli* O78:H11: (A) EIS response recorded at anti-*E. coli* O78:H11 aptamer modified BRG electrode in the presence of increasing conc. of cells. (B) Randles-Sevcik equivalent circuit model is showing the fitted experimental data. The table shows the values of equivalent circuit elements.

However, the functionalization with PLL and the immobilization of anti-*E. coli* aptamer on the sensor surface showed an increase in R_{ct} value due to the formation of an insulating biolayer. The EIS studies were recorded for increasing *E. coli* O78:H11 cells from 10^1 to 10^6 over a frequency range (100 kHz to 0.1 Hz) using an alternative voltage of 0.25 V amplitude. The different concentrations of *E. coli* O78:H11 (10^1 to 10^6 cells) in water were incubated at room temperature for an hour, and then EIS measurements was performed at each concentration, sequentially. It was observed that the value of R_{ct} increases linearly with an increase in the concentration from 10^1 to 10^6 bacteria cells, showing a good regression coefficient of $R^2 = 0.983$ (Figure 2.22). The increase

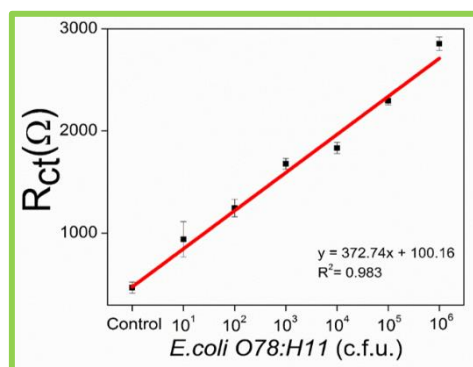


Figure 2.22: Calibration plot: Multiple EIS studies were carried out on the fabricated aptasensor with increasing cfu showing excellent linearity.

in R_{ct} value shows that the binding between anti-*E. coli* aptamer on the sensor surface and the target *E. coli* cells further blocked the electron transfer from the redox probe due to steric hindrance and insulating nature of the large bacteria cells onto the electrode surface. Further, exposure of bacteria on the surface leads to the fouling of the electrode surface, resulting in inconsistent current values. All the experiments were repeated thrice to check the reproducibility of the developed aptasensor. The sensor demonstrated a low detection limit of $\sim 10^1$ cells towards the target bacteria with a dynamic response range from 10^1 to 10^6 cells in water samples.

2.3.4.3 Cross-reactivity & platform validation studies

The cross-reactivity of our developed aptasensor for *E. coli* O78:H11 with the closely related bacterial species viz., *E. coli* DH5 α , *P. vulgaris*, *L. monocytogenes*, *S. boydii*, *S. flexneri*, *E. aerogenes*, *C. braakii* and *B. subtilis* was checked by spiking 10^3 cells of these bacteria individually in water and further exposed to the BRG/PLL/Apta nanostructured electrodes (Figure 2.23). It was observed that the aptasensor showed minimal interference in the presence of other bacterial species.

Moreover, to study the interference of cross-reactive strains in the presence of target analyte, three different concentrations (1×10^1 , 1×10^3 , 1×10^6) of *E. coli* O78:H11 in water were exposed to the aptasensor surface with an equal concentration of different cross-reactive strains viz., *E. coli* DH5 α , *P. vulgaris*, *L. monocytogenes*, *S. boydii*, *S. flexneri*, *E. aerogenes*, *C. braakii* and *B. subtilis*.

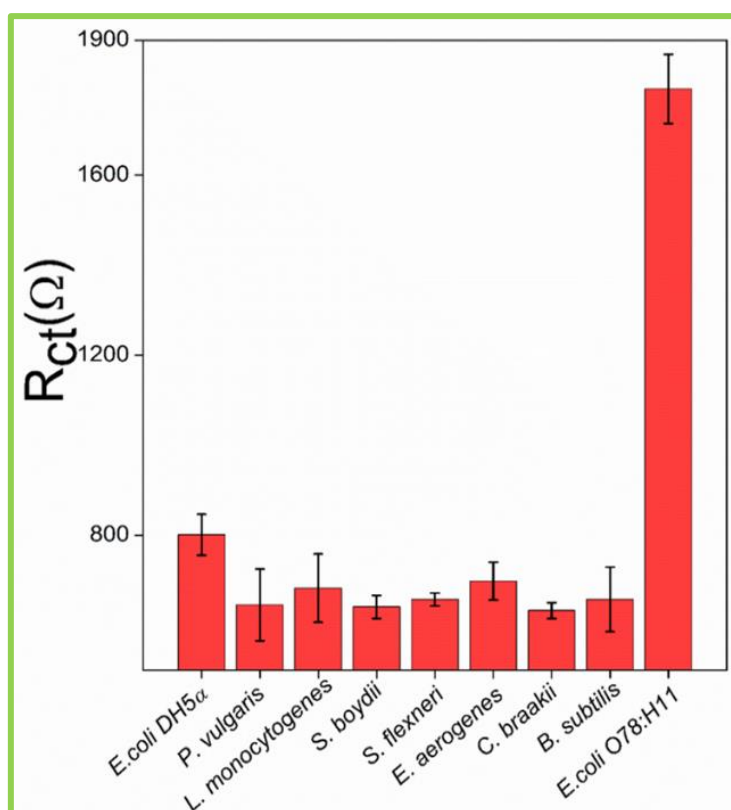


Figure 2.23: Aptasensor cross-reactivity: Cross-reactivity profile of *E. coli* O78:H11 aptasensor against different bacterial species.

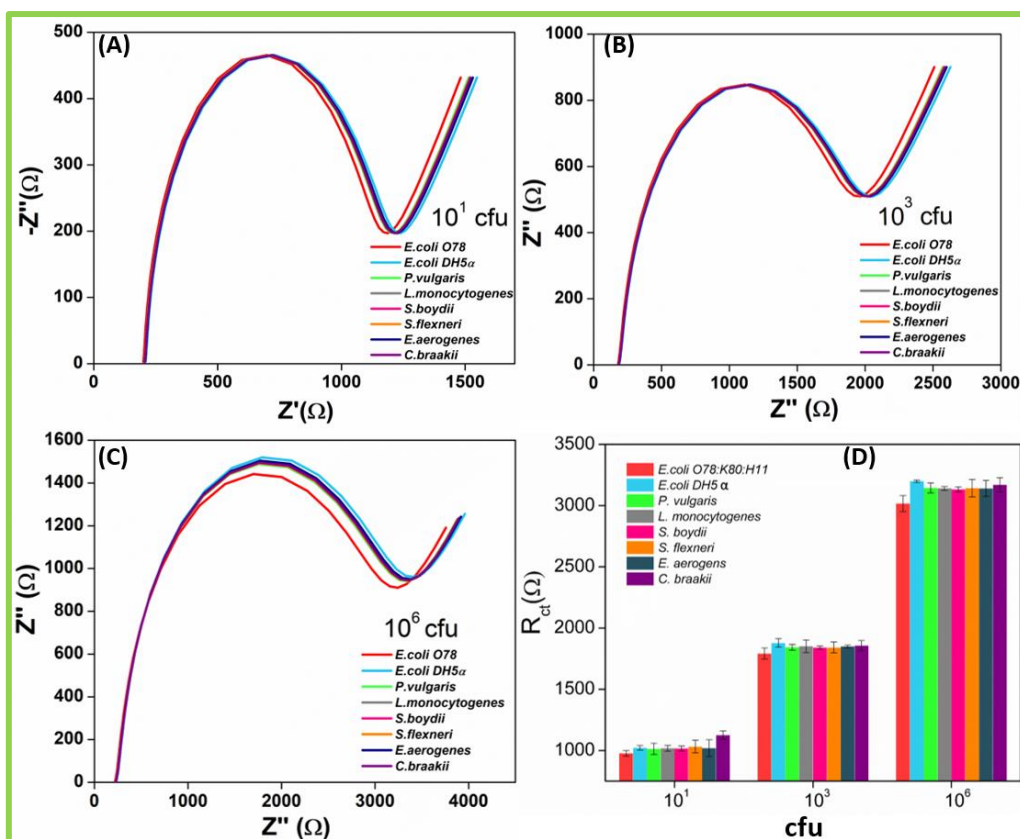


Figure 2.24: Aptasensor interference studies: Nyquist plot showing results of exposure to target bacteria *E. coli* O78:H11 at different concentrations (A) 10^1 , (B) 10^3 , (C) 10^6 respectively with an equal concentration of various interfering cross-reactive bacterial species. (D) The bar graph showing cumulative results.

2.3.4.4 Validation in spiked real samples

Furthermore, the efficacy of the aptasensor was evaluated in real samples by spiking *E. coli* O78:H11 at different concentrations (1×10^1 , 1×10^3 , 1×10^6 cells) in various fruit juices and milk samples. In real-sample analysis, it is essential before estimation that excessive organic matter must be removed, which hinders the electrochemical response due to the presence of insulating bulk matter on the working electrode surface and it also needs to be considered that the interaction medium conditions are maintained closest to that of an ideal aptasensor. The results obtained in real

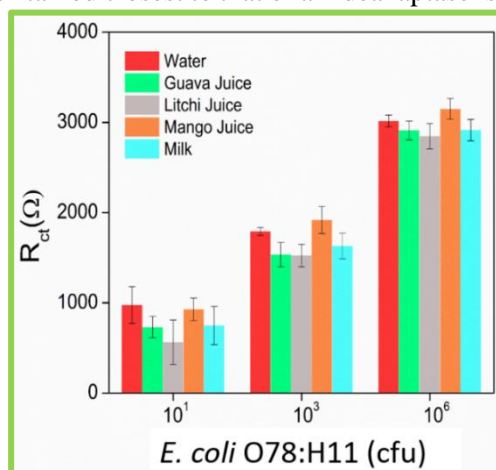


Figure 2.25: Specificity of aptasensor in real spiked samples: R_{ct} values after spiking *E. coli* O78:H11 in various food samples at three different cfu (10^1 , 10^3 , 10^6).

test samples were compared with a signal response deviation $\leq 4\%$ (at 10^6 cells) with respect to water which is without any interfering molecule such as sugars, carbohydrates, proteins, etc., present in juice and milk samples suggesting that the developed aptasensing platform is highly specific to the target analyte (Figure 2.25).

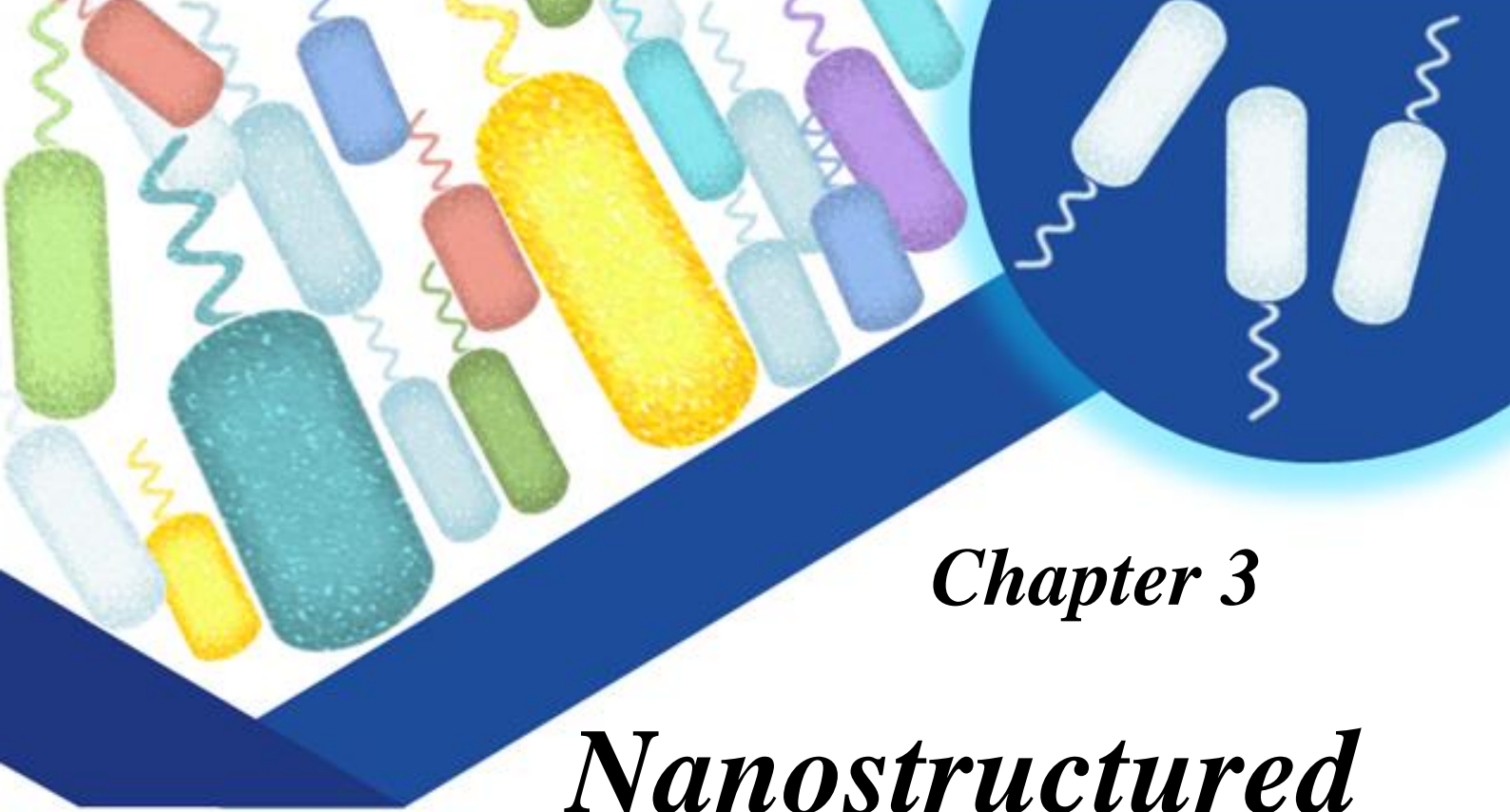
2.4 Conclusion

In conclusion, we successfully were able to fabricate a novel aptamer functionalized bridged rebar graphene based nanostructured aptasensor for label-free impedimetric sensing of pathogenic *E. coli* O78:H11. A novel methodology for cell-SELEX was devised for facile generation of high-affinity aptamers against bacteria, and these specific bacteria-aptamer interactions were captured on BRG nanostructured electrodes. This developed aptasensor demonstrated a low detection limit and sensitivity of $\sim 10^1$ cells towards *E. coli* O78:H11 with a linear response range from 10^1 to 10^6 cells in water, juice, and milk samples.

Bibliography

- (1) Hosangadi, D.; Smith, P. G.; Kaslow, D. C.; Giersing, B. K. WHO Consultation on ETEC and Shigella Burden of Disease, Geneva, 6–7th April 2017: Meeting Report. In *Vaccine*; Elsevier Ltd, 2019; Vol. 37, pp 7381–7390. <https://doi.org/10.1016/j.vaccine.2017.10.011>.
- (2) Anderson, J. D.; Bagamian, K. H.; Muhib, F.; Amaya, M. P.; Laytner, L. A.; Wierzbza, T.; Rheingans, R. Burden of Enterotoxigenic Escherichia Coli and Shigella Non-Fatal Diarrhoeal Infections in 79 Low-Income and Lower Middle-Income Countries: A Modelling Analysis. *Lancet Glob. Heal.* **2019**, *7* (3), e321–e330. [https://doi.org/10.1016/S2214-109X\(18\)30483-2](https://doi.org/10.1016/S2214-109X(18)30483-2).
- (3) Khalil, I. A.; Troeger, C.; Blacker, B. F.; Rao, P. C.; Brown, A.; Atherly, D. E.; Brewer, T. G.; Engmann, C. M.; Houpt, E. R.; Kang, G.; Kotloff, K. L.; Levine, M. M.; Luby, S. P.; MacLennan, C. A.; Pan, W. K.; Pavlinac, P. B.; Platts-Mills, J. A.; Qadri, F.; Riddle, M. S.; Ryan, E. T.; Shoultz, D. A.; Steele, A. D.; Walson, J. L.; Sanders, J. W.; Mokdad, A. H.; Murray, C. J. L.; Hay, S. I.; Reiner, R. C. Morbidity and Mortality Due to Shigella and Enterotoxigenic Escherichia Coli Diarrhoea: The Global Burden of Disease Study 1990–2016. *Lancet Infect. Dis.* **2018**, *18* (11), 1229–1240. [https://doi.org/10.1016/S1473-3099\(18\)30475-4](https://doi.org/10.1016/S1473-3099(18)30475-4).
- (4) Kaper, J. B.; Nataro, J. P.; Mobley, H. L. T. Pathogenic Escherichia Coli. *Nat. Rev. Microbiol.* **2004**, *2* (2), 123–140. <https://doi.org/10.1038/nrmicro818>.
- (5) Evans, D. J.; And, J. R.; Evans, D. G. *Three Characteristics Associated with Enterotoxigenic Escherichia Coli Isolated from Man*; 1973.
- (6) Evans, D. G.; Silver, R. P.; Evans, D. J.; Chase, D. G.; Gorbach, S. L. Plasmid-Controlled Colonization Factor Associated with Virulence in Escherichia Coli Enterotoxigenic for Humans. *Infect. Immun.* **1975**, *12* (3), 656–667.
- (7) Ørskov, F.; Ørskov, I.; Evans, D. J.; Sack, R. B.; Sack, D. A.; Wadström, T. Special Escherichia Coli Serotypes among Enterotoxigenic Strains from Diarrhoea in Adults and Children. *Med. Microbiol. Immunol.* **1976**, *162* (2), 73–80. <https://doi.org/10.1007/BF02121318>.
- (8) Crossman, L. C.; Chaudhuri, R. R.; Beatson, S. A.; Wells, T. J.; Desvaux, M.; Cunningham, A. F.; Petty, N. K.; Mahon, V.; Brinkley, C.; Hobman, J. L.; Savarino, S. J.; Turner, S. M.; Pallen, M. J.; Penn, C. W.; Parkhill, J.; Turner, A. K.; Johnson, T. J.; Thomson, N. R.; Smith, S. G. J.; Henderson, I. R. A Commensal Gone Bad: Complete Genome Sequence of the Prototypical Enterotoxigenic Escherichia Coli Strain H10407. *J. Bacteriol.* **2010**, *192* (21), 5822–5831. <https://doi.org/10.1128/JB.00710-10>.
- (9) Fleckenstein, J. M. Enterotoxigenic Escherichia Coli. In *Escherichia coli: Pathotypes and Principles of Pathogenesis: Second Edition*; Elsevier Inc., 2013; pp 183–213. <https://doi.org/10.1016/B978-0-12-397048-0.00006-1>.
- (10) Nataro, J. P.; Kaper, J. B. Diarrheagenic Escherichia Coli. *Clinical Microbiology Reviews.* January 1998, pp 142–201. <https://doi.org/10.1128/cmr.11.1.142>.
- (11) Clements, A.; Young, J. C.; Constantinou, N.; Frankel, G. Infection Strategies of Enteric Pathogenic Escherichia Coli. *Gut Microbes.* Taylor & Francis March 2012, pp 71–87. <https://doi.org/10.4161/gmic.19182>.
- (12) Reischl, U.; Youssef, M. T.; Wolf, H.; Strockbine, N. A. Real-Time Fluorescence PCR Assays for Detection and Characterization of Heat-Labile I and Heat-Stable I Genes from Enterotoxigenic Coli. *Enterotoxin Genes from Enterotoxigenic Escherichia coli* **2004**, 225. <https://doi.org/10.1128/JCM.42.9.4092-4100.2004>.
- (13) Persson, S.; Olsen, K. E. P.; Scheutz, F.; Krogfelt, K. A.; Gerner-Smidt, P. A Method for Fast and Simple Detection of Major Diarrhoeagenic Escherichia Coli in the Routine Diagnostic Laboratory. **2007**. <https://doi.org/10.1111/j.1469-0691.2007.01692.x>.

- (14) Abu-Rabeah, K.; Ashkenazi, A.; Atias, D.; Amir, L.; Marks, R. S. Highly Sensitive Amperometric Immunosensor for the Detection of Escherichia Coli. *Biosens. Bioelectron.* **2009**, *24* (12), 3461–3466. <https://doi.org/10.1016/j.bios.2009.04.042>.
- (15) Yang, L.; Li, Y.; Erf, G. F. Interdigitated Array Microelectrode-Based Electrochemical Impedance Immunosensor for Detection of Escherichia Coli O157:H7. *Anal. Chem.* **2004**, *76* (4), 1107–1113. <https://doi.org/10.1021/ac0352575>.
- (16) Yang, H.; Li, H.; Jiang, X. Detection of Foodborne Pathogens Using Bioconjugated Nanomaterials. *Microfluid. Nanofluidics* **2008**, *5* (5), 571–583. <https://doi.org/10.1007/s10404-008-0302-8>.
- (17) Baccar, H.; Mejri, M. B.; Hafaiedh, I.; Ktari, T.; Aouni, M.; Abdelghani, A. Surface Plasmon Resonance Immunosensor for Bacteria Detection. *Talanta* **2010**, *82* (2), 810–814. <https://doi.org/10.1016/j.talanta.2010.05.060>.
- (18) Nikkhoo, N.; Gulak, P. G.; Maxwell, K. Rapid Detection of E. Coli Bacteria Using Potassium-Sensitive FETs in CMOS. *IEEE Trans. Biomed. Circuits Syst.* **2013**, *7* (5), 621–630. <https://doi.org/10.1109/TBCAS.2013.2276013>.
- (19) Lazcka, O.; Campo, F. J. Del; Muñoz, F. X. Pathogen Detection: A Perspective of Traditional Methods and Biosensors. *Biosens. Bioelectron.* **2007**, *22* (7), 1205–1217. <https://doi.org/10.1016/j.bios.2006.06.036>.
- (20) Zhou, W.; Jimmy Huang, P. J.; Ding, J.; Liu, J. Aptamer-Based Biosensors for Biomedical Diagnostics. *Analyst*. The Royal Society of Chemistry May 6, 2014, pp 2627–2640. <https://doi.org/10.1039/c4an00132j>.
- (21) Sudeep, P. M.; Narayanan, T. N.; Ganesan, A.; Shaijumon, M. M.; Yang, H.; Ozden, S.; Patra, P. K.; Pasquali, M.; Vajtai, R.; Ganguli, S.; Roy, A. K.; Anantharaman, M. R.; Ajayan, P. M. Covalently Interconnected Three-Dimensional Graphene Oxide Solids. *ACS Nano* **2013**, *7* (8), 7034–7040. <https://doi.org/10.1021/nn402272u>.
- (22) Jiang, X.; Zhao, J.; Li, Y.-L.; Ahuja, R. Tunable Assembly of Sp³ Cross-Linked 3D Graphene Monoliths: A First-Principles Prediction. *Adv. Funct. Mater.* **2013**, *23* (47), 5846–5853. <https://doi.org/10.1002/adfm.201301077>.
- (23) Sha, J.; Salvatierra, R. V.; Dong, P.; Li, Y.; Lee, S. K.; Wang, T.; Zhang, C.; Zhang, J.; Ji, Y.; Ajayan, P. M.; Lou, J.; Zhao, N.; Tour, J. M. Three-Dimensional Rebar Graphene. *ACS Appl. Mater. Interfaces* **2017**, *9* (8), 7376–7384. <https://doi.org/10.1021/acami.6b12503>.
- (24) Tuteja, S. K.; Sabherwal, P.; Deep, A.; Rastogi, R.; Paul, A. K.; Suri, C. R. Biofunctionalized Rebar Graphene (f-RG) for Label-Free Detection of Cardiac Marker Troponin I. *ACS Appl. Mater. Interfaces* **2014**, *6* (17), 14767–14771. <https://doi.org/10.1021/am503524e>.
- (25) Yan, Z.; Peng, Z.; Casillas, G.; Lin, J.; Xiang, C.; Zhou, H.; Yang, Y.; Ruan, G.; Raji, A. R. O.; Samuel, E. L. G.; Hauge, R. H.; Yacaman, M. J.; Tour, J. M. Rebar Graphene. *ACS Nano* **2014**, *8* (5), 5061–5068. <https://doi.org/10.1021/nn501132n>.
- (26) Sefah, K.; Shangquan, D.; Xiong, X.; O'Donoghue, M. B.; Tan, W. Development of DNA Aptamers Using Cell-SELEX. *Nat. Protoc.* **2010**, *5* (6), 1169–1185. <https://doi.org/10.1038/nprot.2010.66>.
- (27) Fortebio. *Amine Reactive Second-Generation (AR2G) Biosensors | Molecular Devices*.
- (28) Fluorescein (FITC) | Thermo Fisher Scientific - IN <https://www.thermofisher.com/in/en/home/life-science/cell-analysis/fluorophores/fluorescein.html> (accessed Oct 23, 2020).
- (29) GraphPad Prism 7 Curve Fitting Guide - Equation: One site -- Specific binding https://www.graphpad.com/guides/prism/7/curve-fitting/reg_one_site_specific.htm (accessed Oct 23, 2020).
- (30) Qiagen. QIAprep Miniprep Handbook. *QIAprep Miniprep Handb.* **2012**, No. May, 1–44.
- (31) Thermo Scientific InsTAclone PCR Cloning Kit.
- (32) Sanger Sequencing Steps | DNA Sequencing | Sigma-Aldrich <https://www.sigmaaldrich.com/technical-documents/articles/biology/sanger-sequencing.html> (accessed Oct 22, 2020).
- (33) Zuker, M. Mfold Web Server for Nucleic Acid Folding and Hybridization Prediction. *Nucleic Acids Res.* **2003**, *31* (13), 3406–3415. <https://doi.org/10.1093/nar/gkg595>.
- (34) Antczak, M.; Popena, M.; Zok, T.; Sarzynska, J.; Ratajczak, T.; Tomczyk, K.; Adamiak, R. W.; Szachniuk, M. New Functionality of RNAComposer: An Application to Shape the Axis of MiR160 Precursor Structure. *Acta Biochim. Pol.* **2016**, *63* (4), 737–744. https://doi.org/10.18388/abp.2016_1329.
- (35) Kikin, O.; D'Antonio, L.; Bagga, P. S. QGRS Mapper: A Web-Based Server for Predicting G-Quadruplexes in Nucleotide Sequences. *Nucleic Acids Res.* **2006**, *34* (Web Server), W676–W682. <https://doi.org/10.1093/nar/gkl253>.
- (36) Kumar, S.; Koh, J. Physicochemical and Optical Study of Chitosan-Terephthaldehyde Derivative for Biomedical Applications. *Int. J. Biol. Macromol.* **2012**, *51* (5), 1167–1172. <https://doi.org/10.1016/j.ijbiomac.2012.09.001>.
- (37) Labib, M.; Zamay, A. S.; Kolovskaya, O. S.; Reshetneva, I. T.; Zamay, G. S.; Kibbee, R. J.; Sattar, S. A.; Zamay, T. N.; Berezovski, M. V.; Zheleznyaka str, P. Aptamer-Based Viability Impedimetric Sensor for Bacteria. *Anal. Chem.* **2012**, *84*, 16. <https://doi.org/10.1021/ac302902s>.
- (38) Principle, C.; Protocols, C. Thermo Scientific CloneJET PCR Cloning Kit. **2016**, 2016 (November), 1–2.
- (39) Mallikaratchy, P. Evolution of Complex Target SELEX to Identify Aptamers against Mammalian Cell-Surface Antigens. *Molecules* **2017**, *22* (2), 1–12. <https://doi.org/10.3390/molecules22020215>.
- (40) Ferrari, A.; Robertson, J. Interpretation of Raman Spectra of Disordered and Amorphous Carbon. *Phys. Rev. B - Condens. Matter Mater. Phys.* **2000**, *61* (20), 14095–14107. <https://doi.org/10.1103/PhysRevB.61.14095>.



Chapter 3

*Nanostructured
aptasensor for
enterohemorrhagic
E. coli*



Chapter 3

Nanostructured aptasensor for enterohemorrhagic

E. coli

This chapter's contents are adapted from: **Kaur, H.**; Shorie, M.; Sabherwal, P. *Electrochemical aptasensor using boron-carbon nanorods decorated by nickel nanoparticles for detection of E. coli O157:H7*. *Microchim. Acta* 2020, 187 (8), 461.

3.1 Introduction

Diarrheal disease alone is responsible for 1.5 million deaths every year, and enterohemorrhagic *E. coli* (EHEC) is responsible for the most frequent diarrheal outbreaks, worldwide^{1,2}. EHEC includes > 100 serotypes that produce Shiga-like toxins (Stx), which show close identity to the enterotoxins produced by *S. dysenteriae* Type 1 and are classified as Shiga toxin-producing *E. coli*. These enteric bacteria are responsible for bloody diarrhea without fever, and thus since these common symptoms are suggestive of various noninfectious etiologies, an EHEC infection should be considered in suspected cases of ischemic colitis, or inflammatory bowel disease³. Bovine animals and farm animals are the main reservoirs of these EHEC bacteria, with significant outbreaks linked to the consumption of infected undercooked meat products or raw vegetables⁴.

3.1.1 Target bacteria *E. coli* O157:H7 - A background

The first case of *E. coli* serotype O157:H7 infection was reported in 1982 in the US and isolated from the stool⁵. *E. coli* O157:H7 produces enterotoxin Stx and may lead to severe complications like hemorrhagic uremic syndrome in conjunction with thrombotic thrombocytopenic purpura, leading to permanent kidney damage. *E. coli* O15:H7 has been studied to emerge from three evolutionary events viz., (i) insertion of *stx* phage gene, (ii) acquisition of pO157 carrying various virulent genes like hemolysin and adhesins, (iii) deletion of the beta-glucuronidase gene or activity^{3,6}. The most prevalent toxic strain of EHEC group - *E. coli* O157:H7 has infectious dose as low as 100 cells which can be transmitted *via* water bodies contaminated with fecal matter & raw/undercooked food items^{7,8}. Currently, no vaccine or therapy is available for EHEC infections, and since the use of antibiotics worsens Shiga toxin-mediated systemic toxicity in humans, the mainstay treatment is supportive⁹. Considering the extent of potable water contamination, detection, and correct identification of pathogens at an early stage is critical to evade an epidemic.

3.1.2 The need for improved sensing platform

Conventionally used approaches for *E. coli* detection include culturing, biochemical analysis, enzyme-linked immunosorbent assay, and others mentioned in Chapter 1, Section 1.3, though are

routinely used by established clinical labs for detection of bacterial pathogens but require extensive sample enrichment to have a detectable bacterial load, and have long detection periods ranging in days. Thus, there is a dire need for the development of diagnostic methods with shorter detection times without compromising the selectivity of the sensors for cross-reactive bacteria in the present scenario. Motivated from our previous study, for the fabrication of a nanostructured aptasensor, we coupled highly specific aptamers generated using microtiter plate-based cell-SELEX with a good electroactive nanomaterial that assists in specific & sensitive recognition of the target pathogen. Voltammetric method for sensing has been chosen due to its highly sensitive nature and ease of operation in case of on-site monitoring with the aid of screen-printed electrodes (SPE). SPE sensors were chosen as they are cost effective, need low sample volume and are easy to use which is desirable in biosensing measurements for point-of care diagnosis. Moreover, a microfluidics-based chip for on-site monitoring of *E. coli* O157 cells using aptamer functionalized channel was studied, which is detailed in Section 3.4 of this chapter.

3.1.3 Objectives

- (i) **Bio-receptor development:** Development of specific aptamer-based receptors against selected *E. coli* O157:H7 using whole-cell target approach.
- (ii) **Transducer synthesis:** Synthesis of doped carbon nanostructured material for modification of the electrochemical electrode surface.
- (iii) **Aptasensor fabrication:** Functionalization of generated high-affinity aptamers onto electrically active nanostructures for apta-assay.
- (iv) **Platform validation:** Testing & validation of aptasensor in spiked food & environmental samples.

3.1.4 Proposed biosensing platform for *E. coli* O157:H7

3.1.4.1 Preface

Aptamers confer high selectivity and sensitivity on electrochemical platforms and have been hailed as competitors to immunoassays in the past decade. The coupling of highly specific aptamers with electroactive materials assists in specific and sensitive target bacteria's recognition with prior enrichment from samples. Since the discovery of carbon nanotubes, many researchers have paid great attention to the synthesis & properties of similar one-dimension materials, such as BN nanotubes and BCN nanotubes enhanced electronic properties¹⁰⁻¹². The thermal substitution of boron in carbon lattice has been successfully shown to confer better conductive & electrochemical properties¹³. Ni nanoparticle infusion with carbon confers faster charge transport and highly conductive structural support to the nanomaterial¹⁴⁻¹⁶.

3.1.4.2 Our aptasensing approach: Whole-cell

Exploiting the excellent properties of these hybrid nanomaterials for detecting bacterial pathogenesis, we have synthesized boron-carbon nanorods decorated with nickel nanoparticles (BC-Ni nanorods) with excellent electrochemical ability to transduce the interaction of specific aptamer with *E. coli* O157:H7 effectively in water and juices samples (Figure 3.1). We have screened anti-*E. coli* O157:H7 DNA based aptamers selected by in-vitro microplate-based cell-SELEX methodology explored in the previous chapter, which has been tuned to increase bio-receptor specificity against the target pathogen by counter-screening against closely related bacterial species. Alongside the implementation of BC-Ni nanorods harboring superior transducing properties has been utilized to fabricate aptasensor, which assists in sensitive recognition. This synergistic approach allows rapid, sensitive and economical diagnosis of pathogenic bacteria, which can be tuned further to monitor other microbial infections.

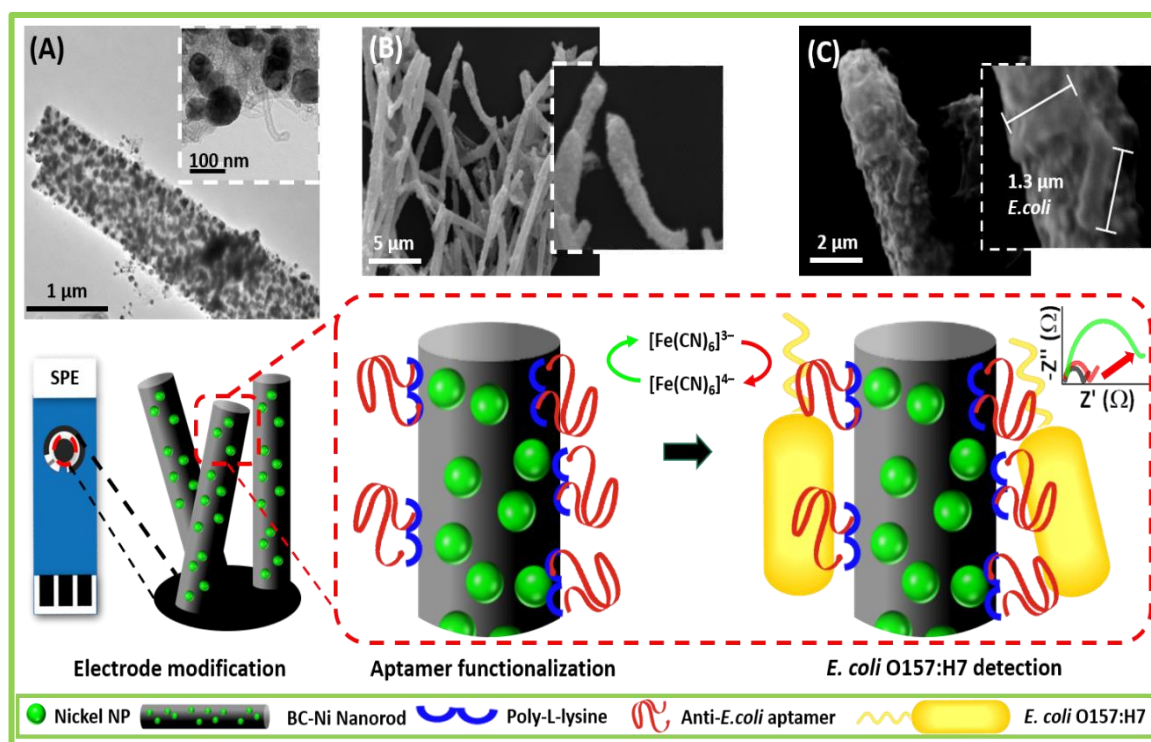


Figure 3.1: Schematic: Diagrammatic illustration showing the modification of the electrode with the developed nanomaterial accompanied by (A) HR-TEM image of BC-Ni nanorods, (B) SEM image of BC-Ni nanorods and (C) bacteria adhered to its surface upon exposure.

3.1.4.3 The novelty of experimental work

- (i) **Bio-receptor:** Specific high-affinity aptamer for *E. coli* O157:H7 whole cell using a Phenylboronic acid-coated microtiter plate for immobilization and aptamer selection tuned to increase the specificity by counter-screening against closely related bacterial species.

- (ii) **Nanostructures:** The implementation of 1D BC-Ni nanorods harboring superior transducing properties in the fabrication of aptasensor assists in sensitive and highly specific recognition.

3.2 Experimental procedure

3.2.1 Aptamer technology: Cell-SELEX for *E. coli* O157:H7

3.2.1.1 Materials

(A) Chemicals & reagents

Phenylboronic acid 95% (PBA), 3-Aminophenylboronic acid monohydrate 98% (APBA), 4',6-diamidino-2-phenylindole (DAPI), 4-Morpholineethanesulfonic acid (MES) buffer, PCR mastermix (2x), PCR grade Dimethyl sulfoxide (DMSO), Streptavidin-Gold from *Streptomyces avidinii* and Poly-L-lysine solution 0.1% w/v in water (PLL) were procured from Sigma-Aldrich (India). *N*-Ethyl-*N'*-(3-dimethylaminopropyl) carbodiimide hydrochloride (EDC), *N*-Hydroxy succinimide (NHS) were purchased from Merck (India). Glycine, Magnesium chloride, Tris base, Tris-HCl, Tryptone soya broth (TSB), and Luria Bertani agar (LB) were purchased from Himedia (India). Nunc Maxisorp F96 microtitre plates and InsTAclone PCR cloning kit from Thermo Fisher Scientific (India) and QIAprep spin miniprep kit from Qiagen (USA) were used the studies. All solutions were prepared with autoclave sterilized deionized Milli Q water (18 M Ω ·cm) and used for rinsing steps to avoid any contamination. The DNA naïve library and primers for SELEX mentioned in Chapter 2, Section 2.2.1.1, were employed in this study also.

(B) Bacterial culture

An avirulent strain of *E. coli* serotype O157:H7 [*E. coli* (Migula) Castellani and Chalmers (ATCC® 43888™)] was procured from HiMedia Laboratories (India).

3.2.1.2 Growth & optimization of *E. coli* O157:H7 culture

The conditions for the growth of the target organism *E. coli* O157:H7 were optimized at 37°C in LB medium, and fresh bacteria were cultured before each experiment. The bacterial cells are harvested by centrifugation at 2500×g for 10 min to form a soft pellet and washed with sterile binding buffer thrice. The washed pellet is finally resuspended in buffer at the optical density (OD_{600nm}) set close to ~1.0. Further desired dilutions for sensing experiments were made in the same.

3.2.1.3 Aptamer selection & characterization for *E. coli* O157:H7

The PBA mediated cell-SELEX methodology mentioned in Chapter 2, Section 2.2.1.3.2, was explored herein to select aptamers specific for *E. coli* O157:H7. The cell-SELEX iterative rounds consisting of binding, elution, amplification & partitioning were carried out using a facile approach previously developed by us, employing PBA functionalized microtiter plate to capture bacteria

generation of specific aptamers. For specific customized aptamer selection against our selected target pathogen, the ssDNA binder population obtained from the SELEX round was subsequently used for exposure to immobilized *E. coli* O157:H7 an increment in the number of wells in every round was done to increase the propensity of good binder sequences. For the positive iteration screening rounds, *E. coli* O157:H7 was immobilized onto the well surface and counter-screening rounds against other enteric bacteria viz., *E. coli* DH5 α , *E. coli* O78:H11, *E. aerogenes*, *C. freundii*, *S. sonnie*, *S. boydii*, *S. enterica*, *L. monocytogenes* and *L. sakei* which is present are food matter^{17,18}. In addition to these SELEX steps against the target cell, the counter-selection is carried out to eliminate the non-specific binders to other related bacterial species. Herein, the cross-related species are incubated with oligomers instead of the target, and those binding to these cross-related species are washed off and eliminated from the DNA pool used for next selection rounds. This addition of a counter-selective step gives an edge over other receptor generation technologies, eliminating DNA aptamers recognizing species other than the target, and aids in the generation of highly specific aptamers. A final positive screening round was performed to amplify and confirm the counter-screened binder population binding to target *E. coli* O157:H7. Similarly, as mentioned in Chapter 2, Section 2.2.1.3.3, the quantity and purity of the binder population after each SELEX round was assessed spectroscopically at 260 nm, and 260/280 and 260/230 ratio were measured to evaluate DNA quantity and quality.

3.2.1.4 Aptamer-*E. coli* O157:H7 bio-interaction studies

The affinity between the aptamer fraction screened and *E. coli* O157:H7 was validated with Biolayer Interferometry (BLI) kinetic studies and fluorescence saturation binding assay. The detailed protocol has been mentioned in Chapter 2, Section 2.2.1.3.3, while the optimizations were done, keeping into consideration the target pathogen.

(A) BLI kinetic studies

The binding of anti-*E. coli* O157 aptamer with *E. coli* O157:H7 was confirmed with BLI Octet system. For studying this interaction, biotin-labeled reverse primer (100 μ M) having complementarity with 3' end of aptamer, acted as tethering DNA and was loaded onto streptavidin biosensor (SSA) after 600 s incubation to achieve maximum loading. This primer functionalized sensor was dipped into stock aptamer solution till a loading plateau was observed, followed by washing with the binding buffer to remove unbound sequences. This anti-*E. coli* O157 aptamer modified sensor was then made to interact with increasing dilutions of *E. coli* O157:H7 cells (0, 1×10^3 , 0.25×10^4 , 1×10^4), and the respective association/dissociation kinetics was carried out to determine bio-interaction between the screened aptamer and *E. coli* O157:H7.

(B) Fluorescence binding studies

A binding fluorescence saturation assay was performed. *E. coli* O157:H7 was immobilized on the microtiter plate and was incubated with an increasing amount of FITC-labelled ssDNA (0, 0.01,

0.10, 1, 10, 100, 1000, 1000 nM) in 100 μ L of binding buffer for an hour at 25°C. The wells were washed off to remove unbound aptamer molecules, and fluorescence signal intensity of FITC was measured using a microtiter plate reader (BioTek Synergy H1, USA) at $\lambda_{\text{excitation}}=485$ and $\lambda_{\text{emission}}=525$ nm wavelengths. The dissociation coefficient (K_d) of aptamer was assessed by plotting fluorescence signal intensity against DNA concentration and fitted with a non-linear model of specific binding using GraphPad Prism 7.01 software. The K_d was calculated using the equation $Y = B_{\text{max}}X/(K_d + X)$, where B_{max} is maximal fluorescence intensity, X is the concentration of the aptamer, and Y is mean fluorescence intensity¹⁹.

The final elute fraction of the oligomer having the aptamer was inserted in pTZ57R/T vector and transformed into competent *E. coli* DH5 α cells using the InsTAclone PCR cloning kit (Thermo Scientific, USA). The transformed cells were screened using XGal/IPTG for positive white colonies, further sub-cultured to eliminate false positives, and then the positive clones were outsourced for sequencing using the Sanger method²⁰. The deduced sequences were later evaluated using online bioinformatics tools, as mentioned in Chapter 2, Section 2.2.1.3.3., for putative structural and thermodynamic properties. This well-characterized aptamer was used for further functionalization of the nanomaterial for the fabrication of electrochemical SPE based aptasensor for *E. coli* O157:H7 detection.

3.2.2 Nanostructured biosensing platform

3.2.2.1 Materials

NiCl₂.6H₂O, dimethylglyoxime (DMG), and phenylboronic acid 95% (PBA) were purchased from TCI Chemicals (India). Potassium ferrocyanide (K₄[Fe(CN)₆].3H₂O), potassium ferricyanide (K₃[Fe(CN)₆]), and poly-L-lysine solution 0.1% in water (PLL) were procured from Sigma-Aldrich (India). TE 100 screen-printed carbon electrodes (SPE) were products of CH Instruments (USA).

3.2.2.2 Nanostructure synthesis: BC-Ni nanorods

The nanostructure was developed for modification of the electrode surface for enhanced electrochemical response and as well as to facilitate optimal functionalization of the aptamer onto the sensor. BC-Ni nanorods were synthesized by modification of a previously reported method^{21,22}. This synthesis process was divided into two steps, as illustrated in Figure 3.2.

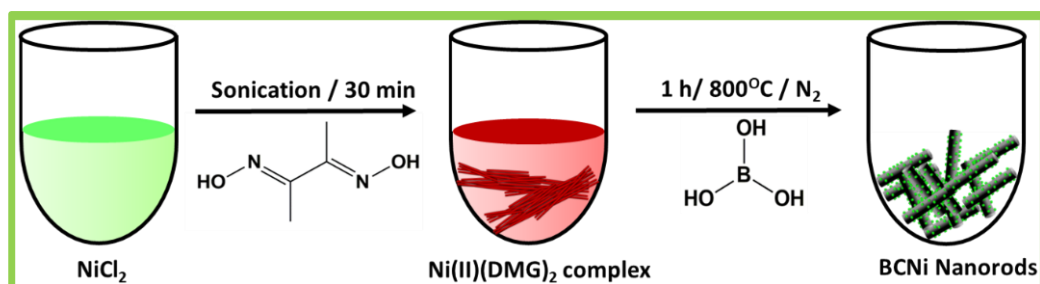


Figure 3.2: Synthesis of BC-Ni nanomaterial: A schematic showing synthesis protocol of BC-Ni nanorod synthesis.

(i) Ni(II)-DMG complex synthesis

Here, 500 mL aqueous solution of NiCl₂·6H₂O (2.5 mg mL⁻¹) was prepared, and 10 mg mL⁻¹ ethanolic solution of dimethylglyoxime (DMG) (pH 13) was added slowly to it with constant sonication using a bath sonicator. The brick-red adduct was allowed to sonicate for an hour at 37°C and then filtered using Whatman paper No.1 and residue is dried at 65°C overnight.

(ii) BC-Ni adduct synthesis

Ni(II)-DMG complex was mixed boric acid in 1:10 w/w ratio and slowly heated at 65°C overnight. The ratio was optimized to maximize boron doping in the synthesized carbon nanotubes. The BC-Ni mixture thus, formed was calcined in an inert atmosphere for an hour at 800°C under N₂ atmosphere.

3.2.2.3 Nanostructures & modified sensor characterization

These synthesized BC-Ni nanorods were characterized by various spectroscopic and microscopic analytical techniques viz., X-ray diffraction (XRD), Fourier transform infra-red (FT-IR) spectroscopy, Raman spectroscopy, Brunauer-Emmett-Teller (BET), scanning & transmission electron microscopy (SEM & TEM), and Zeta-potential (ζ) dynamic light scattering (DLS). The instrumental details have been mentioned in detail in previous Chapter 2, Section 2.2.2.3, which employ overlapping characterization techniques. These respective techniques are given in brief as follows:

(A) X-ray diffraction

XRD (Bruker; D8 Advance X-ray diffractometer) diffraction patterns using Cu K α ($\lambda = 1.54 \text{ \AA}$) radiation covering a wide-angle range from 10–80° to elucidate the crystalline structure of the nanomaterial.

(B) FT-IR and Raman spectroscopy

FT-IR (Agilent; Cary660 FTIR) spectral scan from 400 - 4000 cm⁻¹ with a resolution of 0.5 cm⁻¹ to provide wide range of observation with distinct peaks for characteristic vibrational bonds and surface functional groups and Raman spectrum (WITEC; α 300R) at an low integration time of 1s using 532 nm Nd:YAG laser source for observing vibrational bonds and functional groups in the nanomaterial.

(C) Surface area and pore size distribution

BET (Nova Quantachrome Autosorb iQ) employing Brunauer–Emmett–Teller & Barrett-Joyner-Halenda (BJH) methods for studying surface area and pore size distribution using N₂ at 77 K (liquid nitrogen as adsorbate) with prior degassing of a synthesized nanomaterial at 393 K (to remove other adsorbed gases) for prolonged 12 h.

(D) Surface morphology

SEM (JEOL; JSM IT300) with an acceleration voltage of 20 kV for morphological study of the nanomaterial, as well as bio-interface for bacterial attachment (gold alloy coating) which is

equipped with an energy-dispersive X-ray (EDX) for elemental mapping and TEM (JEOL; JEM 2100) for high-resolution imaging at an acceleration voltage of 200 kV for high resolution nanomaterial visualization.

(E) Nanostructure electrochemical characteristics

The well-characterized nanomaterial was then further used to modify working electrode and electrochemical characterizations, i.e., voltammetry & impedance measurements carried out using the CHI760E electrochemical workstation. The CV experiments were conducted using a scan rate of 100 mV s^{-1} and full potential sweep from -1 to +1 V and the EIS measurements in the frequency range of 100 kHz-10 Hz using an alternative voltage of 0.25 V amplitude²³. For EIS, the obtained Nyquist plot was fitted using a modified Randles–Sevcik circuit and R_{ct} recorded for each concentration of target pathogen. All the electrochemical measurements were performed with thrice using 100 mM PBS buffer solution containing 2.5 mM $\text{K}[\text{Fe}(\text{CN})_6]^{3-/4-}$ redox pair (equimolar ratio)²³. The concentration of redox pair was chosen to obtain high conduction response on the sensor surface in presence of large moieties like bacterial cell. For our sensor fabrication, the amount of BC-Ni nanorods deposited onto the working electrode of SPE was optimized by CV measurements, and the electrochemical stability of modified SPE was tested by repeated cycling (50 cycles). BC-Ni nanorods were used to modify the working electrode of SPE. The BC-Ni concentration was optimized via a gradual increase in the nanomaterial drop-casting quantity onto SPE and annealing at 60°C for an hour. The EIS measurements of the modified electrode were recorded to characterize the impedance of the nanostructure modified electrode surface.

(F) Nanosensor electrochemical assay

For aptamer functionalization onto BC-Ni nanorods, the working electrode was first modified with optimized PLL concentration ($0.001\% \text{ w v}^{-1}$) and subsequently with $200 \mu\text{g mL}^{-1}$ amplified aptamer stock for functionalization of the sensor surface, which was incubated overnight at 4°C. The volume was optimized at $10 \mu\text{L}$, which provided coverage for the working electrode, without leading to fouling. The sensor surface was rinsed to remove any loosely bound aptamer molecules, and this apta-modified nanosensor was used to assess the absence or presence of bacterial cells in subsequent studies. This aptamer functionalized nanostructured SPE was exposed to *E. coli* O157:H7 concentrations ranging from 0 to 10^6 cfu to study the range of detection of the developed aptasensor. The experimental impedance spectra are plotted as a Nyquist plot (Z' vs. $-Z''$), leading to the formation of a partial semi-circle curve at high frequencies with the intercept with Z' axis on the right-side denoting R_{ct} . To mitigate current response deviation from other instrumental faradic processes, Randles-Sevcik equivalent circuit model was used for fitting experimental data. For real spiked samples of water and juices, the similar pre-processing methodology employed in Chapter 2, Section 2.2.2.4, was used.

3.3 Results & discussion

3.3.1 Optimization of *E. coli* O157:H7 culture

The conditions for the growth of the target organism *E. coli* O157:H7 were optimized at 37°C in LB medium and prepared fresh bacteria culture before each experiment. The washed pellet is finally resuspended in buffer at the optical density (OD_{600nm}) set close to ~1.0. Further desired dilutions for sensing experiments were made in the same buffer and visualized using SEM (Figure 3.3). The molecular composition of the bacterial cell surface is in constant dynamics with its growth phase. Thus, to optimize and maintain continuity amongst various studies, all the experiments were carried out using cells harvested at exponential phase.

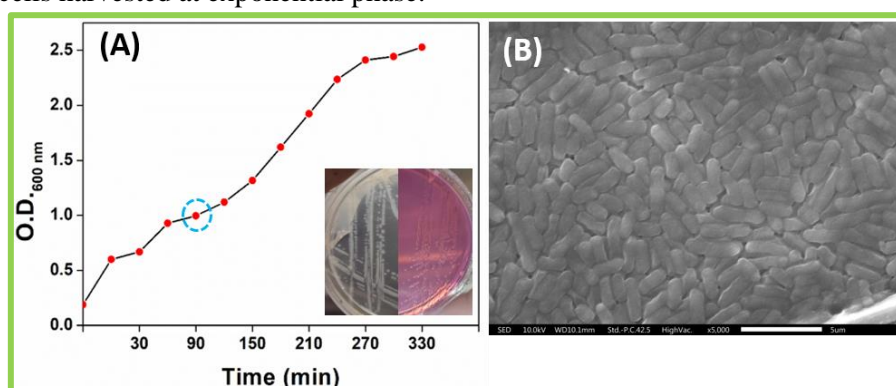


Figure 3.3: Growth curve: (A) Curve showing growth kinetics of *E. coli* O157:H7 and (inset) visual image of the pure culture grown on LB showing translucent white colonies and on SMAC showing transparent colonies. (B) SEM image of the pure culture harvested.

3.3.2 Aptamer technology

3.3.2.1 Anti-*E. coli* O157:H7 aptamer characterization

(A) SELEX progression

Anti-*E. coli* O157:H7 aptamer was screened using PBA coated microtiter plate following the methodology described in the previous Chapter, Section 2.2.1.3.2. The ssDNA library containing a 45-nt random region flanked by an 18-nt fixed region (for PCR amplification) was exposed to the target STEC bacteria immobilized on PBA functionalized microtiter plate, and the binding oligomer fractions were pooled, amplified, and re-exposed till a good affinity oligomer fraction, aptly labeled as 'aptamer,' was screened out. The negative selection against closely related bacterial strains to the target species aids in countering cross-reactivity and hence increases the aptamer pool's selectivity for the target. The assessment of iterations of SELEX rounds shown in Figure 3.4 was done by measuring the quantity and quality of DNA after each SELEX round at 260 nm, which showed a gradual increase in the amount of DNA binding to target cells after each iteration (1 - 5th round) and during counter-selection (6 - 14th round) the bound oligomer fraction was discarded. The unbound pool was enriched and used for exposure to the next round. A positive selection round (15th) was carried after series of positive and negative iterations, to validate that the aptameric pool

is successfully interacting with our target STEC strain and deduce its binding affinity. Though the inclusion of multiple negative iterations in the SELEX, lengthens the process, but it significantly aids in eliminating oligomers that show abundant cross-reactivity with other microorganisms. As shown in Figure 3.4(A), many cross-reactive organisms showed binding with the aptamer pool during screening (denoted in red), which in the case of other selection methodologies, would have gone through without any filtering effect and resulted in broader non-specific sensing of the microbes present in the biological or environmental samples.

(B) Fluorescence saturation assay

As shown in Figure 3.4 (B), K_d of FITC labeled DNA aptamer was estimated by plotting the fluorescence signal intensity obtained from increasing concentration of aptamer bound to cells immobilized on a microtiter plate and using a non-linear fit model of specific binding. A fluorescence saturation curve was obtained, and the dissociation constant K_d was calculated to be 69.73 nM²⁴. This nanomolar affinity is at par with commercially available antibodies and other reported aptamers^{25,26}.

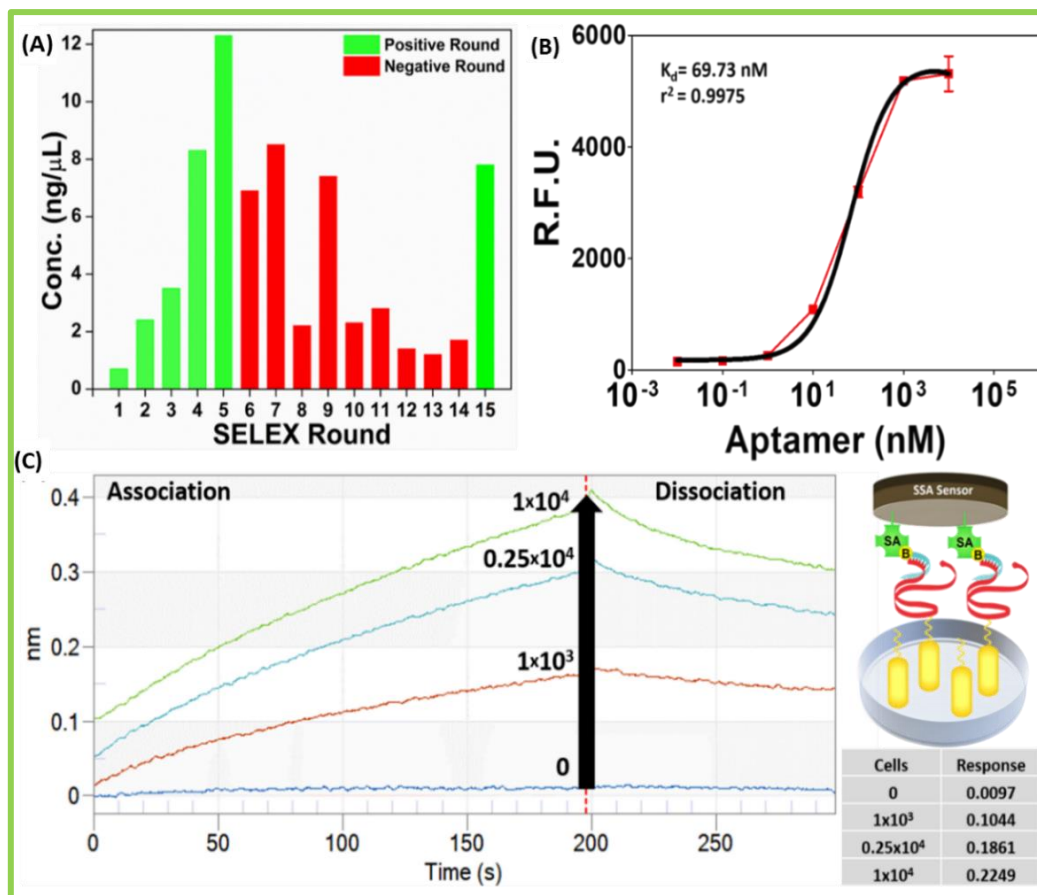


Figure 3.4: Aptamer characterization: (A) SELEX progression monitored by recording ssDNA concentration of elutes at positive (green) and negative (red) round. (B) Fluorescence binding curve of selected aptamer with EHEC bacteria and (C) using BLI platform showing good kinetics.

(C) BLI kinetics studies

Alongside, the interaction of generated anti-*E. coli* aptamer with bacteria was gauged by BLI using biotinylated aptamer functionalized SSA sensors. An overlay of sensograms, as shown in Figure

3(C), denotes a proportional increase in optical thickness at the biosensor tip surface with increasing concentrations of cells being exposed to aptamer coated tip and is indicative of sufficient binding between bacteria & aptamer.

3.3.2.2 Aptamer sequence & structure

The ligated pTZ57R/T plasmid with the aptamer insert was transformed into chemically competent *E. coli* DH5 α cells, and the positive Amp-resistant white colonies obtained on X-gal/IPTG supplemented LB agar plates colonies as shown in Figure 3.5, further sub-cultured to eliminate false positives and then the positive clones were chosen, plasmid purified and outsourced to sequences were obtained via sanger sequencing²⁰.

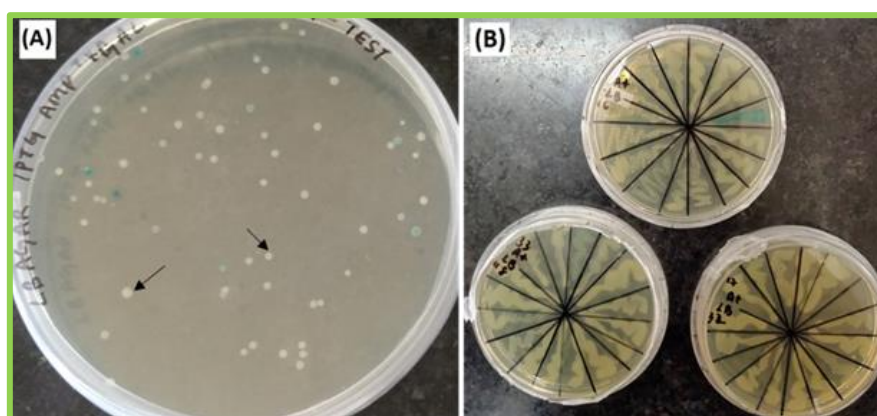


Figure 3.5: Blue-white screening: Cells transformed with aptamer sequences were plated and (A) screened for positive (white) colonies and the positive clones (B) sub-cultured to remove false-positive sequences and then sent for sequencing.

The aptamer sequences for clones were then used to predict the secondary structure of the same using free online webserver ‘mfold’ (Figure 3.6). Out of the clones deduced, the propensity of the sequences conforming to be G-quadruplex was analyzed using an online available software program- QGRS tool to predict the presence of G-quadruplex forming regions. The sequence: - ATCCAGAGTGACGCAGCAGGGTGGCGAGACTGGGCGGGTGTCTGGGAAGTGAACCGTGGCGTGTGGACACGGTGGCTTAGT-3’

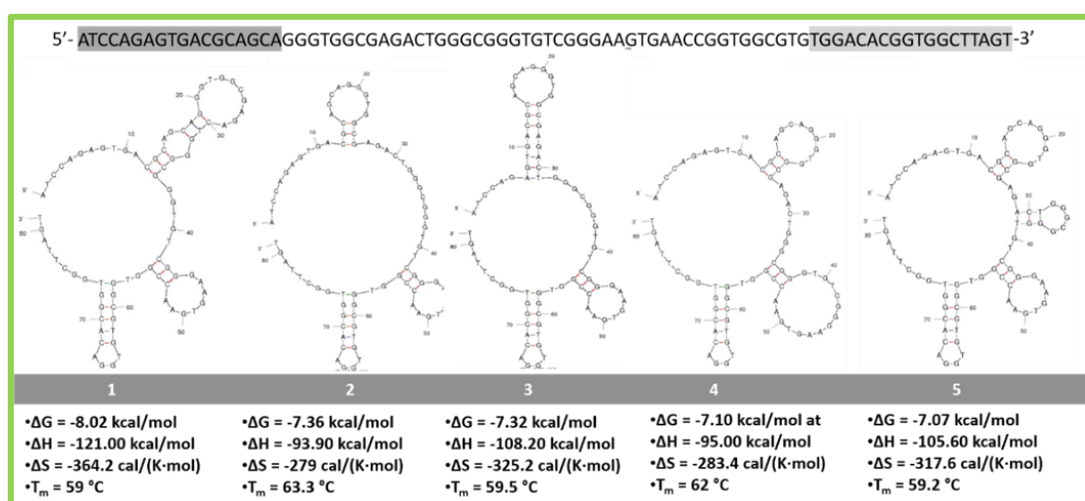


Figure 3.6: Mfold results: Putative secondary structures of *E. coli* DNA aptamer predicted using the mfold online tool along with their various thermodynamic parameters.

TGGCGTGTGGACACGGTGGCTTAGT- showing the best G-score of 33 (two or more G-tetrads) was chosen and its various secondary structures along with their thermodynamic stability of folding. The aptamer structure showed significant helical regions and loop-stem folding, particularly G-quadruplex motifs starting from N-19 & N-58. Furthermore, the 3D rendering of the aptamer structure was done using an RNA composer modeling server and visualized using PyMOL, validating the aptamer's structural complexity (Figure 3.7).

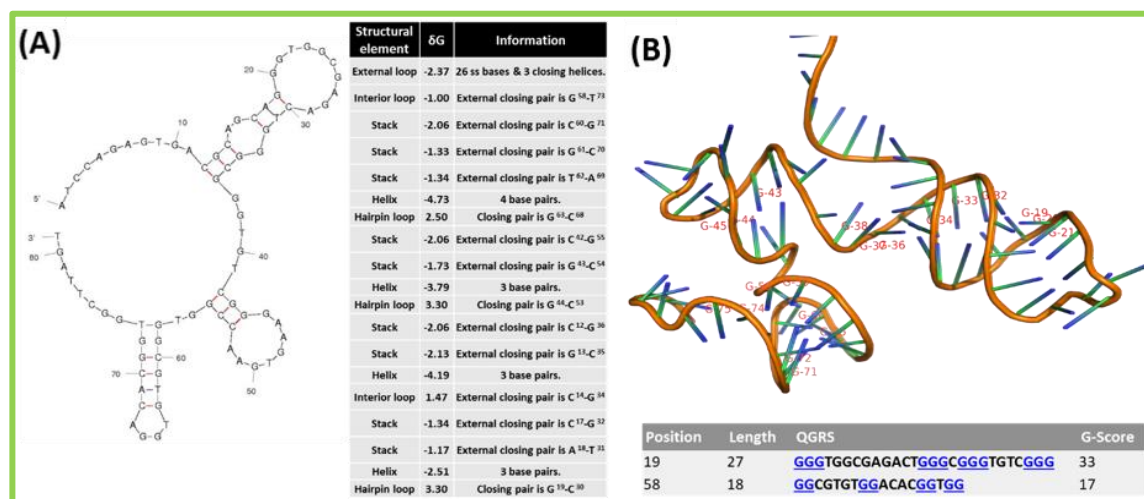


Figure 3.7: Putative aptamer structure: The secondary structure determined using mfold server having the lowest ΔG value, along with its structural motifs and the 3D structure determined using RNA composer, with red highlighted G-quad regions.

3.3.3 Nanostructure synthesis & characterization

3.3.3.1 Synthesis of nanomaterial: BC-Ni nanorods

BC-Ni was synthesized by a two-step carbonization method using Ni(II)-DMG complex and boric acid as reaction precursors. The synthesis of Ni(II)-DMG complex from NiCl₂ (pale green) and DMG (white translucent) resulted in the formation of a complex with red, flaky precipitates. As mentioned in Section 3.2.1.2, the complex admixture with boric acid was calcined in a tube furnace at 800°C resulting in a black colored BC-Ni compound, which was further characterized and used in studies. Change in the coloration of the precursor from brick red to a black product can be visually seen by the naked eye (Figure 3.8)



Figure 3.8: Color change: (A) Ni(II)-DMG complex with a red brick appearance and (B) BC-Ni nanorods product after carbonization.

3.3.3.1.1 Scanning electron microscopy

Figure 3.9 shows the SEM micrographs of nickel and boron infused nanorods with the lateral dimensions of 300 ± 150 nm and longitudinally ranging from 6 to 10 μm , and its further elemental analysis showed weight percentage distribution of boron, carbon, and nickel as 7.7%, 50.3%, and 41%, respectively.

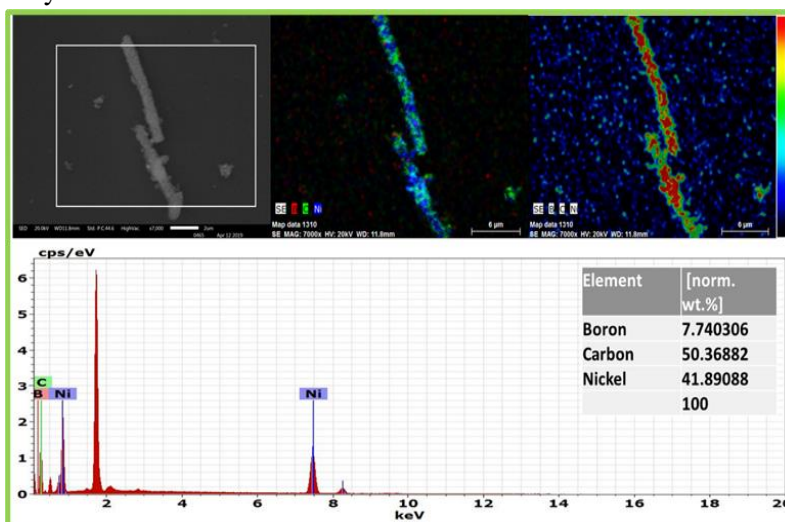


Figure 3.9: Synthesis of BC-Ni nanomaterial: The SEM images of the calcinated nanomaterial along with its EDX spectrum.

3.3.3.1.2 Transmission electron microscopy

In micrographs shown in Figure 3.10, it can be observed that the longitudinal rod-like morphological structure of BC-Ni had been inherited out of its spindle-shaped precursor Ni(II)-DMG suggesting its role as a physical template.

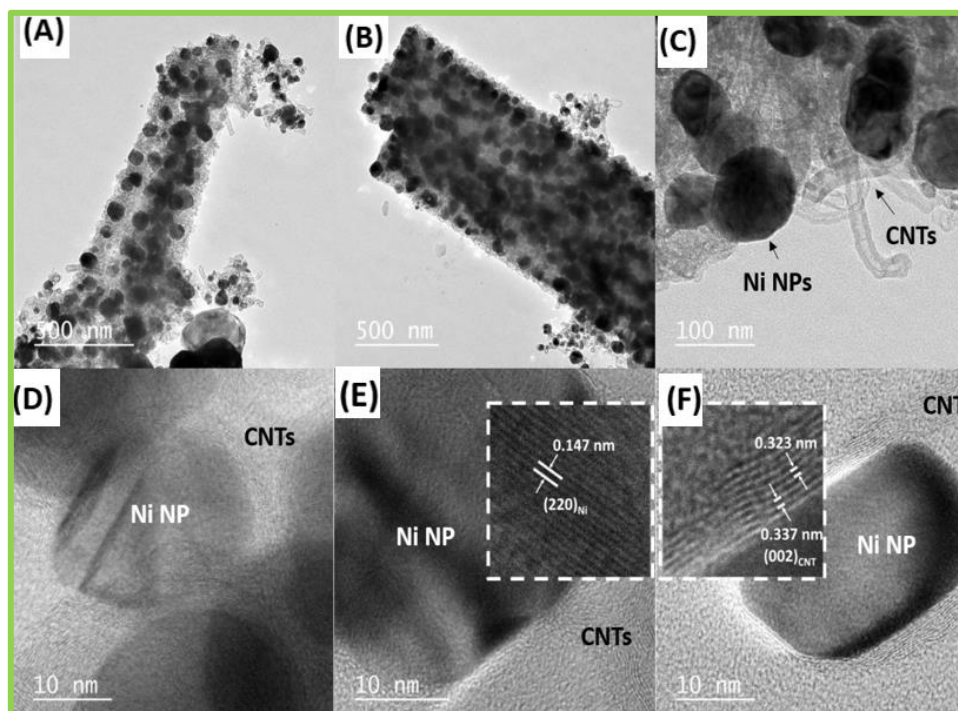


Figure 3.10: TEM micrographs: Showing low and high-resolution TEM images of the Ni-NPs infused bundled nanotube structures.

The carbonization at high temperatures of reactants resulted in the fabrication of bundles of interconnected carbon nanotubes and assisted the thermal substitution of boron. This hierarchical assembly further has metallic character by incorporating nickel nanoparticles (Ni NPs) entrapped in these entangled nanotubes. At high magnification (Figure 3.10 C-D), it was clarified that each nanorod is a bundle of CNTs, and a mesh of CNTs had Ni NPs (ranging from 25-100 nm) incorporated inside it. The presence of Ni (220) was evident from the d-spacing of 0.147 nm upon high-resolution magnification of Ni NPs, and also that of CNT (002) with d-spacing of ~ 0.34 nm and a slightly distorted 0.32 nm was observed (Figure 3.10 E-F). The interplanar spacing in CNTs impregnated with Ni NPs shows lattice distortion due to CNT crystal lattice's contraction upon the growth of metal nanoparticle. In our scientific opinion, these Ni-NPs metal clusters suggestively act as nodes with readily available free electrons for fast transmission through highly conductive nanotube bundles.

3.3.3.2 BC-Ni nanorods characterization

The as-synthesized nanomaterial was characterized using various spectroscopic techniques.

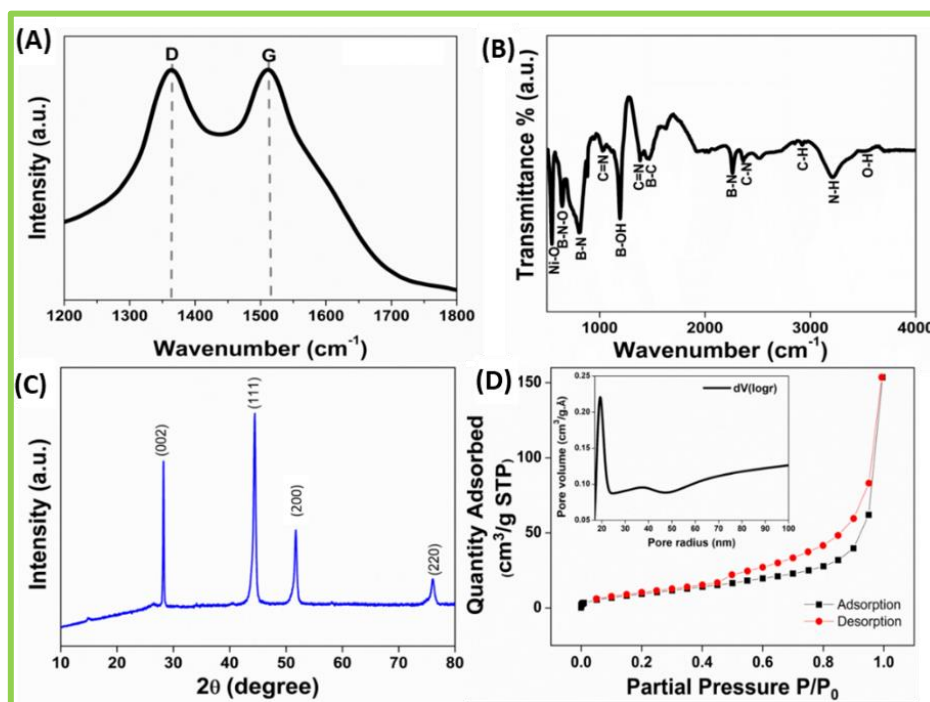


Figure 3.11: Nanomaterial characterization: (A) Raman spectrum, (B) FT-IR spectrum, (C) XRD spectrum and (D) BET N_2 adsorption-desorption curve.

(A) Raman spectroscopy

Raman spectroscopic analysis was carried out with the WiTech Raman spectrophotometer at an integration time of 1s using 532 nm Nd:YAG laser source to characterize the BC-Ni nanorods (Figure 3.11 A). These spectroscopic studies indicate BC-Ni nanorods' formation by showing characteristic D & G bands of crystalline carbon, at ~ 1360 cm^{-1} and ~ 1510 cm^{-1} corresponding to A_{1g} and E_{2g} mode^{27,28}. The ratios of normalized intensities of D & G bands for the nanomaterial

was observed to be 0.99, which shows high disorder associated with graphitic natured nanomaterial. This pattern is comparable to that of metallic SWNT, suggesting breathing of sp^2 atoms in rings and bond stretching in both rings and chains²⁹. Further characterizations were carried to ascertain this fact.

(B) FT-IR spectroscopy

The IR spectrum (Figure 3.11 B) recorded by Agilent Cary660 from 400 to 4000 cm^{-1} with a resolution of 0.5 cm^{-1} showed significant characteristic peaks denoting different vibrational modes for B-N stretching (815 cm^{-1} , 2265 cm^{-1}), B-N-O stretching (660 cm^{-1}), C-N (2365 cm^{-1}) and C=N (1015 cm^{-1} , 1380 cm^{-1}) stretching, Ni-O (430 cm^{-1}) and N-H (3215 cm^{-1}) stretching. The abundance of these bonds, validate the presence of boron doping in the carbon based nanomaterial and as well as inclusion of nickel nanoparticles, which is in accordance with prior literature³⁰. These functional groups further assist in the increased electroactive response of the nanomaterial during electrochemical studies.

(C) X-Ray diffraction spectroscopy

The XRD spectrum was recorded using Bruker D8 Advance X-ray diffractometer, and diffraction patterns generated using Cu $K\alpha$ ($\lambda = 1.54 \text{ \AA}$) radiation in the wide-angle range (10 – 80°). The diffraction pattern, as observed in Figure 3.11(C), showed sharp peaks at 2θ of 28°, 43°, 51°, and 76° corresponding to (002), (111), (200) and (220) planes respectively. The diffraction peaks at 28° and 43° are reflections of graphitic nature, while 51° and 76° are characteristic diffraction reflections of nickel particles. These are highly suggestive of the crystalline nature of the synthesized nanohybrid material.

(D) BET analysis

To analyze the surface area and pore size distribution BET (Nova Quantachrome Autosorb iQ) employing Brunauer–Emmett–Teller & Barrett–Joyner–Halenda (BJH) methods using N_2 at 77 K with prior degassing of a synthesized nanomaterial at 393 K for 12 h was carried out (Figure 3.11 D). Upon analysis and surveying reference literature, we deduced that the N_2 adsorption-desorption isotherms features a Type IV isotherm associated with capillary condensation taking place in mesopores and a Type H3 hysteresis loop, which is a characteristic of aggregates with slit-shaped pores^{31–33}. The BET surface area of synthesized BC-Ni was calculated to be 59.313 $m^2 g^{-1}$, the pore volume of 0.245 $cc g^{-1}$ and pore radius of 19.080 \AA , indicating high surface area & porosity. This enhancement in surface area and porosity is a highly desirable property for increasing the net electrochemical area on the electrode surface, providing wider range of detection and sensitivity to the bio-assays.

(E) Electrochemical analysis

The electrochemical impedance spectroscopy (EIS) studies were carried out using the CHI760E electrochemical workstation for aptasensor characterization. An initial comparative analysis, result detailed below, to check the electrochemical activity of the precursor, Ni(II)-DMG complex showed

a minimal two-fold increase in electrochemical response with up to 10 μg material drop-casted on the working electrode.

(i) Precursor comparative

The precursor's SEM images showed long flat spindles with sharp edges and the minimal electrochemical response with material drop-casted on the working electrode (up to 10 μg), as seen in the voltammogram (Figure 3.12). A comparative analysis to check the precursor's electrochemical activity, Ni(II)-DMG complex showed a minimal increase from 23 μA of bare carbon electrode to 45 μA in electrochemical response with up to 10 μg material drop-casted on the working electrode.

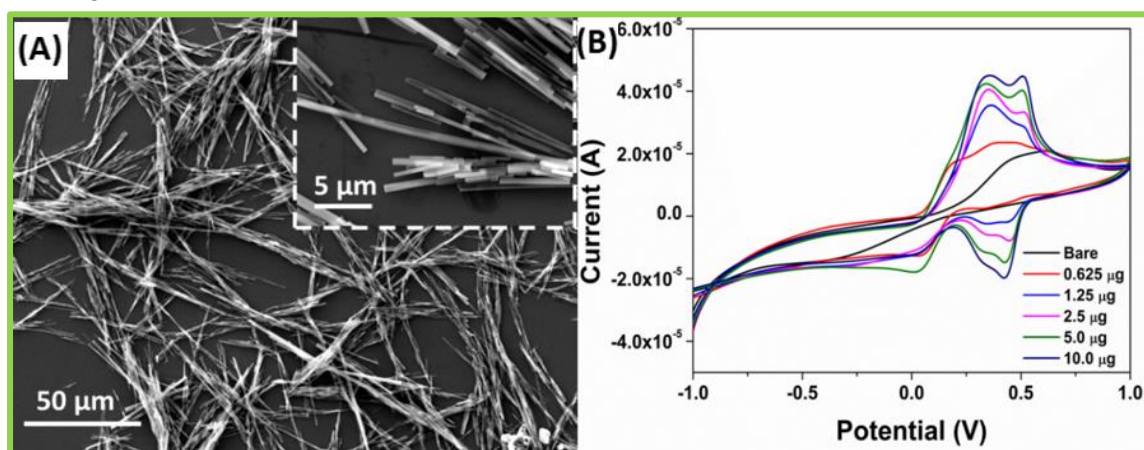


Figure 3.12: Electrochemical characterization of C-Ni: (A) SEM images and (B) CV curves.

(ii) BC-Ni modified SPE

The nanostructured electrode showed a staggering seventeen-fold increase in current response cathodic (I_{pc}) and anodic (I_{pa}) peak current response ($I_{\text{pc}} = 397 \mu\text{A}$, $I_{\text{pa}} = 432 \mu\text{A}$) in comparison to that of the bare electrode ($I_{\text{pc}} = 23 \mu\text{A}$, $I_{\text{pa}} = 25 \mu\text{A}$) suggesting a valid modification of the sensor surface by the synthesized BC-Ni nanorods (Figure 3.13 A-B). The CV curves indicate that the electrochemical signals resulting from the redox probe are based on the nanomaterial's pseudocapacitive behavior. The modified electrode furthermore showed stable increase in current response with ramped scan rate (Figure 3.13 C).

The electrochemical stability of modified SPE was tested by scan rate scanning and repeated cycling (50 cycles), which showed insignificant change in the peak current (Figure 3.13 D). This validates the necessity of the thermal carbonization step, which leads to the BC-Ni nanorod formation.

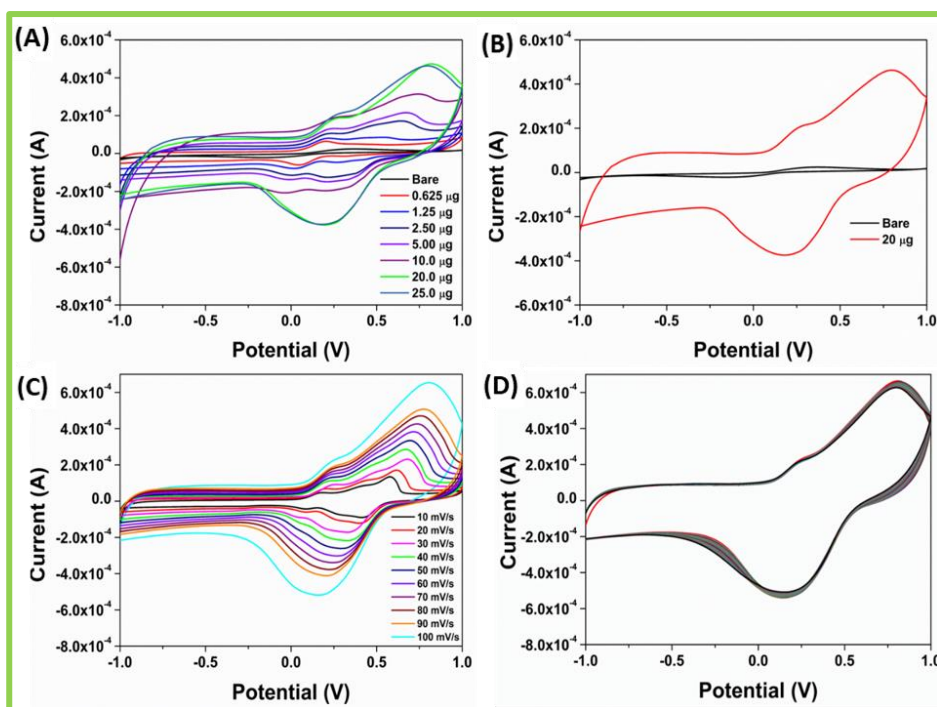


Figure 3.13: BC-Ni nanomaterial characterization: (A) Nanomaterial amount optimization, (B) increase in electrochemical activity vs. bare, (C) scan-rate dependent CV curves, and (D) multiple CV curves.

The nanostructured SPE showed a linear response in I_{pa} & I_{pc} with the square root of increasing scan rate (10 mV s^{-1} to 100 mV s^{-1}), suggesting good reversibility of fast charge-discharge response and also indicating that the process is under linear diffusion control, as clearly seen in Figure 3.14.

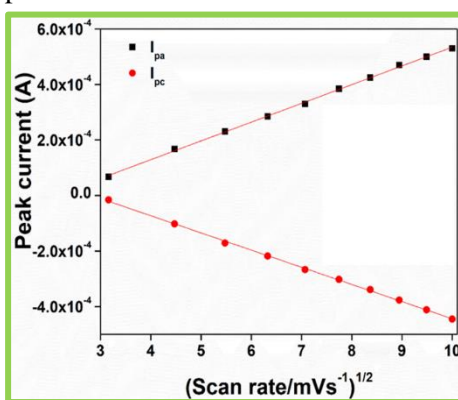


Figure 3.15: Scan rate: Scan rate square root vs. anodic and cathodic peak current response.

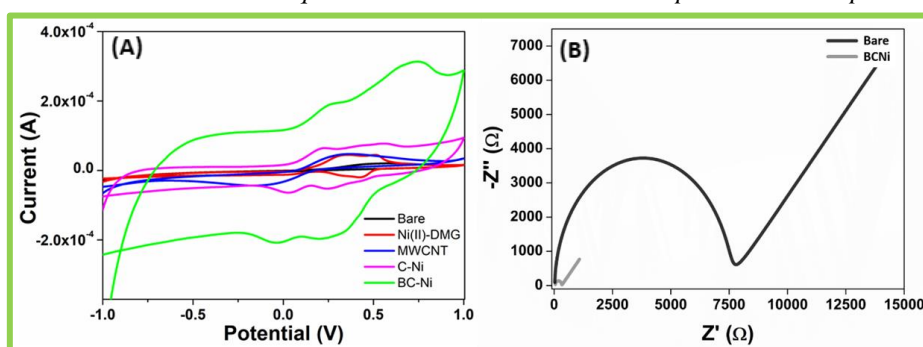


Figure 3.14: Nanosensor Characterization: (A) Comparative CV response curves with $10 \mu\text{g}$ of precursor Ni(II)-DMG , multiwalled CNT, C-Ni nanorods and boron doped C-Ni nanorods. (B) Nyquist Plot showing the response curve of bare SPE (black) and with BC-Ni nanorods (grey) drop cast on the working electrode.

Moreover, as shown in Figure 3.15, the synergistic effect of boron, carbon, and nickel nanoparticles is established by a comparative CV study of BC-Ni nanorods with bare carbon electrode by drop-casting 10 μg of C-Ni nanorods, multiwalled CNTs, and precursor Ni(II)-DMG. Furthermore, the nanomaterial efficacy as an excellent impedimetric sensor was validated with EIS, and it was found that the R_{ct} value of the modified sensor (320 Ω) had reduced to 10% of the non-modified sensor (7200 Ω) electrode. This nanomaterial property was exploited to our benefit, and further sensing assays were performed using this BC-Ni nanorod modified SPE.

3.3.4 BC-Ni nanostructured aptasensing platform

3.3.4.1 Electrode aptamer functionalization

Besides the high electrochemical sensitivity of a nanostructured platform, specificity was provided to BC-Ni nanorod modified SPE with further functionalization with our screened anti-*E. coli* O157:H7 aptamer. This was achieved by modifying the electrode surface with a positively charged linker polymer PLL, which helps hold the aptamer moieties on the surface of the sensor via ionic charges. This was experimentally validating using spectroscopic and optimized via electrochemical studies.

(A) UV-Vis spectroscopy studies

UV-Vis spectroscopic measurements of BC-Ni nanomaterial and its PLL modified conjugate and the BC-Ni nanomaterial functionalized with PLL and aptamer were carried out to confirm the binding of DNA on the nanomaterial surface. The sample concentrations utilized to modify the sensor electrode were diluted 1:10 in DI water for spectroscopy evaluation. UV-Vis spectroscopic characterization of BC-Ni, as seen in Figure 3.16, showed an increase in absorption by $\pi-\pi^*$ electron transition at 210 nm, which may be attributed to the presence of abundant sp^2 -carbon atoms present in BC-Ni. After PLL functionalization, BC-Ni + PLL nanohybrid showed an absorption peak at 223 nm with a redshift, indicating the interaction of PLL side chains and carbonyl groups on BC-Ni. This, upon further conjugation with DNA, showed a bump at 260 nm, clearly indicating the presence of immobilized DNA over BC-Ni + PLL nanohybrid.

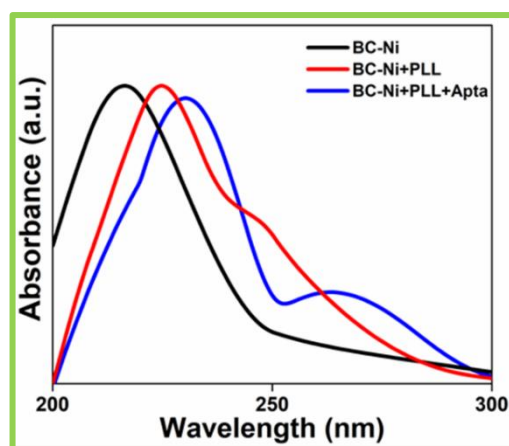


Figure 3.16: UV-Vis spectra: Absorbance spectra of BC-Ni, its PLL conjugate and aptamer conjugate.

(B) Zeta potential studies

For the validation of aptamer functionalization on to the surface of BC-Ni nanorods using PLL as an ionic linker molecule, zeta potential (ζ) measurements were carried out using Zetasizer Nano ZSP (Malvern, UK), which showed that BC-Ni nanorods themselves are negatively charged with ζ value of -12.13 mV, while the PLL modified BC-Ni was positively charged with a ζ value of -2.6 mV, and 500 ng aptamer immobilization changed to -2.94 mV, and 5000 ng further reduced it to -7.0 mV. This positive ζ charge of lysine molecules on the surface of BC-Ni nanorods helps in electrostatic interaction and binding with the DNA aptamers' negatively charged backbone. This conjugate formed on the working electrode's surface helps in capturing and subsequent detection of *E. coli* O157:H7.

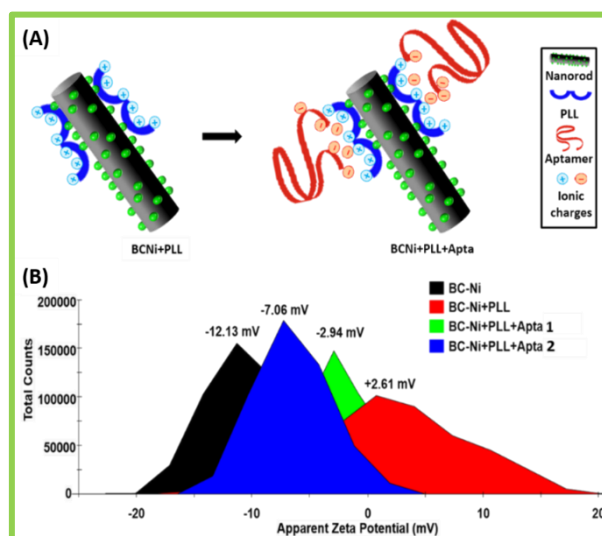


Figure 3.17: Zeta potential studies: (A) Schematic showing a modification of nanomaterial surface and (B) corresponding apparent zeta potential values.

(C) Electrochemical studies

For the efficient modification of the electrode surface with the aptamer, different aptamer concentrations were allowed to incubate on the PLL modified sensor surface overnight at 4°C and gently rinsed with water to remove unbound molecules.

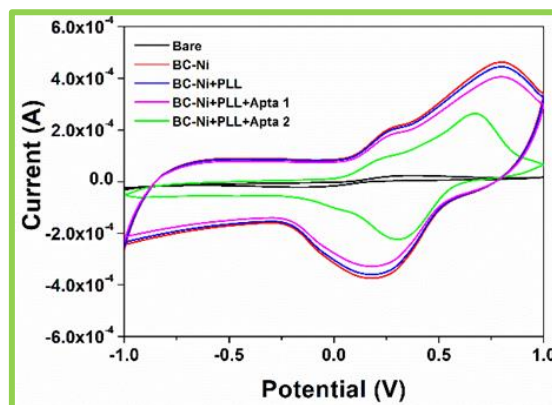


Figure 3.18: Aptamer concentration optimization: CV curves showing the change in peak currents upon functionalization of the nanostructured sensor surface. Apta 1 depicts 500 ng aptamer and Apta 2 depicts 5000 ng aptamer incubated for immobilization.

To analyze the effect of surface immobilization, CV scans from -1 V to +1 V at a scan rate of 100 mV s⁻¹ were carried out, and it was observed that the addition of PLL and overlaying with 500 ng of aptamer resulted in a minimal decrease in peak current (360 and 328 μA, respectively), which was expected due to the insulating effect of the biomolecules. However, further addition of aptamer (5000 ng) drastically reduced the cathodic peak current to 220 μA, resulting in an excessive dampening of the electrochemical signal (Figure 3.18). Thus, keeping the electrochemical sensitivity into consideration, 500 ng was optimal for further bacterial assays.

3.3.4.2 *E. coli* O157:H7 aptasensing assay

These aptamers functionalized nanostructured SPE were exposed to *E. coli* O157:H7 concentrations ranging from 0 to 10⁶ cfu for studying the range of detection of the developed aptasensor over a frequency range of 100 kHz – 10 Hz using an alternative voltage of 0.25 V amplitude. The impedance response of the platform is fitted using an equivalent circuit shown in Figure 3.19. The experimental impedance spectra are plotted as a Nyquist plot (Z' vs. -Z''), leading to the formation of a partial semi-circle curve at high frequencies with the intercept with Z' axis on the right-side denoting R_{ct}. To mitigate current response deviation from other instrumental faradic processes, Randles-Sevcik equivalent circuit model was used for fitting experimental data. Upon aptamer functionalization of the nanostructure, a minor increase in R_{ct} is observed. A linear increase was observed till in R_{ct} value from 455 ± 60 Ω at 10⁰ cfu to 1016 ± 25 Ω at 10⁵ cfu, while the sensor saturated at the next higher concentration of 10⁶ cfu. Given this, a limit of detection of 10 cfu with a dynamic range of detection from 10⁰ to 10⁵ cfu has been verified on this EIS aptasensor.

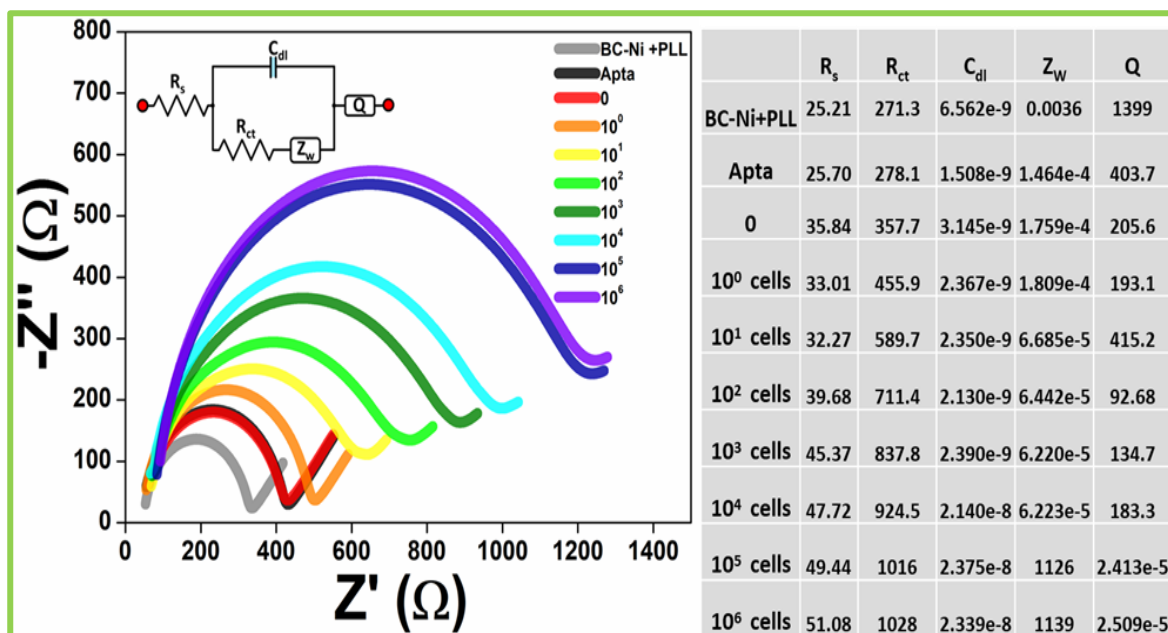


Figure 3.19: Fitted Nyquist plots: Increasing conc. of *E. coli* O157:H7 were subjected to the modified electrode surface and their EIS spectra recorded and fitted using Randles-Sevcik equivalent cell.

3.3.4.3 Aptasensing platform: validation studies

A calibration plot using buffer spiked samples were generated for easy estimation in real samples (Figure 3.20A). The R_{ct} value thus obtained can be used to estimate the number bacterial cells present in the sample, using the following equation:

$$y = 103.27x + 260.69,$$

where, x = positional value at x axis and y = observed R_{ct} value

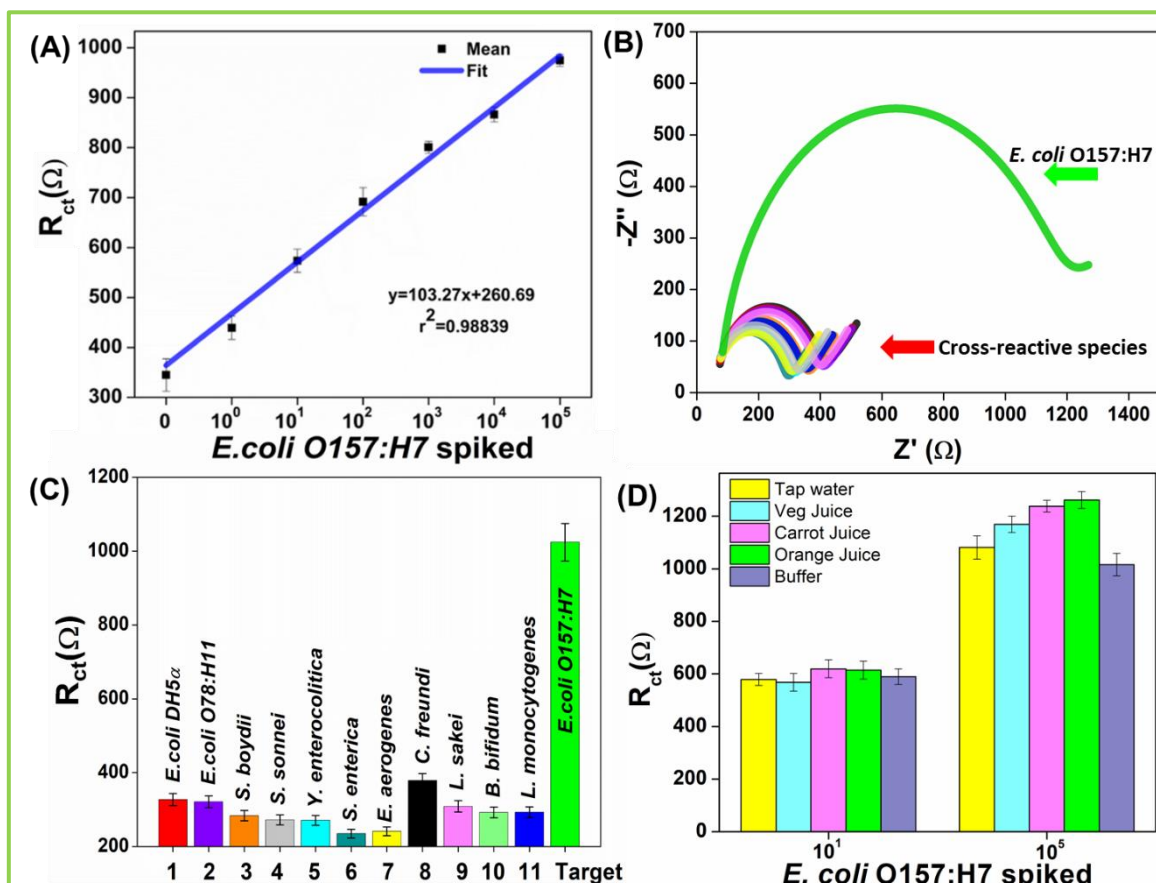


Figure 3.20: Aptasensor validation: (A) Calibration plot (B) EIS plot of cross-reactive strains on platform and (C) cross-reactivity bar-graph. (D) Real samples spiked with *E. coli* O157:H7.

Thus, from a given R_{ct} value, the number of bacterial cells present in the sample can be easily extrapolated using the calibration plot. Similarly, to validate platform cross-reactivity upon exposure with 10^5 cells of previously mentioned related species, an insignificant response change was observed, except *C. freundii* showing a minor deviation from ideal (Figure 3.20 B-C). This deviation can be attributed to the fact that *C. freundii* surface antigens present structural mimicry to *E. coli* O157:H7, especially in the polysaccharide O-antigen abundantly present on the cell surface and acts as a significant receptor recognition site^{34,35}. The real samples viz., tap water and juices extracts spiked with *E. coli* O157:H7 cells (10^1 , 10^5) were analyzed; the aptasensor platform response showed a good ideal response at both lower and higher bacterial concentrations with intact reproducibility. A minute over-response was observed, majorly due to other biochemicals present in these spiked sample extracts (Figure 3.20D). The comparative analysis of various nanostructured

bio-sensing platforms for detecting *E. coli* O157:H7 has been tabulated in Table 3.1, which validates the superiority of the aptasensor for *E. coli* O157:H7 developed in this work. Conclusively, electrochemical characterization of aptamer functionalized BC-Ni nanorods showed a good impedimetric response and high specificity towards target bacteria *E. coli* O157:H7.

Nanomaterial	Detection Method	Limit of detection	Range	Ref.
Single wall CNT	Cyclic voltammetry	1.7×10^1 cfu	$1.7 \times 10^1 - 1.1 \times 10^7$ cfu	36
3D-interdigitated electrode array	Impedance spectroscopy	2.9×10^2 cfu	$10^1 - 10^5$ cfu	37
Dendrimer modified microfluidic chip	Fluorescence spectroscopy	10^2 cfu	–	38
Gold nanoparticles	Impedance spectroscopy	48 cfu	$10^3 - 10^7$ cfu	39
Titanium dioxide nanoparticles	I-V measurements	10^{-11} M <i>E. coli</i> O157 DNA	$10^{-12} - 10^{-5}$ M DNA	40
Gold nanoparticles	Raman spectroscopy	10^1 cfu	$10^2 - 10^6$ cfu	41
Graphene quantum dots	Fluorescence spectroscopy	10^2 cfu	-	42
Gold nanoparticles	Colorimetry	5.0×10^1 cfu	$5.0 \times 10^1 - 5.0 \times 10^4$ cfu	43
Up-conversion nanoparticles and tungsten disulfide nanosheets	Fluorescence spectroscopy	17 cfu	$85 - 85 \times 10^7$ cfu	44
BC-Ni nanorods	Impedance spectroscopy	10 cfu	$10^0 - 10^5$ cfu	This study

Table 3.1: Comparative table: Showing the various recent nanostructured biosensing platforms for *E. coli* O157:H7 detection along with their merits.

3.4 Microfluidics- An introduction

Scarcity of clean water for consumption is a massive issue worldwide, with several countries suffering from water shortage. This state is detrimental for both human health and socio-economic development of a country. Although much progress has been made in water purification and sanitation systems, access to clean drinking water, sanitation and hygiene maintenance are a challenge in rural areas. According to WHO, one in three people do not have access to safe drinking water and more than 673 million people still practice open defecation⁴⁵. Municipal water and sewage treatment methodologies should be efficient for removal and monitoring of the faecal pathogenic microbial indicators in water. Pathogenic *E. coli* bacteria can enter the drinking water sources due to open defecation or leakage from septic tanks and result in diarrheal infections. Thus, monitoring of enteric pathogens especially *E. coli* O157:H7 which are resistant to standard water treatment methods and carry enterotoxins is crucial in wake of recent *E. coli* outbreaks. Far from being a sole problem of the developing world, waterborne bacterial diseases are also a threat to citizens of the developed world. The COVID-19 pandemic has established the grave importance of sanitation and necessity of clean purified water for preventing microbial diseases⁴⁶. In recent years there have been numerous research advances in methods for monitoring waterborne pathogens.

Monitoring plays several key roles in the design and implementation of water safety plans and can be applied for surveillance or investigation. Miniaturization, in particular using microfluidic systems, can play in the delivery of ‘lab-on-chip’ devices to perform monitoring procedures^{47,48}. Microfluidic technology, i.e., liquid/fluid channeling technology with micron dimensions have been developed immensely worked upon by research labs during the past decade and has found many

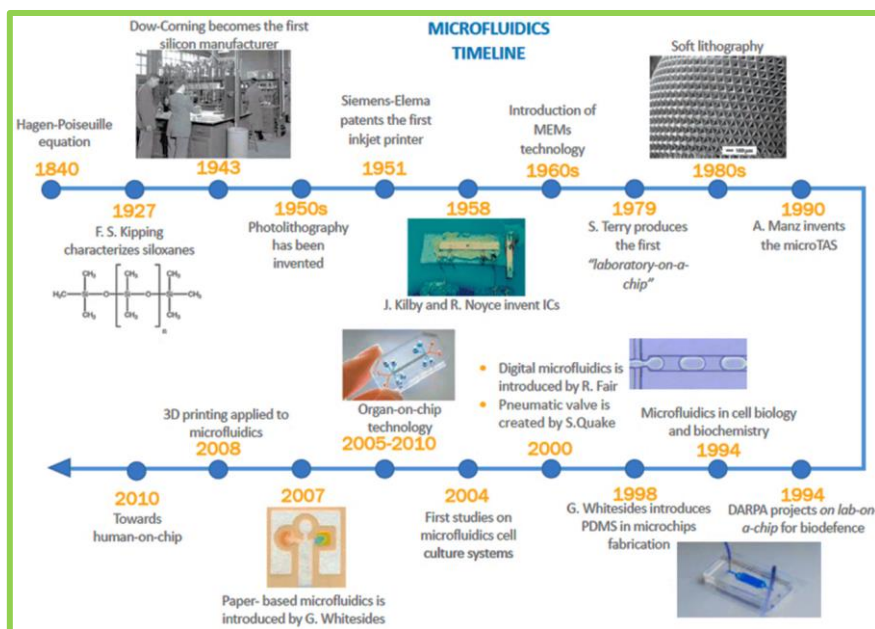


Figure 3.21: History: Timeline of development of microfluidics technology.⁵⁴

on-site applications, especially for chemical and biological assessment. The first miniaturized analytic system exploiting this technology was developed by Manz *et al.*, in 1990^{49–51}. Since then, many platforms have been fabricated by researchers worldwide for analytical measurements using various fabrication methodologies, device materials and bioassay techniques. Several fabrication techniques are available for development and integration of microfluidics-based platforms such as molding, soft-lithography, chemical etching, laser ablation. Amongst these, soft-lithography technique developed by Whitesides *et al.*, 1998 utilizing polydimethylsiloxane (PDMS) is a highly efficient and prevalent methodology^{52,53}. Figure 3.21 shows a timeline of history of microfluidics-based systems⁵⁴.

The advantages of performing on-chip monitoring are^{55,56}:

- (i) Reduced sample volume resulting in a lower background noise signal.
- (ii) Small sample volume needed and control of flow enhancing binding kinetics.
- (iii) Reduced consumption of reagents.
- (iv) Automation reduces monitoring time and overall cost of application.

In microfluidic flow, as the length of the channel and the fluidic flow is extensively reduced, the properties of the fluid at microscale become very important. Thus, having the correct viscosity and estimation of the shear force generated by fluid flow through microscale channels is essential. The Reynolds number (R_e) is defined for microfluidic channel, as the ratio of fluid viscosity and the

channel length and Re values of the channels should be modulated on basis of the microfluidic module applications. In the coming sections, we have explored soft-photolithography technique for fabrication of PDMS based aptamer functionalized platform for water filtration and monitoring of microorganisms in water samples.

3.4.1 Proposed microfluidic platform

For the early diagnosis of bacterial infections, the efficient capture and monitoring of bacteria from aqueous fluids is indispensable. In this section, we propose an aptamer integrated opto-electrochemical microfluidic platform as a sensitive monitoring device (Figure 3.22). The multi-channel device enables the enhanced capture of *E. coli* O157:H7 from water samples with the help of our anti-*E. coli* O157:H7 aptamer developed, and for further qualitative analyses of water samples for detection of bacteria in eluting water via electrochemical impedance spectroscopy, as widely explored in this thesis in previous chapters. For the fabrication of the microfluidic platform, Top-down photo-lithography based SU-8 molds were casted on silicon wafers and used for replica molding of PDMS molds bonded with gold electrodes deposited on glass or silicon substrates. A two-channel syringe pump was utilized for maintaining the flow of the bacteria spiked water samples and aptamer binding buffer (recipe as mentioned in Chapter 2, Section 2.2.1.1.1) and the water elutes verified for microbial presence with aid of impedance measurements using a CHI760E electrochemical workstation. As a proof-of-concept we successfully demonstrated the capture of pathogenic *E. coli* O157:H7 which maybe further explored for other bacterial pathogens and modulated as per requirement of the target of interest. This will aid in future studies for (i) continuous monitoring as well as filtration of water resources for specific pathogens, especially in case of emergent infectious agents.

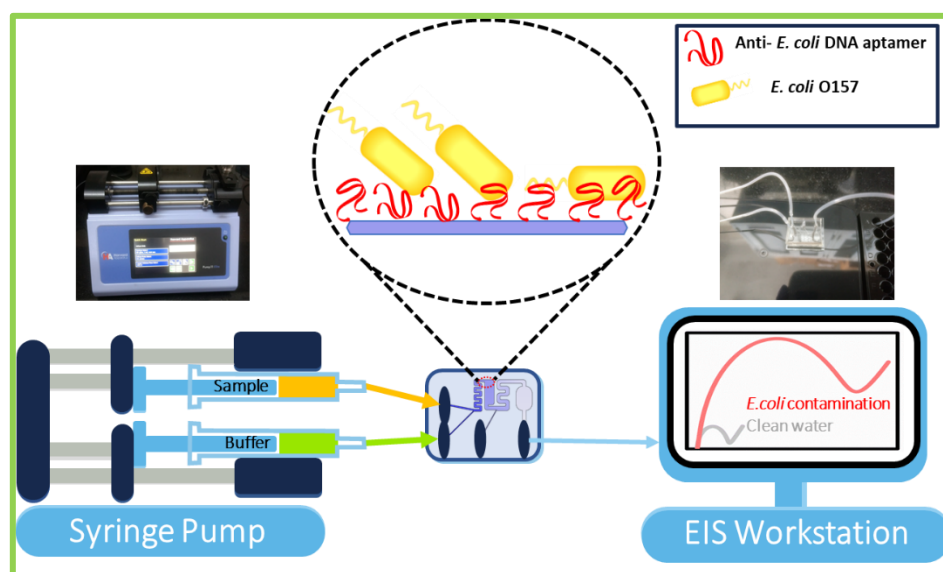


Figure 3.22: Schematic representation: An illustration showing the setup for water quality monitoring for *E. coli* O157 using a syringe pump, microfluidic platform and electrochemical impedance spectroscopy workstation along with the actual setup images.

3.4.2 Microfluidic experimental details

(A) Materials

Silicon wafer (4 inches) and Silicon Dioxide wafer (4 inches) were obtained from in-house CeNSE Facility. Sylgard 184 PDMS and curing agent were procured from Dow Corning, US and SU 8-2035 photoresist was procured from Microchem, US. The BD Intramedic Polyethylene Tubing (1 mm outer diameter) was procured from Becton Dickinson, USA. Trichlorosilane and Amino-phenylboronic acid were purchased from Sigma Aldrich, India. All steps of fabrication were carried out in clean room (class 100/1000) of CeNSE Facility, IISc Bengaluru as per normalized protocols⁵⁷.

(B) Microfluidic chip design & fabrication

(i) Designing of microfluidic pattern

- The microfluidic channel patterns were designed in AutoCAD (.dxf /.dwg) with the respective dimensions (units: micron). A minimal inter-distance of 2.5 mm was kept between patterns and multiple patterns were aligned in four quadrants of a circle (different layers).
- The pattern was designed to include a Y-shaped inlet (Inlet A and B) for the input of the water sample and the buffer solution into the mixer zone (Zone I) and then binding chamber zone (Zone II) which would be pre-functionalized with anti-*E. coli* aptamer with help of poly-lysine (PLL) alternatively via the Inlet C. To monitor impedimetrically the quality of eluted water, a window for included in the Zone III for incorporation of electrodes with the parameters described in Figure 3.23. Three different variations of the pattern were studied for optimization of the chamber area and height. Alongside, the pattern of the electrodes was also generated in a different file for its gold deposition.

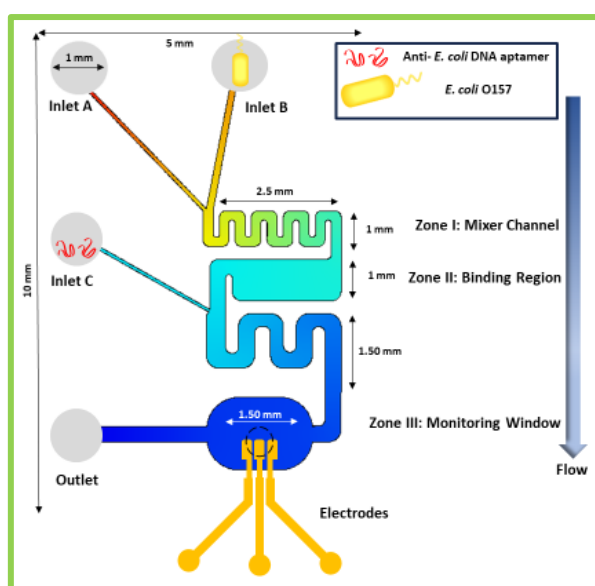


Figure 3.23: Microfluidic design: Schematic showing the pattern of the microfluidic design along with its specifics.

(ii) Fabrication of SU-8 microfluidic masters

➤ Mask writing

- The .dxf format extension files were used as input for Clewin 4 layout editor software. Mask size is set 1 inch more than pattern size during layout and this file is saved as .cif format, which is used as the format file for the Mask writer Heidelberg uPG-501.
- A dark field mask was generated for negative photoresist (PR) of SU-8 series. Here, the colored blue portion in .cif file will be etched out to generate a transparent pattern on mask.
- The pattern was etched out via the Mask writer onto a chrome coated soda-lime glass plate. This chrome mask plate was cleaned with Acetone/IPA for 8 min each and a final 10s rinse in freshly prepared Piranha solution.
- A final rinse with de-ionized water (DI) was given and blow dried the mask plate using compressed nitrogen gas. This dark chrome mask plate was then used for designing the pattern onto SU-8 coated prime silicon wafer.

➤ Photolithography

The following steps were carried out in accordance with the optimized protocol set by Microchem for SU-8 2035 negative photoresist with full caution⁵⁸. SU-8 is a high contrast epoxy-based photoresist, which provides high aspect ratio structures and is ideal for vertical sidewalls.

• Wafer cleaning

P-type silicon wafer (4 inch) was taken and cleaned using Piranha solution for 10 min.

• Dehydration bake

The wafer was dehydrated at 250°C for 10 min using hot plate pre-set at the given temperature.

• Cooling

It was allowed to cool to room temperature for further processing.

• Spin coating PR

SU-8 2035 was spin coated onto the wafer as per the product application note of Microchem, to generate a thickness of 50 μm . In brief as per the standard company protocol⁵⁸:

- (a) Dispense 1 mL of resist for each inch of substrate diameter.
- (b) Spin at 500 rpm for 5-10 seconds with acceleration of 100 rpm s^{-1} .
- (c) Spin at 2500 rpm for 30 seconds with acceleration of 300 rpm s^{-1} .
- (d) Remove the excess photoresist edge beads built up at the substrate edges with help of streaming solvent.
- (e) Soft-bake at 65°C for 3 min and 95°C for 9 min before photo exposure.

• Mask alignment

The mask and PR coated silicon wafer were aligned using Mask Aligner MJB-4 and photo exposed using 365 nm laser source with 180 mJ per cm^2 .

- **Post-exposure bake and development**

(a) The coated wafer was bake at 65°C for 2 min and 95°C for 7 min before development.

(b) The exposed patterns were developed using SU-8 developer for 7-10 min and finally washed with IPA till the undeveloped regions are removed.

- **Hard bake**

The microfluidic mold was hard baked at 150°C for 10 min and stored in desiccator until further utilized for making PDMS molds.

(iii) Fabrication of PDMS microfluidic chips

➤ Development of PDMS replica molds

- A 10:1 ratio of PDMS elastomer and curing agent (Sylgard 184) was made and desiccated to remove any gas bubbles.

- The degassed PDMS was poured into the Petri dish containing SU-8 mold and allowed to solidify at 50°C for 3-4 h.

- The solidified patterns were extracted and individual patterns cut and inlets/outlets punched using a biopsy puncher (0.75 mm) and kept in desiccator till surface bonding and the tubing were inserted manually and checked for leakage prior to application.

➤ Plasma bonding with glass substrates

- The PDMS molds were bonded with cleaned gold electrode deposited glass slides or silicon wafers using oxygen plasma bonder.

- The molds (channel side up) and glass slides were exposed to oxygen plasma for 3 min at 0.300 mbar chamber pressure.

- After exposure, the surfaces were placed immediately together for bonding.

- The sandwiched cartridge was kept for baking in oven for 15 min at 80°C.

(C) Microfluidic chip characterization & assessment

(i) Computational analysis

Computational simulation of microfluidics flow aids in prediction and design of microfluidic systems before actual fabrication. This in fact, helps understand the various dynamics of the designed microfluidic device and eliminates the need of fabricating prototypes at each step for optimization. We performed prior microfluidics analysis to understand the channel velocity and pressure flow and optimize the channel dimensions for various zones. For modelling a microfluidic device for simulation, the geometry is defined using AutoCAD software. The geometry is exported to Microfluidics module of COMSOL Multiphysics software. The initial conditions of the type of device material and fluid are setup, along with boundary conditions at the channel interface. The model is defined by a physics-dependent mesh modulated for microfluid platforms. This designed

platform is then solved by the module with application of laminar flow physics and the results analyzed, which help in further optimization of the microfluidic device.

The finite element flow modelling was performed using COMSOL Multiphysics software using primitive elements for incompressible Newtonian fluid under steady state flow with the inlet velocity of 0.001 m s^{-1} along the length of the channel with wall height of $50 \text{ }\mu\text{m}$ and no-slip boundary at the channel surface and zero pressure at the outlet. The Navier-Stokes equations and aqueous parameters used in the study were carried out in accordance with prior literature⁵⁹. The channel layout and dimensions were taken from the AutoCAD generated design and mesh refinements were carried out to optimize the fluid mechanics. The velocity and pressure simulations were observed and analyzed for the various patterns.

(ii) Morphological analysis

The morphological visualization of the fabricated microfluidic platform was carried out with the help of Optical (Leica DM2500) and Fluorescence (Olympus BX-53F) microscopy, Surface Profiling (Bruker Dektak XT) and Scanning Electron Microscopy (Jeol JSM IT1300).

(iii) Surface functionalization

The surface functionalization of the microfluidic chamber with the aptamer after mixing of the sample with the binding buffer was carried out with the help of cationic linker PLL. In this method, the PLL concentration was optimized to 0.01 mg mL^{-1} and injected through Inlet C for functionalization of the microfluidic chamber. This was allowed to incubate for 30 min for efficient before flushing the channels with DI water to remove any excess linker. The aptamer stock solution was diluted 1:1 in nuclease free water to minimize residual salt artifacts in the channel and then injected into the microfluidic chamber and allowed for functionalization of the surface of the chamber for 20 min at least for cationic PLL interaction^{60,61}. This was allowed to dry overnight and then finally rinsed with water, before application. All the processes were carried out with the aid of syringe pump (Harvard Apparatus, Pump 11Elite).

(iv) Bacterial assay & device assessment

The *E. coli* O157:H7 cells were harvested as detailed in previous Chapter 3 and spiked in DI water. Platforms both without and with aptamer functionalized in the microfluidic chamber were primed by flushing with binding buffer at optimized flow rate of $1 \text{ }\mu\text{L min}^{-1}$ for 15 min. This flow-rate was optimized to minimize the pressure generated on the walls of PDMS channels and give optimal time for mixing of the sample and buffer. Then the different concentrations of bacterial cells were injected in the system from Inlet B with simultaneous injection of the binding buffer from Inlet A. The flow-rate was controlled to maximize the interaction of the aptamer and bacterial cells and also maintaining positive efflux pressure for the outlet. The captured *E. coli* was imaged using fluorescence microscopy and elutes monitored by EIS using parameters optimized in previous chapters for whole cell bacteria.

3.4.3 Microfluidics - Results & discussion

(i) Computational studies

The microfluidic channel pattern was designed to incorporate a mixer design with ‘Y’ inlet junction for sample and buffer injection, serpentine Dean’s vortex mixer for dilution and mixing of water samples with buffer and further aptamer binding zone for the adherence of the bacterial cells to the functionalized surface and finally one outlet after an observation window. The velocity and pressure profiles were simulated for the different variations of the pattern labeled as (i),(ii) and (iii), as shown in Figure 3.24. These profiles in combination show high flow as well as stagnant regions in the channels. The serpentine staggered geometry of the mixer zone shows hot pockets in the middle lamella whereas cold pockets at the edges of the serpentine channels, projecting formation of turbulence in the channel as predicted^{62–64}. The study helped decipher that pattern (ii) maintained a high velocity equivalent to the inlet velocity in the mixer and significantly dropped in the binding zone. Other patterns (i) and (iii) showed low velocity and higher pressures or very low-pressure regions throughout the pattern, respectively which are inimical for the device and fluid flow. It is imperative of the system to keep flowing to omit clogging or rupture of the bonded device; thus, the pattern (ii), was utilized for the bacterial assay assessment.

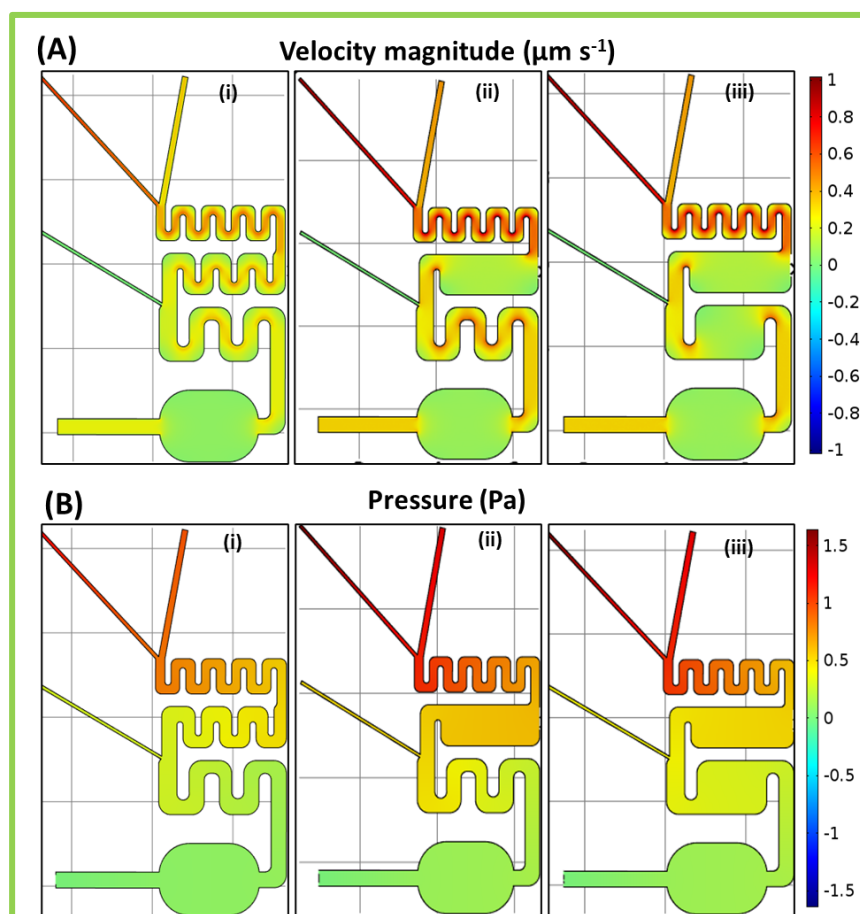


Figure 3.24: Computational studies: (A) Velocity and (B) Pressure profiles of various microfluidic patterns.

(ii) Microfluidics chip characterization

The microfluidic platform was fabricated by replica molding of silanized SU-8 Master device with PDMS epoxy bonded onto glass or silicon wafer substrate (Figure 3.25). The microfluidic mixing

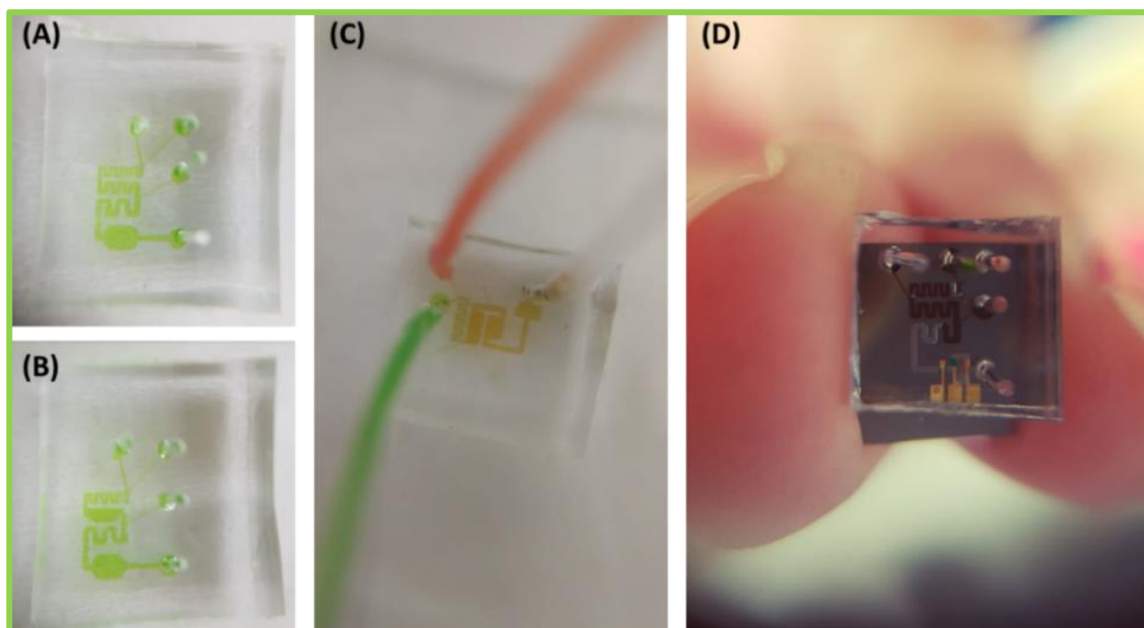


Figure 3.25: Optical images of device: Green dye flushed PDMS molds of two patterns bonded onto glass surface (A-B) and (C) intermixing of red and green dye in the microfluidic channel. (D) An early prototype PDMS device bonded onto silicon wafer with deposited gold electrodes.

is an essential part of miniaturized systems, which is incorporated in the platform with designing a serpentine geometry, consisting of recurring U-shaped units. It has been reported to enhance the performance of microfluidic biosensors by increasing the presence of eddies at bends and inducing stretching and folding of the fluid. The flow-rate was optimized via COMSOL computational studies at $1 \mu\text{m min}^{-1}$ to minimize laminar flow in the mixer zone while delivering homogenous buffer salt mixing and ensuring that the test water sample stream is mixed with the buffer fluid stream before interaction with the aptamer.

This was validated by introduction of dyes in the two channels that merge to form a coloured front as clearly seen in Figure 3.25 (C). In the next step, the capture of the bacteria on the aptamer functionalized microfluidic chamber was visually validated with aid of FITC-labelled aptamer sequences, which were coated onto the substrate surface with aid of cationic polymer PLL (Figure 3.26). The interaction between PLL and DNA aptamer has earlier been verified by zeta-potential based studies in this chapter, Section 3.3.4.1.

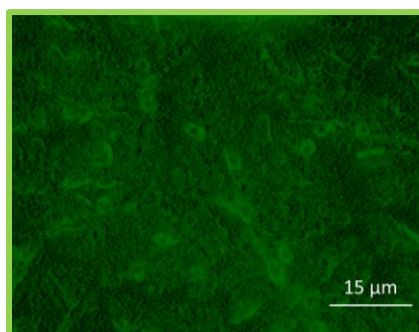


Figure 3.27: Fluorescence imaging: FITC labelled aptamer visualized in the Zone II of the microfluidic chamber after functionalization.

The surface morphology of the SU8 Master was analysed with optical microscopy inline of the clean room, to ascertain the geometry and dimensions of the various microstructures lithographed onto the silicon wafer. Figure 3.27 shows the various surface morphology observations carried out and validated the width (250 μm) and height (50 μm) of the channels with good periodicity. Next, the electron micrography of PDMS mould was also carried out to observe the final device channels, which showed well-formed structures with dimensions equivalent to SU8 master.

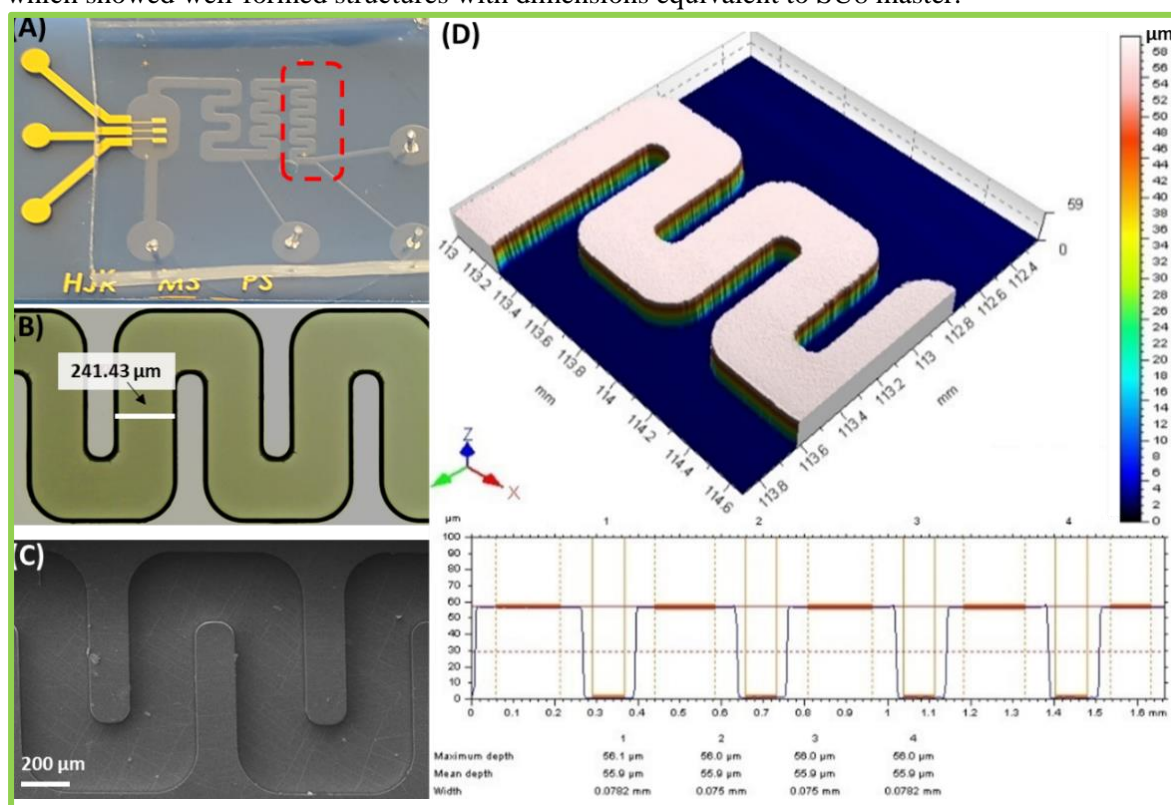


Figure 3.26: Surface characterization of microfluidic master & device: (A) A PDMS fabricated microfluidic device (B) Optical imaging of the SU-8 master pattern showing the channel dimensions. (C) SEM image of the PDMS mold replicated from the master and (D) Surface profiling of the master showing the height profile of the serpentine channel.

(iii) Bacterial assay and impedimetric monitoring

The bacterial monitoring experiments were carried out between two streams containing *E. coli* spiked water test samples and binding buffer, which were exposed to aptamer functionalized

chamber. The binding was detected using DAPI dye labelled bacterial cells (methodology adopted from Chapter 2) the increase in the adherence visualized using fluorescence microscopy (Figure 3.28).

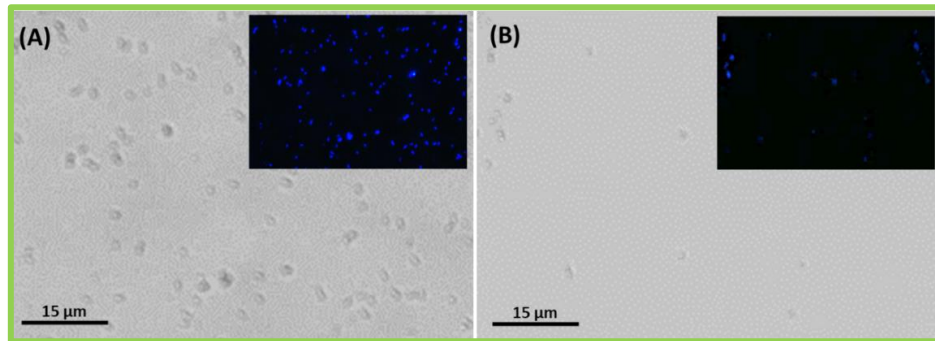


Figure 3.28: Microscopic evaluation: Micrographs of the channel (20X) showing bacteria contaminated water (A) 1×10^4 cfu (B) 1×10^2 cfu flushed from the aptamer functionalized zone and corresponding DAPI labeled (blue emission) fluorescence imaging of the same area, ascertaining retention of bacteria.

The impedance spectroscopy of the elutes for monitoring the bacterial presence in microfluidic chip was carried out utilizing gold (Au) electrodes coated onto the bonded substrate of the microfluidic platform and results fitted using Randles-Sevcik circuit. Figure 3.29(A) shows the generalized lamellar architecture of the platforms. The bare impedance of the electrodes was recorded in 1:1 diluted binding buffer which showed characteristic high conductive response as seen in Figure

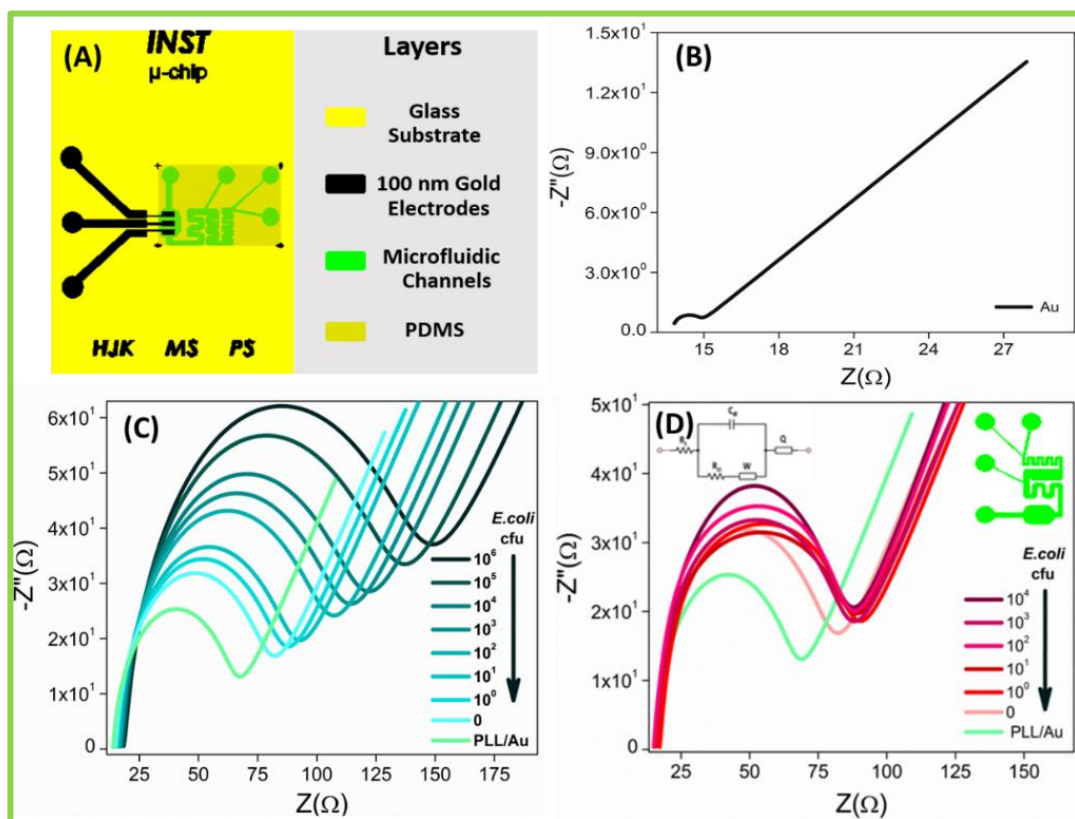


Figure 3.29: EIS Studies: (A) Layer-by-layer scheme of a microfluidic device pattern, (B) Nyquist plot showing the impedance spectra of bare gold (Au) electrode, (C) *E. coli* O157:H7 concentrations flushed through unfunctionalized channel showing control values onto PLL modified electrode and (D) *E. coli* O157:H7 flushed through aptamer functionalized device.

3.29(B). Furthermore, prior to aptamer based capture of bacterial cells, a control assessment impedance spectroscopy assay was carried out on unfunctionalized microfluidic chip which showed increasing high R_{ct} values in response to increasing bacterial cell presence in the elutes, Figure 3.29(C). In the test assay, similar bacterial concentrations were injected into the PDMS chip and allowed to interact with the aptamer zone for capture and adherence onto the chip surface. This was also monitored impedimetrically and it was observed that the chip pattern showed good capture capability till 1×10^4 cfu, after which the platform developed clogging. Thus, this platform presents a proof-of-concept of bacterial capture and monitoring with the aid of aptamer functionalized microfluidic platform, which can be further enhanced for other bacterial species suspended in water samples and aid in real-time detection for microbial load in water bodies.

3.5 Conclusion

An electrochemical sensing platform using aptamer functionalized boron-carbon nanorods decorated by nickel nanoparticles is demonstrated for the specific detection of STEC strain *E. coli* O157:H7. A novel high affinity & specificity aptamer ($K_d \sim 69$ nM) was screened via microtiter plate-based SELEX, which can be used to functionalize detection platforms for specific *E. coli* O157:H7 monitoring & diagnostics. The established BC-Ni nanorods modified aptasensor successfully sensed target O157:H7 serotype as low as ~ 10 cfu with a response range from $10^0 - 10^5$ cfu in water and with minor pre-processing steps in food samples. Alongside, we presented a proof-of-concept for the fabrication of a simple microfluidic platform (10 mm \times 5 mm) for visualization and monitoring of aqueous suspension of pathogenic bacteria (*E. coli* O157:H7) in a microfluidic chamber. The microfluidic platform was functionalized with aptamers that acted as capture moieties for removal of bacteria from the water sample and further coupled with an impedimetric system for water quality analysis. This platform can currently capture and detect up to 10^4 cells in water samples and further multiple arrays of these chips may increase the potential of these platforms.

Bibliography

- (1) WHO. *WHO | Diseases and Risks*; World Health Organization, 2019.
- (2) Parsons, B. D.; Zelyas, N.; Berenger, B. M.; Chui, L. Detection, Characterization, and Typing of Shiga Toxin-Producing Escherichia Coli. *Front. Microbiol.* **2016**, *7*, 478. <https://doi.org/10.3389/fmicb.2016.00478>.
- (3) Infection by Escherichia coli O157:H7 and Other Enterohemorrhagic E. coli (EHEC) - Infectious Diseases - MSD Manual Professional Edition <https://www.msmanuals.com/professional/infectious-diseases/gram-negative-bacilli/infection-by-escherichia-coli-o157-h7-and-other-enterohemorrhagic-e-coli-ehc> (accessed Oct 5, 2020).
- (4) Nguyen, Y.; Sperandio, V. Enterohemorrhagic E. Coli (EHEC) Pathogenesis. *Front. Cell. Infect. Microbiol.* **2012**, *2*, 90. <https://doi.org/10.3389/fcimb.2012.00090>.
- (5) Epidemiologic Notes and Reports Isolation of E. coli 0157:H7 from Sporadic Cases of Hemorrhagic Colitis -- United States <https://www.cdc.gov/mmwr/preview/mmwrhtml/00001184.htm> (accessed Oct 5, 2020).
- (6) Lim, J. Y.; Yoon, J. W.; Hovde, C. J. A Brief Overview of Escherichia Coli O157:H7 and Its Plasmid O157. *Journal of Microbiology and Biotechnology*. Korean Society for Microbiology and Biotechnology 2010, pp 1–10. <https://doi.org/10.4014/jmb.0908.08007>.
- (7) Mateo-Sagasta, J.; Marjani, S.; Turrall, H.; Burke, J. Water Pollution from Agriculture: A Global Review. *FAO y IWMI* **2017**, *35*. <https://doi.org/http://www.fao.org/3/a-i7754e.pdf>.
- (8) Croxen, M. A.; Finlay, B. B. Molecular Mechanisms of Escherichia Coli Pathogenicity. *Nat. Rev. Microbiol.*

- 2010, 8 (1), 26–38. <https://doi.org/10.1038/nrmicro2265>.
- (9) Lee, W. C.; Kwon, Y. H. Comparative Study on the Epidemiological Aspects of Enterohemorrhagic Escherichia Coli Infections between Korea and Japan, 2006 to 2010. *Korean J. Intern. Med.* **2016**, *31* (3), 579–584. <https://doi.org/10.3904/kjim.2014.255>.
 - (10) Iijima, S. Helical Microtubules of Graphitic Carbon. *Nature* **1991**, *354* (6348), 56–58. <https://doi.org/10.1038/354056a0>.
 - (11) Ma, F.; Wang, M.; Shao, Y.; Wang, L.; Wu, Y.; Wang, Z.; Hao, X. “Thermal Substitution” for Preparing Ternary BCN Nanosheets with Enhanced and Controllable Nonlinear Optical Performance. *J. Mater. Chem. C* **2017**, *5* (10), 2559–2565. <https://doi.org/10.1039/c7tc00131b>.
 - (12) Thaweesak, S.; Wang, S.; Lyu, M.; Xiao, M.; Peerakiathajohn, P.; Wang, L. Boron-Doped Graphitic Carbon Nitride Nanosheets for Enhanced Visible Light Photocatalytic Water Splitting. *Dalt. Trans.* **2017**, *46* (32), 10714–10720. <https://doi.org/10.1039/c7dt00933j>.
 - (13) Panchakarla, L. S.; Govindaraj, A.; Rao, C. N. R. Nitrogen- And Boron-Doped Double- Walled Carbon Nanotubes. *ACS Nano* **2007**, *1* (5), 494–500. <https://doi.org/10.1021/nn700230n>.
 - (14) Cardoso, W. S.; Dias, V. L. N.; Costa, W. M.; De Araujo Rodrigues, I.; Marques, E. P.; Sousa, A. G.; Boaventura, J.; Bezerra, C. W. B.; Song, C.; Liu, H.; Zhang, J.; Marques, A. L. B. Nickel-Dimethylglyoxime Complex Modified Graphite and Carbon Paste Electrodes: Preparation and Catalytic Activity towards Methanol/Ethanol Oxidation. *J. Appl. Electrochem.* **2009**, *39* (1), 55–64. <https://doi.org/10.1007/s10800-008-9636-x>.
 - (15) Mansour, N. Ben; Najeh, I.; Mansouri, S.; El Mir, L. Effect of Pyrolysis Temperature on the Properties of Carbon/Nickel Nanocomposites Prepared by Sol–Gel Method. *Appl. Surf. Sci.* **2015**, *337*, 158–165. <https://doi.org/10.1016/j.apsusc.2015.02.084>.
 - (16) Jabbar, A.; Yasin, G.; Khan, W. Q.; Anwar, M. Y.; Korai, R. M.; Nizam, M. N.; Muhyodin, G. Electrochemical Deposition of Nickel Graphene Composite Coatings: Effect of Deposition Temperature on Its Surface Morphology and Corrosion Resistance. *RSC Adv.* **2017**, *7* (49), 31100–31109. <https://doi.org/10.1039/C6RA28755G>.
 - (17) Alnajar, S.; Gupta, R. S. Phylogenomics and Comparative Genomic Studies Delineate Six Main Clades within the Family Enterobacteriaceae and Support the Reclassification of Several Polyphyletic Members of the Family. *Infect. Genet. Evol.* **2017**, *54*, 108–127. <https://doi.org/10.1016/j.meegid.2017.06.024>.
 - (18) Endo, A.; Futagawa-Endo, Y.; Dicks, L. M. T. Diversity of Lactobacillus and Bifidobacterium in Feces of Herbivores, Omnivores and Carnivores. *Anaerobe* **2010**, *16* (6), 590–596. <https://doi.org/10.1016/j.anaerobe.2010.10.005>.
 - (19) GraphPad Prism 7 Curve Fitting Guide - Equation: One site -- Specific binding https://www.graphpad.com/guides/prism/7/curve-fitting/reg_one_site_specific.htm (accessed Oct 23, 2020).
 - (20) Sanger Sequencing Steps | DNA Sequencing | Sigma-Aldrich <https://www.sigmaaldrich.com/technical-documents/articles/biology/sanger-sequencing.html> (accessed Oct 22, 2020).
 - (21) Panchakarla, L. S.; Govindaraj, A.; Rao, C. N. R. Boron- and Nitrogen-Doped Carbon Nanotubes and Graphene. *Inorganica Chim. Acta* **2010**, *363* (15), 4163–4174. <https://doi.org/10.1016/j.ica.2010.07.057>.
 - (22) Li, L.; Yang, H.; Yang, J.; Zhang, L.; Miao, J.; Zhang, Y.; Sun, C.; Huang, W.; Dong, X.; Liu, B. Hierarchical Carbon@Ni₃S₂@MoS₂ Double Core–Shell Nanorods for High-Performance Supercapacitors. *J. Mater. Chem. A* **2016**, *4* (4), 1319–1325. <https://doi.org/10.1039/C5TA08714G>.
 - (23) Labib, M.; Zamay, A. S.; Kolovskaya, O. S.; Reshetneva, I. T.; Zamay, G. S.; Kibbee, R. J.; Sattar, S. A.; Zamay, T. N.; Berezovski, M. V.; Zheleznyaka str, P. Aptamer-Based Viability Impedimetric Sensor for Bacteria. *Anal. Chem* **2012**, *84*, 16. <https://doi.org/10.1021/ac302902s>.
 - (24) Gu, H.; Duan, N.; Wu, S.; Hao, L.; Xia, Y.; Ma, X.; Wang, Z. Graphene Oxide-Assisted Non-Immobilized SELEX of Okadaic Acid Aptamer and the Analytical Application of Aptasensor. *Sci. Rep.* **2016**, *6*. <https://doi.org/10.1038/srep21665>.
 - (25) Anti-E. coli serotype O157 Antibodies | Invitrogen <https://www.thermofisher.com/antibody/primary/target/e.coli.serotype.o157> (accessed Oct 22, 2020).
 - (26) Lee, Y. J.; Han, S. R.; Maeng, J. S.; Cho, Y. J.; Lee, S. W. In Vitro Selection of Escherichia Coli O157:H7-Specific RNA Aptamer. *Biochem. Biophys. Res. Commun.* **2012**, *417* (1), 414–420. <https://doi.org/10.1016/j.bbrc.2011.11.130>.
 - (27) Ferrari, A.; Robertson, J. Interpretation of Raman Spectra of Disordered and Amorphous Carbon. *Phys. Rev. B - Condens. Matter Mater. Phys.* **2000**, *61* (20), 14095–14107. <https://doi.org/10.1103/PhysRevB.61.14095>.
 - (28) Palomäki, T.; Peltola, E.; Sainio, S.; Wester, N.; Pitkänen, O.; Kordas, K.; Koskinen, J.; Laurila, T. Unmodified and Multi-Walled Carbon Nanotube Modified Tetrahedral Amorphous Carbon (Ta-C) Films as in Vivo Sensor Materials for Sensitive and Selective Detection of Dopamine. *Biosens. Bioelectron.* **2018**, *118*, 23–30. <https://doi.org/10.1016/j.bios.2018.07.018>.
 - (29) Ferrari, A. C. Raman Spectroscopy of Graphene and Graphite: Disorder, Electron–Phonon Coupling, Doping and Nonadiabatic Effects. *Solid State Commun.* **2007**, *143* (1–2), 47–57. <https://doi.org/10.1016/j.ssc.2007.03.052>.
 - (30) Arunkumar, S.; Jegatheesh, V.; Soundharya, R.; Jesy Alka, M.; Mayavan, S. BCN Based Oil Coatings for Mild Steel under Aggressive Chloride Ion Environment. *Appl. Surf. Sci.* **2018**, *449* (February), 287–294. <https://doi.org/10.1016/j.apsusc.2018.01.030>.
 - (31) Sing, K. S. W. Reporting Physisorption Data for Gas/Solid Systems with Special Reference to the Determination of Surface Area and Porosity (Recommendations 1984). *Pure Appl. Chem.* **1985**, *57* (4), 603–619. <https://doi.org/10.1351/pac198557040603>.
 - (32) Wang, Q.; Zhao, Y.; Yang, Q.; Du, D.; Yang, H.; Lin, Y. Amperometric Sarcosine Biosensor with Strong Anti-

- Interference Capabilities Based on Mesoporous Organic-Inorganic Hybrid Materials. *Biosens. Bioelectron.* **2019**, *141*, 111431. <https://doi.org/10.1016/j.bios.2019.111431>.
- (33) Tomer, V. K.; Singh, K.; Kaur, H.; Shorie, M.; Sabherwal, P. Rapid Acetone Detection Using Indium Loaded WO₃/SnO₂ Nanohybrid Sensor. *Sensors Actuators B Chem.* **2017**, *253*, 703–713. <https://doi.org/10.1016/j.snb.2017.06.179>.
- (34) Vinogradov, E.; Conlan, J. W.; Perry, M. B. Serological Cross-Reaction between the Lipopolysaccharide O-Polysaccharide Antigens of *Escherichia Coli* O157:H7 and Strains of *Citrobacter Freundii* and *Citrobacter Sedlakii*. *FEMS Microbiol. Lett.* **2000**, *190* (1), 157–161. <https://doi.org/10.1111/j.1574-6968.2000.tb09279.x>.
- (35) Nishiuchi, Y.; Doe, M.; Hotta, H.; Kobayashi, K. Structure and Serologic Properties of O-Specific Polysaccharide from *Citrobacter Freundii* Possessing Cross-Reactivity with *Escherichia Coli* O157:H7. *FEMS Immunol. Med. Microbiol.* **2000**, *28* (2), 163–171. <https://doi.org/10.1111/j.1574-695x.2000.tb01472.x>.
- (36) Housaindokht, M. R.; Verdian, A.; Sheikhzadeh, E.; Pordeli, P.; Rouhbakhsh Zaeri, Z.; Janati-Fard, F.; Nosrati, M.; Mashreghi, M.; Haghparast, A. R.; Nakhaeipour, A.; Esmaeili, A. A.; Solimani, S. A Sensitive Electrochemical Aptasensor Based on Single Wall Carbon Nanotube Modified Screen Printed Electrode for Detection of *Escherichia Coli* O157:H7. *Adv. Mater. Lett.* **2018**, *9* (5), 369–374. <https://doi.org/10.5185/amlett.2018.1701>.
- (37) Brosel-Oliu, S.; Ferreira, R.; Uria, N.; Abramova, N.; Gargallo, R.; Muñoz-Pascual, F. X.; Bratov, A. Novel Impedimetric Aptasensor for Label-Free Detection of *Escherichia Coli* O157:H7. *Sensors Actuators, B Chem.* **2018**, *255*, 2988–2995. <https://doi.org/10.1016/j.snb.2017.09.121>.
- (38) Hao, X.; Yeh, P.; Qin, Y.; Jiang, Y.; Qiu, Z.; Li, S.; Le, T.; Cao, X. Aptamer Surface Functionalization of Microfluidic Devices Using Dendrimers as Multi-Handled Templates and Its Application in Sensitive Detections of Foodborne Pathogenic Bacteria. *Anal. Chim. Acta* **2019**, *1056*, 96–107. <https://doi.org/10.1016/j.aca.2019.01.035>.
- (39) Lin, D.; Pillai, R. G.; Lee, W. E.; Jemere, A. B. An Impedimetric Biosensor for *E. Coli* O157:H7 Based on the Use of Self-Assembled Gold Nanoparticles and Protein G. *Microchim. Acta* **2019**, *186* (3), 1–9. <https://doi.org/10.1007/s00604-019-3282-3>.
- (40) Nadzirah, S.; Hashim, U.; Gopinath, S. C. B.; Parmin, N. A.; Hamzah, A. A.; Yu, H. W.; Dee, C. F. Titanium Dioxide-Mediated Resistive Nanobiosensor for *E. Coli* O157:H7. *Microchim. Acta* **2020**, *187* (4), 1–9. <https://doi.org/10.1007/s00604-020-4214-y>.
- (41) Díaz-Amaya, S.; Lin, L. K.; Deering, A. J.; Stanciu, L. A. Aptamer-Based SERS Biosensor for Whole Cell Analytical Detection of *E. Coli* O157:H7. *Anal. Chim. Acta* **2019**, *1081*, 146–156. <https://doi.org/10.1016/j.aca.2019.07.028>.
- (42) Yang, X.; Feng, L.; Qin, X. Preparation of the Cf-GQDs-*Escherichia Coli* O157: H7 Bioprobe and Its Application in Optical Imaging and Sensing of *Escherichia Coli* O157: H7. *Food Anal. Methods* **2018**, *11* (8), 2280–2286. <https://doi.org/10.1007/s12161-018-1207-0>.
- (43) Zheng, L.; Cai, G.; Wang, S.; Liao, M.; Li, Y.; Lin, J. A Microfluidic Colorimetric Biosensor for Rapid Detection of *Escherichia Coli* O157:H7 Using Gold Nanoparticle Aggregation and Smart Phone Imaging. *Biosens. Bioelectron.* **2019**, *124–125*, 143–149. <https://doi.org/10.1016/j.bios.2018.10.006>.
- (44) Wang, P.; Wang, A.; Hassan, M. M.; Ouyang, Q.; Li, H.; Jiao, T.; Chen, Q. A Highly Sensitive Upconversion Nanoparticles-WS₂ Nanosheet Sensing Platform for *Escherichia Coli* Detection. *Sensors Actuators B Chem.* **2020**, 128434. <https://doi.org/10.1016/j.snb.2020.128434>.
- (45) Goal 6: Clean water and sanitation | UNDP <https://www.undp.org/content/undp/en/home/sustainable-development-goals/goal-6-clean-water-and-sanitation.html> (accessed Oct 17, 2020).
- (46) Water and Sanitation – United Nations Sustainable Development <https://www.un.org/sustainabledevelopment/water-and-sanitation/> (accessed Oct 17, 2020).
- (47) Yew, M.; Ren, Y.; Koh, K. S.; Sun, C.; Snape, C. A Review of State-of-the-Art Microfluidic Technologies for Environmental Applications: Detection and Remediation. *Glob. Challenges* **2019**, *3* (1), 1800060. <https://doi.org/10.1002/gch2.201800060>.
- (48) Weng, X.; Neethirajan, S. Ensuring Food Safety: Quality Monitoring Using Microfluidics. *Trends Food Sci. Technol.* **2017**, *65* (May), 10–22. <https://doi.org/10.1016/j.tifs.2017.04.015>.
- (49) Manz, A.; Graber, N.; Widmer, H. M. Miniaturized Total Chemical Analysis Systems: A Novel Concept for Chemical Sensing. *Sensors Actuators B Chem.* **1990**, *1* (1–6), 244–248. [https://doi.org/10.1016/0925-4005\(90\)80209-I](https://doi.org/10.1016/0925-4005(90)80209-I).
- (50) Prakash, S.; Pinti, M.; Bhushan, B. Review Article: Theory, Fabrication and Applications of Microfluidic and Nanofluidic Biosensors. *Philos. Trans. R. Soc. A Math. Phys. Eng. Sci.* **2012**, *370* (1967), 2269–2303. <https://doi.org/10.1098/rsta.2011.0498>.
- (51) Yoon, J. Y.; Kim, B. Lab-on-a-Chip Pathogen Sensors for Food Safety. *Sensors (Switzerland)* **2012**, *12* (8), 10713–10741. <https://doi.org/10.3390/s120810713>.
- (52) Whitesides, G. M. The Origins and the Future of Microfluidics. *Nature*. Nature Publishing Group July 27, 2006, pp 368–373. <https://doi.org/10.1038/nature05058>.
- (53) Nie, Z.; Nijhuis, C. A.; Gong, J.; Chen, X.; Kumachev, A.; Martinez, A. W.; Narovlyansky, M.; Whitesides, G. M. Electrochemical Sensing in Paper-Based Microfluidic Devices. *Lab Chip* **2010**, *10* (4), 477–483. <https://doi.org/10.1039/b917150a>.
- (54) The history of microfluidics - Elveflow <https://www.elflow.com/microfluidic-reviews/general-microfluidics/history-of-microfluidics/> (accessed Oct 14, 2020).
- (55) Peric, O.; Hannebelle, M.; Adams, J. D.; Fantner, G. E. Microfluidic Bacterial Traps for Simultaneous Fluorescence and Atomic Force Microscopy. *Nano Res.* **2017**, *10* (11), 3896–3908.

- <https://doi.org/10.1007/s12274-017-1604-5>.
- (56) Bridle, H.; Miller, B.; Desmulliez, M. P. Y. Application of Microfluidics in Waterborne Pathogen Monitoring: A Review. *Water Res.* **2014**, *55*, 256–271. <https://doi.org/10.1016/j.watres.2014.01.061>.
- (57) CeNSE. National Nano Fabrication Centre (NNFC) Tool and Process Capabilities.
- (58) *SU-8 2000 Permanent Epoxy Negative Photoresist PROCESSING GUIDELINES*.
- (59) Itomlenskis, M.; Fodor, P. S.; Kaufman, M. *Design of Passive Micromixers Using the COMSOL Multiphysics Software Package*.
- (60) (No Title) https://www.tedpella.com/technote_html/18021,18026_TN.pdf (accessed Oct 27, 2020).
- (61) Di Iorio, D.; Marti, A.; Koeman, S.; Huskens, J. Clickable Poly-L-Lysine for the Formation of Biorecognition Surfaces. *RSC Adv.* **2019**, *9* (61), 35608–35613. <https://doi.org/10.1039/c9ra08714a>.
- (62) Sudarsan, A. P.; Ugaz, V. M. Multivortex Micromixing. *Proc. Natl. Acad. Sci. U. S. A.* **2006**, *103* (19), 7228–7233. <https://doi.org/10.1073/pnas.0507976103>.
- (63) Nivedita, N.; Ligrani, P.; Papautsky, I. Dean Flow Dynamics in Low-Aspect Ratio Spiral Microchannels. *Sci. Rep.* **2017**, *7* (1), 1–10. <https://doi.org/10.1038/srep44072>.
- (64) Lee, W.; Kwon, D.; Choi, W.; Jung, G. Y.; Au, A. K.; Folch, A.; Jeon, S. 3D-Printed Micro Fluidic Device for the Detection of Pathogenic Bacteria Using Size-Based Separation in Helical Channel with Trapezoid Cross-Section. *Sci. Rep.* **2015**, *5*, 1–7. <https://doi.org/10.1038/srep07717>.



Chapter 4

*Aptasensing
optical assay for
E. coli surface
antigens*



Chapter 4

Aptasensing optical assay for *E. coli* surface antigens

*The contents of this chapter are adapted from: **Kaur, H.**; Shorie, M.; Sabherwal, P. Aptamer functionalized carbon dots mediated fluorescence turn-on assay for endotoxin detection. (Under revision).*

4.1 Introduction

All gram-negative bacteria including *E. coli* are serologically categorized on the basis of membrane polysaccharides and flagellar protein. These antigens are highly polymorphic in nature and the multitude of variations in their molecular structure facilitate the evolution of species. Lipopolysaccharides (LPS) and flagellin are prominent bacterial surface markers used for serological determination and denoted as O-antigen and H-antigen, respectively. This terminology has been used interchangeably in the chapter. These moieties present on the bacterial surface place a significant role as antigens in the development of an immune response upon infection. Usually serology techniques employing rabbit sera against these surface antigens, PCR based loci identification analysis and mass spectrometry techniques^{1,2}. These surface-exposed molecules are an ideal choice as biomarkers given their distinct role in pathogenesis. Therefore, the development of a specific and rapid diagnostic assay is the need of the hour, which is explored in this chapter.

4.1.1 Target *E. coli* surface antigens – A background

4.1.1.1 O-antigen

LPS is a major structural tri-partite component of the cell of Gram negative bacteria, comprising of variable polysaccharide region (O-antigen), and conserved regions- core oligosaccharide and Lipid-A (endotoxin). Upon infection, this may enter the bloodstream, which is recognized via the Toll-like receptor 5 and promotes increased expression of inflammatory molecules like interleukins and tumor necrosis factors, which initiate an immune cascade, resulting in fatal septic shock. Additionally, endotoxin which is synonymous with LPS is one of the most dangerous pyrogenic (fever-inducing) contaminants of pharmaceutical products and equipment, as they are pervasive due to the ability of bacteria proliferating even in water, highly stable even under extreme temperatures & thus, may be retained even after sterilization, and has high toxicity³. As per cGMP guidelines, it is mandatory that all injectables be dually checked for the presence of endotoxin and labelled pyrogen-free, to negate any clinical mishap, especially in intensive care^{4,5}.

The currently available methods employed by companies for testing for LPS presence gravitate around (i) rabbit pyrogen test, which requires animal testing; (ii) limulus amoebocyte lysate test, and (iii) monocyte activation test, which are based on aqueous extract of amoebocyte cells found in *Limulus polyphemus*, the Atlantic horseshoe crab, threatening the already depleting horseshoe crab populations⁶. The significant lacunae in LPS sensing are that no rapid detection systems are available, which may aid in timely sensing and subsequent therapeutic support.

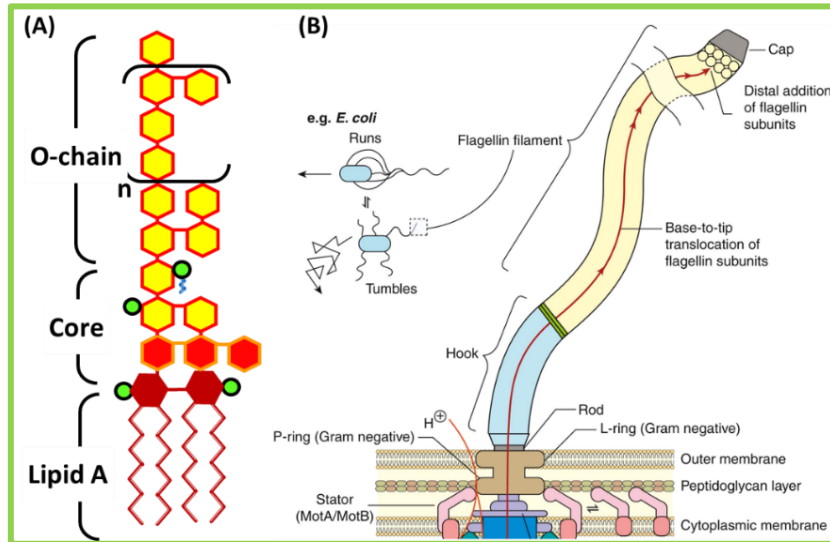


Figure 4.1: Surface antigens: Structural components of (A) LPS (B) flagella^{7,8}.

4.1.1.2 H-antigen

Additionally, pathogenic *E. coli* species produce flagella, which plays a significant role as mediators in pathogenesis, i.e., invasion, adhesion, and modulation of virulence factors via Type III secretion (Figure 4.1)^{8,9}. *E. coli* flagella, called the H-antigen in classical bacteriology, are fine long tubular structures, the walls of which consist of flagellin subunits whose immunological specificities are determined by surface exposed epitopes displayed upon the outer flagellar surface. The genetic diversity of H-antigens varies distinctly in various strains of *E. coli* subtypes and though numerous flagellar antigens are known, *fliC* loci on the bacterial chromosome is the most significant^{10,11}. It has been well-noted that these flagellar proteins act as adhesins, responsible for specific adhesion to the mucosa of the GI tract and subsequently resulting in disease manifestation¹². Similar to LPS, the mammalian host cells detect the conserved domain on flagellin monomers through TLR-5, which triggers pro-inflammatory responses, resulting in immune shock^{13,14}.

4.1.2 Objectives

- (i) **Bio-receptor generation:** Development of specific aptamer against surface antigens of *E. coli* O157:H7 using selective purified targets with help of competitive microtiter plate-based SELEX.

- (ii) **Transducer development:** Synthesis of carbon quantum dots using green sustainable chemistry and silver nanoparticles as an energy transfer pair as fluorophore and quencher for ‘turn-on’ fluorescence assay.
- (iii) **Aptasensor fabrication:** Functionalization of generated high-affinity aptamers onto carbon-based quantum dots via charge-based chemistry and application as ‘turn-on’ fluorescence sensor.
- (iv) **Platform validation:** Testing & validation of aptasensor in spiked water & sera samples.

4.1.3 Proposed biosensing platform for surface antigens

4.1.3.1 Preface

Recently, aptamers (single-stranded nucleic acids) have been employed as bio-recognition elements and have shown advantages over other capture moieties in terms of affinity, low-cross-reactivity, and stability. Coupling of these specific aptamers with sensitive nanostructures derives the synergistic potential to develop biosensing platforms for monitoring bacterial antigens. Nanostructures for biosensing of endotoxins have been widely explored owing to the enhanced transducer properties¹⁵. Quantum sized nanoparticles (1 – 10 nm), primarily carbon dots (c-dots), have received tremendous attention as optical probes due to their significantly high photoluminescent properties, stability, tunability, and low toxicity with varied applications in sensing^{16,17}. Numerous reports of their synthesis by a wide variety of organic materials and molecular precursors spanning the visible spectrum have been reported^{18,19}. In another study (not included in this thesis), we have also successfully reported the synthesis of gCN based quantum dots, which were applied for the detection of heavy metal ions. Therein, the quantum dots showed high specificity for palladium and mercury ions even without the presence of a bioreceptor when screened for a milieu of heavy metal ions, which pose an immense threat as pollutants from industrial effluents. Using these agarose-gCN conjugates were applied for the development of a flow-through cartridge, that helped in both visual detection and removal of heavy metals from various water sources¹⁹.

4.1.3.2 Our aptasensing approach: Surface antigens

This chapter brings into light the first report of the development of carbon dots from tris-base, which acts as both carbon and nitrogen source and its surface passivation with ss-DNA aptamers directed against lipopolysaccharides from *E. coli*. These conjugated probes show emission intensity loss in the presence of silver nanoparticles due to energy transfer, which is restored upon exposure of target LPS molecules. Using this concept, a similar study was used to evaluate the presence of flagellar protein extracted from *E. coli* O157:H7 cells, and the detection methodology is schematically illustrated in Figure 4.2.

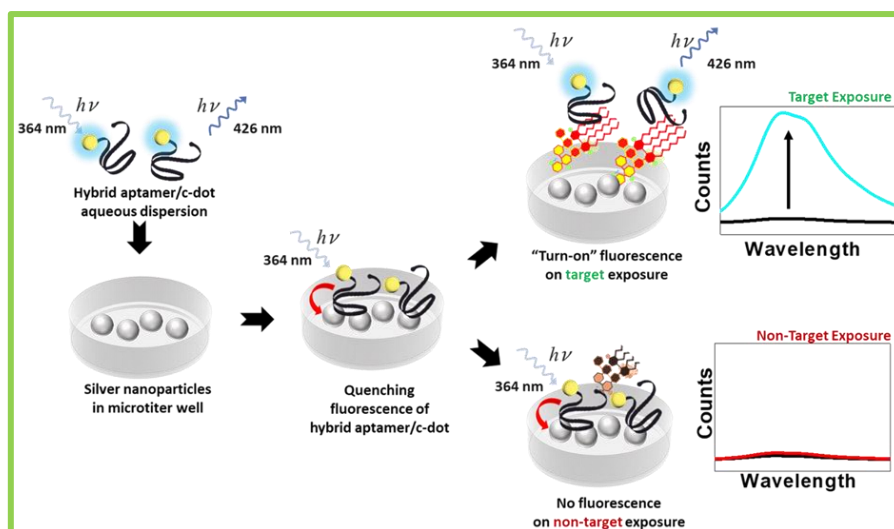


Figure 4.2: Schematic: Schematic showing step-by-step assay of detection of LPS/flagellin via aptamer mediated c-dot 'turn-on' assay.

As schematically illustrated, we synthesized Tris(hydroxymethyl)aminomethane derived water-soluble bright cyan carbon-dots via the simple solvothermal method and their high-affinity aptamer conjugates were used for sensitive fluorometric detection of surface antigens from *E. coli*. Besides, we have selected aptamers against O-antigen of *E. coli* O157:H7 using competitive microtiter-plate based SELEX having high affinity to the target molecules ($K_d \sim 5.3$ nM). This 'turn-on' fluorescence assay was based on the quenching of the fluorescence of hybrid aptamer c-dots by silver nanoparticles (AgNPs) via fluorescence resonance energy transfer. However, in the presence of the target endotoxin ($0.001 - 10$ ng mL⁻¹), the specific aptamer mediated interaction releases the hybrid aptamer-carbon dots away from the quencher nanoparticles, and the dampened fluorescence was recovered. This aptamer mediated assay showed a wide endotoxin target range and strong response even in unbuffered pure water & sera samples. Using a similar methodology, an anti-flagellin apt/c-dot conjugate assay was carried out for the flagellar protein (H-antigen) of *E. coli* O157:H7 showing significant fluorescence restoration from $0.001 - 1$ ng mL⁻¹ with a LOD of 0.1 pg mL⁻¹.

4.1.3.3 The novelty of experimental work

- (i) **Bio-receptor generation:** We have screened anti-O and anti-H *E. coli* O157:H7 aptamers generated by a competitive microtiter plate-based in-vitro route of selection with increasing stringency by the inclusion of competitive ligand molecules.
- (ii) **Nanostructure fabrication:** Synthesis of novel 0D quantum sized carbon dots from tris-base via hydrothermal approach, showing excellent optical properties, which are dispersive in aqueous medium and which can be efficiently applied as fluorescent tags in biological systems.

4.2 Experimental procedure

4.2.1 Materials

Silver nitrate, tris(Hydroxymethyl)aminomethane (Tris-base), NaBH₄, ethanolamine, bovine serum albumin (BSA), 2-Keto-3-deoxyoctonate (Kdo) ammonium salt was procured from Merck Sigma-Aldrich (India). Amino-Phenylboronic acid 95% (PBA) and Poly-vinyl-Pyrrolidone (PVP) were purchased from TCI Chemicals (India). All solutions were prepared with autoclave sterilized MilliQ water (18 M $\Omega \cdot \text{cm}$) inside a Class II Type A2 Biosafety Cabinet to avoid any contamination. All spectroscopic measurements were carried out in Nunc MaxiSorp, or Nunc FluoroNunc 96-Well Plates using 200 μL sample per well and monitored & recorded using BioTek Synergy H1 Multimode plate reader unless specified otherwise. The DNA naïve library & primers and buffers for SELEX and avirulent bacterial strains mentioned in Chapter 2, Section 2.2.1.1., were employed in this study also.

4.2.2 Isolation of surface antigens

4.2.2.1 O-antigen from *E. coli* O157:H7

4.2.2.1.1 Extraction & purification

(A) Modified hot-phenol method

The LPS was isolated using modified hot-aqueous-phenol extraction from freshly harvested *E. coli* O157:H7 cells. The methodology relies on the separation of LPS molecules in hot aqueous phenol based on their lipophilicity from other biomolecules like nucleic acids and proteins. Briefly, to the harvested cell pellet (5 g), 50 mL of 100 mM NaCl were added and heated to 68 °C in a water bath. Subsequently, an equal volume of hot phenol (68°C) was added, stirred for one hour, and later chilled on ice. The organic phase was separated by centrifugation at 12,000 \times g for 15 min at 4°C. The upper (water) layer was transferred and dialyzed (3.5 KDa) against the water until all residual phenol was removed. To this fully dialyzed extract, MgCl₂ (5 mM), DNase (20 $\mu\text{g mL}^{-1}$) & RNase (20 $\mu\text{g mL}^{-1}$) were added, and nuclear degradation was allowed for two hours at 37°C, and later on, proteinase-K (30 $\mu\text{g mL}^{-1}$) was added, incubated for two hours at 55°C and then centrifuged to obtain crude LPS²⁰. The crude LPS was then subjected to chloroform: methanol extraction using 1mL chloroform and 2 mL methanol added to 0.8 mL of extract for separation of any residual protein matter.

(B) Size-exclusion chromatography

Furthermore, the crude LPS was filtered by a 0.45 μm sterile syringe filters, degassed, and was subjected to purification using Fast-Protein Liquid Chromatography (FPLC) with the help a SEC80 column stabilized at physiological pH 7.5 in PB buffer at flow rate of 0.5 mL min⁻¹ (maintained to get good resolution) connected to a DuoLogic system (Bio-Rad). The fractions having maxima absorbance at 206 nm for polysaccharide presence were eluted and further characterized^{21,22}.

4.2.2.1.2 Quantification & visualization

(A) Kdo colorimetric assay

The purified LPS fractions were then quantified using standardized Kdo assay²³. Herein, the LPS is hydrolyzed under mild acidic conditions (such as 1 % acetic acid) to release the Kdo sugar and then oxidized with periodic acid (HIO₄) and sodium arsenite (NaAsO₂) forming formyl pyruvic acid which reacts with thiobarbituric acid (TBA) to give a chromophore with an absorption maximum at 552 nm. For the estimation of LPS, the Kdo standard (0, 40, 80, 120, 160 µg Kdo) was added to 0.5 N H₂SO₄ for 100 µL total volume and agitated using a vortex. These were then heated at 100 °C for 8 min, and subsequently brought to room temperature. To this 50 µL periodic acid (22.8 mg mL⁻¹) was added, mixed and incubated for 10 min at room temperature. Further, 200 µL arsenite reagent (40 mg mL⁻¹ in 0.5 N HCl) was added and mixed using a vortex. Next, 800 µL TBA reagent (6 mg mL⁻¹) was added, and samples are placed in a 100 °C heating block for 10 min. Finally, 1.5 mL butanol reagent (5.0 % v/v concentrated HCl; 95 % v/v *n*-butanol) was added for extraction of the chromophore, and the absorbance was measured at 552 nm.

(B) Modified LPS-PAGE gel electrophoresis

The purified LPS was characterized using polyacrylamide gel electrophoresis (on 12% separating gel to obtain high resolution amongst LPS molecules with minute molecular weight differences) and visualized using a modified silver staining procedure²⁴. In brief, the gel was submerged in 0.7% periodic acid in 40% ethanol, 5% acetic acid at for 20 min in the dark. After extensive rinsing with water 4 mL of ammonium hydroxide, 56 mL of 0.1 M sodium hydroxide, 200 mL water was added along with 10 mL of 20% (w/v) silver nitrate (added in drops while stirring). The gel was developed using 10 mg citric acid, 0.1 mL of 37% formaldehyde in aqueous solution, and the bands visualized using the gel-documentation system (Bio-Rad, USA).

4.2.2.2 H-antigen from *E. coli* O157:H7

4.2.2.2.1 Extraction & purification

The extraction was carried out using a reported methodology using overnight grown culture of bacteria, which were centrifuged at 4500×g, and the pellet gently washed with 0.9% saline (sterile) thrice and cells collected and finally resuspended in sterile petri dish plate²⁵. The inoculum suspension was lifted from the sterile petri dish plate with a sterile Luer lock tip and ejected back in the petri dish. This process was repeated ten times with the same material to shear off cell-associated flagella. The sheared off cells and flagella were transferred to a centrifuge tube and centrifuged at 17000×g for 10 min at 4°C. The supernatant containing sheared-off flagella was additionally concentrated by the addition of 250 mL of cold trichloroacetic acid solution (20%) for one hour on ice and centrifuged for 40 min at 4°C at 17000 ×g to remove the supernatant. The TCA was washed off by using cold ethanol washings, and finally, a dialysis using a 3.5 kDa membrane

was carried out. This sheared flagellar protein was injected into the FPLC system as mentioned in earlier section, and the elutes at 280 nm were collected.

4.2.2.2 Quantification

Of the purified elutes, the protein concentration measurement was carried out using Bradford's reagent. A standard curve with BSA (2 - 10 μg per 100 μL) was plotted with the addition of 500 μl of Bradford's reagent to each vial and mix and incubated at 30°C for 10 min as per standardized Himedia protocol²⁶. When the protein in the test sample binds to Bradford's reagent, the color of the solution turns from brown to blue visibly and the coloration was observed and the absorbance maxima at 595 nm measured for the complex.

4.2.3 Aptamer technology for target antigens

4.2.3.1 Competitive microtiter-SELEX

The microtiter-SELEX iterative rounds are consisting of binding, elution, amplification & partitioning, which were carried out per our previous Chapter 2 with modifications to include competitive counter screening for the oligomers with already known molecules having binding affinity. Briefly, a naïve library consisting of a random pool of oligomers was exposed to purified O-antigen (1 μg well⁻¹) coated on microtiter well. The positive binder fraction eluted, amplified, partitioned to single-strand, and re-exposed to target. In case of LPS, this was done in the presence of increasing concentrations of competing ligands (0 - 25 μM) viz., phenylboronic acid (PBA) and polymyxin B (PMB) in each subsequent SELEX round to increase stringency and the counter rounds were carried out against albumin and flagellar protein from *E. coli* O157:H7 & O78:H11, to minimize cross-reactivity due to other cellular moieties which may be present in biological samples. As shown in Figure 4.3, PBA and PMB are both selective molecules that bind to the two distinct regions of LPS, i.e., polysaccharides and lipid regions, respectively.

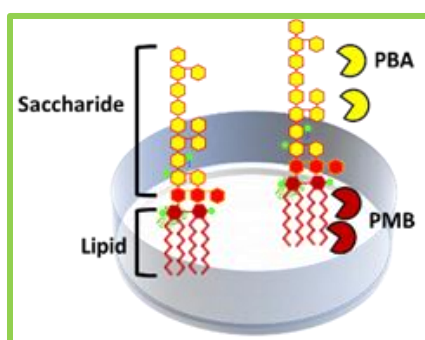


Figure 4.3: Competitive ligands of LPS: Illustrating the binding sites of competing molecules.

The quantity and purity of the binder population after each SELEX round was assessed spectroscopically at 260 nm to evaluate DNA quantity and quality. Similarly, the aptamers were selected for H-antigen, with increasing stringency with the inclusion of albumin and counter-selection against albumin, flagellar protein from *E. coli* O157:H7 & O78:H11. The binder fractions

were then purified, cloned & sequenced to elucidate the individual aptamer's putative primary, secondary, and tertiary structure following our previous detailed procedures in Chapters 2, Section 2.2.1.3.3.

4.2.3.2 Aptamer characterization

(A) Binding affinity

The binding affinity of the selected aptamers was investigated using BLI. For the bio-interaction, using the similar biotin-labelled primer technique explored in previous chapters, the anti-LPS aptamer was attached to the SSA sensor and allowed to associate and dissociate with three different concentration of LPS. On a similar note, the studies for aptamer-protein bio interaction and aptamer-whole cell interaction for flagellar protein was carried out. Furthermore, to verify the binding of the aptamer to whole-cell, various dilutions of *E. coli* O157:H7 were also exposed to an aptamer modified sensor.

(B) Aptamer structure

The secondary & tertiary structures were elucidated using online bioinformatic tools; 'mfold' & 'RNA composer' as in mentioned in previous chapters. Briefly, 'the mfold' was employed to predict secondary structures of the ss-DNA aptamers from the deduced sequence. Using the Vienna bracket format, a 3D model was constructed for selected aptamer using the RNAComposer, which were later manually altered and energy minimized into ssDNA structures using the PyMOL mutation tool^{27,28}.

4.2.3.3 Interaction studies for flagellar protein- A bioinformatic study

The bio-interaction between the anti-flagellin aptamer and flagellin was studied with the help of Zdock 3.0.2²⁹. Zdock is an automated online bioinformatic tool which assists in protein-protein and protein-nucleic acid interactions. It evaluates the various binding modes in the translational and rotational space between the two molecules and evaluates each pose using an energy-based scoring function³⁰. For this study, the sequence was retrieved for flagellin *E. coli* O157:H7 (accession ID. Q7AD06_ECO57) and modeled using Swiss-Modeler (<https://swissmodel.expasy.org/>). Furthermore, the protein structure was energy minimized using YASARA³¹. Using the energy minimized 3D structure of the flagellin monomer and that of aptamer, the Zdock server was used for predicting the interactions between the two. The pre-automated 192×1.2×1 grid was used for performing the docking function, denoting the spacing between grid cells (1.2Å) and where the protein-ligand (being the larger molecule) was kept stationary and allowed to interact with the DNA aptamer sequence.

Furthermore, to simulate the interaction between flagella and the aptamer, this flagellin protofilament was restructured by symmetric multimerization of the FliC sequence using a free-online protein docking tool M-Zdock (<http://zdock.umassmed.edu/m-zdock/>)³². For predicting the structure of cyclically symmetric multimers based on the structure of a flagella filament, the

monomers were cyclically arranged in pre-automated 200×1.2×1 grid with an inter-grid spacing of 1.2 Å for the docking of 11 monomeric units. The finalized structure was energy minimized using Swiss-Modeler, and was allowed to interact with the aptamer DNA using Zdock. A similar study for LPS and aptamer was attempted but no bioinformatic tools in public access domain were found currently available to simulate interactions between complex lipid and polysaccharide units. Simulations regarding the same will be addressed in future works.

4.2.4 Fabrication of nanostructured optical platform

4.2.4.1 Synthesis of c-dots

The c-dots were synthesized via a one-step hydrothermal pyrolysis approach using Tris-base as carbon and nitrogen source (Figure 4.4). Briefly, 10 g tris-base was added to 25 mL of deionized water and transferred to a 50 mL teflon-lined stainless-steel autoclave and kept at 180°C for varied time periods. The obtained carbonized solution was centrifuged at 25,000×g to remove larger charred particles and the supernatant collected & filtered with 0.45 µm filter paper to remove any aggregates. Finally, the c-dots were dialyzed using a 3.5 KDa dialysis membrane overnight to remove any non-reactant precursor molecules. These were then concentrated in a vacuum concentrator and a stock solution of 10 µg mL⁻¹ prepared and diluted to 1% for further assays. The silver nanoparticles (AgNPs) were synthesized with PVP & NaBH₄ using an optimized method³³.

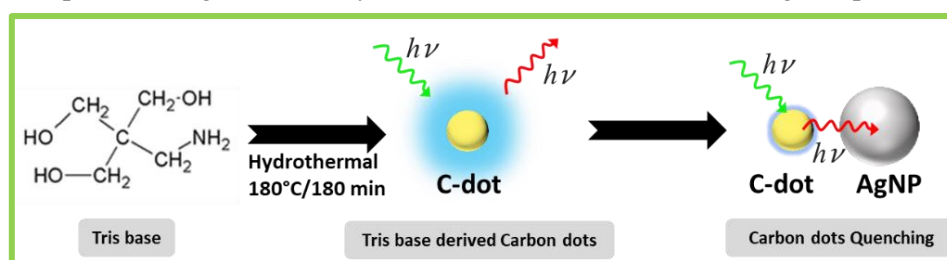


Figure 4.4: Synthesis schematic: Showing in brief c-dot synthesis and its optical activity.

4.2.4.2 C-dots mediated optical assay development

4.2.4.2.1 Characterization of nanostructures

The synthesized c-dots were characterized by various spectroscopic techniques (UV-Vis, DLS, XRD, FT-IR & confocal Raman) and electron microscopy with specifications as mentioned in Chapter 2. Furthermore, to evaluate the excitation λ_{\max} and emission λ_{\max} , an excitation-emission matrix (EEM) was generated to record the wavelength range with the highest fluorescence intensity and as well as the spectrum overlap with that of silver nanoparticles necessary for energy transfer.

4.2.4.2.2 Optimization of synthesis parameters

To further optimize the amount of time needed to generate highly fluorescent c-dots, the hydrothermal time of the reaction was varied from 0 - 210 min at a constant temperature of 180°C. Also, the effect of pH variation on the fluorescence was evaluated and the fully characterized water dispersed c-dots were then used for conjugation with specific aptamers for the optical assay.

4.2.4.2.3 Bio-conjugation of c-dots

The aptamers ($200 \mu\text{g mL}^{-1}$) & c-dots were incubated overnight at 4°C to allow conjugation via ionic interactions. The free-molecules were removed via dialysis and vacuum concentrated at 4°C . The conjugation was spectroscopically observed via UV-Vis & DLS techniques. and to experimentally validate if the conjugation had taken place, zeta potential (ζ) measurements were carried out.

4.2.4.2.4 Assay optimizations

Further optimization of assay parameters was carried out to study binding interaction of LPS and aptamer functionalized c-dots. Here, the microtiter well coated with overnight with different concentrations of LPS ($0- 2 \mu\text{g mL}^{-1}$) was exposed to increasing concentrations of apt/c-dots and the fluorescence signal recorded. Also, the fluorescence quenching behavior of AgNPs on prepared c-dots was studied when increasing volumes of AgNPs (1 OD stock) was titrated to apt/c-dots. This optimized conjugate was used for the bio-assay of our target molecules, O-antigen and H-antigen of *E. coli* O157:H7.

4.3 Results & discussion

4.3.1 Quantification & visualization of surface antigens

4.3.1.1 O-antigen from *E. coli* O157:H7

The LPS was isolated using modified hot-aqueous-phenol extraction from freshly harvested *E. coli* O157:H7 cells and then subjected to chloroform: methanol extraction for separation of any residual protein matter. The crude LPS was subjected to purification using liquid chromatography using SEC80 column, Figure 4.5A shows the fractions having maxima absorbance at 206 nm for polysaccharide presence, and which were eluted for further characterization. The purified LPS fractions were then quantified using Kdo assay, and the absorbance was measured at 552 nm. The

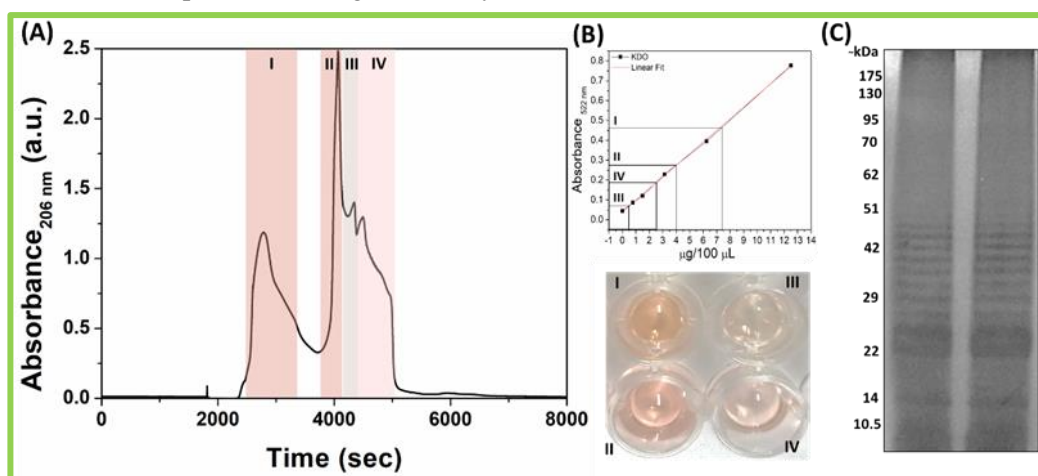


Figure 4.5: O-antigen purification & characterization: (A) FPLC spectrum showing the peak intensity of LPS monitored and eluted at 206 nm. (B) The Kdo assay standard curve, along with optical images showing the colorimetric change and presence of Kdo in various elutes. (C) The elute with the highest intensity was visualized using modified silver staining to obtain the characteristic ladder type pattern of purified LPS.

sample concentration was determined from the standard curve for each batch of LPS extracted for the studies. The test samples (fractions I, II, III, IV) showed a chromogenic change from colorless to reddish pink with an increasing concentration of Kdo in the elutes (Figure 4.5 B). The elute with highest concentration was taken and the purified LPS was run on a PAGE gel and visualized using a modified silver staining procedure and the characteristic ladder-type pattern observed for smooth LPS (Figure 4.5C).

4.3.1.2 H-antigen from *E. coli* O157:H7

The H-antigen was extracted by shearing-off technique and purified via FPLC and the extracted flagellar protein was quantified by Bradford's reagent. The change of color from brown to blue gives a qualitative visual clue for protein presence. The samples were transferred to a microtiter well plate, and the absorbance maxima at 595 nm measured for quantitative measurement. Finally, the purified H-antigen protein was visualized via polyacrylamide gel electrophoresis using 10% separating gel which is apt for resolving 35-100 kDa proteins. This was then visualized with help of Coomassie dye which stains the protein bands blue.

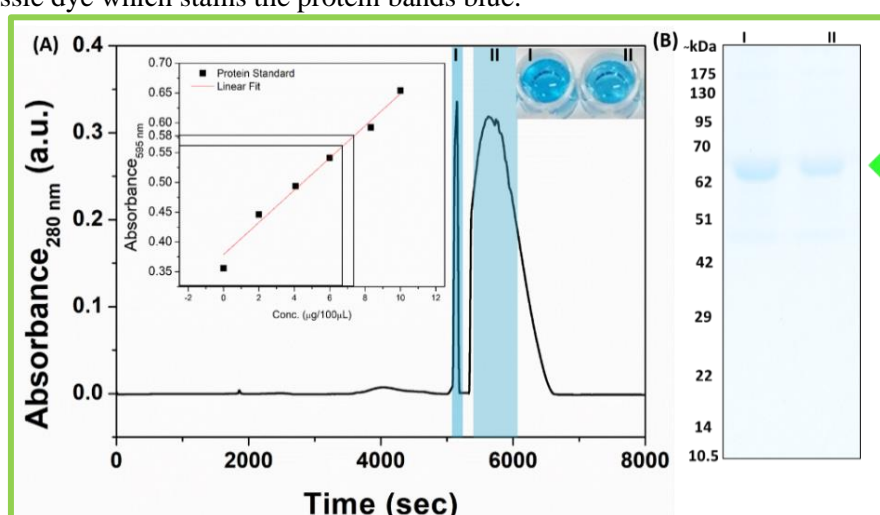


Figure 4.6: H-antigen purification & quantification: (A) FPLC spectrum showing significant peaks alongside the Bradford standard curve and test samples. (B) The Coomassie-stained native-PAGE gel visualized using gel-doc. Green arrow showing the stained band at ~65 kDa.

4.3.2 Anti-O and anti-H aptamer selection

Respective aptamers for the somatic and flagellar antigens were selected using 45-nt DNA oligomer library via a competitive ligand induced microtiter plate-based SELEX technology. As observed in Figure 4.7, the SELEX process was monitored by measuring the ssDNA concentration eluted after each SELEX round at $\lambda_{260\text{ nm}}$, which showed a gradual increase in binder population after each positive round (1 – 5th rounds) where the target binder fractions were amplified, single-stranded and re-introduced into the next selection iterative round. During counter-selection (6-8th rounds), the binder oligomer fractions were discarded, and the non-binder pool against non-target molecules was similarly processed and exposed in the subsequent round. A final positive selection round (9th)

was necessary to validate that the selected aptamer pool was efficaciously interacting with our target molecule and proved so with high concentration ($5 \text{ ng } \mu\text{L}^{-1}$) of DNA binders in the elute.

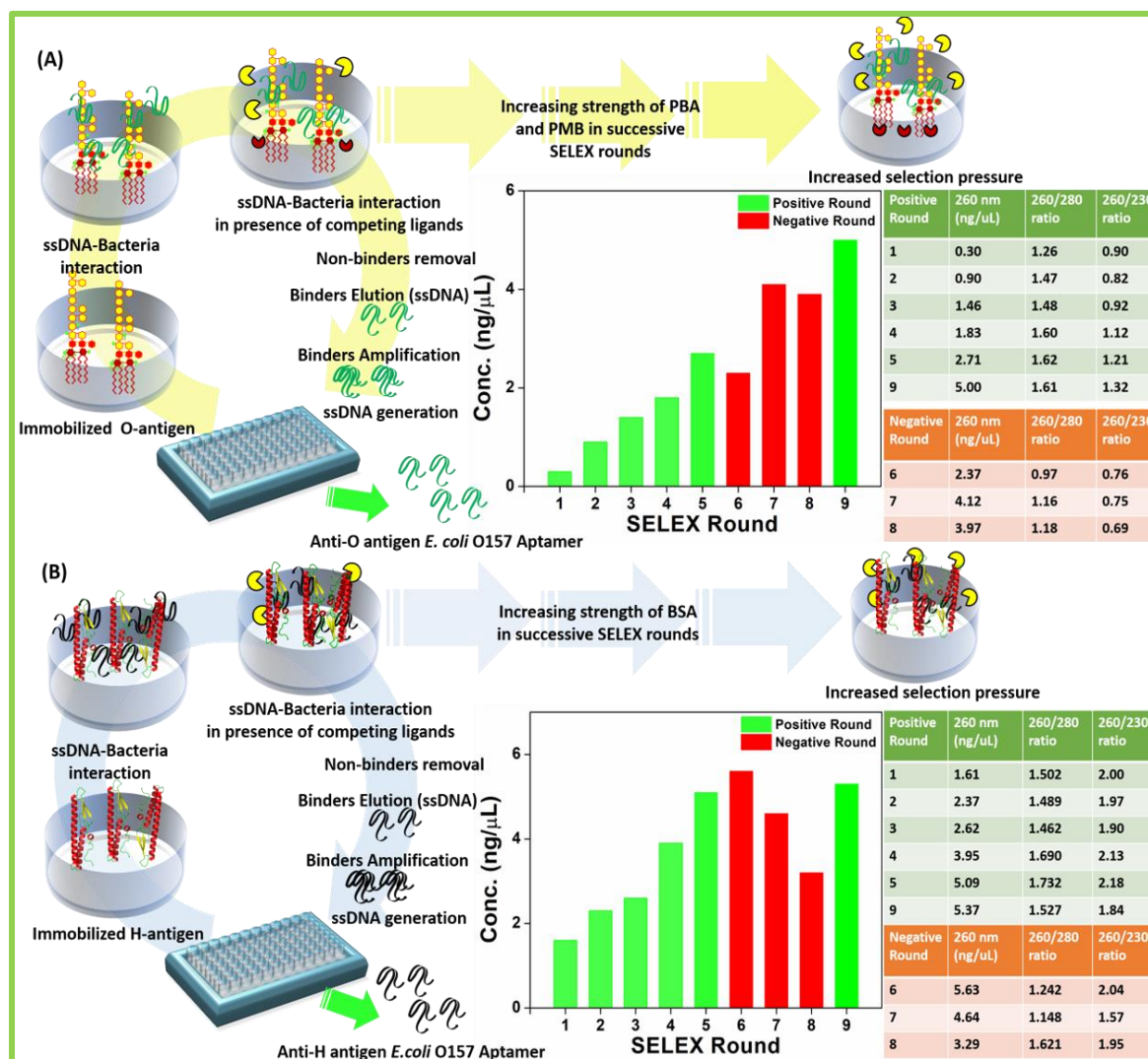


Figure 4.7: Competitive microtiter-SELEX: Schematic and spectrophotometric progression of competitive microtiter plate-based SELEX of purified (A) O-antigen and (B) H-antigen of *E. coli* O157:H7.

4.3.3 K_d estimation – BLI studies

The binding affinity of the selected aptamers was investigated using BLI. For the bio-interaction, using the similar biotin-labelled primer technique explored in previous chapters, the anti-LPS aptamer was attached to the SSA sensor and allowed to associate and dissociate with three different concentration of purified O-antigen. The K_d was estimated to be $\sim 5.3 \text{ nM}$ for anti-O antigen specific aptamer (Figure 4.8A). Furthermore, to verify the binding of the aptamer to whole-cell, various dilutions of *E. coli* O157:H7 were also exposed to another Anti-O antigen aptamer modified sensor, which showed that the aptamer had good association/dissociation kinetics with whole cell also. (Figure 4.8B). On a similar note, the studies for aptamer-protein interaction and aptamer-whole cell interaction for H-antigen was carried out, showing functional kinetics and a K_d value of $\sim 4.6 \text{ nM}$ for anti-H antigen specific aptamer and affinity kinetics for whole-cell (Figure 4.8C-D).

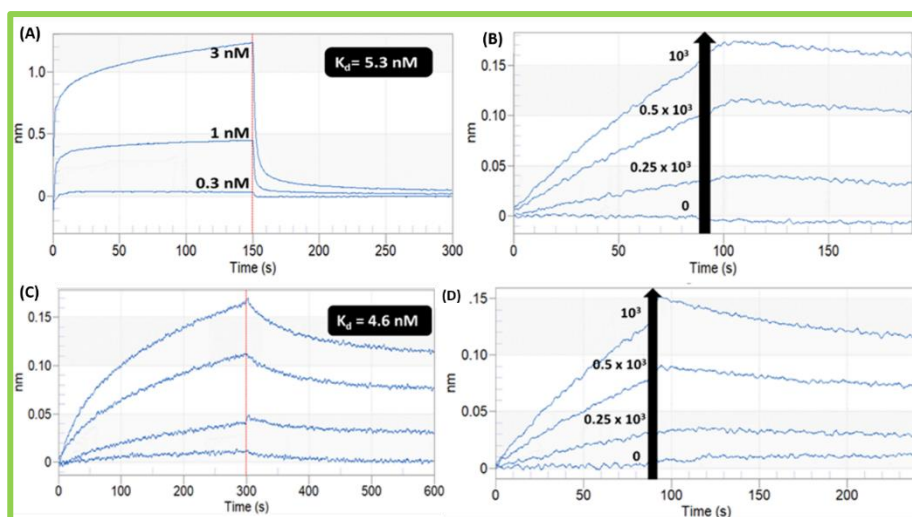


Figure 4.8: BLI bio-interaction studies: (A) *O*-antigen and aptamer interaction and (B) Anti-*O* aptamer-whole cell interaction. (C) *H*-antigen and aptamer interaction and (D) Anti-*O* aptamer and whole cell interaction.

4.3.4 Aptamer binding site

In the comparison of study undertaken in Chapter 3, where the whole cell aptamer showed $K_d \sim 69$ nM, the current anti-*O* antigen aptamer showed a higher affinity to its target. Moreover, to improve our knowledge of the bio-interaction between the aptamer and target LPS, a fluorescence assay between LPS blocked with an excess of LPS ligands (PBA and PMB) and FITC labeled anti-LPS aptamer were carried out (Figure 4.9). Possible scenarios were investigated viz., the aptamer binding to whole LPS moiety without specificity; with PBA pre-blocking sugar region, the aptamer must be binding to lipid region, and; with PMB blocking lipid region the aptamer must be preferentially binding to saccharide region. The fluorescence interaction assay showed maximum fluorescence counts when FITC-labelled aptamer was allowed to interact with whole LPS, followed

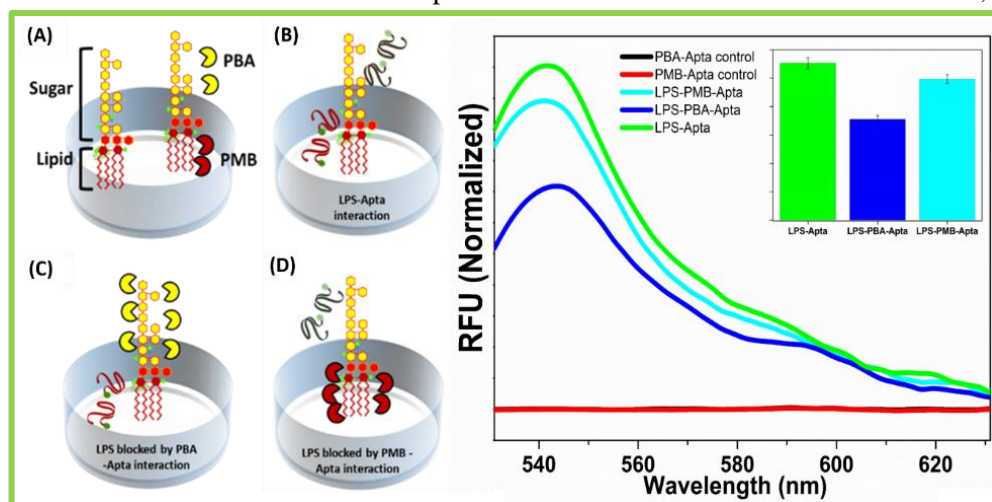


Figure 4.9: Anti-*O* aptamer interaction site: (Left) (A) PBA binds & blocks saccharide binding, while PMB binds & blocks lipid A binding in LPS. Possible scenarios were investigated viz., (B) the aptamer binding to whole LPS moiety without specificity; (C) with PBA pre-blocking sugar region, the aptamer must be binding to lipid region, and; (D) with PMB blocking lipid region the aptamer must be preferentially binding to saccharide region. (Right) The fluorescence binding assay showed maximum FITC counts when FITC-labelled aptamer was allowed to interact with whole LPS and then PMB and PBA pre-blocked LPS.

by PMB and PBA pre-blocked LPS, respectively. Thus, denoting that the anti-O antigen aptamer showed more significant interaction towards saccharide (PMB blocked LPS) than lipid region (PBA blocked LPS) in the LPS.

4.3.5 Modelling studies

4.3.5.1 Aptamer structure

The final aptamers were inserted in pTZ57R/T vector and transformed into competent *E. coli* DH5 α cells using the InsTAclone PCR cloning kit and were outsourced for sequencing as per protocols mentioned in Chapter 2, Section 2.2.1.3.3. and further analyzed for the secondary & tertiary structures using online bioinformatic tools; ‘mfold’ & ‘RNA composer’ as in previous studies. The sequence clones were analysed using the QGRS tool to predict the presence of quadruplex forming G rich sequences, and those conforming to G-quadruplex structure were chosen and further analysed. Figure 4.9 shows the structural and thermodynamic results for anti-O antigen and anti-H antigen aptamer, respectively.

Here, the optimal anti-O antigen aptamer sequence was found to be:

```
5'-ATCCAGAGTGACGCAGCACAGGGGAATCGGCGCCCCGATTATGCTG  
GCGGGTGTGACGGGATGTGGACACGGTGGCTTAGT-3'
```

This sequence showing two G-quadruplex motifs starting from position N₂₁ & N₅₀ was selected. Secondary structures, along with the thermodynamic stability of folding ($\Delta G = -8.6$ kcal mol⁻¹) and melting temperature ($T_m = 61.4$ °C) using mfold bioinformatic tool were predicted assuming a 2-state model for linear DNA folding (Figure 4.10 A). The aptamer structure showed significant helical and loop-stem folding, particularly three hairpin loops from G₁₀-C₁₇, G₃₀-C₃₅, T₅₂-A₆₇, and internal loops from G₄₉-C₇₀ and G₄₆-T₇₃.

The optimal anti-H antigen aptamer sequence was found to be:

```
5'ATCCAGAGTGACGCAGCATGTGTTCGGTGTCTGACGTCGAGGTGCTGTGGGGG  
CGGATGAGGCTGGACACGGTGGCTTAGT-3'
```

This sequence showing two G-quad motifs from N₂₆ & N₅₅ was chosen, which was computed to have minimal $\Delta G = -3.7$ kcal mol⁻¹ and melting temperature $T_m = 56.4$ °C amongst the others (Figure 4.10 B). The aptamer also showed loop-stem folding giving distinct structure to the aptamer from A₁₁-T₂₃ and A₄₀-T₇₇. Furthermore, the 3D rendering of the aptamer structure was done using an RNA composer modeling server and validating the structural complexity of the aforementioned aptamer sequences.

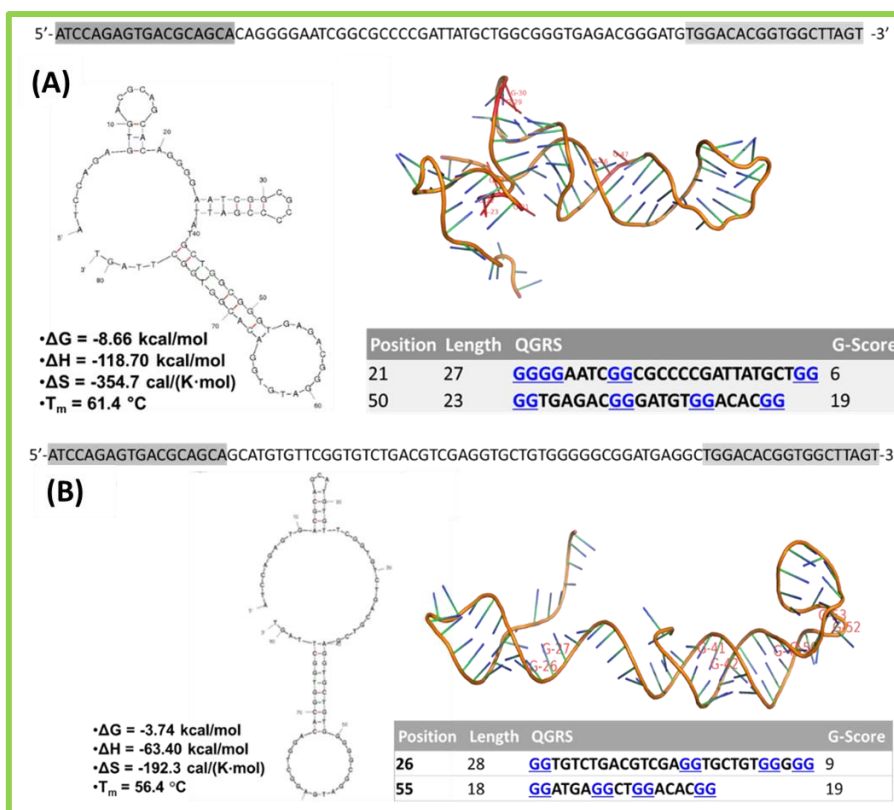


Figure 4.10: Aptamer structures: The sequences of the aptamers along with their 2D and 3D structure and QGRS results are listed (A) Anti-O antigen aptamer and (B) Anti-H antigen aptamer.

4.3.5.2 Z-dock interaction studies for H-antigen

The bio-interaction between the anti-flagellin aptamer and flagellin was studied with the help of Zdock 3.0.2³⁴. Zdock evaluates the various binding modes in the translational and rotational space between the two molecules and evaluates each pose using an energy-based scoring function. For this study, the sequence was retrieved for flagellin *E. coli* O157:H7 (accession ID. Q7AD06_ECO57) and modeled using Swiss-Modeler (Figure 4.11):

```
>tr|Q7AD06|Q7AD06_ECO57 Flagellin OS=Escherichia coli O157:H7 OX=83334 GN=fliC PE=3 SV=1
MAQVINTNSLSLITQNNINKNQSALSSSIERLSSGLRINSAKDDAAGQAIANRFTSNIKGLTQAARNA
NDGISVAQTTEGALSEINNNLQRIRELTVQATTGTNSDSDLDSIQDEIKSRLDEIDRVSGQTQFNGV
NVLAKDGSMKIQVGANDGETITIDLKIDSRTLGLNGFNVNGKGTITNKAATVSDLTSAGAKLNTT
TGLYDLKTENTLLTTDAAFDKLGNQDKVTVGGVDYTYNAKSGDFTTTKSTAGTGVDAAAQAAD
SASKRDALAATLHADVVGKSVNGSYTTKDGTVSFETDSAGNITIGGSQAYVDDAGNLTNNAGSAA
```

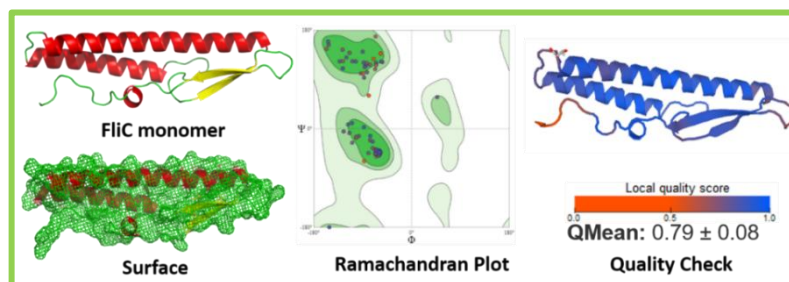


Figure 4.11: Flagellin monomer: The sequence optimized 3D structure of FliC using the Swiss-model, along with its Ramachandran plot and quality check of the structure generated out of homology modeling.

KADMKALLKAASEGSDGASLTFNGTEYTIAKATPATTTPVAPLIPGGITYQATVSKDVLSETKAA
 AATSSITFNSGVLSKTIGFTAGESSDAAKSYVDDKGGITNVADYTVSYSVNKDNGSVTVAGYASAT
 DTNKDYAPAIGTAVNVNSAGKITTETTSAGSATTNPLAALDDAISSIDKFRSSLGAIQNRLDSAVTN
 LNNTTTLSEAQSRIQDADYATEVSNMSKAQIIQQAGNSVLAKANQVPQQVLSLLQG

Using the energy minimized 3D structure of the flagellin monomer and that of aptamer, the Zdock online server was used for predicting the interactions between the two and out of the numerous results, the interaction showing the highest Zdock score 1215.283 was analyzed, and the blue denoted regions depicting the DNA molecules interacting with the protein were seen. Zdock score is a docking scoring function that includes shape complementarity, electrostatics, and a pairwise atomic statistical potential developed using contact propensities of transient complexes³⁵. Three significant binding pockets of the aptamer with the monomer were observed, showing the interaction of the aptamer with the protein monomer (Figure 4.12).

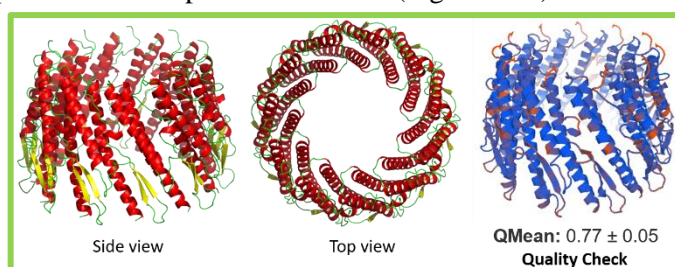


Figure 4.12: Flagellin multimer: Flagellin multimer generated with help of M-Zdock and energy optimized by Swiss-Modeler.

Furthermore, to simulate the interaction between flagella and the aptamer, this flagellin protofilament was restructured by symmetric multimerization of the FliC sequence using a free-online protein docking tool M-Zdock. For predicting the structure of cyclically symmetric multimers based on the structure of a flagella filament, the monomers were cyclically arranged in a pre-automated 200×1.2×1 grid for the docking of 11 monomeric units with an inter-grid spacing of 1.2 Å. The finalized structure was energy minimized using Swiss-Modeler, as shown in Figure 4.13. This minimized multimer was allowed to interact with the aptamer DNA using Zdock server as in previous study. The visualization of the docking results showed four major interacting sites

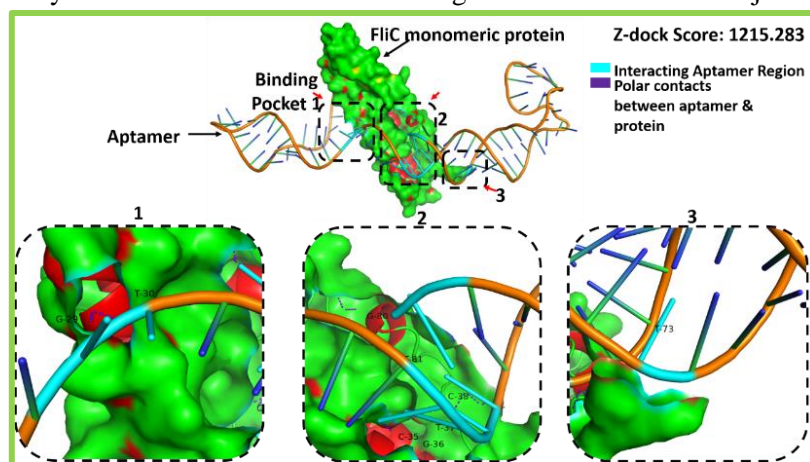


Figure 4.13: Z-dock interaction studies: Aptamer-flagellin monomer interaction, showing the various interaction points (highlighted in cyan) and non-covalent interactions (highlighted in purple).

(denoted in blue) with the multimer having a high Z-dock score of 1247.5 (Figure 4.14). Thus, it was ascertained that the aptamer did interact with the H-antigen in-silico via abundant non-covalent interactions as well as structural induced fitting.

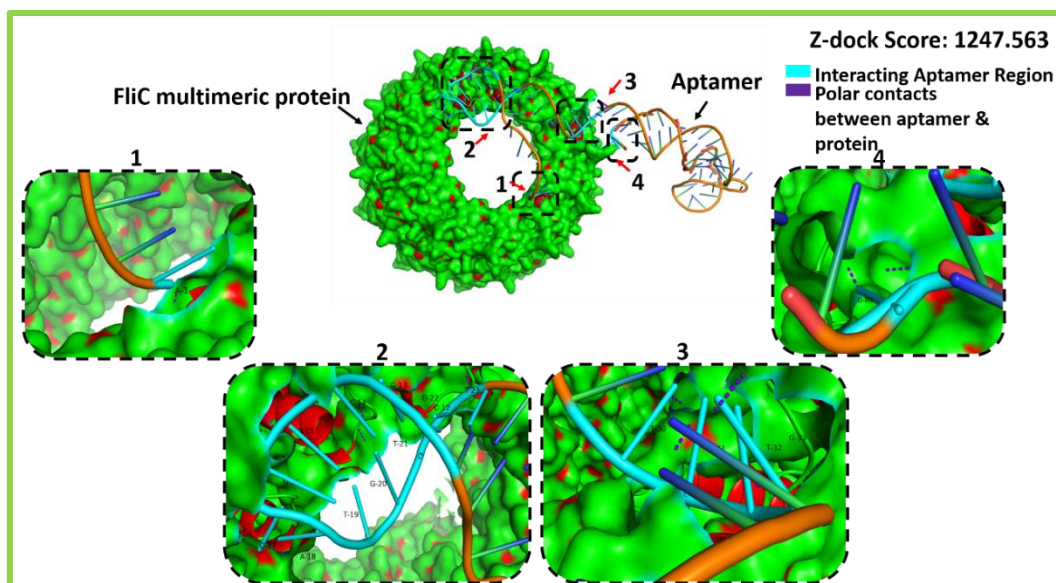


Figure 4.14: *M-Zdock studies for multimer interaction: Flagellin multimer generated with help of M-Zdock and DNA aptamer interaction showing zoomed in points of contact.*

4.3.6 Nanostructured platform characterization

4.3.6.1 Synthesis & characterization of C-dots

The c-dots were synthesized via a one-step hydrothermal pyrolysis approach using Tris-base as carbon and nitrogen source. These were characterized by various spectroscopic techniques (UV-vis, DLS, XRD, FT-IR & confocal Raman) and electron microscopy. The prepared c-dot dilution showed bright blue color upon UV light exposure suggesting its excellent fluorescence properties (Figure 4.15 A). This optical fluorescence was supported by UV-Vis extinction spectra showing an absorption at 337 nm and upon excitation showed fluorescence in the range of 425-475 nm. Also, the extinction spectra of AgNPs were obtained, which showed significant overlapping with the fluorescence emission of c-dots. Thus, this gave us an insight that these can act as energy transfer couple, with c-dots acting as donor and AgNPs as quencher unit.

Furthermore, to evaluate the excitation λ_{\max} and emission λ_{\max} , an EEM was generated (Figure 4.15 B). Here, the c-dots were excited from 300-410 nm at a pitch of 10 nm and the emission recorded at each step. The EEM plotted revealed that the fluorescence pattern showed two high-intensity emissions, with the highest fluorescence intensity recorded at excitation λ_{\max} of 364 nm and emission λ_{\max} of 426 nm. Using this information, all the latter studies were recorded at these wavelengths.

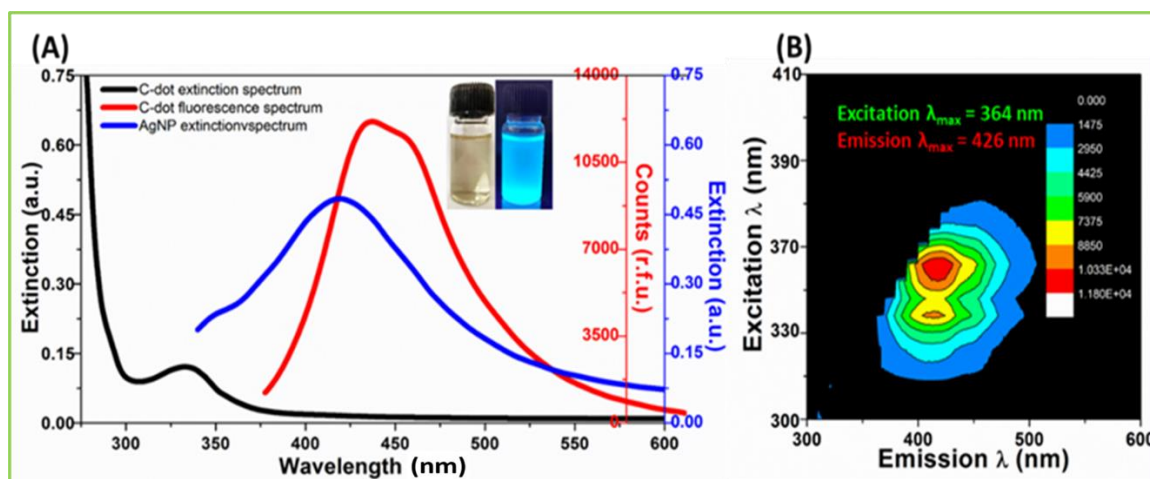


Figure 4.15: Spectrophotometric characterization: (A) Spectra showing the extinction spectra of the synthesized c-dots and the fluorescence spectra, extinction spectra of AgNPs overlapping with it and the optical images under white and UV light (inset). (B) The excitation-emission matrix of c-dots.

4.3.6.2 C-dots optimization & characterization studies

The amount of time needed to generate highly fluorescent c-dots; the hydrothermal time of the reaction was varied from 0 - 210 min at a constant temperature of 180°C. It was observed that the fluorescence intensity shoots after 120 min of reaction but doesn't show any significant increase

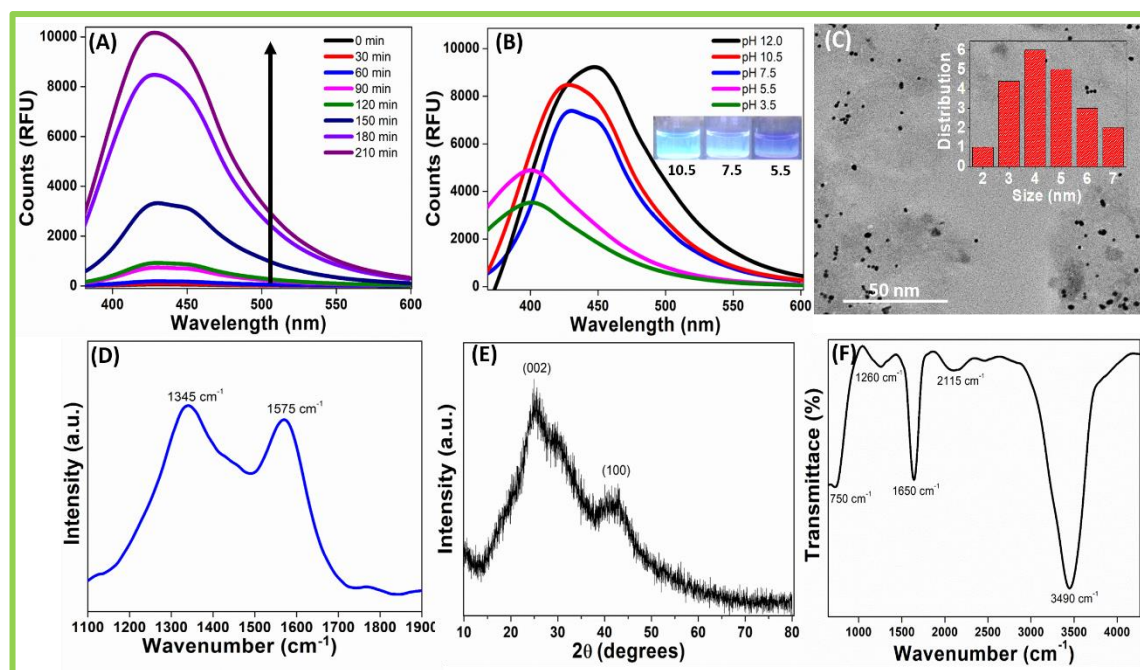


Figure 4.16: C-dot characterization: (A) Hydrothermal time optimization (B) shift in fluorescence emission and intensity with pH variation and optical images (inset). (C) TEM image showing the dispersed c-dots with an average diameter of 4 nm. (D) Raman spectrum showing the carbon signature D and G peaks. (E) XRD spectrum showing the amorphous nature of the c-dots. (F) FT-IR spectrum showing major surface functionalization with -CO, CN and -OH vibrations.

after 180 min (Figure 4.16A). Thus, this time was optimized and used for the synthesis of nanomaterial used in further studies. Also, the effect of pH variation on the fluorescence was

evaluated, and it was observed that it was most enhanced in an alkaline environment, but showed a decrease in intensity as well as a blue shift with a decrease in pH (Figure 4.16B).

(A) TEM microscopy

The TEM micrographs shown in Figure 4.16 (C) supported the generation of c-dots, which appeared quasi-spherical in nature with an average diameter of 4 nm.

(B) Raman spectroscopy

However, Raman spectroscopic analysis showed characteristic D and G bands of carbon at 1345 cm^{-1} and 1575 cm^{-1} , hinting that although highly disordered, the carbon dots are graphitic in nature³⁶ (Figure 4.16 D).

(C) XRD spectroscopy

Furthermore, the crystal structure of the prepared C-dots was studied using X-ray diffraction, and it became evident from the broad peak at around 25° which represents the (002) plane of graphite and at 45° corresponding to (100) plane originated due to the in-plane diffraction of graphitic c-dots³⁷ (Figure 4.16 E).

(D) FT-IR spectroscopy

The FT-IR analysis showed prominent peaks at 750, 1260, 1650, 2115, and 3490 cm^{-1} as indicated in Figure 4.16 (F) arising due to C-H bending, C-N stretching, C=O stretching, C≡C stretching and -OH stretching, respectively confirming surface functionalization of these quantum dots³⁸. These functional groups impart admirable properties to c-dots rendering them highly dispersible and stable in aqueous medium.

4.3.6.3 C-dots quantum yield estimation

The quantum yield (Φ) of the c-dot was estimated using quinine sulfate (QS) as reference fluorophore (Figure 4.17). To calculate the quantum yield, multiple dilutions of each sample and reference were made having absorbance less than 0.1 at 344 nm, which is the excitation λ_{maxima} of QS. The dilutions of QS were made in 0.05M H_2SO_4 ($\Phi_{\text{QS}} = 0.54$, $\eta_{\text{QS}} = 1.33$) and the c-dots was diluted in pure water ($\Phi_{\text{c-dot}} = \text{unknown}$, $\eta_{\text{c-dot}} = 1.33$) and their corresponding fluorescence spectra recorded at $\lambda_{344 \text{ nm}}$. The data was plotted and the slopes of the plots were determined using formula:

$$\Phi_{\text{c-dot}} = \Phi_{\text{QS}} (b_{\text{c-dot}} / b_{\text{QS}}) (\eta_{\text{c-dot}}^2 / \eta_{\text{QS}}^2)$$

$$\Phi_{\text{c-dot}} = 0.54 (166999.475 / 604532.330) (1.33^2 / 1.33^2)$$

$$\Phi_{\text{c-dot}} = 0.149$$

$$\Phi_{\text{c-dot}} \% = 14.9 \%$$

where, Φ is the quantum yield, b is slope and η is the refractive index of the solvent (water) The quantum efficiency for our developed c-dots was found to be 14.9% in reference of QS.

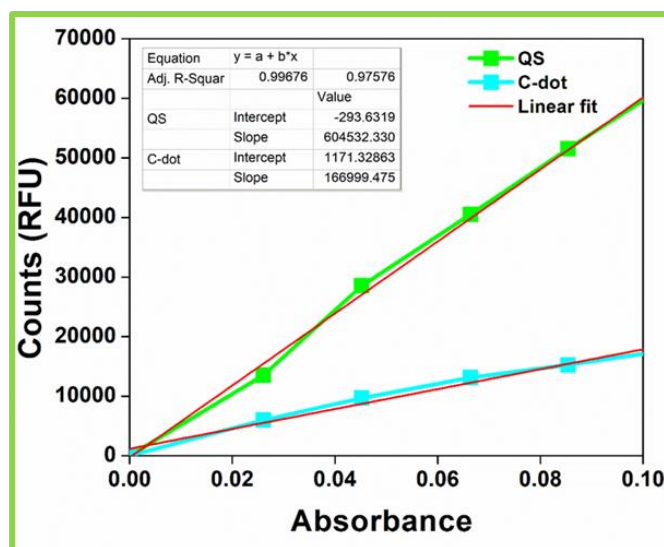


Figure 4.17: Quantum yield plot: Absorbance vs. fluorescence signal intensity plot of reference quinine sulfate and test c-dots.

4.3.6.4 Aptamer functionalization of C-dots

The apt/c-dot nanoconjugates were spectroscopically validated via UV-Vis & DLS studies. Figure 4.18 (A) shows the before and after conjugation spectra of the aptamer functionalized c-dots displaying the presence of DNA at 260 nm. Furthermore, to experimentally validate if the conjugation had taken place, zeta potential (ζ) measurements were carried out, which showed a shift from -18.4 mV to -45.8 mV in ζ value after DNA functionalization (Figure 4.18 B). This also points to the excellent stability of the dispersion in the aqueous medium due to the presence of a highly charged surface. Additionally, it was observed that the hydrodynamic size of the nanoparticles increased from 30 to 38 nm upon conjugation, proving adherence of aptamer molecules on the surface of synthesized carbon dots.

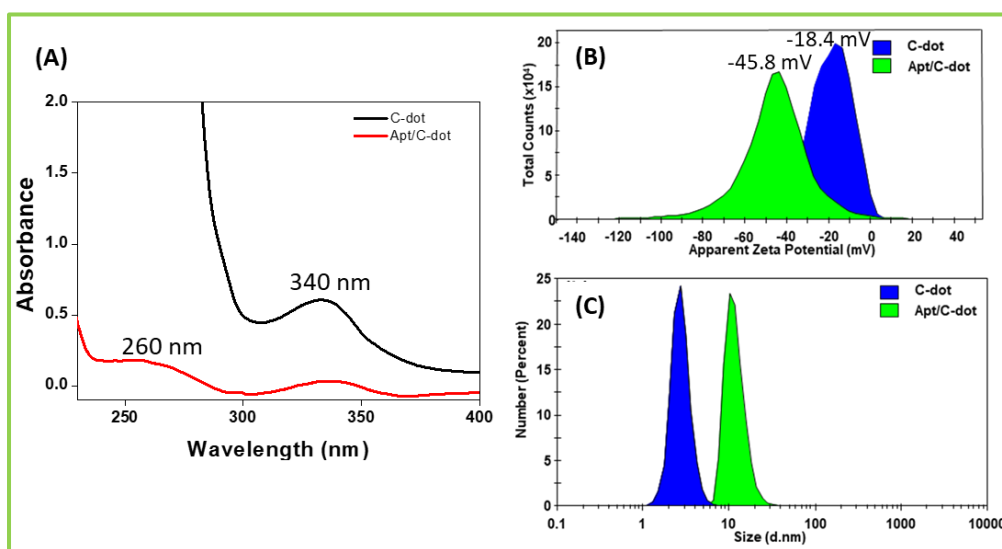


Figure 4.18: C-dot functionalization: (A) Spectrophotometric evaluation of conjugation, showing a hump at 260 nm denoting the presence of DNA in the dialyzed hybrid apt/c-dot. (B) zeta potential (C) size before and after aptamer coating of the c-dots.

4.3.7 Aptamer mediated ‘turn-on’ fluorescence assay

4.3.7.1 Assay optimizations

For studying the interaction between LPS and the hybrid probe, the microtiter well was coated overnight with LPS (1 μg) and was exposed to increasing concentrations of apt/c-dots (0.01 – 2 $\mu\text{g mL}^{-1}$) and allowed to interact for an hour at room temperature, rinsed thoroughly and the fluorescence intensity recorded. As observed in Figure 4.19 (A), a corresponding increase in fluorescence was recorded with increasing amounts of nanostructure denoting efficient interaction between the two. The fluorescence quenching behavior of AgNPs on prepared c-dots was studied, and a strong quenching effect was observed when increasing volumes of AgNPs were titrated against apt/c-dots (Figure 4.19 B). Also, PVP coated AgNPs were chosen as PVP prevented unwanted adhesion of LPS molecules onto their surface during the assay, to analyze this LPS-APBA conjugate (APBA binds to the polysaccharide region and shows intrinsic fluorescence at 372 nm) was allowed to bind on PVP modified and non-modified microtiter well surfaces³⁹. APBA showed high fluorescence signal which aided in monitoring the binding as shown in Figure 4.19 (C). The fluorescence kinetics with 1 ng of target analytes into the apt/c-dot system was measured for over 20 min with an interval of 5 s, which in Figure 4.19 (D) showed that within 20 s of target addition the fluorescence was stabilized.

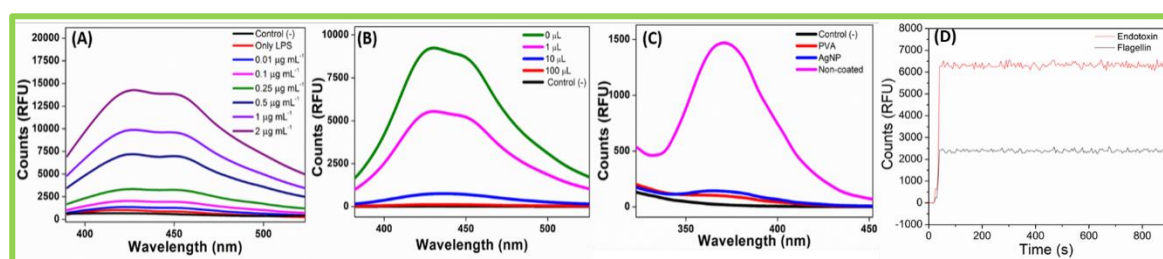


Figure 4.19: Assay optimizations: (A) Apt/c-dot binding to LPS (1 μg per well), (B) different volumes of AgNPs (1 OD stock) titrated to analyze quenching of apt/c-dots, (C) binding of LPS onto microtiter well coated and non-coated, (D) Response time upon addition of 1 ng target analytes into the respective apt/c-dot system.

4.3.8 Aptasensing ‘turn-on’ assay

4.3.8.1 O-antigen assay

We initially used O-antigen for the development of the assay, which employed apt/c-dots fluorescence quenched via colloidal silver, was restored upon exposure of the target. However, in the presence of non-specific molecules, the apt/c-dot probe failed to show any fluorescence. The apt/c-dot probe was optimized at $\sim 10\text{k}$ counts for the assay study with dilution in 1 mM Tris-HCl and was added to AgNPs present in well which was exposed to a series of increasing concentrations of LPS and the fluorescence of the system recorded at $\lambda_{\text{excitation}} = 364 \text{ nm}$ and $\lambda_{\text{emission}} = 426 \text{ nm}$. Figure 4.20 A shows the increase in fluorescence recorded from 0-10 ng mL^{-1} , showing a ‘turn on’ in the initial range of 0.1 – 10 pg mL^{-1} but was exponentially increase in range of 0.1 – 10 ng mL^{-1} and above this range, the saturated system showed a drop in fluorescence. LPS are amphiphilic

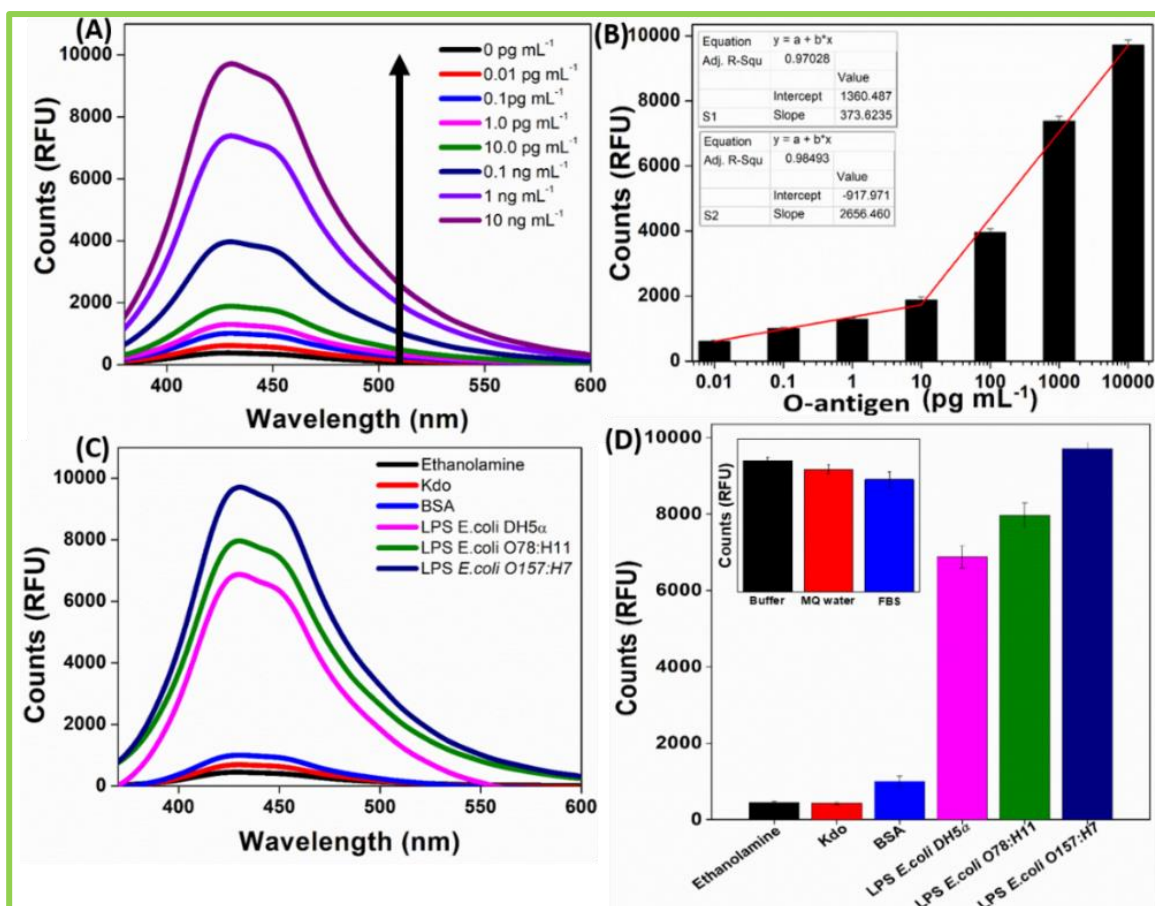


Figure 4.20: O-antigen assay: (A) Target concentration dependent 'turn-on' spectra, (B) calibration plot (C) specificity of the assay (D) bar-graph showing fluorescence restoration upon interaction other molecules.

molecules that tend to form micelles in solution above a critical concentration, which may affect the linearity of range of detection for particular species and as well as of those extracted from other bacterial species. A calibration plot for the same was generated (Figure 4.20 B) and also the assay tested with other moieties viz., ethanolamine, Kdo, BSA, and LPS from *E. coli* DH5 α and O78:H11. As seen in Figure 4.20 C&D, though the system showed negligible variation in the presence of ethanolamine, Kdo, and BSA but showed an increase in fluorescence in the presence of other LPS fractions also. Thus, from the results, we concluded that the aptamer generated showed a wide range of specificity for LPS of *E. coli* species. This may be attributed to the fact that the core oligosaccharide and the Lipid A, which forms a significant part of the LPS moiety is conserved amongst the genus.

For comparison, a summary of the recent relevant studies with their merits has been listed in Table 4.1. Thus, proving the efficacy of this methodology for bioassay development and clinical application.

Receptor	Detection Method	Limit of Detection	Range	Ref.
Living cells	Optical	0.01 ng mL ⁻¹	> 0.01 ng mL ⁻¹	40
Aptamers	Fluorescence	35 ng mL ⁻¹	50 ng – 10 µg mL ⁻¹	41
Aptamers	Voltammetry	0.033 pg mL ⁻¹	0.05 – 10 pg mL ⁻¹	42
Aptamers	Fluorescence	8.7 ng mL ⁻¹	10 – 500 ng mL ⁻¹	43
Synthetic peptides	SPR	32.5 ng mL ⁻¹	50 ng – 1 µg mL ⁻¹	44
Polymyxin B	Fiber optics	0.4 ng mL ⁻¹	0.1 – 100 ng mL ⁻¹	45
Concanavalin A	Impedance	2 µg mL ⁻¹	1 – 50 µg mL ⁻¹	46
Chloro-platinum (II) complex	Fluorescence	5.7 nM	0.33 – 6.65 µM	47
Imprinted polymers	SPR	0.4 ng mL ⁻¹	1 – 200 ng mL ⁻¹	48
Aptamers	Fluorescence	0.12 pg mL ⁻¹	0.001 – 10 ng mL ⁻¹	This study

Table 4.1: Comparative platforms: Table showing the comparison between our developed assay and LPS sensing platforms.

4.3.8.2 H-antigen assay

Using a similar methodology (Figure 4.21), an anti-H antigen apt/c-dot conjugate assay was carried out for the flagellar protein of *E. coli* O157:H7 from 0 – 1 ng mL⁻¹. However, unlike the O-antigen assay, a low fluorescence ‘turn on’ was observed with a mere ~30 % restoration even at the highest concentration of 10 ng mL⁻¹, after which a decline was observed. This variability in the platform for lipopolysaccharides vs. protein can be ascribed to the large oligomeric structures that provide spatial distancing of apt/c-dot bio-probe from the quencher molecules.

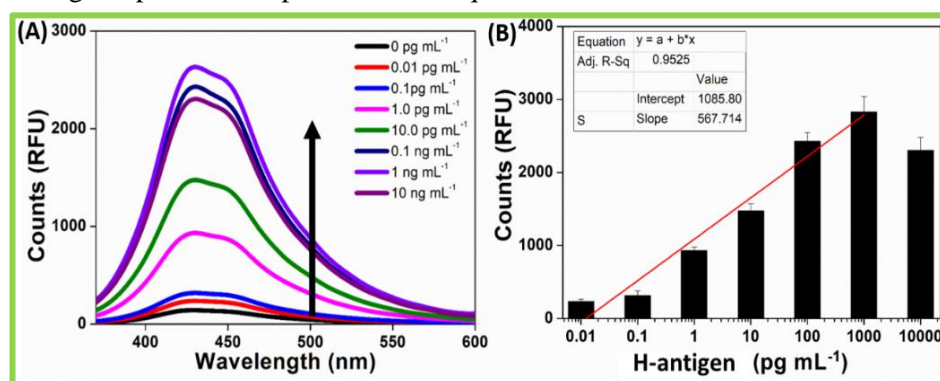


Figure 4.21: H-antigen assay: (A) Target concentration-dependent ‘turn-on’ assay spectra, (B) histogram showing variation in counts upon exposure.

4.4 Conclusion

In this chapter, we report the development of a fluorescence aptasensor for sensitive detection of O and H antigens from *E. coli* O157:H7 using aptamer conjugated tris-base derived carbon dots. These novel carbon-dots showed quenching in the presence of metal nanoparticles, which, when subjected to the target molecules, was restored significantly. These specific anti-O and anti-H aptamers ($K_d \sim 5.3$ and 4.5 nM), used as bio-recognition moieties in the studies, were screened using a highly

selective microtiter plate-based SELEX, in the presence of competing ligands to increase the stringency of the methodology. This ‘turn-on’ aptasensing assay demonstrated to detect targeted surface antigens with a detection limit of 0.1 pg mL⁻¹ for LPS and wide detection range from 0.1 pg mL⁻¹ to 10 ng mL⁻¹. Thus, this cost-effective alternative apta-assay, along with high sensitivity, promises routine assessment of laboratory reagents and biological samples for bacterial and endotoxin contamination.

Bibliography

- (1) Fratamico, P. M.; DebRoy, C.; Liu, Y.; Needleman, D. S.; Baranzoni, G. M.; Feng, P. Advances in Molecular Serotyping and Subtyping of Escherichia Coli†. *Front. Microbiol.* **2016**, *7* (MAY), 644. <https://doi.org/10.3389/fmicb.2016.00644>.
- (2) Cheng, K.; She, Y. M.; Chui, H.; Domish, L.; Sloan, A.; Hernandez, D.; McCorrister, S.; Ma, J.; Xu, B.; Reimer, A.; Knox, J. D.; Wang, G. Mass Spectrometry-Based Escherichia Coli H Antigen/Flagella Typing: Validation and Comparison with Traditional Serotyping. *Clin. Chem.* **2016**, *62* (6), 839–847. <https://doi.org/10.1373/clinchem.2015.244236>.
- (3) Bacterial Endotoxin Testing | Lonza https://bioscience.lonza.com/lonza_bs/CH/en/endotoxin-testing (accessed Jun 4, 2020).
- (4) Vincent, J. L.; Rello, J.; Marshall, J.; Silva, E.; Anzueto, A.; Martin, C. D.; Moreno, R.; Lipman, J.; Gomersall, C.; Sakr, Y.; Reinhart, K. International Study of the Prevalence and Outcomes of Infection in Intensive Care Units. *JAMA - J. Am. Med. Assoc.* **2009**, *302* (21), 2323–2329. <https://doi.org/10.1001/jama.2009.1754>.
- (5) Hurley, J. C. The Role of Endotoxin in Septic Shock. *JAMA - Journal of the American Medical Association*. American Medical Association March 5, 2019, pp 902–903. <https://doi.org/10.1001/jama.2018.20874>.
- (6) Adamik, B.; Zielinski, S.; Smiechowicz, J.; Kübler, A. Endotoxin Elimination in Patients with Septic Shock: An Observation Study. *Arch. Immunol. Ther. Exp. (Warsz)*. **2015**, *63* (6), 475–483. <https://doi.org/10.1007/s00005-015-0348-8>.
- (7) Stenutz, R.; Weintraub, A.; Widmalm, G. The Structures of Escherichia Coli O-Polysaccharide Antigens. *FEMS Microbiology Reviews*. Oxford Academic May 1, 2006, pp 382–403. <https://doi.org/10.1111/j.1574-6976.2006.00016.x>.
- (8) Khan, S.; Scholey, J. M. Assembly, Functions and Evolution of Archaeella, Flagella and Cilia. *Current Biology*. Cell Press March 19, 2018, pp R278–R292. <https://doi.org/10.1016/j.cub.2018.01.085>.
- (9) Imada, K. Bacterial Flagellar Axial Structure and Its Construction. *Biophys. Rev.* **2018**, *10* (2), 559–570. <https://doi.org/10.1007/s12551-017-0378-z>.
- (10) Ratiner, Y. A.; Salmenlinna, S.; Eklund, M.; Keskimäki, M.; Siitonen, A. Serology and Genetics of the Flagellar Antigen of Escherichia Coli O157:H7a,7c. *J. Clin. Microbiol.* **2003**, *41* (3), 1033–1040. <https://doi.org/10.1128/JCM.41.3.1033-1040.2003>.
- (11) Haiko, J.; Westerlund-wikström, B. The Role of the Bacterial Flagellum in Adhesion and Virulence. **2013**, 1242–1267. <https://doi.org/10.3390/biology2041242>.
- (12) Hajam, I. A.; Dar, P. A.; Shahnawaz, I.; Jaume, J. C.; Lee, J. H. Bacterial Flagellin—a Potent Immunomodulatory Agent. *Exp. Mol. Med.* **2017**, *49* (9), e373–e373. <https://doi.org/10.1038/emmm.2017.172>.
- (13) Duan, Q.; Zhou, M.; Zhu, L.; Zhu, G. Flagella and Bacterial Pathogenicity. *J. Basic Microbiol.* **2013**, *53* (1), 1–8. <https://doi.org/10.1002/jobm.201100335>.
- (14) Moens, S.; Vanderleyden, J. Functions of Bacterial Flagella. *Critical Reviews in Microbiology*. Informa Healthcare 1996, pp 67–100. <https://doi.org/10.3109/10408419609106456>.
- (15) Sondhi, P.; Maruf, H. U.; Stine, K. J. Nanomaterials for Biosensing Lipopolysaccharide. **2020**.
- (16) Liu, M. L.; Chen, B. Bin; Li, C. M.; Huang, C. Z. Carbon Dots: Synthesis, Formation Mechanism, Fluorescence Origin and Sensing Applications. *Green Chemistry*. Royal Society of Chemistry February 4, 2019, pp 449–471. <https://doi.org/10.1039/c8gc02736f>.
- (17) Sun, Y. P.; Zhou, B.; Lin, Y.; Wang, W.; Fernando, K. A. S.; Pathak, P.; Mezziani, M. J.; Harruff, B. A.; Wang, X.; Wang, H.; Luo, P. G.; Yang, H.; Kose, M. E.; Chen, B.; Veca, L. M.; Xie, S. Y. Quantum-Sized Carbon Dots for Bright and Colorful Photoluminescence. *J. Am. Chem. Soc.* **2006**, *128* (24), 7756–7757. <https://doi.org/10.1021/ja062677d>.
- (18) Wang, T.; Wang, A.; Wang, R.; Liu, Z.; Sun, Y.; Shan, G.; Chen, Y. Carbon Dots with Molecular Fluorescence and Their Application as a “ Turn-off ” Fluorescent Probe for Ferricyanide Detection. **2019**, No. July, 1–9. <https://doi.org/10.1038/s41598-019-47168-7>.
- (19) Shorie, M.; Kaur, H.; Chadha, G.; Singh, K.; Sabherwal, P. Graphitic Carbon Nitride QDs Impregnated Biocompatible Agarose Cartridge for Removal of Heavy Metals from Contaminated Water Samples. *J. Hazard. Mater.* **2019**, *367* (September 2018), 629–638. <https://doi.org/10.1016/j.jhazmat.2018.12.115>.
- (20) Henderson, J. C.; O’Brien, J. P.; Brodbelt, J. S.; Trent, M. S. Isolation and Chemical Characterization of Lipid A from Gram-Negative Bacteria. *J. Vis. Exp.* **2013**, No. 79, 1–11. <https://doi.org/10.3791/50623>.
- (21) Wang, X.; Zhang, C.; Shi, F.; Hu, X. Purification and Characterization of Lipopolysaccharides. *Subcell. Biochem.* **2010**, *53*, 27–51. https://doi.org/10.1007/978-90-481-9078-2_2.

- (22) Perdomo, R.; Montero, V. *Purification of E. Coli 055:B5 Lipopolysaccharides by Size Exclusion Chromatography*; 2006; Vol. 23.
- (23) Lee, C. H.; Tsai, C. M. Quantification of Bacterial Lipopolysaccharides by the Purpald Assay: Measuring Formaldehyde Generated from 2-Keto-3-Deoxyoctonate and Heptose at the Inner Core by Periodate Oxidation. *Anal. Biochem.* **1999**, *267* (1), 161–168. <https://doi.org/10.1006/abio.1998.2961>.
- (24) Fomsgaard, A.; Freudenberg, M. A.; Galanos, C. Modification of the Silver Staining Technique to Detect Lipopolysaccharide in Polyacrylamide Gels. *J. Clin. Microbiol.* **1990**, *28* (12), 2627–2631. <https://doi.org/10.1128/jcm.28.12.2627-2631.1990>.
- (25) Guyon, S.; Rhen, M.; Romling, U. Rapid Preparation of Unsheathed Bacterial Flagella. *BIO-PROTOCOL* **2015**, *5* (6). <https://doi.org/10.21769/bioprotoc.1425>.
- (26) *Bradford Reagent Kit Packing Product Name Bradford Reagent 100 ML Product Code MLI06-100ML MLI06-500 ML 500 ML*.
- (27) Zuker, M. Mfold Web Server for Nucleic Acid Folding and Hybridization Prediction. *Nucleic Acids Res.* **2003**, *31* (13), 3406–3415. <https://doi.org/10.1093/nar/gkg595>.
- (28) Antczak, M.; Popena, M.; Zok, T.; Sarzynska, J.; Ratajczak, T.; Tomczyk, K.; Adamiak, R. W.; Szachniuk, M. New Functionality of RNAComposer: An Application to Shape the Axis of MiR160 Precursor Structure. *Acta Biochim. Pol.* **2016**, *63* (4), 737–744. https://doi.org/10.18388/abp.2016_1329.
- (29) Pierce, B. G.; Wiehe, K.; Hwang, H.; Kim, B.-H.; Vreven, T.; Weng, Z. Structural Bioinformatics ZDOCK Server: Interactive Docking Prediction of Protein-Protein Complexes and Symmetric Multimers. **2014**, *30* (12), 1771–1773. <https://doi.org/10.1093/bioinformatics/btu097>.
- (30) ZDOCK Server: Help <http://zdock.umassmed.edu/help.html> (accessed Jun 4, 2020).
- (31) Krieger, E.; Koraimann, G.; Vriend, G. Increasing the Precision of Comparative Models with YASARA NOVA—a Self-Parameterizing Force Field. *Proteins Struct. Funct. Bioinforma.* **2002**, *47* (3), 393–402. <https://doi.org/10.1002/prot.10104>.
- (32) Pierce, B.; Tong, W.; Weng, Z. M-ZDOCK: A Grid-Based Approach for C n Symmetric Multimer Docking. *Bioinforma. Orig. Pap.* **2005**, *21* (8), 1472–1478. <https://doi.org/10.1093/bioinformatics/bti229>.
- (33) Wang, H.; Qiao, X.; Chen, J.; Wang, X.; Ding, S. Mechanisms of PVP in the Preparation of Silver Nanoparticles. *Materials Chemistry and Physics*. Elsevier December 15, 2005, pp 449–453. <https://doi.org/10.1016/j.matchemphys.2005.05.005>.
- (34) Chen, R.; Li, L.; Weng, Z. ZDOCK: An Initial-Stage Protein-Docking Algorithm. *Proteins Struct. Funct. Genet.* **2003**, *52* (1), 80–87. <https://doi.org/10.1002/prot.10389>.
- (35) Pierce, B. G.; Hourai, Y.; Weng, Z. Accelerating Protein Docking in ZDOCK Using an Advanced 3D Convolution Library. *PLoS One* **2011**, *6* (9), e24657. <https://doi.org/10.1371/journal.pone.0024657>.
- (36) Yan, Y.; Liu, J. H.; Li, R. S.; Li, Y. F.; Huang, C. Z.; Zhen, S. J. Carbon Dots Synthesized at Room Temperature for Detection of Tetracycline Hydrochloride. *Anal. Chim. Acta* **2019**, *1063*, 144–151. <https://doi.org/10.1016/j.aca.2019.02.047>.
- (37) Jones, S. S.; Sahatiya, P.; Badhulika, S. One Step, High Yield Synthesis of Amphiphilic Carbon Quantum Dots Derived from Chia Seeds: A Solvatochromic Study. *New J. Chem.* **2017**, *41* (21), 13130–13139. <https://doi.org/10.1039/c7nj03513f>.
- (38) Liu, S. G.; Mo, S.; Han, L.; Li, N.; Fan, Y. Z.; Li, N. B.; Luo, H. Q. Oxidation Etching Induced Dual-Signal Response of Carbon Dots/Silver Nanoparticles System for Ratiometric Optical Sensing of H₂O₂ and H₂O₂-Related Bioanalysis. *Anal. Chim. Acta* **2019**, *1055*, 81–89. <https://doi.org/10.1016/j.aca.2018.12.015>.
- (39) Kur-Kowalska, K.; Przybył, M.; Ziółczyk, P.; Sowiński, P.; Miller, E. Fluorescence Properties of 3-Amino Phenylboronic Acid and Its Interaction with Glucose and ZnS:Cu Quantum Dots. *Spectrochim. Acta - Part A Mol. Biomol. Spectrosc.* **2014**, *129*, 320–325. <https://doi.org/10.1016/j.saa.2014.03.039>.
- (40) Jiang, H.; Jiang, D.; Shao, J.; Sun, X.; Wang, J. High-Throughput Living Cell-Based Optical Biosensor for Detection of Bacterial Lipopolysaccharide (LPS) Using a Red Fluorescent Protein Reporter System. **2016**. <https://doi.org/10.1038/srep36987>.
- (41) Ma, L.; Sun, N.; Meng, Y.; Tu, C.; Cao, X.; Wei, Y.; Chu, L.; Diao, A. Harnessing the Affinity of Magnetic Nanoparticles toward Dye-Labeled DNA and Developing It as an Universal Aptasensor Revealed by Lipopolysaccharide Detection. *Anal. Chim. Acta* **2018**, *1036*, 107–114. <https://doi.org/10.1016/j.aca.2018.06.060>.
- (42) Wang, N.; Dai, H.; Sai, L.; Ma, H.; Lin, M. Copper Ion-Assisted Gold Nanoparticle Aggregates for Electrochemical Signal Amplification of Lipopolysaccharide Sensing. *Biosens. Bioelectron.* **2019**, *126*, 529–534. <https://doi.org/10.1016/j.bios.2018.11.021>.
- (43) Wen, L. xin; Lv, J. jiang; Chen, L.; Li, S. bo; Mou, X. jing; Xu, Y. A Fluorescent Probe Composed of Quantum Dot Labeled Aptamer and Graphene Oxide for the Determination of the Lipopolysaccharide Endotoxin. *Microchim. Acta* **2019**, *186* (2). <https://doi.org/10.1007/s00604-018-3218-3>.
- (44) Zhang, J.; Khan, I.; Zhang, Q.; Liu, X.; Dostalek, J.; Liedberg, B.; Wang, Y. Lipopolysaccharides Detection on a Grating-Coupled Surface Plasmon Resonance Smartphone Biosensor. *Biosens. Bioelectron.* **2018**, *99*, 312–317. <https://doi.org/10.1016/j.bios.2017.07.048>.
- (45) Manoharan, H.; Kalita, P.; Gupta, S.; Sai, V. V. R. Plasmonic Biosensors for Bacterial Endotoxin Detection on Biomimetic C-18 Supported Fiber Optic Probes. *Biosens. Bioelectron.* **2019**, *129*, 79–86. <https://doi.org/10.1016/j.bios.2018.12.045>.
- (46) Brosel-Oliu, S.; Galyamin, D.; Abramova, N.; Muñoz-Pascual, F. X.; Bratov, A. Impedimetric Label-Free Sensor for Specific Bacteria Endotoxin Detection by Surface Charge Registration. *Electrochim. Acta* **2017**, *243*, 142–151. <https://doi.org/10.1016/j.electacta.2017.05.060>.

- (47) Zhu, Y.; Xu, C.; Wang, Y.; Chen, Y.; Ding, X.; Yu, B. Luminescent Detection of the Lipopolysaccharide Endotoxin and Rapid Discrimination of Bacterial Pathogens Using Cationic Platinum(II) Complexes. *RSC Adv.* **2017**, *7* (52), 32632–32636. <https://doi.org/10.1039/c7ra03312e>.
- (48) Altintas, Z.; Abdin, M. J.; Tohill, A. M.; Karim, K.; Tohill, I. E. Ultrasensitive Detection of Endotoxins Using Computationally Designed NanoMIPs. *Anal. Chim. Acta* **2016**, *935*, 239–248. <https://doi.org/10.1016/j.aca.2016.06.013>.



Chapter 5

*Nanostructured
aptasensor for E. coli
Stx subtypes*



Chapter 5

Nanostructured aptasensor for *E. coli* Stx subtypes

*The contents of this chapter are adapted from: **Kaur, H.**; Shorie, M.; Sabherwal, P. Biolayer Interferometry-SELEX for shiga toxin antigenic-peptide aptamers & detection via chitosan-WSe₂ aptasensor. Biosens. Bioelectron. 2020, 167, 112498.*

5.1 Introduction

The chapter accounts for the development of a BLI based in-vitro SELEX technique for fishing out specific aptamers against *E. coli* shiga toxin subtypes viz., Stx1 & Stx2 via specific epitopically relevant peptides. Since the inception of, systematic evolution of ligands by exponential enrichment (SELEX), 'aptamers' with the ability to bind specific ligands with high affinities have been purported as next-generation antibody mimics^{1,2}. These single-stranded nucleic acid molecules screened in-vitro via iterated alternate rounds of selection & amplification, harbor pico-nanomolar affinities & high target selectivity^{3,4}. These strikingly appreciable recognition moieties arise out of a milieu of random & unique sequences, binding to their target of interest via non-covalent interactions⁵. Over the last three decades, although numerous labs have reported SELEX variants, a majority of these are modulations of traditional multiple iteration technique, thus rendering them relatively slow & cumbersome⁶. Especially in urgent global scenarios, these are impractical beyond basic research in lab settings⁷.

5.1.1 Target enterotoxins- A background

As introduced in Chapter 1 and later in Chapter 3, STEC are a major source of food poisoning associated with 2.5 million cases annually, has a low infectious dose of 100 cells enough for disease manifestation and alongside, development of HUS in 5-15% cases⁸. This damage is a direct result of hemolytic & rRNA-glycosidase activity of Shiga-like toxins (Stx). These are proteinous toxins, which bind via B₅ subunit to specific glycolipids (Gb3/Gb4) abundantly present on microvascular cells of the kidney, colon, and central nervous system⁹. Though similar in action, its subtypes (Stx1 & Stx2) are non-homologous, sharing only ~56% sequence identity amongst themselves. It has been reported that Stx2 (LD₅₀ of 50 ng kg⁻¹) is 100 times more lethal than Stx1¹⁰.

Moreover, lack of vaccines, neutralizing drugs & unjustified antibiotic therapy further aggravates the condition leading to the systemic release of toxins. Therefore, specific identification in clinical samples is essential.

5.1.2 The need for improved sensing platform

The current detection techniques revolve around culture identification or PCR based screening using *stx1/stx2* specific primers requiring extensive sampling, expensive machinery & skilled personnel for analyses¹¹. So far, only a few studies of polyclonal antibodies, a camelid antibody, and two low-affinity aptamers have been reported¹²⁻¹⁴. Thus, a niche is promised for aptamers as recognition moiety for Stx subtypes. Correspondingly, conventionally employed diagnostics platforms are antibody-based, which are costly, susceptible to denaturation, and show cross-talk amongst subtypes.

5.1.3 Objectives

- (i) **Bio-receptor development:** Development of specific aptamer-based receptors against selected Shiga-like toxin subtypes using enterotoxin targeting approach.
- (ii) **Transducer synthesis:** Synthesis of Tungsten diselenide (WSe₂) nanostructured material for modification of the electrochemical electrode surface.
- (iii) **Aptasensor fabrication:** Functionalization of generated high-affinity aptamers onto electrically active nanostructures for voltammetric apta-assay.
- (iv) **Platform validation:** Testing & validation of aptasensor in spiked complex matrix samples.

5.1.4 Proposed biosensing platform

5.1.4.1 Preface

Aptamers conferred with high selectivity & binding affinities have been lately exploited for diagnostic & therapeutic applications¹⁵. Needless to say, the integration of specific aptamers with 2D nanomaterials has opened avenues for the development of high sensitivity low-cost electrochemical diagnostic platforms¹⁶. Recent advances in TMDs are focused on tungsten dichalcogenide due to their unique physical & chemical properties particularly, tunable direct bandgap corresponding to atomic layers^{17,18}. Exploiting the semi-conductive nature of WSe₂, we employed a green exfoliating method using an aqueous suspension of chitosan for simultaneous exfoliation & functionalization of layered WSe₂ and subsequent immobilization of our selected aptamers for sensing application. For the electrochemical studies, square-wave voltammetry (SWV) was used for analytical measurements, which is a rapid & reliable electrochemical technique capable of generating sensing results in a short time¹⁹⁻²¹. This voltammetric detection method is widely used for sensitive detection of biomolecules and allows quantitative sensing of Shiga toxin subtypes in a simplified, cost-effective chip format. This platform gives an edge over immunoassays as label-free technology with high sensitivity to the presence of target antigens in real samples and, thus, is explored in this study as the detection technique.

5.1.4.2 Our aptasensing approach: Toxins

Hence, a pragmatic approach towards the development of a robust alternative, BLI based SELEX has been successfully achieved, enabling rapid selection of aptamers against protein biomarkers in a single microplate format eliminating the need of enrichment iterations and concomitantly allowing real-time monitoring of SELEX progression & binding affinity. Using this methodology, we targeted Shiga toxin subtypes for the selection of novel high-affinity aptamers and demonstrated its detection over voltammetric sensors. As illustrated in Figure 5.1, our current study revolves around two major aspects of an efficient biosensor:

- (i) Facile selection of novel aptamers against protein toxins, herein exploiting antigenically distinct peptide epitopes of Stx1 & Stx2 using a single microplate format screening and monitoring via BLI platform.
- (ii) Voltammetric sensing of the toxins using individual-specific aptamer functionalized onto chito-WSe₂ electrochemical platforms.

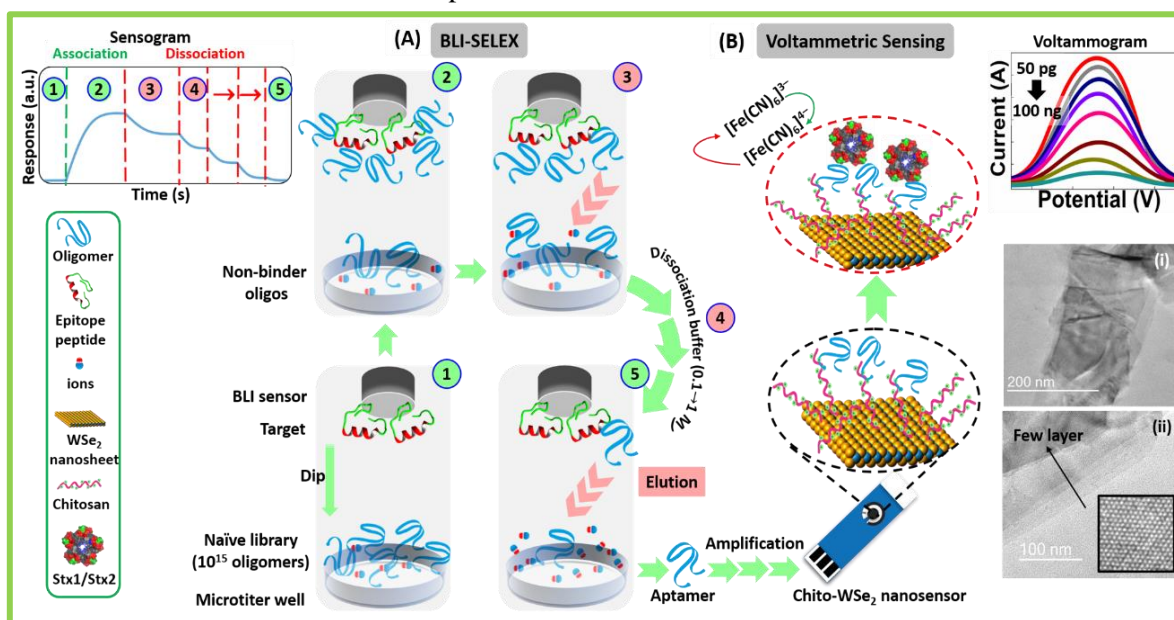


Figure 5.1: Schematic: An illustration of (A) step-by-step BLI based SELEX and sensogram showing the characteristic real-time kinetics (B) chito-WSe₂ modified electrochemical nanosensor for the detection of Stx1 & Stx2, along with TEM images of chito-WSe₂ showing (i) layered nanosheet morphology, (ii) distinct few layers & (inset) high-resolution image showing hexagonal lattice structure.

5.1.4.3 The novelty of experimental work

- (i) **Bio-receptor:** Specific high-affinity aptamers for Stx1b and Stx2b using a biolayer-interferometry based aptamer selection.
- (ii) **Nanostructures:** The green exfoliation of 2D WSe₂ exfoliated with chitosan to yield layered nanomaterial with excellent conductive properties.

5.2 Experimental procedure

5.2.1 Aptamer technology: BLI-SELEX

5.2.1.1 Materials

NaCl, KCl, Na₂HPO₄, KH₂PO₄, MgCl₂, potassium ferrocyanide (K₄[Fe(CN)₆]·3H₂O), potassium ferricyanide (K₃[Fe(CN)₆]), anhydrous acetic acid, EDC, sulfo-NHS, MES sodium salt, and ethanolamine were purchased from Merck (India). Purified & characterized custom peptides were synthesized from Xcelris Genomics (India), purified *E. coli* Stx1b and Stx2b were purchased from MyBioSource, Inc (USA). The DNA naïve library and primers for SELEX mentioned in Chapter 2, Section 2.2.1.1 were employed in this study also. Optimized binding buffer: Phosphate buffer (PB) 10 mM, pH 7.2 supplemented with 100 mM NaCl, 2.5 mM KCl, 5 mM MgCl₂. Here, PB was preferred over Tris based binding buffers used in earlier Chapters, to limit non-specific amine group interactions with the BLI sensors.

5.2.1.2 Peptide epitope screening

5.2.1.2.1 Background

A biomolecule like protein, forms various folded conformations based on its primary sequence along with interplay of inter & intra molecular interactions, which provide three-dimensional stability. These collectively form various structures, where each different motif or subunit may have many different surface exposed antigen determinants. Therefore, immune responses are directed against the various exposed antigenic sites of the protein, with antibodies binding to different regions with varied preference or binding efficiency. It is well known that bio-receptors are generated against particular stretches known as antigen determinants or epitopes rather than the whole protein. Thus, exploiting this notion, the toxin subtypes were screened for surface exposed epitopes lying in non-homologous regions to impart selectivity to the receptors that would be generated against them.

5.2.1.2.2 Bioinformatic analysis

The protein sequences of Stx1b and Stx2b (accession no. NP_311000.1, NP_309233.1) retrieved from GenPept (NCBI database) were used to screen antigenic sites. These epitopes were processed using an online immunogenicity tool (<http://imed.med.ucm.es/Tools/antigenic.pl>), which predicts antigenic segments from within a protein sequence based on the propensity of amino acid residues in experimentally known epitopes. The surface accessibility of the selected antigenic sites was determined using the NetsurfP server²². The tertiary structure of the energy minimized epitopes were analyzed using the PEPstr tool & Yasara view^{23,24}. The selected antigenic peptides of the two toxin subtypes were custom synthesized and utilized in studies without further modification for aptamer selection.

5.2.1.3 Biolayer interferometry-based SELEX

5.2.1.3.1 BLI principle

The BLI-SELEX based aptamer selection was carried out on BLI instrument, Octet® Red96 system (FortéBio) using 96-well plate in kinetics mode. In principle, the Octet system provide dip sensors with real time monitoring of the bio-interactions. The binding event on sensor surface led to change in thickness of bio-molecular layer which results in a wavelength shift of interference patterns from internal reference. This shift is real-time monitored to show the process kinetics.

5.2.1.3.2 BLI-SELEX protocol

The BLI-SELEX based aptamer selection was carried out on Octet® Red96 system in kinetics mode as per company application note, which emphasizes on proprietary BLI sensors and specific black microtiter plates for BLI studies. Prior to the loading of the target peptide onto the amine-reactive 2nd generation (AR2G) sensors, the sensors were hydrated for 15 min in biosensor tray inside the Octet instrument set at 30°C for optimum kinetics as per the instrument manual. The hydration time is necessary for subsequent steps. The AR2G sensors have amine-reactive groups present on the surface, which can be conjugated with carboxyl groups on the binding ligand using carbodiimide chemistry. Also, each test sensor is supplemented with a reference sensor for normalizing the raw data to remove blank sensor interactions with the sample buffers. The essential SELEX steps are as following:

(A) Target immobilization

Step	Type	Time (s)	Shake speed (rpm)
1	Baseline	30	750
2	Activation	100	500
3	Loading	600	750
4	Quenching	100	500
5	Baseline	30	750

Table 5.1: Optimized loading parameters: The steps are carried out in different wells in microplate.

The AR2G sensors were activated using carbodiimide chemistry (EDC/NHS) that generate reactive NHS esters. The peptides prepared in MES buffer (pH 5.5) were allowed to couple with NHS esters resulting in surface immobilization. This step should be carried out using fresh peptide solution to minimize any chances of peptide hydrolysis in acidic environment. The unreacted free groups of NHS esters were quenched by dipping in 0.5 M ethanolamine (pH 8) and the baseline is set to zero. Table 5.1 details the optimal loading parameters used in the study.

(B) Selection

For the preparation of the naïve library, 1 µL of 100 µM ssDNA library was added to 99 µL of selection buffer, mixed and incubated at 95°C for 10 min and snap-chilled on ice immediately to prevent rehybridization of the single stranded sequences. This was transferred to 30°C and allowed to take their respective tertiary conformations. This conditioned naïve library (1 µM) diluted in

selection buffer ($>10^{14}$ oligomers) was exposed to AR2G sensor loaded with target peptide. The optimal kinetic parameters are listed in Table 5.2.

Step	Type	Time (s)	Shake speed (rpm)
1	Baseline	300	750
2	Association	200	500
$\times 10$ 3	Dissociation	30	500
13	Baseline	60	750

Table 5.2: Optimized SELEX kinetics parameters: The steps are carried out in different wells in microplate viz., baseline: selection buffer, association: selection buffer, dissociation: selection buffers with increasing ionic conc. (0.1-1M NaCl).

(C) Elution

The binders that associate with target were fished out of the random pool of oligomers & sequentially dissociated into different microtiter wells containing dissociation buffer of increasing ionic strength in accordance to binding affinity (0.1-1M). This is schematically explained in Figure 5.2. The progression of SELEX was monitored real-time and the elutes were collected, spectrophotometrically quantified, purified & PCR amplified as per optimized protocols mentioned

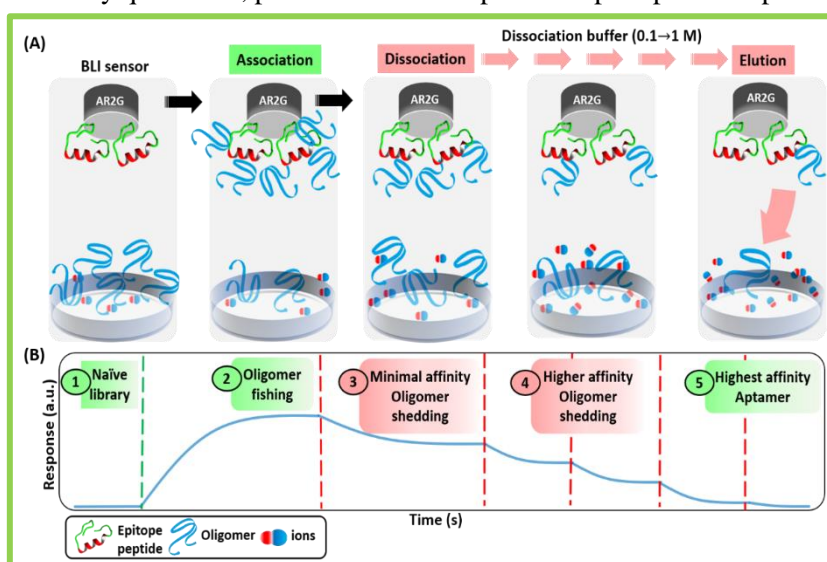


Figure 5.2: BLI SELEX: Schematic representation showing the step-by-step protocol carried out in different wells in sample microplate. The bottom panel shows a pictorial representation of the real-time kinetics sensorgram during a BLI-SELEX.

in previous Chapter 2, Section 2.2.1.3.2. Similarly, this process was carried out for all the epitope peptides of the two toxins, result datasets normalized against reference sensor and globally fitted using 1:1 binding model using FortéBio Data analysis 8. Similar studies were carried out for other epitopes of Stx1 & Stx2.

5.2.1.4 Aptamer characterization

(A) BLI interaction studies

The positive aptamer pools selected against each epitope peptide were analyzed to confirm their affinity against peptides using BLI. For these aptamer-epitope interaction studies, the individual peptide-loaded sensors were dipped into the selected pool solution (2.5 μ g peptide per BLI sensor

was recommended as per the FortéBio technical note²⁵) and the association/dissociation kinetics was observed. The pools with the best binding affinity to each target epitope were chosen, and further, their interaction with the toxin was also confirmed. BLI kinetics at various concentrations of the individual champion aptamers ranging from 0, 25, 50 to 100 nM were carried out, and the average K_d value determined.

(B) Fluorescence studies

The champion aptamer for each of the toxin subtypes was further scrutinized to corroborate the binding results using plate-binding assays. Herein, Stx1 and Stx2 were individually coated on a microtiter plate (up to $10 \mu\text{g mL}^{-1}$) in carbonate buffer (pH 9.5, favors high hydrophobic interactions between protein and polystyrene microtiter plate²⁶) overnight, washed and then incubated with an increasing concentration of FITC-labelled aptamers (0, 0.1, 0.5, 1, 5, 10, 50, 100 nM), diluted in binding buffer for an hour at room temperature. The non-binder fraction was washed off, and the FITC fluorescence signal intensity of binders was measured using a microtiter plate reader (BioTek Synergy H1, USA) at $\lambda_{\text{excitation}}=485 \text{ nm}$ and $\lambda_{\text{emission}}=525 \text{ nm}$ ²⁷. The binding was assessed by plotting signal intensity vs. aptamer concentration and fitted using a non-linear model in GraphPad Prism 7.01 software. The selected aptamers with the highest affinity for the toxin subtypes were cloned & sequenced and the obtained sequences were characterized by structure modeling & docking studies using various bioinformatic tools as per previous Chapter 4, Section 4.2.3.3.

5.2.2 Nanostructured biosensing platform

5.2.2.1 Materials

Tungsten (IV) Selenide 99.8% from Alfa Aesar (India), chitosan (Low MW) extra pure was purchased from SRL (India), and fetal bovine serum (FBS) from Gibco (India). TE 100 screen-printed carbon electrodes (SPE) were products of CH Instruments (USA).

5.2.2.2 Synthesis of nanomaterial: chito-WSe₂ nanosheets

The exfoliation of layered WSe₂ flakes was carried out via a modified liquid exfoliation protocol²⁸. The concentration of exfoliant chitosan was optimized, and finally, 2.5 mg mL^{-1} was dissolved in 2 mL aqueous acetic acid (0.5 % v/v, pH 6.5), along with bulk WSe₂ powder (1 mg mL^{-1}) and thoroughly vortexed. This dispersion was then probe sonicated (30% amplitude, 5 s pulsed on/off cycles) and the time was optimized to obtain high yield of exfoliated nanosheets. The unexfoliated bulk was removed by centrifugation ($1000\times g$ for 10 min) and the supernatant siphoned out. Further, extensive rinsing of dispersions with distilled water was carried out to remove excess unused chitosan. The exfoliated nanomaterial was vacuum dried & re-dispersed in water for further studies. These chitosan exfoliated & functionalized WSe₂ nanosheets were characterized using various spectrophotometric (UV-Vis, Raman, XRD) and microscopic (AFM, TEM) tools.

5.2.2.2.1 Electrochemical characterization

The CV and EIS studies were carried out as mentioned in previous Chapter 2, Section 2.3.4.1 using PBS (100 mM, pH 7) containing 2.5 mM $K[Fe(CN)_6]^{3-/4-}$ redox probe. The Stx1 and Stx2 sensing assay was carried out using square wave voltammetry (SWV) with a potential sweep from -0.1 to +0.4 V with an increment rate of 0.005 V, the amplitude of 0.025 V and 10 Hz frequency²⁹. The potential sweep window was optimized to include the redox peak of the redox probe and minimize the time required to take the readings. Figure 5.3 provides a glimpse into the overall strategy adopted for from exfoliation, electrode modification to sensing technique used on SPE.

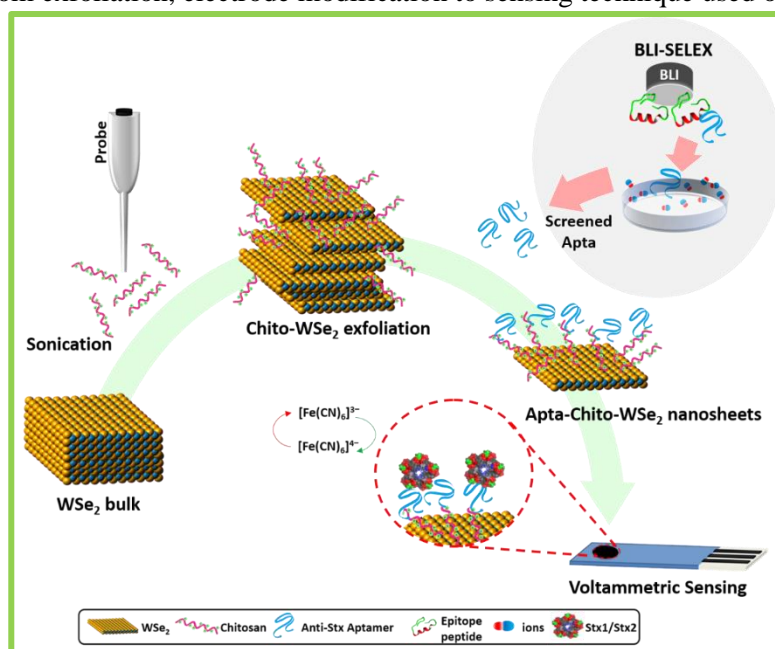


Figure 5.3: *Synthesis & fabrication of chito-WSe₂ nanostructured platform: Overview of exfoliation of nanomaterial and modification of electrochemical sensors.*

5.2.2.2.2 Sensor modification

As starting electrode modification nanomaterial, 1 mg mL⁻¹ of chito-WSe₂ nanosheets dispersed in aqueous media, were used to modify the working electrode of the screen-printed electrode (SPE) and the concentration was optimized by a stepwise increase in the volume of drop-casted nanomaterial & subsequent drying at 40°C. For bio-receptor functionalization, the selected aptamers were diluted in binding buffer (pH 7), drop-casted on the modified sensor surface, and incubated overnight at 4°C. The sensor surface was rinsed with distilled water to remove any un-immobilized molecules and stored at 4°C when not in use.

5.2.2.3 Aptasensing assay

(A) Nanosensor electrochemical assay

The sensing bioassay was carried out using SWV, wherein varying amounts of Stx1 & Stx2 (0.01-1000 ng mL⁻¹) were subjected to the sensor, followed by washing & voltammetric scanning. The voltammograms were recorded, and the current maxima vs. toxin concentration plotted to analyze the range of detection & limit of detection. The cross-reactivity of the individual apta-nanosensors

was investigated with BSA, purified *E. coli* O157:H7 endotoxin, and the subtypes Stx1 for Stx2 sensor & vice-versa.

(B) Complex matrix sample pre-processing

The real samples viz., pasteurized milk, and 10% FBS were diluted 1:10 in PB and filter sterilized before being spiked with the target analytes to mitigate interference due to any unwanted particulate or pathogen. This is necessary as high matrix samples lead to fouling of the electrode surface and show high signal to noise ratio.

5.3 Results & discussion

5.3.1 Peptide epitope screening

The protein sequences of Stx1b and Stx2b (accession no. NP_311000.1, NP_309233.1) retrieved from GenPept (NCBI database) are as following:

>gi|15832227|ref|NP_311000.1| Shiga toxin I subunit B [Escherichia coli O157:H7 str. Sakai]
 MKKTLLIAASLSFFSASALATPDCVTGKVEYTKYNDTFTVKVGDKELFTNRWNLQSLLSAQIT
 GMTVTIKTNACHNGGGFSEVIFR

>gi|15830460|ref|NP_309233.1| Shiga toxin 2 subunit B [Escherichia coli O157:H7 str. Sakai]
 MKKMFMAVLFALASVNAMAADCAKGGKIEFSKYNEEDTFTVKVDGKEYWTSRWNLQPLLQSAQL
 TGMTVTIKSSTCESGSGFAEVQFNND

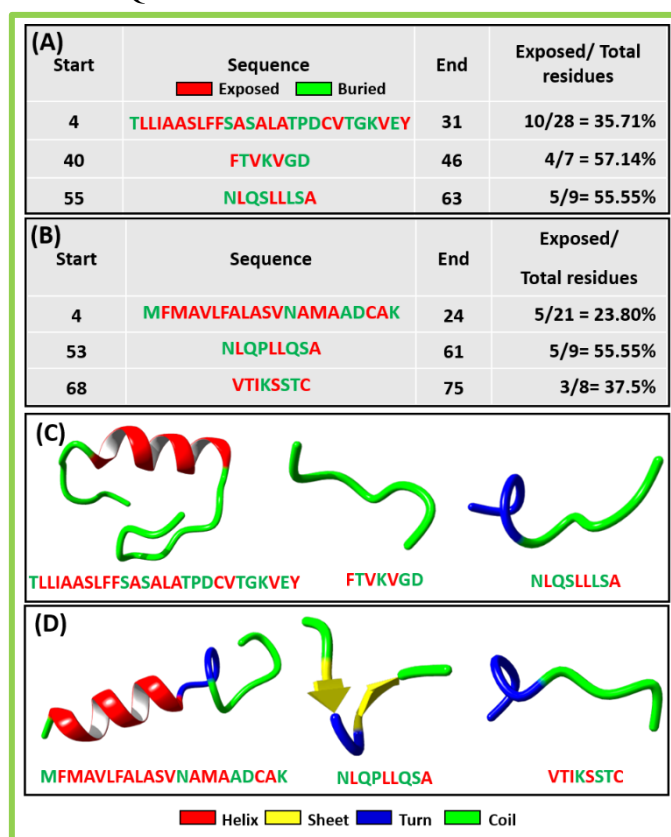


Figure 5.4: Epitope screening results: Elucidation of antigenic sites along with surface accessibility using online immunomedicine antigenicity tool and NetsurfP web server for (A) Stx1 & (B) Stx2 showing a decent surface exposure >20%. The tertiary structure was analyzed using PEPstr tool and peptides energy minimized and visualized using and Yasara view showing segments with prominent secondary structures in the peptides.

This is processed using online immunogenicity tool which predicts antigenic segments from within a protein. Figure 5.4 shows the three distinct epitopes for each Stx subtypes with >20% surface

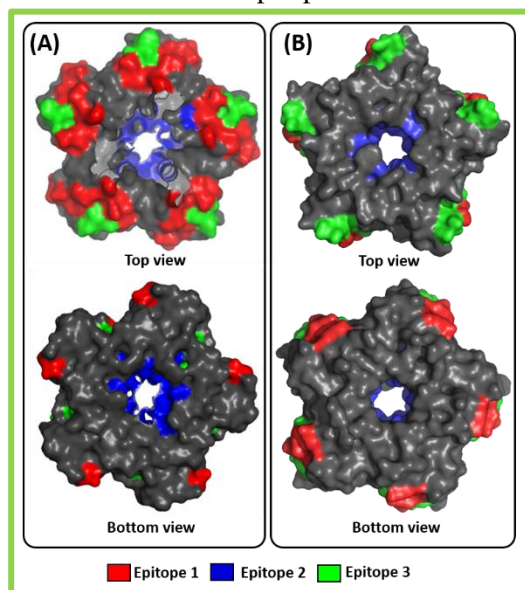


Figure 5.5: Location of predicted epitopes in the Stx model: A cartoon view of the structural model of the proteins (A) *Stx1b* & (B) *Stx2b* toxins are showing the corresponding screened epitopes highlighted on its surface.

accessibility, with motifs rich in α -helix & β -turn, which are reported to be present in the recognition domains of known proteins³⁰. The localization of predicted epitopes on the exposed surface of toxins in Figure 5.5 confirmed the same. Thus, the aptamer generation was achieved by exposing the naïve library to the peptides that form the antigenic region.

5.3.2 Aptamer selection & characterization: BLI-SELEX

(A) Loading

The initial step of target loading is of prime-most importance, which determines the efficiency of the selection step. Figure 5.6 shows the normalized sensogram showing the gradual rise in response (Step 3) during the loading of target peptide onto the AR2G sensor, which causes an increase in biolayer thickness on sensor surface denotes immobilization of the peptide. Similarly, the rest of the peptides were loaded on respective sensors for the ensuing aptamer selection step.

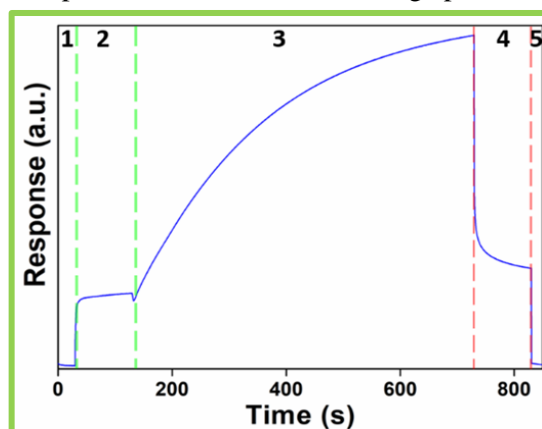


Figure 5.6: Peptide loading sensogram: Baseline referenced sensogram showing the various steps (demarcated by dotted lines) of target peptide loading onto AR2G sensor.

(B) Exposure & elution

These peptide coated sensors were then exposed to the naïve library, and the binders then dissociated gradually according to their binding strength. The naïve library consisting of a random pool of oligomers interacts and binds to the target molecules with varying affinities attributed by their structure and sequence. Multiple oligomers interact with the target (not exclusively unique sequence), which are sequentially dissociated from the target by dipping in individual wells containing dissociation buffers of increasing strength.

(C) SELEX monitoring

The progression of SELEX was monitored in real-time, and Figure 5.7 (A) shows the sensogram of an association-dissociation cycle of peptide Stx1.1 coated AR2G sensor.

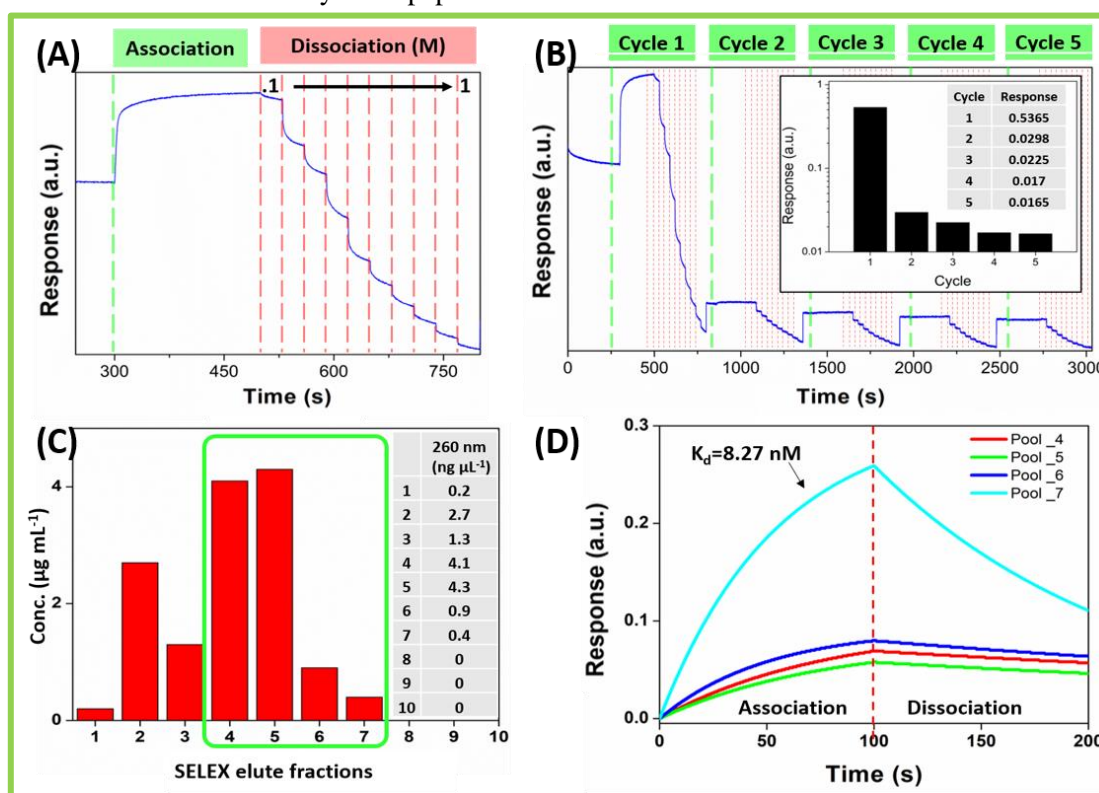


Figure 5.7: BLI SELEX for Stx1.1: (A) Sensogram of a cycle showing association-dissociation kinetics of Stx1.1 coated AR2G sensor with oligomer library & subsequent dissociation with increasing concentration of NaCl (0.1-1 M). (B) SELEX cycle iterations to enrich binders from the naïve library and the binding response to target with each iteration shown as a histogram (inset). (C) Spectrophotometric quantification ($\lambda_{260 \text{ nm}}$) of ssDNA in elutes. The highlighted elutes were purified, amplified & generated aptamer pools characterized for binding affinity. (D) Sensogram is showing the association-dissociation curves of selected positive pools.

The step increase in binding response in association step shows the fishing of sequences from exposed oligomer library and subsequent dips are recorded sequentially after the oligo/peptide complex is allowed to dissociate in increasing concentration of NaCl (0.1-1 M), depicting a decrease in the biolayer formed on the sensor and henceforth shedding of sequences from the peptide coated sensor. The enrichment of other possible aptamers from the naïve library, the process was repeated multiple times (Figure 5.7 B).

However, it was observed that in the first association itself most of the binders from the library had interacted with the sensor, and an almost negligible association was recorded in further iterations (inset in Figure 5.7 B). This efficiency can be attributed to the interacting potency of the various sequences of the naïve library with the chosen target and will tend to differ with different library-target combinations. In our present study, noteworthy results were obtained with the single primary cycle, and further enrichment did not significantly enhance the screening process, as evident from Figure 5.7B. From the first round (Figure 5.7C), the initial two elutes (0.1-0.2 M) were disregarded due to the nominal stringency of their dissociation buffer, which merely constituted as wash buffers. Thus, the latter DNA elutes pools in higher strength buffers were chosen, purified, amplified, and studied for binding affinity against the target peptide. These dissociated molecules ($13.9 \text{ ng } \mu\text{L}^{-1}$) collectively constituted $\sim 56\%$ sequences of the exposed naïve library ($24.5 \text{ ng } \mu\text{L}^{-1}$). In our knowledge, such binding efficiency from a single initial SELEX cycle has not been reported yet and particularly for the first time using BLI SELEX. The binding sensogram in Figure 5.7D shows the massive difference in the association curve of the eluted pools, denoting an increase in binding affinity of latter fractions. The pool with the best binding affinity (in this particular case) pool 7 with $K_d = 8.27 \text{ nM}$ against peptide Stx1.1 was chosen for further study. Similar protocol for selection and monitoring was carried out for Stx2 peptides and the best binding affinity pool 6 with $K_d = 4.6 \text{ nM}$ against peptide Stx2.3 was chosen for further study (Figure 5.8).

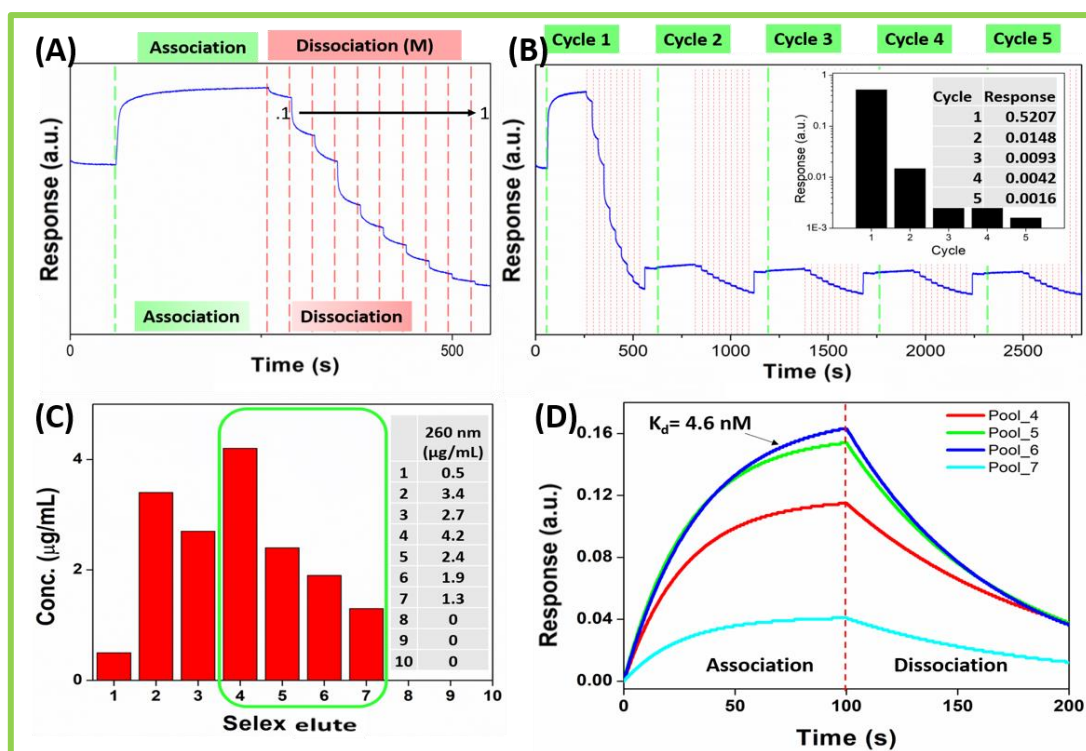


Figure 5.8: BLI-SELEX of Stx2.3: (A) Sensogram of a cycle showing association- dissociation kinetics of Stx2.3 coated AR2G sensor with oligomer library and subsequent dissociation with increasing conc. of NaCl (0.1-1 M). (B) SELEX cycle iterations. (Inset) The oligomer binding response to the peptide coated sensor with each iteration is shown in the histogram. (C) Spectrophotometric ($\lambda_{260 \text{ nm}}$) quantification of aptamer concentration of eluting fractions collected after SELEX progression. (D) Sensogram is showing the association-dissociation curves of selected positive pools.

The selected pools were cloned and sequenced, providing multiple aptamer sequences, out of which few were chosen based on their variability in cladogram phylogenetic tree clusters generated by Clustal Omega online tool (<https://www.ebi.ac.uk/Tools/msa/clustalo/>) were used for further application (Figure 5.9).

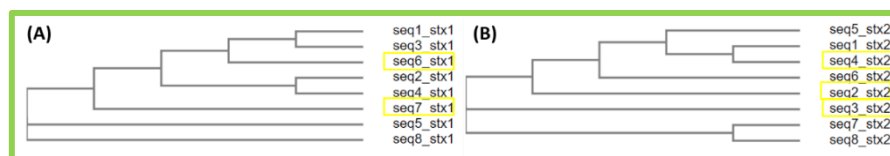


Figure 5.9: Potential aptamer sequences: Cladograms generated for aptamer sequences (using the 45-nt random region) obtained by BLI-SELEX against Shiga toxin subtypes viz. (A) Stx1 and (B) Stx2. The highlighted aptamers in the respective cladograms were renamed to Apt(Stx1.1), Apt(Stx1.2) for stx1 and Apt(Stx2.1), Apt(Stx2.2) and Apt(Stx2.3) for stx2. These selected sequences were processed for further analysis and application.

5.3.2.1 Aptamer-target binding interaction

5.3.2.1.1 BLI studies

The binding affinity of the selected aptamers with the whole protein toxin was analyzed using BLI at various concentrations of the individual champion aptamers for Stx1 and Stx2. The affinity measurements were analyzed using BLI technique, with the cognate toxins immobilized onto sensors and dipped sequentially into increasing dilutions of each selected aptamers (0, 25, 50, 100 nM). The affinity of selected aptamers was estimated on Octet Red96 using FortéBio Data analysis software using 1:1 binding model and global fitting³¹. For the simple binding reaction:



where, A is an aptamer, and T is target,

The interactions of the aptamer and target are denoted by dissociation constant for affinity:

$$K_d = [A][T]/[AT] = k_{off}/k_{on},$$

which is the ratio between the two rate constants, the dissociation rate constant (k_{off}) and the association rate constant (k_{on}). The average K_d value was estimated from the mean sum of the K_d

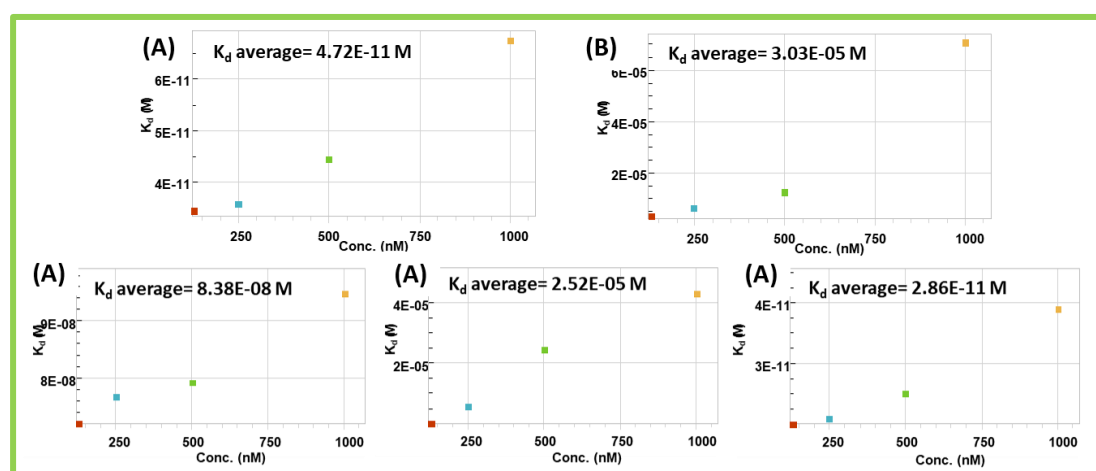


Figure 5.10: K_d BLI studies: The BLI study plots (concentration vs. K_d) with varying concentrations of selected aptamer (0, 25, 50, 100 nM) allowed to interact with their cognate toxins to estimate the average K_d value of the aptamer sequences viz., (a) Apt(Stx1.1), (b) Apt(Stx1.2), (c) Apt(Stx2.1), (d) Apt(Stx2.2) and (e) Apt(Stx2.3).

values at the different concentrations using the fore-mentioned relation and was found to be 4.72×10^{-11} , 3.03×10^{-5} , 8.38×10^{-8} , 2.52×10^{-5} , 2.86×10^{-11} M for Apt(Stx1.1), Apt(Stx1.2), Apt(Stx2.1), Apt(Stx2.2) and Apt(Stx2.3), respectively. The affinity was observed to be relatively marginally higher at lower concentrations due to slow k_{off} (10 s^{-1}) rates which can be attributed to efficient [AT] complex formation at the bio-interface. At very high aptamer concentrations (100 nM), it is observed the k_{on} is reduced [e.g., 1.6×10^{-6} to 0.3×10^{-6} for Apt(Stx1.1)] which may be due to the oligomer crowding at the binding interface, reducing the association rate and subsequently with the free receptor molecules concentration predominating the reaction, skewing the k_{off}/k_{on} ratio towards product dissociation (Figure 5.10). The marginal variation (\pm) lies within the individual acceptable K_d range. These aptamer-protein interactions are modulated by the intra and inter molecular electrostatic and hydrophobic interactions and deviate from the equimolar stoichiometric relationships^{32,33}. The representative sensograms at 100 nM aptamer concentration for the selected aptamers against Stx1 and Stx2 have been shown in Figure 5.11 A-B, and the dissociation constants of various aptamers along with their sequences in Figure 5.11 C. It was observed that Apt(Stx1.1) and Apt(Stx2.3) showed low dissociation constants of 47.2 pM and 28.6 pM, respectively, with their cognate toxins.

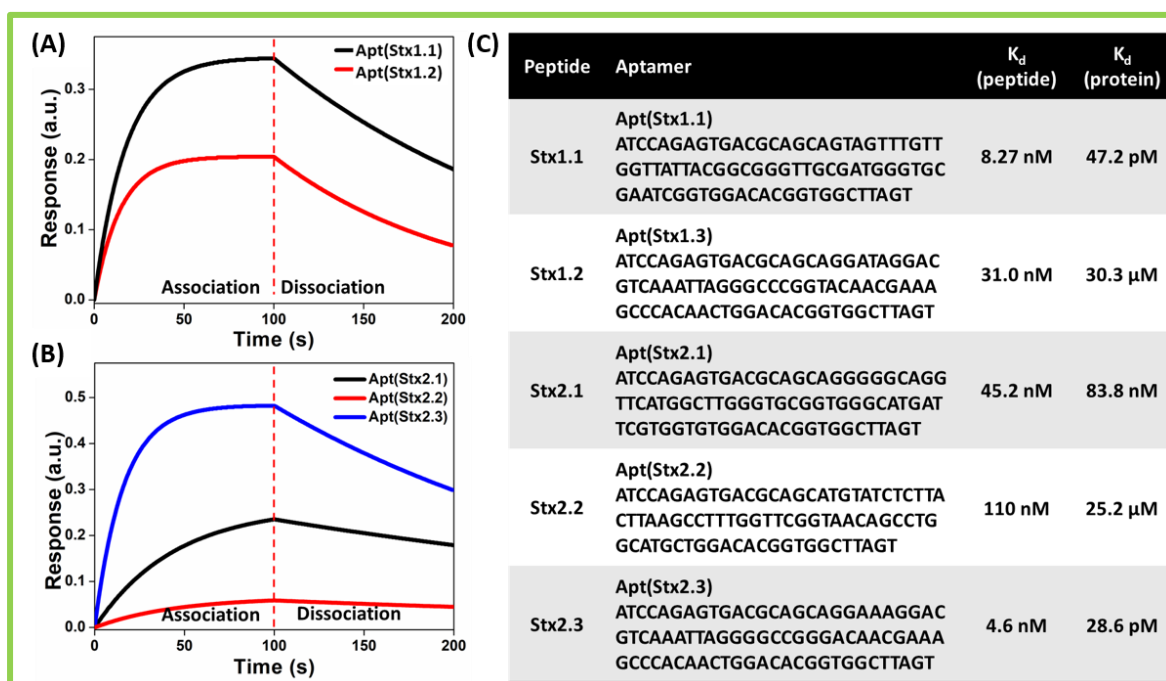


Figure 5.11: Binding affinity results: BLI binding affinity assays for best-of-pool aptamers at 100 nM concentration against whole protein toxin (A) Stx1 & (B) Stx2 showing functional association-dissociation kinetics. (C) List of best-of-pool aptamers along with their average K_d values against both targeted epitope peptides & whole cognate toxins.

5.3.2.1.2 Fluorescence plate binding

These binding capabilities of the selected champion aptamers were further corroborated using fluorescence plate binding assay (Figure 5.12), showing increasing binding of cognate targets with respective FITC labeled aptamers.

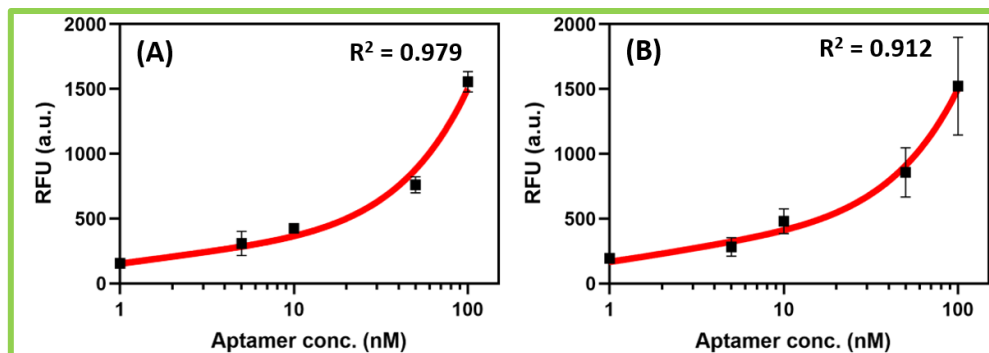


Figure 5.12: Fluorescence binding assay: Plate binding curves are showing the efficient binding of aptamers to cognate toxins (A) Stx1 and (B) Stx2.

5.3.2.2 Aptamer sequence & structure – Bioinformatic study

5.3.2.2.1 Structure elucidation

Out of the clones sequenced, those conforming to Guanine-quadruplex (G-quad) motifs in sequence regions were analyzed, therein Apt(Stx1.1) containing G-quad from N²⁹-N⁵³ and N⁶²-N⁷⁶ & in Apt(Stx2.3) from N¹⁹-N⁴⁵ were successfully selected. The ‘mfold’ tool generated putative structures of the selected aptamers presented in Figure 5.14 show different structural conformations and

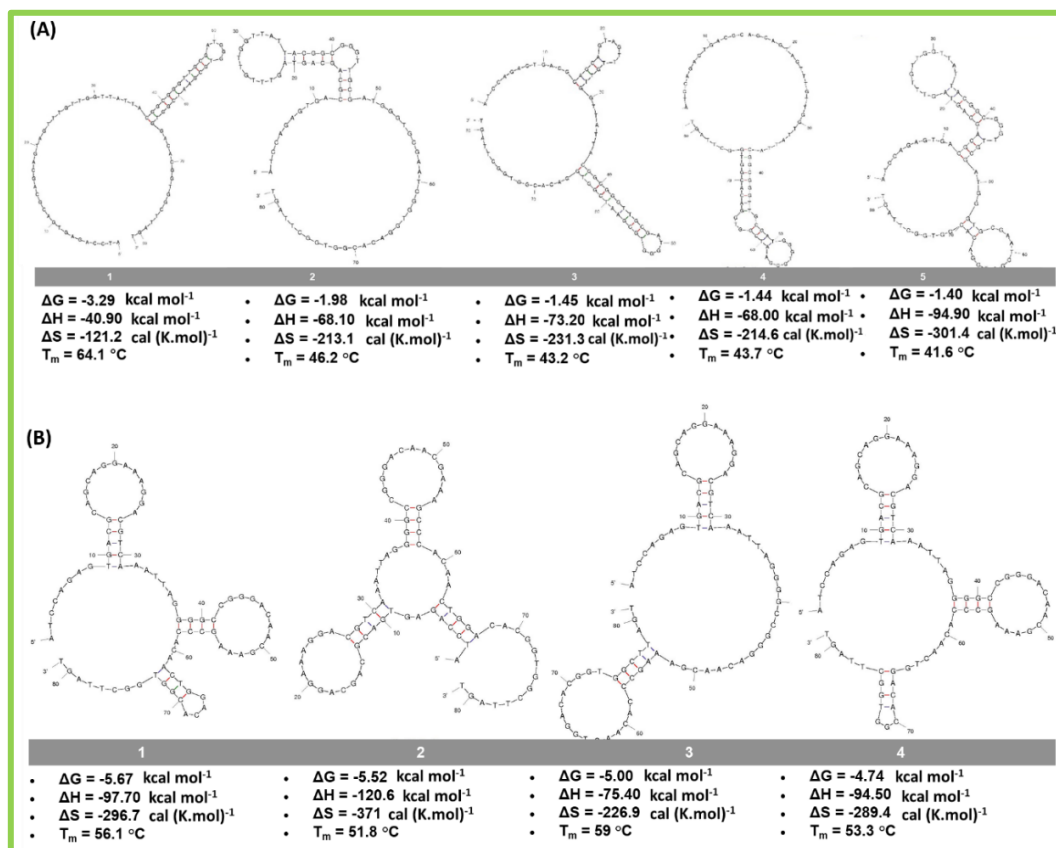


Figure 5.13: Mfold results: (A) Apt(Stx1.1) & (B) Apt(Stx2.3).

thermodynamic properties of the sequences Apt(Stx1.1) and Apt(Stx2.3) at standardized binding buffer ionic conditions of $[Na^+] = 0.10\text{ M}$, $[Mg^{2+}] = 0.005\text{ M}$ at 37°C . The individual structures with the lowest ΔG ($-3.29\text{ kcal mol}^{-1}$ and $-5.67\text{ kcal mol}^{-1}$) for the two subtypes were chosen, and their structure models rendered. Both of these aptamers as seen in Figure 5.13 showed significant secondary structural elements viz., stacks, helix & loops resulting in high complexity structures with Apt(Stx1.1) showing a hairpin loop motif from $G^{48} - T^{54}$ and Apt(Stx2.3) showing three prominent hairpin loops viz., $G^{65}-C^{70}$, $C^{41}-G^{55}$, and $G^{13}-C^{27}$.

5.3.2.2.2 Salt concentration studies

These putative structures were also generated for the selected aptamers at varying $[Na^+] = 0.1 - 1\text{ M}$, showing that the secondary structure of the aptamer (Figure 5.14). Though rigid within some concentration range, the aptamers changed their folded conformation when the environmental salt concentration was considerably altered. Given this, though the oligomer structures would vary in different dissociating buffers during the BLI-SELEX, for the study of association interaction and as well in further application studies, the concentration of Na^+ was kept standard at 0.1 M in the binding buffer. Thus, for all our other simulations, this parameter has been fixed for the ease of our experimental study.

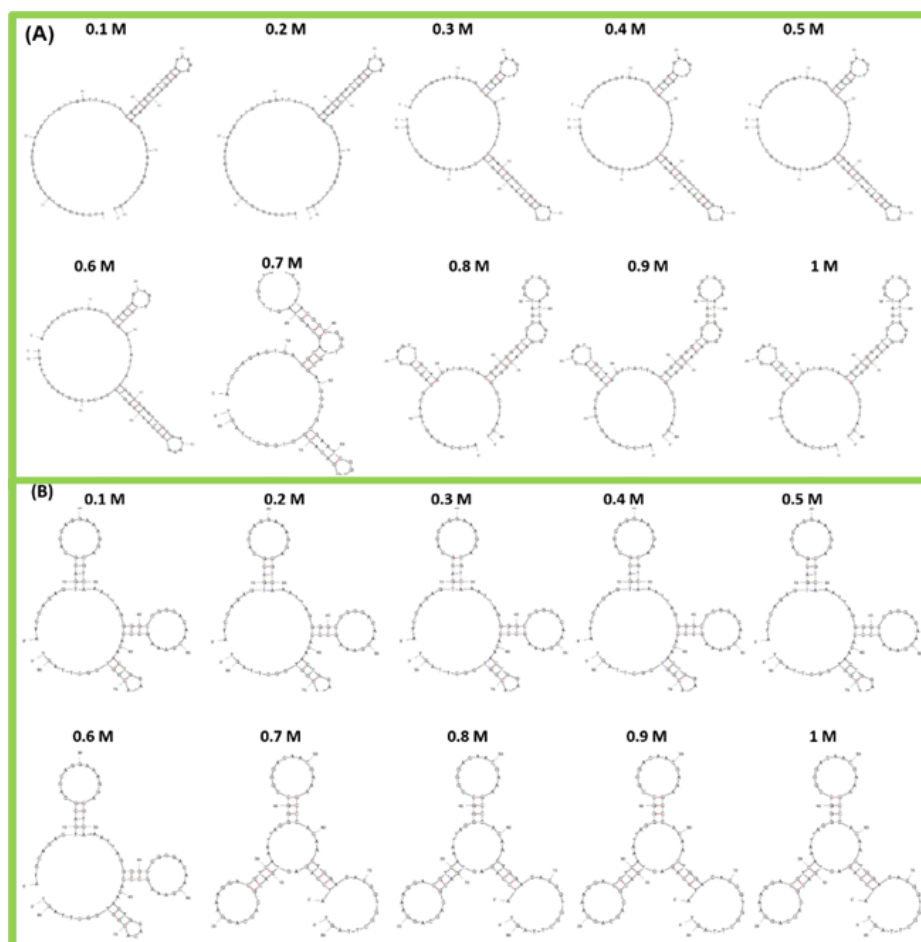


Figure 5.14: Mfold putative structures of Apt(Stx1.1) with varying NaCl concentration: The putative structures are calculated for linear DNA at 37°C with ionic conditions: $[Na^+] = 0.1-1\text{ M}$, $[Mg^{2+}] = 0.005\text{ M}$ showing altered folded structures for the same sequence at different ionic concentrations.

5.3.2.2.3 Z-dock docking studies

The docking studies simulated for apta-peptide interactions were carried out using Zdock (version 3.0.2) at a pre-automated interparticle distance of 1.2 Å in the vacuum, which showed extensive intramolecular polar interactions & conformational fitting of the target into the aptamer binding pockets (Figure 5.15). Though this interaction might vary in the solution phase, this is a preliminary attempt in understanding bio-interaction amongst the target and ligand. These well-characterized champion aptamers (with the highest K_d value to protein toxin) were chosen as bio-receptors for subsequent bio-sensing assays.

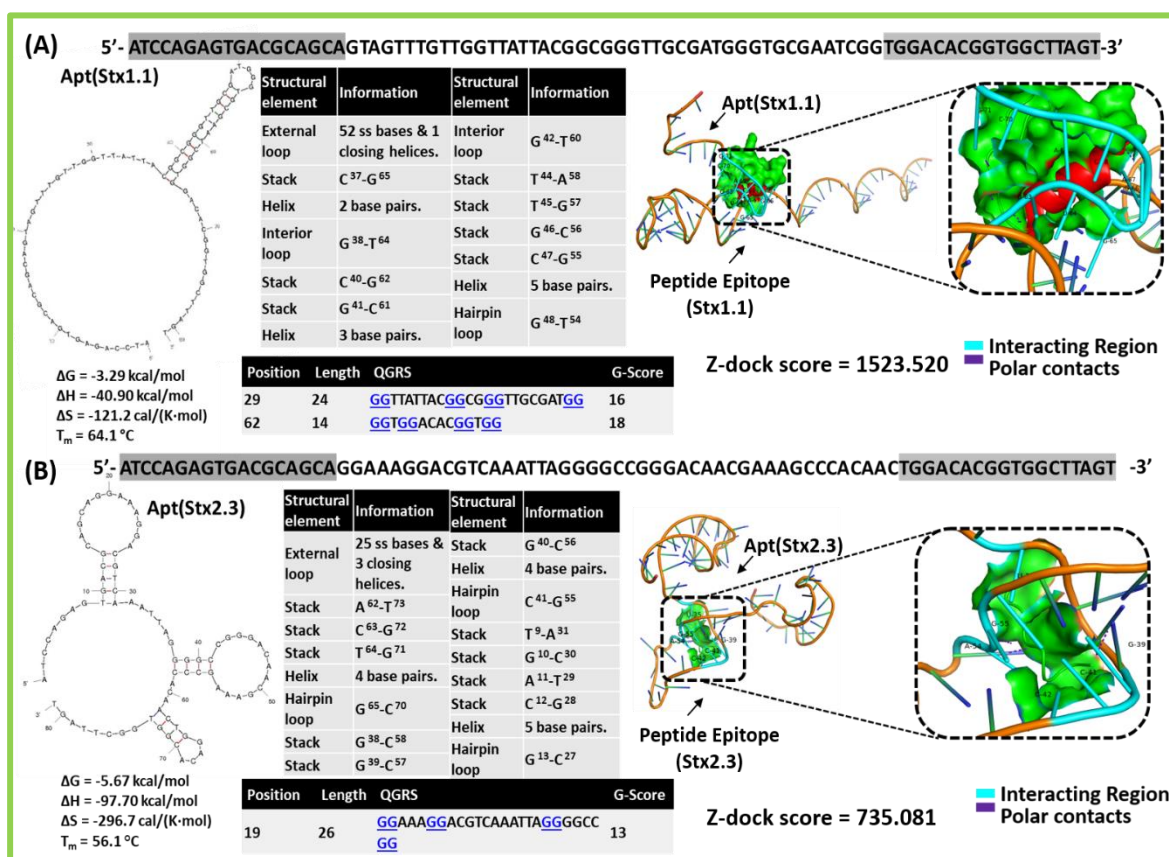


Figure 5.15: Structure and docking studies: The *mfold* structures (left) of selected aptamers Apt(Stx1.1) (Upper Panel) and Apt(Stx2.3) (Lower Panel) were found to have G-quadruplex estimated by using QGRS online tool. Out of the several possibilities, the structures with the lowest Gibbs free energy were selected, and their 3D model rendered. The Zdock studies (right) were simulated for apta-peptide showing both intramolecular polar interactions and structural fitting of binding pockets. The cyan highlighted region depicts the interacting region of the DNA aptamer with the respective target peptide.

Correspondingly, similar studies were carried out for other epitopes of Stx1 & Stx2 and the best-of-pool aptamers were selected (Figure 5.16).

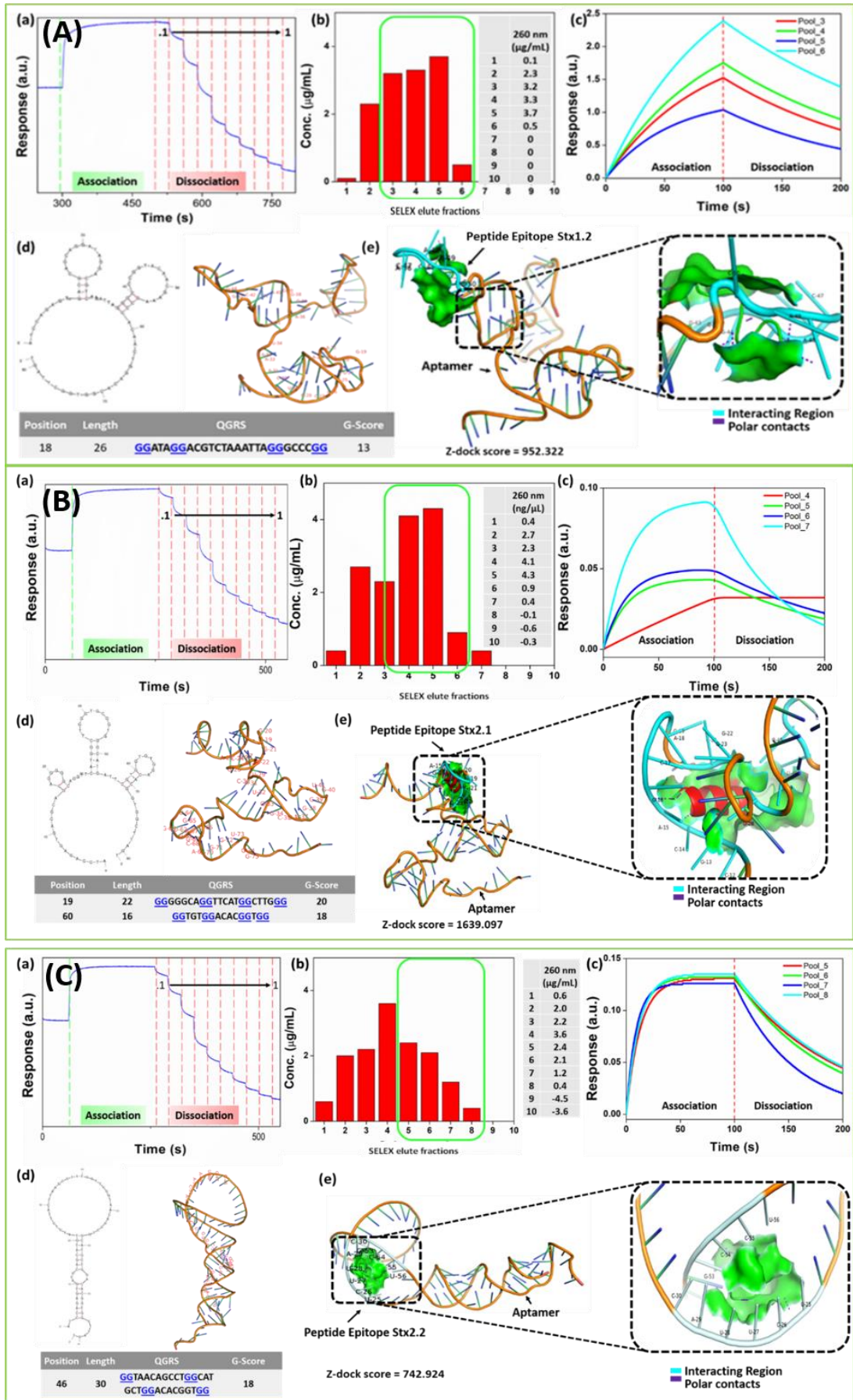


Figure 5.16: Comprehensive SELEX aptamer studies: (A) Stx1.2 (B) Stx2.1 (C) Stx2.2 peptide aptamer characterizations; (a) BLI-SELEX progression, (b) elute ssDNA conc., (c) elute pools sensograms showing binding characteristics to target, (d) mfold aptamer structure, (e) z-dock interaction view.

5.3.3 Nanosensor development & characterization

5.3.3.1 Chito-WSe₂ nanosheets characterization

The chito-WSe₂ nanosheets synthesis was optimized and characterized as shown in Figure 5.17.

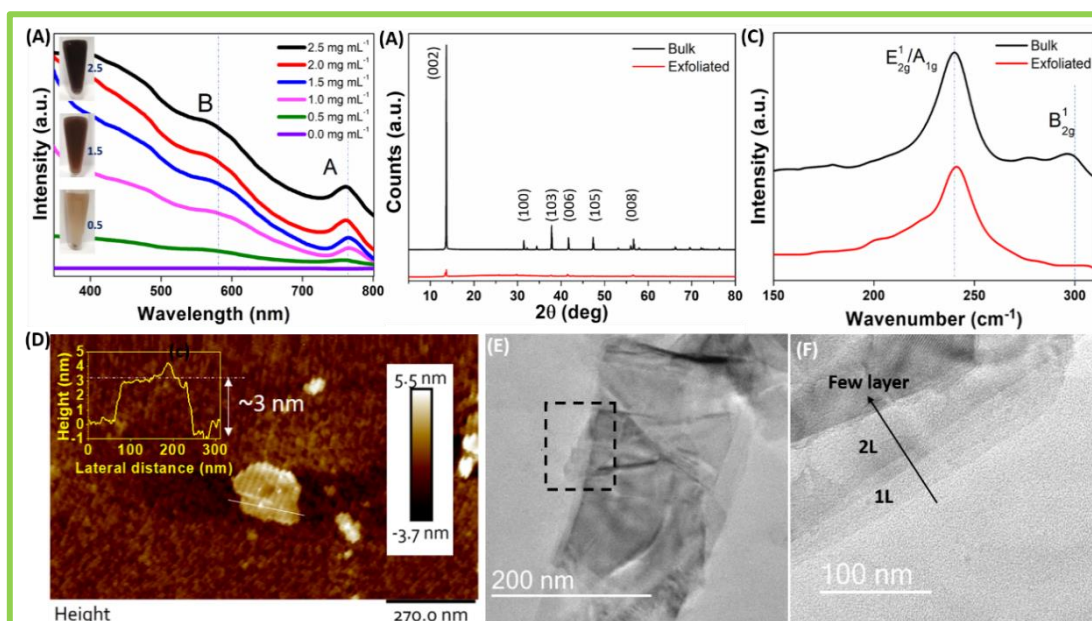


Figure 5.17: Nanomaterial characterization: (A) Extinction spectra are showing the characteristic 'A' & 'B' excitons of WSe₂ and proportional intensity increase with an increase in exfoliant chitosan concentration along with optical images of various dispersions (inset) (B) comparative XRD spectra and (C) Raman spectra of bulk and exfoliated material. (D) AFM image along with the height profile and (E-F) TEM images showing exfoliated few layers.

(A) UV-Vis studies

The liquid exfoliated chito-WSe₂ nanosheets appeared as a reddish dispersion (inset of Figure 5.17A). It can be easily observed that with increasing concentration of chitosan, the extent of exfoliation increased as depicted in Figure 5.17A. Higher concentrations were observed to have increased viscosity, difficult for homogenous dilutions & correct estimations. A good exfoliated nanomaterial amount (0.43 mg exfoliated per 1 mg bulk) was obtained after 30 min of pulsated exfoliation and used for further experiments. In the extinction spectra, typical excitonic peaks A & B corresponding to valence band split & spin-orbital coupling were well observed³⁴.

(B) Raman & XRD Pattern

As observed in Figure 5.17C, the XRD spectra of bulk & exfoliated nanomaterial were consistent with the hexagonal lattice structure of WSe₂ (reference JCPDS card no. 00-038-1388), and a broad overlapped peak at 245 cm⁻¹ for E_{2g}¹ (in-plane) & A_{1g} (out-of-plane) were observed in Raman spectra. The reduction in peak intensity of (002) plane in XRD spectra and B_{2g}¹ peak at 301 cm⁻¹ in Raman spectra of exfoliated nanomaterial are indicative of few-layered sheets³⁵.

(C) AFM microscopy

AFM analysis revealed the ultrathin sheet-like nature of the chito-WSe₂ of a thickness ~3 nm suggesting few-layered nanostructure (provided being chitosan-coated) with a lateral length of ~250 nm.

(D) TEM images

HR-TEM images supplemented with EDX maps (Figure 5.18) show the wrinkled few-layer sheets with mono & bilayers being observed. The hexagonal symmetry of WSe₂ with a lattice spacing of 0.326 nm corresponding to a single layer (100) plane was seen³⁶.

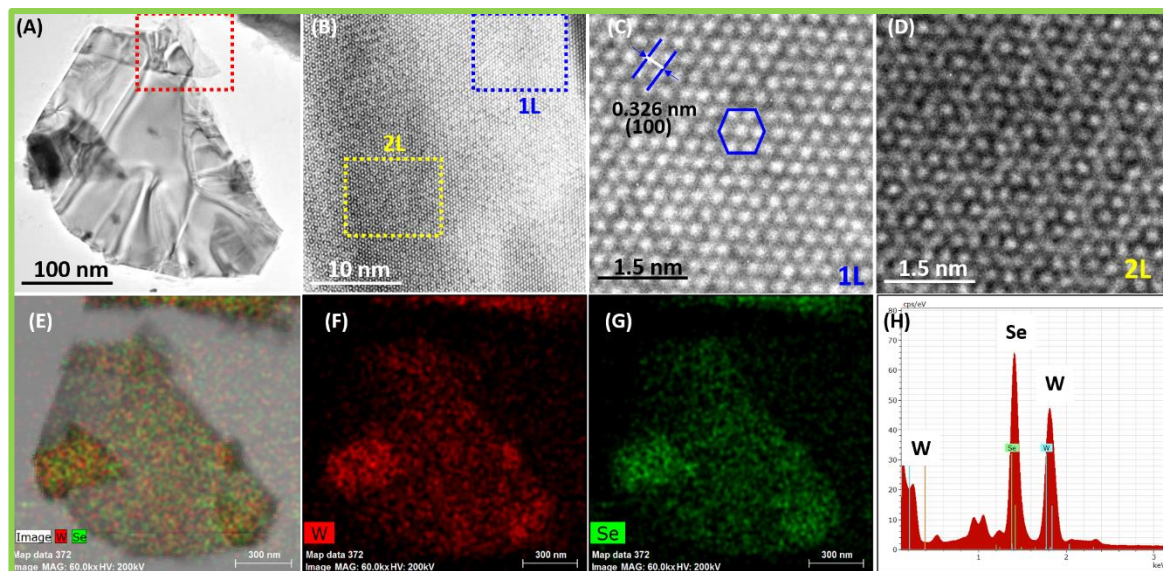


Figure 5.18: TEM micrographs: Displaying low magnification image of (A) exfoliated chito-WSe₂ nanosheet (B) magnified few-layer region of overlapped flakes & high-resolution images of (C) monolayer & (D) bilayer region along with (E-G) corresponding EDX elemental mapping & spectra.

5.3.3.2 Chito-WSe₂ aptamer functionalization

Zeta potential measurements carried out using Malvern Zetasizer Nano ZSP (Figure 5.19). The zeta potential studies suggest that chito-WSe₂ nanosheets dispersed in mild acetic acid (0.5 % v/v; pH 6.5) were positively charged with a zeta potential of 11.8 mV, which correlates with the presence of protonated amine groups on chitosan ($pK_a = 6.3$). To optimize maximum functionalization as a function of pH variation in apt-chito-WSe₂ interaction, 10 μ L aptamer ($230 \mu\text{g mL}^{-1}$) and 100 μ L chito-WSe₂ nanosheets ($100 \mu\text{g mL}^{-1}$) were incubated together for 15 min at pH 6.0, 6.5, 7.0 and 7.5. before analyses. The apparent zeta potential was recorded at increasing pH values as -22.7, -20.1, -16.3, and 2.6, respectively. A large redshift to -22.7 mV is observed at pH 6 when DNA aptamer is functionalized over chito-WSe₂ due to the electrostatic interactions between abundant NH_3^+ of chitosan & negatively charged DNA, suggesting maximum binding. Keeping in view the higher probability of acid hydrolysis of ssDNA at lower pH, and a comparative loading of aptamer at pH 6.5 and 7.0, the latter was chosen as the best environment.

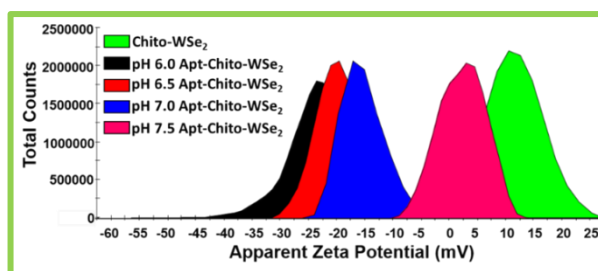


Figure 5.19: Zeta potential measurements: Zeta potential measurements are confirming the interaction between DNA aptamer & chito-WSe₂ nanosheets and the effect of acidic, neutral & basic pH on the binding of the aptamer to the nanomaterial.

5.3.3.3 Aptasensor microscopic characterization

The SEM studies of sensor surface showed good area coverage and morphological change of the sensor surface upon aptamer immobilization, validating efficient functionalization (Figure 5.20).

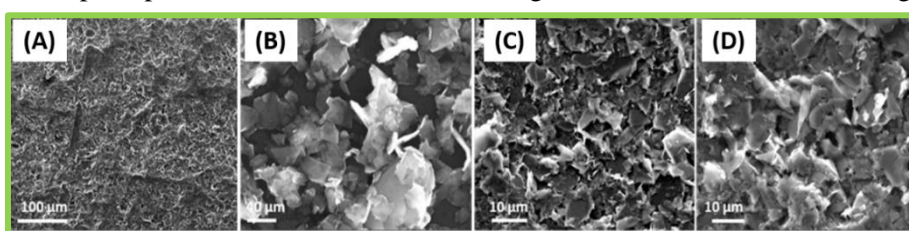


Figure 5.20: SEM morphology of electrode surface: (A) Morphology of bare carbon working electrode, (B) bulk WSe₂ material, (C) chito-WSe₂ nanosheets modified surface, (D) aptamer functionalized chito-WSe₂ sensor surface.

5.3.3.4 Aptasensor electrochemical characterization

The electrochemical characterization was carried out via both CV and EIS studies (Figure 5.21) and CV measurements optimized the amount of chito-WSe₂ deposited onto working electrode of SPE.

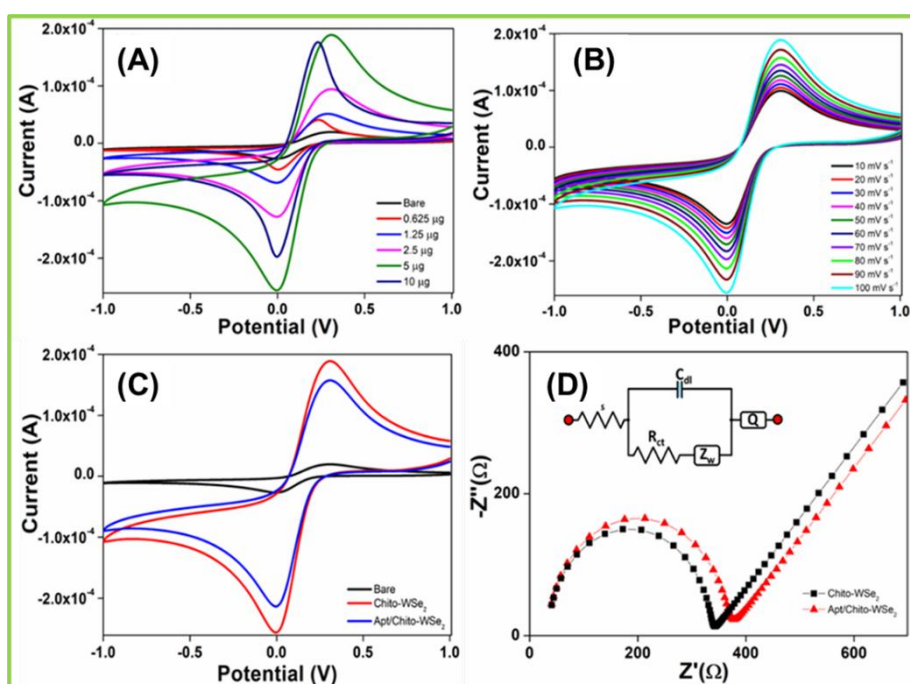


Figure 5.21: Electrochemical nanosensor characterization: (A) The modification of working electrode with increasing concentrations of chito-WSe₂ and (B) scan rate studies from 10-100 mV s⁻¹ at optimized 10 μg concentration. (C) Comparative CV responses of electrode. (D) Nyquist plots for comparative modified and functionalized electrode showing a minor increase in R_{ct} upon functionalization.

Maximum current response was observed for 5 μg of nanomaterial, and this optimized concentration was used for further modifications (Figure 5.21 A). The nanostructured sensor showed a linear increase in the current intensity with the square root of the increasing scan rate (10 mV s^{-1} to 100 mV s^{-1}), indicating the diffusion control process (Figure 5.21 B). A small drop in current in CV scan & R_{ct} value in EIS were observed upon aptamer immobilization, which proves its deposition on sensor surface (Figure 5.21 C-D).

5.3.3.5 Aptasensing assay

5.3.3.5.1 Voltammetric detection of Stx1

The respective Apt(Stx1.1) modified nanosensors were used for the detection toxin subtypes using the square wave voltammetry technique (SWV). Figure 5.22 shows a sequential decrease in current when the sensors were subjected to cognate toxin Stx1, with a linear range of detection from 50 pg - 100 ng . The developed nanosensor showed a sensitivity of $\sim 5 \mu\text{A ng}^{-1} \text{mL}$ with a LOD of 44.5 pg mL^{-1} for Stx1.

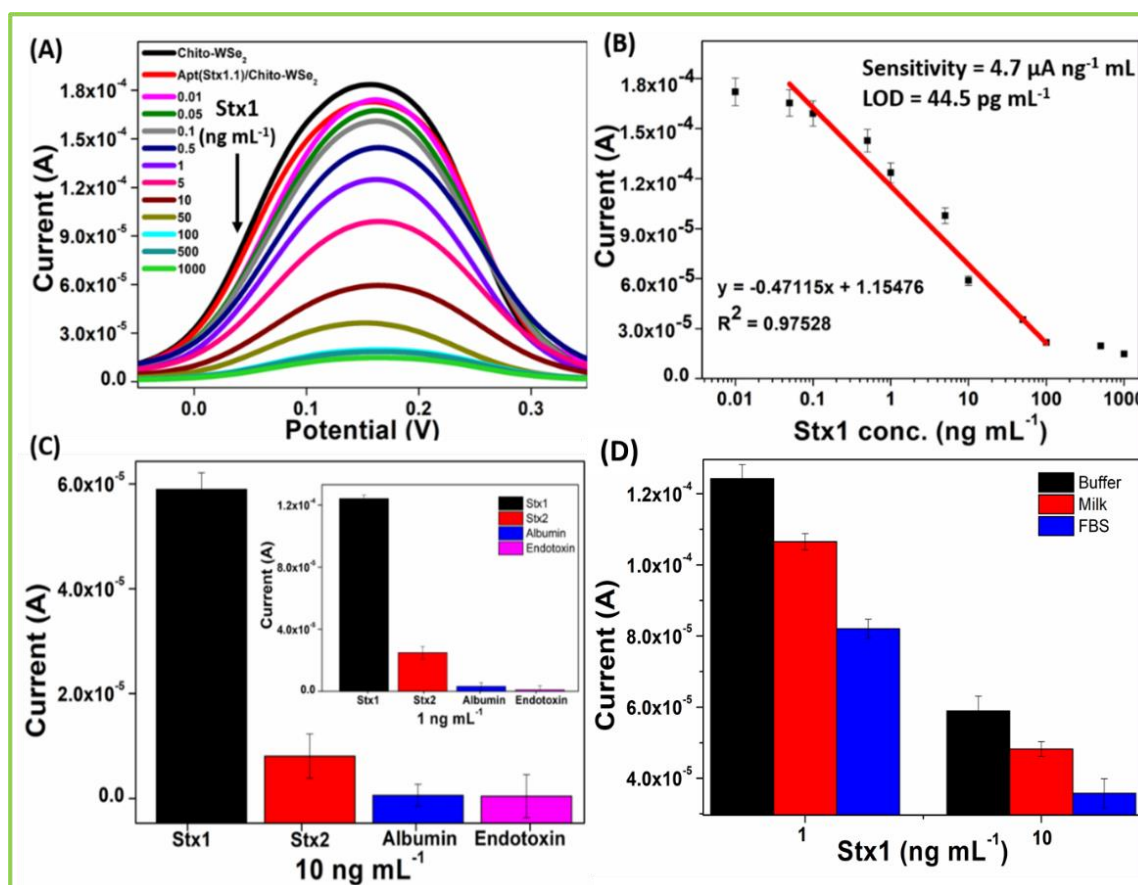


Figure 5.22: Voltammetry bioassay for Stx1: (A) SWV curves (B) calibration plot and, (C) bar graph showing the comparative response upon detection of other cross-reactive molecules at 10ng mL^{-1} and (inset) 1ng mL^{-1} (D) bar graph depicting SWV response in pre-processed spiked real samples at 1 & 10ng mL^{-1} .

The comparative analysis of various nanostructured bio-sensing platforms for detecting *E. coli* Stx has been tabulated in Table 5.3, which validates the superiority of our platforms fabricated in this chapter.

Receptor	Detection method	Limit of detection	Range	Ref.
Polyclonal antibodies	ELISA	115 ng mL ⁻¹ of Stx2	0.93 - 7.5 µg mL ⁻¹	37
RNA aptamers	Filter-binding assay	0.5 µM Stx1 or Stx2	-	14
Polyclonal antibodies	ELISA	1 µg mL ⁻¹ of Stx	-	38
Monoclonal antibodies	ELISA	-	10 - 50 pg mL ⁻¹	39
Monoclonal antibodies	ELISA	0.13 ng mL ⁻¹ of Stx2	0.5 - 10 ng mL ⁻¹	40
DNA aptamers	Square wave voltammetry	Stx1: 44.5 pg mL ⁻¹ Stx2: 41.3 pg mL ⁻¹	50 pg mL ⁻¹ -100 ng mL ⁻¹	This study

Table 5.3: Comparative platforms: Relevant Stx detection platforms with their merits.

5.3.3.5.2 Voltammetric detection of Stx2

The Apt(Stx2.3) modified nanosensors were used for the detection of respective toxin subtypes using the SWV technique and the developed nanosensor showed a LOD of 41.3 pg mL⁻¹ for Stx2 (Figure 5.23).

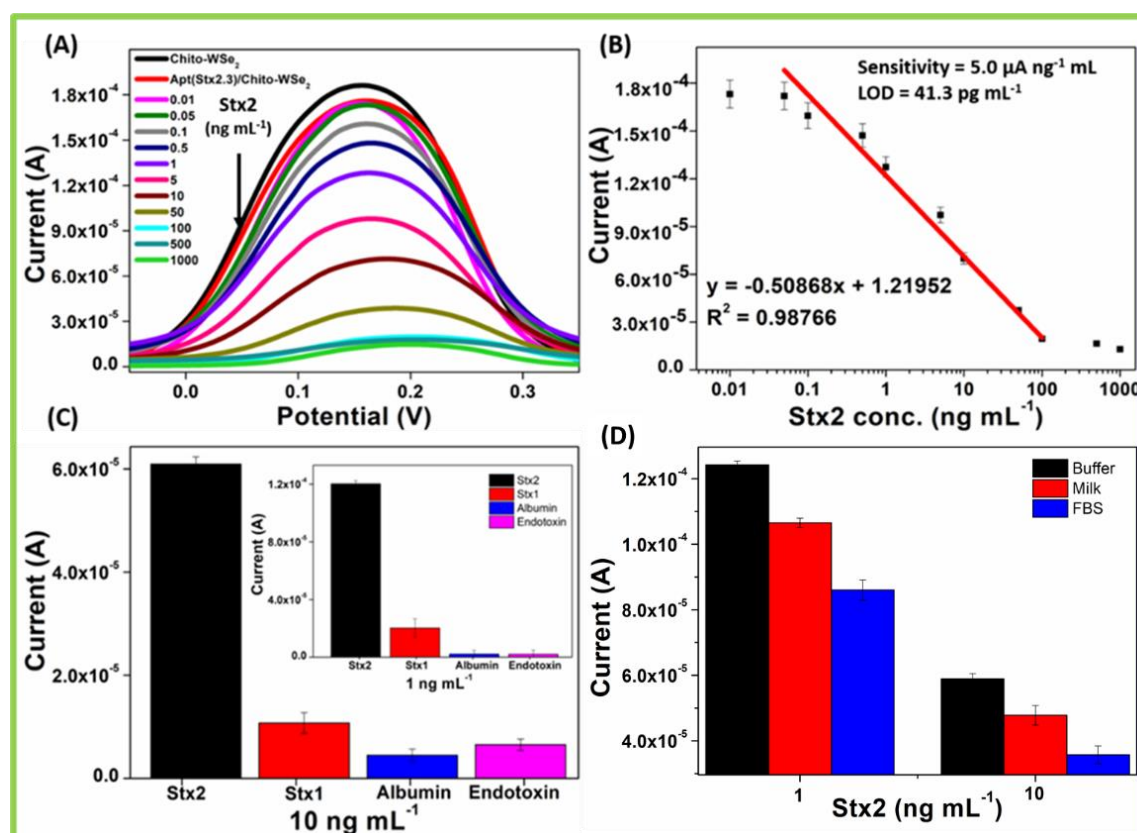


Figure 5.23: Voltammetry bioassay for Stx2: (A) SWV curves upon sensing of Stx2 and (B) calibration plot. (C) Bar graph showing the comparative response upon detection of other cross-reactive molecules at 10 ng mL⁻¹ and (inset) 1 ng mL⁻¹ (D) Bar graph depicting SWV response in pre-processed spiked real samples at both 1.0 and 10 ng mL⁻¹ concentration.

5.4 Conclusion

The study reports real-time & label-free aptamer selection using BLI-SELEX, yielding novel high-affinity aptamers against antigenically distinct *E. coli* Shiga toxins subtypes via specific epitopic peptides. These fully characterized aptamers, Apt (Stx1.1) & Apt(Stx2.3) with a picomolar affinity of K_d (~47 pM & ~29 pM, respectively) were successfully used to fabricate respective voltammetric diagnostic assays via immobilization onto chitosan exfoliated & functionalized 2D tungsten diselenide nanosheet platforms.

These aptamers modified nanosensors showed high sensitivity of $\sim 5.0 \mu\text{A ng}^{-1} \text{mL}$, a dynamic response range from 50 pg mL^{-1} to 100 ng mL^{-1} with a detection limit of 44.5 pg mL^{-1} & 41.3 pg mL^{-1} for Stx1 & Stx2, respectively with low cross-reactivity in spiked sera and milk samples.

Bibliography

- (1) Tuerk, C.; Gold, L. Systematic Evolution of Ligands by Exponential Enrichment: RNA Ligands to Bacteriophage T4 DNA Polymerase. *Science* (80). **1990**, 249 (4968), 505–510. <https://doi.org/10.1126/science.2200121>.
- (2) Panigaj, M.; Johnson, M. B.; Ke, W.; McMillan, J.; Goncharova, E. A.; Chandler, M.; Afonin, K. A. Aptamers as Modular Components of Therapeutic Nucleic Acid Nanotechnology. *ACS Nano* **2019**. <https://doi.org/10.1021/acsnano.9b06522>.
- (3) Negahdary, M. Aptamers in Nanostructure-Based Electrochemical Biosensors for Cardiac Biomarkers and Cancer Biomarkers: A Review. *Biosensors and Bioelectronics*. Elsevier Ltd March 15, 2020, p 112018. <https://doi.org/10.1016/j.bios.2020.112018>.
- (4) Goto, S.; Tsukakoshi, K.; Ikebukuro, K. Development of Aptamers against Unpurified Proteins. *Biotechnology and Bioengineering*. John Wiley and Sons Inc. December 1, 2017, pp 2706–2716. <https://doi.org/10.1002/bit.26389>.
- (5) Dupont, D. M.; Larsen, N.; Jensen, J. K.; Andreassen, P. A.; Kjems, J. Characterisation of Aptamer-Target Interactions by Branched Selection and High-Throughput Sequencing of SELEX Pools. *Nucleic Acids Res.* **2015**, 43 (21). <https://doi.org/10.1093/nar/gkv700>.
- (6) Wang, T.; Chen, C.; Larcher, L. M.; Barrero, R. A.; Veedu, R. N. Three Decades of Nucleic Acid Aptamer Technologies: Lessons Learned, Progress and Opportunities on Aptamer Development. *Biotechnol. Adv.* **2019**, 37 (1), 28–50. <https://doi.org/10.1016/j.biotechadv.2018.11.001>.
- (7) Kelly-Cirino, C. D.; Nkengasong, J.; Kettler, H.; Tongio, I.; Gay-Andrieu, F.; Escadafal, C.; Piot, P.; Peeling, R. W.; Gadde, R.; Boehme, C. Importance of Diagnostics in Epidemic and Pandemic Preparedness. *BMJ Glob. Heal.* **2019**, 4 (Suppl 2), e001179. <https://doi.org/10.1136/bmjgh-2018-001179>.
- (8) Kirk, M. D.; Pires, S. M.; Black, R. E.; Caipo, M.; Crump, J. A.; Devleeschauwer, B.; Döpfer, D.; Fazil, A.; Fischer-Walker, C. L.; Hald, T.; Hall, A. J.; Keddy, K. H.; Lake, R. J.; Lanata, C. F.; Torgerson, P. R.; Havelaar, A. H.; Angulo, F. J. World Health Organization Estimates of the Global and Regional Disease Burden of 22 Foodborne Bacterial, Protozoal, and Viral Diseases, 2010: A Data Synthesis. *PLOS Med.* **2015**, 12 (12), e1001921. <https://doi.org/10.1371/journal.pmed.1001921>.
- (9) Kavaliauskiene, S.; Dyvelingelem, A. B.; Skotland, T.; Sandvig, K. Protection against Shiga Toxins. *Toxins (Basel)*. **2017**, 9 (2), 44. <https://doi.org/10.3390/toxins9020044>.
- (10) Rahman, M.; Nabi, A.; Asadulghani, M.; Faruque, S. M.; Islam, M. A. Toxigenic Properties and Stx Phage Characterization of Escherichia Coli O157 Isolated from Animal Sources in a Developing Country Setting. *BMC Microbiol.* **2018**, 18 (1), 98. <https://doi.org/10.1186/s12866-018-1235-3>.
- (11) Vallières, E.; Saint-Jean, M.; Rallu, F. Comparison of Three Different Methods for Detection of Shiga Toxin-Producing Escherichia Coli in a Tertiary Pediatric Care Center. *J. Clin. Microbiol.* **2013**, 51 (2), 481–486. <https://doi.org/10.1128/JCM.02219-12>.
- (12) He, X.; Patfield, S.; Hnasko, R.; Rasooly, R.; Mandrell, R. E. A Polyclonal Antibody Based Immunoassay Detects Seven Subtypes of Shiga Toxin 2 Produced by Escherichia Coli in Human and Environmental Samples. *PLoS One* **2013**, 8 (10). <https://doi.org/10.1371/journal.pone.0076368>.
- (13) Mejías, M. P.; Hiriart, Y.; Lauché, C.; Fernández-Brando, R. J.; Pardo, R.; Bruballa, A.; Ramos, M. V.; Goldbaum, F. A.; Palermo, M. S.; Zylberman, V. Development of Camelid Single Chain Antibodies against Shiga Toxin Type 2 (Stx2) with Therapeutic Potential against Hemolytic Uremic Syndrome (HUS). *Sci. Rep.* **2016**, 6 (1), 24913. <https://doi.org/10.1038/srep24913>.
- (14) Challa, S.; Tzipori, S.; Sheoran, A. Selective Evolution of Ligands by Exponential Enrichment to Identify Rna Aptamers against Shiga Toxins. *J. Nucleic Acids* **2014**, 2014. <https://doi.org/10.1155/2014/214929>.
- (15) Kudlak, B.; Wiczczak, M. Aptamer Based Tools for Environmental and Therapeutic Monitoring: A Review

- of Developments, Applications, Future Perspectives. *Crit. Rev. Environ. Sci. Technol.* **2020**, *50* (8), 816–867. <https://doi.org/10.1080/10643389.2019.1634457>.
- (16) Li, F.; Yu, Z.; Han, X.; Lai, R. Y. Electrochemical Aptamer-Based Sensors for Food and Water Analysis: A Review. *Analytica Chimica Acta*. Elsevier B.V. March 21, 2019, pp 1–23. <https://doi.org/10.1016/j.aca.2018.10.058>.
 - (17) Rahmani, E.; Mayorga-Martinez, C. C.; Malekfar, R.; Luxa, J.; Sofer, Z.; Pumera, M. 1T-Phase Tungsten Chalcogenides (WS₂, WSe₂, WTe₂) Decorated with TiO₂ Nanoplatelets with Enhanced Electron Transfer Activity for Biosensing Applications. *ACS Appl. Nano Mater.* **2018**, *1* (12), 7006–7015. <https://doi.org/10.1021/acsanm.8b01796>.
 - (18) Shi, Q.; Shih, E.-M.; Gustafsson, M. V.; Rhodes, D. A.; Kim, B.; Watanabe, K.; Taniguchi, T.; Papić, Z.; Hone, J.; Dean, C. R. Odd- and Even-Denominator Fractional Quantum Hall States in Monolayer WSe₂. *Nat. Nanotechnol.* **2020**, *15* (7), 569–573. <https://doi.org/10.1038/s41565-020-0685-6>.
 - (19) Meirinho, S. G.; Dias, L. G.; Peres, A. M.; Rodrigues, L. R. Voltammetric Aptasensors for Protein Disease Biomarkers Detection: A Review. *Biotechnology Advances*. Elsevier Inc. September 1, 2016, pp 941–953. <https://doi.org/10.1016/j.biotechadv.2016.05.006>.
 - (20) Chen, A.; Shah, B. Electrochemical Sensing and Biosensing Based on Square Wave Voltammetry. *Analytical Methods*. May 7, 2013, pp 2158–2173. <https://doi.org/10.1039/c3ay40155c>.
 - (21) Ikebukuro, K.; Kiyohara, C.; Sode, K. Electrochemical Detection of Protein Using a Double Aptamer Sandwich. *Anal. Lett.* **2004**, *37* (14), 2901–2909. <https://doi.org/10.1081/AL-200035778>.
 - (22) Klausen, M. S.; Jespersen, M. C.; Nielsen, H.; Jensen, K. K.; Jurtz, V. I.; Sønderby, C. K.; Sommer, M. O. A.; Winther, O.; Nielsen, M.; Petersen, B.; Marcatili, P. NetSurfP-2.0: Improved Prediction of Protein Structural Features by Integrated Deep Learning. *Proteins Struct. Funct. Bioinforma.* **2019**, *87* (6), 520–527. <https://doi.org/10.1002/prot.25674>.
 - (23) Harpreet Kaur; Aarti Garg; G.P.S. Raghava. PEPstr: A de Novo Method for Tertiary Structure Prediction of Small Bioactive Peptides. *Protein Pept. Lett.* **2007**, *14* (7), 626–631. <https://doi.org/10.2174/092986607781483859>.
 - (24) Krieger, E.; Koraimann, G.; Vriend, G. Increasing the Precision of Comparative Models with YASARA NOVA—a Self-Parameterizing Force Field. *Proteins Struct. Funct. Bioinforma.* **2002**, *47* (3), 393–402. <https://doi.org/10.1002/prot.10104>.
 - (25) Biosensors, A. R. G. Dip and Read™ Amine Reactive Second-Generation (AR2G) Biosensors. 1–5.
 - (26) Zangi, R.; Hagen, M.; Berne, B. J. Effect of Ions on the Hydrophobic Interaction between Two Plates. *J. Am. Chem. Soc.* **2007**, *129* (15), 4678–4686. <https://doi.org/10.1021/ja068305m>.
 - (27) Fluorescein (FITC) | Thermo Fisher Scientific - IN <https://www.thermofisher.com/in/en/home/life-science/cell-analysis/fluorophores/fluorescein.html> (accessed Oct 23, 2020).
 - (28) Uysal Unalan, I.; Wan, C.; Trabattini, S.; Piergiovanni, L.; Farris, S. Polysaccharide-Assisted Rapid Exfoliation of Graphite Platelets into High Quality Water-Dispersible Graphene Sheets. *RSC Adv.* **2015**, *5* (34), 26482–26490. <https://doi.org/10.1039/c4ra16947f>.
 - (29) Chen, A.; Shah, B. Electrochemical Sensing and Biosensing Based on Square Wave Voltammetry. *Anal. Methods* **2013**, *5* (9), 2158–2173. <https://doi.org/10.1039/c3ay40155c>.
 - (30) Kozlova, E. E. G.; Cerf, L.; Schneider, F. S.; Viart, B. T.; NGuyen, C.; Steiner, B. T.; de Almeida Lima, S.; Molina, F.; Duarte, C. G.; Felicori, L.; Chávez-Olórtegui, C.; Machado-de-Ávila, R. A. Computational B-Cell Epitope Identification and Production of Neutralizing Murine Antibodies against Atrolysin-I. *Sci. Rep.* **2018**, *8* (1), 1–13. <https://doi.org/10.1038/s41598-018-33298-x>.
 - (31) ForteBio. Octet System Data Analysis User Guide. **2011**, 230.
 - (32) Pan, A. C.; Borhani, D. W.; Dror, R. O.; Shaw, D. E. Molecular Determinants of Drug-Receptor Binding Kinetics. *Drug Discov. Today* **2013**, *18*. <https://doi.org/10.1016/j.drudis.2013.02.007>.
 - (33) Tobias, R.; Yao, D.; Kumaraswamy, S. Analysis of FcRn-Antibody Interactions on the Octet Platform. *ForteBio Appl. Note 17* **2019**, 1–13.
 - (34) Packiaseli, S. A.; Rajendran, V.; Vijayalakshmi, R. Structural, Optical and Morphological Study of Tungsten Selenide Thin Films. *Nanosyst. Physics, Chem. Math.* **2016**, *7* (4), 703–706. <https://doi.org/10.17586/2220-8054-2016-7-4-703-706>.
 - (35) Jia, X.; Bai, J.; Ma, Z.; Jiang, X. BSA-Exfoliated WSe₂ Nanosheets as a Photoregulated Carrier for Synergistic Photodynamic/Photothermal Therapy. *J. Mater. Chem. B* **2017**, *5* (2), 269–278. <https://doi.org/10.1039/c6tb02525k>.
 - (36) Wu, P. C.; Yang, C. L.; Du, Y.; Lai, C. H. Scalable Epitaxial Growth of WSe₂ Thin Films on SiO₂/Si via a Self-Assembled PtSe₂ Buffer Layer. *Sci. Rep.* **2019**, *9* (1), 1–10. <https://doi.org/10.1038/s41598-019-44518-3>.
 - (37) Parma, Y. R.; Chacana, P. A.; Lucchesi, P. M.; Rogé, A.; Granobles Velandia, C. V.; Krüger, A.; Parma, A. E.; Fernández-Miyakawa, M. E. Detection of Shiga Toxin-Producing Escherichia Coli by Sandwich Enzyme-Linked Immunosorbent Assay Using Chicken Egg Yolk IgY Antibodies. *Front. Cell. Infect. Microbiol.* **2012**, *2*, 84. <https://doi.org/10.3389/fcimb.2012.00084>.
 - (38) Guirro, M.; Piazza, R. M. F.; de Souza, R. L.; Guth, B. E. C. Humoral Immune Response to Shiga Toxin 2 (Stx2) among Brazilian Urban Children with Hemolytic Uremic Syndrome and Healthy Controls. *BMC Infect. Dis.* **2014**, *14* (1), 320. <https://doi.org/10.1186/1471-2334-14-320>.
 - (39) He, X.; Kong, Q.; Patfield, S.; Skinner, C.; Rasooly, R. A New Immunoassay for Detecting All Subtypes of Shiga Toxins Produced by Shiga Toxin-Producing E. Coli in Ground Beef. *PLoS One* **2016**, *11* (1), e0148092. <https://doi.org/10.1371/journal.pone.0148092>.
 - (40) Brandon, D. L.; Korn, A. M. Immunosorbent Analysis of Toxin Contamination in Milk and Ground Beef Using IgY-Based ELISA. *Food Agric. Immunol.* **2016**, *27* (4), 496–508.

<https://doi.org/10.1080/09540105.2015.1126809>.



Chapter 6

Conclusion



Chapter 6

Conclusion

This chapter summarizes the work detailed in the Chapters 1-5 and presents the future perspectives for the thesis entitled, 'Aptamer functionalized nanostructured biosensing platforms for enteric pathogenic bacteria'.

6.1 Summary of the thesis

6.1.1 Introduction

This introductory chapter brings into light our target of interest– pathogenic *E. coli*, synthesis of aptamers, and novel nanostructures and their sensing application with respect to the conventionally used techniques. We venture into the world of biosensors, which upon its inception, rested on enzymes and antibodies as recognition moieties but gradually moved onto more stable and cost-effective alternatives 'aptamers'. Exploring the synergistic properties of efficient bio-receptor and excellent transducer nanomaterials, we were inspired to develop aptamer functionalized nanostructured sensing platforms known as apta-nanosensors.

6.1.1.1 Enteric pathogenic bacteria

Out of the vast myriad of bacterial species that colonize the gastrointestinal tract, *E. coli* has been a persistent member of the mammalian gut microflora where a majority of its strains maintain a commensal or mutualistic relationship with the human host¹. However, its disease-causing variants genetically encoded with specific virulence factors also exist^{2,3}. Pathogenic *E. coli* has been reported as a significant etiological agent of bacterial gastroenteritis with an infectious dose as low as ~100 cells^{4,5}. These are responsible for chronic or persistent diarrhea, with certain pathotypes producing enterotoxins responsible for the hemolytic uremic syndrome as sequela⁶⁻⁸.

This chapter also describes the various mainstay conventional techniques both microbiological and molecular methods conventionally used for detection of bacteria. Conventional 'gold standard' microbiological tools require 2-3 days for identification and are mostly qualitative in nature^{9,10}. The current diagnostic approaches are majorly reliant on antibody-based assays or mass spectrometry, which utilize costly reagents and require specific instrumentations for estimation¹¹. Thus, the challenge lies in developing sensitive, rapid, non-culture dependent, and cost-effective methodologies for the sensing of enteric pathogenic bacteria, which are required for timely monitoring in food, clinical, and municipal sectors. This problem at hand was addressed by development of nanostructured aptasensors using novel indigenous methods, described in Chapters 2-5.

6.1.1.2 Nanostructured aptasensors

Integrated biosensing platforms with specific nucleic acid aptamers and sensitive nanostructured transducers, providing near real-time information on the presence of enteric targets, are proposed in this doctoral thesis. With the advent of nanomaterials and advances in nucleic acid research, the biosensing domain supplemented with bioinformatics has radically evolved, enabling analyte detection at low levels with high precision. Consequently, both these aspects were extensively researched upon in the thesis to develop *nanostructured aptasensors* for sensing pathogenic *E. coli* serotypes and associated biomolecules.

Nanostructures of various dimensions based on carbon, metal-carbon nanohybrids, and more recently, its 2D analogs transition metal chalcogenides, harboring fascinating electronic, optoelectronic, and physical qualities such as abundant surface charges, high surface-to-volume ratio, and easy functionalization abilities were synthesized indigenously via various top-down and bottom-up approaches and utilized as transducers in the biosensing platforms.

Simultaneously, for the bio-receptor component, DNA aptamers (single-stranded oligomers with high binding affinity with the specific target) were chosen, providing low cross-reactivity and high stability than conventionally available counterparts^{12,13}. The generation of aptamer-based bio-receptor against a pathogen gives an added advantage to synthetically produced aptamers versus antibodies raised in animal models both physiologically and ethically¹⁴. The studies reported in this thesis majorly gravitate around biosensing pathogenic *E. coli* (serotypes O78:H11 and O157:H7) with aptamer-based nanostructured sensing technology as the critical line of detection approach.

6.1.1.3 Our aptasensing approaches

We devised a three-way approach for aptamer generation stemming from alternative enhanced binding affinities for the target in various environments, which was based on the hypothesis that the presence of both whole-cell or its components is possible for monitoring the bacterial targets. Therefore, multiple respective aptamers were screened against the avirulent strains of whole-cell *E. coli* (enterotoxigenic serotype O78:H11 and enterohemorrhagic serotype O157:H7), surface antigens (O & H-antigen) for serotype O157:H7, and Shiga-like toxins (Stx1 and Stx2) utilized as bio-recognition moieties, which are comprehensively explored one-by-one during the doctoral studies and comprehensively tabulated in Table 6.1.

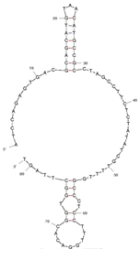
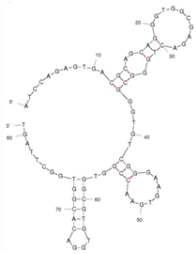
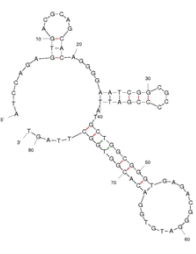

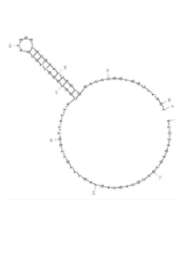
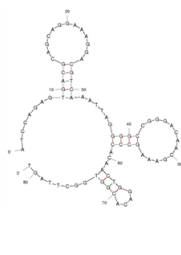
Enteric target	Aptamer sequence	Mfold structure	K _d	T _m (°C)	ΔG (kcal mol ⁻¹)	ΔH (kcal mol ⁻¹)	ΔS (cal K·mol ⁻¹)	G-quad position
Whole cell <i>E. coli</i> O78:H11	ATCCAGAGTGACGCAGCAT GTAACATGCCGCCTAGCCT TCTCTATATCGTTTTGGCCC TCCTTTGGACACGGTGGCTT AGT		14.1 nM	51.1	-4.10	-93.9	-289	N-54 (GGCCCTCCTTTGGAC ACGGTGG)
Whole cell <i>E. coli</i> O157:H7	ATCCAGAGTGACGCAGCAG GGTGGCGAGACTGGCGGG TGTCCGGGAAGTGAACCCGGT GGCGTGTGGACACGGTGGC TTAGT		69.0 nM	59.0	-8.02	-121	-364	N-19 (GGGTGGCGAGACTGG GCCGGTGTCCGGG) N-58 (GGCGTGTGGACACGG TGG)
O-antigen <i>E. coli</i> O157:H7	ATCCAGAGTGACGCAGCAC AGGGAAATCGGCCGCCCGA TTATGCTGGCGGTTGAGAC GGGATGTGGACACGGTGGC TTAGT		5.30 nM	61.4	-8.66	-118.7	-354	N-21 (GGGGAATCGGCCGCC CGATTATGCTGG) N-50 (GGTGAGACGGGATGT GGACACGG)
H-antigen <i>E. coli</i> O157:H7	ATCCAGAGTGACGCAGCAT GTGTTCCGGTGTCTGACGTC GAGGTGCTGTGGGGGGGGA TGAGGCTGGACACGGTGGC TTAGT		4.60 nM	56.4	-3.74	-63.4	-192	N-26 (GGTGTCTGACGTCGA GGTGTCTGTGGGGG) N-55 (GGATGAGGCTGGACA CGG)
Stx1	ATCCAGAGTGACGCAGCAG TAGTTTGTGGTTATTACGG CGGGTTGCCGATGGGTGCGA ATCGGTGGACACGGTGGCT TAGT		47.0 pM	53.5	-2.07	-40.9	-125	N-29 (GGTTATTACGGCGGG TTGCCGATGG) N-62 (GGTGGACACGGTGG)
Stx2	ATCCAGAGTGACGCAGCAG GAAAGGACGTCAAAATTAGG GGCCGGGACAAACGAAAGCC CACAACTGGACACGGTGGC TTAGT		29.0 pM	56.0	-5.67	-97.7	-296	N-26 (GGAAAGGACGTCAAA TTAGGGGGCCGG)

Table 6.1: Generated aptamers: A comparative table showing the specific aptamers selected for various bacterial targets in this thesis.

The objective was also to explore methodologies for aptamer generation and the simultaneous synthesis of nanostructures relevant for aptasensing via spectroscopic and electrochemical tools. Furthermore, the various aptamer functionalized nanostructured biosensing platforms were developed and tested & validated in buffer and spiked food samples. Table 6.2 gives an overview of the various developed biosensing platforms discussed in the thesis chapters.

Target	Nanostructure	Method	LOD	Range
Whole cell <i>E. coli</i> O78:H11	BRG	EIS	10 ¹ cfu	10 ¹ – 10 ⁶ cells
Whole cell <i>E. coli</i> O157:H7	BC-Ni nanorods	EIS	10 ⁰ cfu	10 ⁰ – 10 ⁵ cells
Surface antigens <i>E. coli</i> O157:H7	C-dots	Fluorescence spectroscopy	O: 0.1 pg mL ⁻¹ H: 1.0 pg mL ⁻¹	O: 0.1 pg mL ⁻¹ - 10 ng mL ⁻¹ H: 1.0 pg mL ⁻¹ – 1.0 ng mL ⁻¹
<i>E. coli</i> Stx subtypes	chito-WSe ₂ nanosheets	SWV	Stx1: 44 pg mL ⁻¹ Stx2: 41 pg mL ⁻¹	50 pg mL ⁻¹ -100 ng mL ⁻¹

Table 6.2: Aptasensing nanostructured platforms: A comparative table showing the merits of the various aptamer functionalized nanostructured platforms fabricated in this thesis. (O: O antigen and H: H antigen)

6.1.2 Nanostructured aptasensor for enterotoxigenic *E. coli*

Thus, in line with our aim both major components of a biosensor for detection of one of the selected enterotoxigenic *E. coli* strain O78:H11 was carried out using whole-cell approach.

6.1.2.1 Bioreceptor generation: Microtiter cell-SELEX

DNA aptamer with an excellent affinity K_d of 14 nM for *E. coli* serotype O78:H11 was successfully screened from a naïve oligomer library of 81 nt with 45 random nt region, implementing indigenous in-vitro selection SELEX methodology of oligomer panning for the selected target. This novel microtiter cell-SELEX used phenylboronic acid as a capturing agent for *E. coli* bacteria accompanied by counter screening to mitigate aptamer cross-talk with other closely related bacterial species. These respective novel aptamers were characterized, and their target-ligand bio-interaction studied using wet-lab techniques (UV-vis spectroscopy, fluorescence binding assays, BLI kinetic assays, confocal fluorescence microscopy) augmented with dry-lab bioinformatic tools (mfold, QGRS mapper, RNA composer) to present the putative aptamer structures showing complex conformations like loop-stem folding and G-quad motifs¹⁵⁻¹⁷.

6.1.2.2 Nanostructure synthesis: BRG

BRG was synthesized from MWCNT using a modified chemical facilitated un-scrolling method followed by intra-sheet bridging with terephthaldehyde to form a 3D hierarchical nanostructure showing enhanced surface and electrical properties. This 3D nanostructure was fully characterized using scanning electron microscopy, ultraviolet-visible spectroscopy, confocal Raman spectroscopy, Fourier transform Infra-red spectroscopy and X-ray diffraction, zeta potential, cyclic voltammetry and impedance spectroscopy. Surface modification with selected high-affinity

aptamers were carried out using cationic biopolymer PLL, which aided in the functionalization of DNA aptamers onto PLL-modified surfaces, aiding fabrication of aptasensing platforms.

6.1.2.3 Nanostructured aptasensing platform

Label-free impedimetric sensing of *E. coli* O78:H11 was successfully demonstrated using novel selected aptamer functionalized BRG onto disposable screen-printed electrodes demonstrating a limit of detection of ~ 10 cells and a dynamic response range from 10^1 to 10^6 cells.

6.1.3 Nanostructured aptasensor for enterohemorrhagic *E. coli*

6.1.3.1 Bioreceptor generation: Microtiter cell-SELEX

Specific DNA aptamer-based receptors against selected *E. coli* O157:H7 using whole-cell target with an excellent nanomolar affinity $K_d \sim 69$ nM was successfully screened using similar modified cell-SELEX methodology. Consequently, these respective novel aptamers were fully characterized using wet and dry-lab tools employed in the previous chapter.

6.1.3.2 Nanostructure synthesis: BC-Ni nanorods

Conductive boron-carbon nanorods decorated by nickel nanoparticles synthesized by a two-step carbonization method using Ni(II)- dimethylglyoxime complex and boric acid as reaction precursors showing a manifold increase in the electrode current response. This 1D nanostructure was fully characterized using transmission electron microscopy, energy-dispersive X-ray elemental mapping, ultraviolet-visible spectroscopy, confocal Raman spectroscopy, Fourier transform Infra-red spectroscopy and X-ray diffraction, zeta potential, cyclic voltammetry and impedance spectroscopy. The aptamers were functionalized with the aid of PLL onto the nanomaterial modified working electrode of screen-printed electrodes for analysis.

6.1.3.3 Nanostructured aptasensing platform

Label-free impedimetric sensing of *E. coli* O157:H7 was showed using specific aptamer functionalized boron-carbon nanorods decorated by nickel nanoparticles with a similar limit of detection and a dynamic detection range of 10^0 to 10^5 cells in water and juice samples. The developed nanostructured aptasensors showed quick results, negating the enrichment of bacterial load in test samples as required in conventional systems. The aptamers also showed admirable application as capture & detection for bacterial populations onto soft-lithographed polydimethylsiloxane based microfluidic platforms, which is presented as a proof-of-concept.

6.1.4 Aptasensing optical assay for *E. coli* surface antigens

6.1.4.1 Bioreceptor generation: Competitive microtiter-SELEX

Competitive microtiter-SELEX employing rival ligands for raising stringency for purified *E. coli* O157:H7 endotoxin and flagellar proteins (K_d of 5.3 and 4.6 nM, respectively) was developed. Consequently, these respective novel aptamers were fully characterized using wet and dry-lab tools

employed in the previous chapters. Alongside, the bio-interaction modelling studies for H-antigen with the aptamer selected were also carried out with the aid of online bioinformatic tools; Zdock and M-Zdock.

6.1.4.2 Nanostructure synthesis: Tris base based C-dots

Fluorescent tris(hydroxymethyl)aminomethane derived water-soluble bright cyan *c-dots* having $\lambda_{\text{emission}} \sim 426$ nm, with a quantum yield of 14.9 % vs. quinine sulfate. These aqueous carbon quantum dots were synthesized using hydrothermal approach and in conjugation with silver nanoparticles acted as an energy transfer pair ‘turn-off’ fluorescence assay. These 0D nanostructure were fully characterized using fluorescence spectroscopy, transmission electron microscopy, ultraviolet-visible spectroscopy, confocal Raman spectroscopy, Fourier transform Infra-red spectroscopy and X-ray diffraction and zeta potential techniques. The aptamer/*c-dot* conjugates were developed with aid of charge-based interaction and employed in a fluorescence-based assay.

6.1.4.3 Nanostructured aptasensing platform

Fluorescence ‘turn on’ bioassay based on fluorescence quenching of aptamer functionalized carbon-dots by silver nanoparticles, to detect targeted surface antigens with a detection limit of 0.1 pg mL^{-1} for O-antigen and wide detection range from 0.1 pg mL^{-1} to 10 ng mL^{-1} and an anti-H antigen apt/*c-dot* conjugate assay was carried out for the H-antigen of *E. coli* O157:H7 showing significant fluorescence restoration from $0.001 - 1.0 \text{ ng mL}^{-1}$ with a limit of detection of 0.1 pg mL^{-1} . These apta-assays showed the stable response recorded even in pure water.

6.1.5 Nanostructured aptasensor for *E. coli* Shiga-like toxin

6.1.5.1 Bioreceptor generation: BLI SELEX

BLI based SELEX using Octet Red96 system, a one-step technique for rapidly generating aptamers against *E. coli* Shiga toxin subtypes viz., Stx1 & Stx2 via specific epitopic peptides (K_d of 47 pM & 29 pM, respectively) in a dip microtiter plate format, obliterating the need for multiple oligomer enrichment cycles was designed and demonstrated. The elucidates aptamers were fully characterized with tools and techniques described in previous chapters.

6.1.5.2 Nanostructure synthesis: chito-WSe₂ nanosheets

Liquid-exfoliated 2D-transition metal dichalcogenide WSe₂ nanosheets utilizing green biopolymer chitosan imparting high sensitivity to the aptasensing assay. These were fully characterized using microscopic and electrochemical techniques. This chitosan exfoliated and functionalized nanosheets helped in further modification with aptamer via surface charges on biopolymer chitosan and negatively charged nucleic acid-based aptamers.

6.1.5.3 Nanostructured aptasensing platform

The developed square-wave voltammetry based aptasensor showed a sensitivity of $\sim 5 \mu\text{A ng}^{-1} \text{ mL}$ with a limit of detection of 44.5 pg mL^{-1} for toxin Stx1 and 41.3 pg mL^{-1} for Stx2. The selectivity of

the sensors for target toxins far exceeded that of cross-reactive toxin subtype and other interfering proteins or polysaccharides and showed low cross-reactivity in spiked sera and milk samples.

6.2 Concluding remarks & future perspectives

6.2.1 Thesis contributions

(i) Advancements in aptamer technology

This thesis gives a vision into the development of tailor-made in-vitro, facile, rapid, specific, and robust nucleic acid-based aptamer selection approaches for bacterial pathogens, associated surface markers & toxins, which can be further extrapolated after finer tuning for other disease markers like diabetes mellitus, cardiovascular diseases, hypertension, carcinoma, sepsis, parasitic infections like malaria & chikungunya and viral infections like hepatitis and influenza. In view of current COVID-19 pandemic, aptamers may be exploited as a diagnostic probe against coronavirus and its specific antigens like spike protein, nucleocapsid that discern SARS-Cov2 from its variants for rapid and cost-effective diagnosis due to its in-vitro synthesis, especially in case of infectious viral agents where antibody generation has been a hassle. Furthermore, fluorophore labelled aptamers maybe used for imaging viral RNA. Aptamers specific to different and multiple epitopes may be generated by BLI SELEX technology in a single pot methodology and utilized for specific multiplexed assays.

(ii) Functional nanostructured bio-probes

The design, synthesis & characterization of unique nanostructures showing extra-ordinary optical and semiconducting properties and bio-functionalization of these synthesized nanomaterial with generated aptamers as receptors, with the aid of linker molecules like PLL or charge based interactions, enhances their potential application as specific biosensing platforms.

6.2.2 Future explorations

Connect between bio-receptor chemistry, bio-physical analytical techniques and material science is important for advances in device fabrications. In this thesis we have tried to achieve the same, but further, comprehensive explorations in the realm of aptasensing platforms is needed.

(i) Flexible aptamer structure, environmental influences and thermodynamic parameters is required for core understanding of the intra and inter-molecular interactions for improving application of aptamers as both bioreceptor in diagnostic platforms and well as in theranostic approaches.

(ii) Truncation and mutagenesis methods for identification of aptamer binding domains, which play significant role in target recognition are required.

(iii) Development of high-throughput selection methodologies for facile generation of nuclease-resistant aptamers is required.

Nonetheless, the works included in this thesis are advantageous for the development of advanced analytical platforms using easy, cost & reagent-effective protocols for pathogen or bio-analyte determination and holds promising future perspectives in the field of in-vitro clinical diagnostics.

Bibliography

- (1) Biomechanics of the Digestive System. In *Integrated Nano-Biomechanics*; Elsevier, 2018; pp 71–99. <https://doi.org/10.1016/b978-0-323-38944-0.00003-6>.
- (2) Kaper, J. B.; Nataro, J. P.; Mobley, H. L. T. Pathogenic Escherichia Coli. *Nat. Rev. Microbiol.* **2004**, 2 (2), 123–140. <https://doi.org/10.1038/nrmicro818>.
- (3) Leimbach, A.; Hacker, J.; Dobrindt, U. E. Coli as an All-Rounder: The Thin Line between Commensalism and Pathogenicity. *Curr. Top. Microbiol. Immunol.* **2013**, 358, 3–32. https://doi.org/10.1007/82_2012_303.
- (4) Pennington, H. Escherichia Coli O157. *Lancet* **2010**, 376 (9750), 1428–1435. [https://doi.org/10.1016/S0140-6736\(10\)60963-4](https://doi.org/10.1016/S0140-6736(10)60963-4).
- (5) Nataro, J. P.; Kaper, J. B. Diarrheagenic Escherichia Coli. *Clinical Microbiology Reviews.* January 1998, pp 142–201. <https://doi.org/10.1128/cmr.11.1.142>.
- (6) Saxena, T.; Kaushik, P.; Krishna Mohan, M. Prevalence of E. Coli O157: H7 in Water Sources: An Overview on Associated Diseases, Outbreaks and Detection Methods. *Diagn. Microbiol. Infect. Dis.* **2015**, 82 (3), 249–264. <https://doi.org/10.1016/j.diagmicrobio.2015.03.015>.
- (7) Yang, S. C.; Lin, C. H.; Aljuffali, I. A.; Fang, J. Y. Current Pathogenic Escherichia Coli Foodborne Outbreak Cases and Therapy Development. *Arch. Microbiol.* **2017**, 199 (6), 811–825. <https://doi.org/10.1007/s00203-017-1393-y>.
- (8) Croxen, M. A.; Law, R. J.; Scholz, R.; Keeney, K. M.; Wlodarska, M.; Finlay, B. B. Recent Advances in Understanding Enteric Pathogenic Escherichia Coli. *Clin. Microbiol. Rev.* **2013**, 26 (4), 822–880. <https://doi.org/10.1128/CMR.00022-13>.
- (9) Lazcka, O.; Campo, F. J. Del; Muñoz, F. X. Pathogen Detection: A Perspective of Traditional Methods and Biosensors. *Biosens. Bioelectron.* **2007**, 22 (7), 1205–1217. <https://doi.org/10.1016/j.bios.2006.06.036>.
- (10) Humphries, R. M.; Linscott, A. J. Laboratory Diagnosis of Bacterial Gastroenteritis. *Clin. Microbiol. Rev.* **2015**, 28 (1), 3–31. <https://doi.org/10.1128/CMR.00073-14>.
- (11) BAM Chapter 4A: Diarrheagenic Escherichia coli | FDA <https://www.fda.gov/food/laboratory-methods-food/bam-chapter-4a-diarrheagenic-escherichia-coli> (accessed Aug 22, 2020).
- (12) Wu, Y. X.; Kwon, Y. J. Aptamers: The “Evolution” of SELEX. *Methods* **2016**, 106, 21–28. <https://doi.org/10.1016/j.ymeth.2016.04.020>.
- (13) Ali, M. H.; Elsherbiny, M. E. Updates on Aptamer Research. **2019**, 1–23.
- (14) Gu, M. B.; Kim, H. S. Biosensors Based on Aptamers and Enzymes. *Adv. Biochem. Eng. Biotechnol.* **2014**, 140. <https://doi.org/10.1007/978-3-642-54143-8>.
- (15) Zuker, M. Mfold Web Server for Nucleic Acid Folding and Hybridization Prediction. *Nucleic Acids Res.* **2003**, 31 (13), 3406–3415. <https://doi.org/10.1093/nar/gkg595>.
- (16) Kikin, O.; D’Antonio, L.; Bagga, P. S. QGRS Mapper: A Web-Based Server for Predicting G-Quadruplexes in Nucleotide Sequences. *Nucleic Acids Res.* **2006**, 34 (Web Server), W676–W682. <https://doi.org/10.1093/nar/gkl253>.
- (17) Antczak, M.; Popenda, M.; Żok, T.; Sarzynska, J.; Ratajczak, T.; Tomczyk, K.; Adamiak, R. W.; Szachniuk, M. New Functionality of RNAComposer: An Application to Shape the Axis of MiR160 Precursor Structure. *Acta Biochim. Pol.* **2016**, 63 (4), 737–744. https://doi.org/10.18388/abp.2016_1329.

Publications

- (1) * **Kaur, H.**; Shorie, M.; Sharma, M.; Ganguli, A. K.; Sabherwal, P. Bridged rebar graphene functionalized aptasensor for pathogenic *E. coli* O78:K80:H11 detection. *Biosens. Bioelectron.* 2017, 98 (June), 486–493. <https://doi.org/10.1016/j.bios.2017.07.004>.
- (2) * **Kaur, H.**; Shorie, M.; Sabherwal, P. Electrochemical aptasensor using boron-carbon nanorods decorated by nickel nanoparticles for detection of *E. coli* O157:H7. *Microchim. Acta* 2020, 187 (8), 461. <https://doi.org/10.1007/s00604-020-04444-y>.
- (3) * **Kaur, H.**¹; Shorie, M.¹; Sabherwal, P. Biolayer interferometry-SELEX for shiga toxin antigenic-peptide aptamers & detection via chitosan-WSe₂ aptasensor. *Biosens. Bioelectron.* 2020, 167, 112498. <https://doi.org/10.1016/j.bios.2020.112498>.
- (4) Shorie, M.¹; **Kaur, H.**¹; Chadha, G.; Singh, K.; Sabherwal, P. Graphitic carbon nitride QDs impregnated biocompatible agarose cartridge for removal of heavy metals from contaminated water samples. *J. Hazard. Mater.* 2019, 367 (September 2018), 629–638. <https://doi.org/10.1016/j.jhazmat.2018.12.115>.
- (5) Kumar, V.; Brent, J. R.; Shorie, M.; **Kaur, H.**; Chadha, G.; Thomas, A. G.; Lewis, E. A.; Rooney, A. P.; Nguyen, L.; Zhong, X. L.; Burke, M. G.; Haigh, S. J.; Walton, A.; McNaughten, P. D.; Tedstone, A. A.; Savjani, N.; Murny, C. A.; O'Brien, P.; Ganguli, A. K.; Lewis, D. J.; Sabherwal, P. Nanostructured aptamer-functionalized blackphosphorus sensing platform for label-free detection of myoglobin, a cardiovascular disease biomarker. *ACS Appl. Mater. Interfaces* 2016, 8 (35), 22860–22868. <https://doi.org/10.1021/acsami.6b06488>.
- (6) Tomer, V. K.; Singh, K.; **Kaur, H.**; Shorie, M.; Sabherwal, P. Rapid acetone detection using indium loaded WO₃/SnO₂ nanohybrid sensor. *Sensors Actuators B Chem.* 2017, 253, 703–713. <https://doi.org/10.1016/j.snb.2017.06.179>.
- (7) Shorie, M.; Kumar, V.; **Kaur, H.**; Singh, K.; Tomer, V. K.; Sabherwal, P. Plasmonic DNA hotspots made from tungsten disulfide nanosheets and gold nanoparticles for ultrasensitive aptamer-based SERS detection of Myoglobin. *Microchim. Acta* 2018, 185 (3). <https://doi.org/10.1007/s00604-018-2705-x>.
- (8) * **Kaur, H.**; Shorie, M.; Sabherwal, P. Aptamer functionalized carbon dots mediated fluorescence turn-on assay for endotoxin detection. (*Under revision*)

NB: *Articles included in the doctoral thesis

¹ Equal contribution

Vita

Harmanjit Kaur

PhD Fellow

Institute of Nano Science and Technology, Mohali, India

Indian Institute of Science Education and Research, Mohali, India



Ms. Harmanjit Kaur earned her Bachelor in Bio-Technology (Honours) and Master in Bio-Technology (Honors School) degrees from Panjab University, India in 2011 and 2013, respectively. Over the period, she underwent various academic & industrial training in bio-techniques ranging from plant tissue culture, molecular biology, microbiology & cell culture. In 2014, she joined the Institute of Nano Science and Technology (INST), Mohali as a PhD researcher under the guidance of Dr. Priyanka Sabherwal & Prof. Ashok Ganguli (founder Director, INST). Later she concluded her doctoral studies under the mentorship of Dr. Priyanka Sabherwal and Dr. Sharmistha Sinha. Her research work majors in the development of nanostructures & aptamers for biosensing applications and has since authored several research articles in reputed peer reviewed journals with >300 citations. Her research interests include development & study of recognition moieties, especially aptamers, fabrication of novel nanostructures, and the development of optical, electrochemical & microfluidic platforms for food, environmental & clinical applications.

